UNIVERSITY OF LIVERPOOL

Synthesis and Analysis of New Lithium-Ion Battery Cathode Materials

Thesis submitted in accordance with the requirements of the University of Liverpool for the degree of Doctor in Philosophy by:

Zoe Nicola Taylor

December 2017

Supervised by

Professor M. J. Rosseinsky FRS

Dr J. B. Claridge

Abstract

The work presented in this thesis focuses on the synthesis and structural characterisation of functional materials for lithium-ion battery cathode applications, with the most promising class of lithium-ion battery cathodes were determined to be lithium-rich rock-salt superstructures. In addition to oxidation of transition metal cations during charging (cationic redox), the anionic redox process involves partial oxidation of lattice oxide (O^{2-}) to form intermediate peroxo-type species (O_2^{n-}) to enable additional lithium extraction to maintain electroneutrality in the delithiated structure. Suppression of full oxidation of lattice oxide to molecular oxygen is a key requirement to utilising the lattice oxygen to reversibly extract additional capacity, without compromising the safety and longevity of the battery materials. The mechanisms of lithium ion extraction and insertion into cathode materials are discussed in relation to their structures.

Chapter 3 focuses on the structural solution of new lithium-rich rock-salt superstructures of the form $Li_{4+x}Ni_{1-x}WO_6$ (x = 0, 0.1, 0.15), by combined Rietveld refinement of high-resolution synchrotron and neutron powder diffraction data. Li_4NiWO_6 was found to crystallise in the *C*2/*c* space group, determined to be a monoclinic distortion of the *Fddd* $Li_3Ni_2TaO_6$ structural archetype. $Li_{4.1}Ni_{0.9}WO_6$ and $Li_{4.15}Ni_{0.85}WO_6$ were found to crystallise into the non-centrosymmetric *Cm* space group, comparable to the layered *C*2/*m* Li_5ReO_6 archetype.

Chapter 4 assesses the electrochemical behaviour of $Li_{4.15}Ni_{0.85}WO_6$, obtaining a specific discharge capacity of 200-210 mA·h g^{-1}, with a reversible capacity of 173 mA·h g^{-1} when cycled between 1-5 V; attributed to cumulative cationic and anionic redox reactions. *Ex-situ* X-ray photoelectron spectroscopy (XPS) was used to

determine the oxidation states of the cations and oxygen species, showing the reversibility of the redox reaction between lattice oxide and peroxo-type species during the first two electrochemical cycles. By comparison to the observed nickel oxidation states from XPS and X-ray near-edge structure (XANES) spectroscopic analysis, the reversible anionic redox was determined to be responsible for ~2/3 of the observed discharge capacity.

Chapter 5 details the solid state synthesis of an unreported solid solution (1-*x*)$LiCoO_2$·*x*Li_4WO_5, with successful doping of small amounts of rock-salt Li_4WO_5 ($P\bar{1}$) into the layered $LiCoO_2$ ($R\bar{3}m$) structure determined by analysis of powder X-ray diffraction (PXRD) data. Electrochemical testing was performed on $x = 0.010$ and $x = 0.025$, exhibiting initial discharge capacities of 124 and 128 mA·h g^{-1}, respectively. The analogously prepared parent phase, $LiCoO_2$, displayed an initial discharge capacity of 121 mA·h g^{-1}. A considerably greater proportion of the available capacity could be extracted from $x = 0.010$ and $x = 0.025$ at fast discharge rates by comparison to $LiCoO_2$; with the doped materials exhibiting a greater retention of the higher discharge capacity during continued cycling.

Chapter 6 assesses the synthetic method of flame spray pyrolysis (FSP) for known lithium-ion battery cathodes, using a simple laboratory setup. This technique is used for the production of nanoparticulate products from liquid precursors. The intention was to improve the diffusion kinetics through a reduction in particle size. The merits and limitations of the technique are discussed in relation to the purity, crystallinity and morphology of simple lithium metal oxides assessed by PXRD, scanning electron microscopy and ICP-OES. In addition, due to slow diffusion kinetics being a limiting factor in the performance of polyanionic cathode materials, the possibility of synthesis of such materials by FSP is assessed.

Acknowledgements

Firstly, I would like to thank my supervisor, Professor Matt Rosseinsky for allowing me this opportunity. Many thanks also go to Dr John Claridge, primarily for having patience with me, despite my ‘shocking behaviour(!)’. Thanks also to the EPSRC and the unknowing taxpayer for their monetary contributions. Special thanks go to Dr Mike Pitcher and Dr Matthew Dyer for coordinating my 4+ years of research, with additional thanks to Mike for being my primary proof-reader. Special mentions for Dr Julia Payne for directing me during my first 6 months, Dr Chris Collins for the genuine powder diffraction help, Dr Troy Manning for the career advice and guiding me through my first year and Jane Remmer for being the group’s shoulder to cry on. Special thanks go to Dr Marco Zanella, Dr Hongjun Nui and Richard Feetham for keeping our research running smoothly, and for the office banter. Having spent so long in such a large research group, there are far too many to name individually, most people through the years have helped me in some way or another.

Huge thanks go to my best friends I have made throughout my time here. Jibreel Haddad, nearly 4 fantastic years together. We laughed, and we cried…but we made it out alive! Oliver ‘lovely Oliver’ Wilcox, my main man, for always being there. And proving that procrastination works. If you choose not to read the email, does it even exist? Harry Sansom, my long time desk neighbour. We sang, we danced, and we occasionally lost the will to live. I could not have made it through without these three. Massive appreciation for Daniel Warrilow-Brennan, my fellow sceptical people-hater, whose knowledge of how the world works is actually quite helpful, if not bleak. Thanks for telling it how it is. Friends and colleagues who have come and gone over the years: Gethin (a genuinely lovely person with a fantastic accent), Tom

(a fascinating grumpy northerner), Rachel (with an individuality I truly admire), Tim (for those puns), George (my fellow cat lover) and Jyoti (always up for an Alton Towers trip). Those I leave behind (Bernhard and that dry sense of humour, Verity for a nonplussed attitude I admire, Luis the coolest guy I have ever met, Jason and his enviable carefree attitude, Aris for the best laugh in the whole word - just to name a few) – thanks for making it somewhat bearable, usually over a few drinks.

To my parents I want to say thank you, mainly for the financial support and the occasional compliment about how clever I am, and their encouragement in my pursuit of a career in chemistry. Special mention to Aunty Chris and Gordon, my most reliable drinking buddies; Aunty Chris for helping put life into perspective, and Gordon for being the only person in my family who is remotely interested in what I spent these 4 years doing.

Finally I want to thank Emma, for her unrelenting encouragement and reassurance, genuine belief in me and those much needed food and coffee deliveries that probably kept me alive.

Contents

Chapter 1: Introduction

The drive towards decreasing the world's reliance on finite fossil fuel resources hence reducing their environmental impact such as carbon dioxide emissions has made the development of renewable energy supplies a primary focus of scientific research. In addition to the development of technology required for harvesting renewable energy sources, such as solar and wind power, it is imperative that the development of energy storage devices keep pace with this advancing technology for safe and long term storage of electrical energy.

Aside from secondary lithium ion batteries, many researchers are focused on the development of intercalation compounds for Na^+, K^+, Mg^{2+}, Ca^{2+} and Al^{3+} for battery applications, due to their greater natural abundance than lithium. Batteries based on the redox of these ions are thought to be safer than LIBs, and have the potential to exhibit higher capacity per ion due to utilising higher charge density ions but at the expense of heavier cations and less negative reduction potentials, meaning they are more suitable for stationary batteries for storage of electrical power.[1]

1.1 Rechargeable Lithium Ion Batteries

The advancement of electric vehicles (EVs) is not only being climatologically desirable, but increasingly necessary due to the depletion of oil resources. For the foreseeable future, this is an ideal which can be realised with rechargeable batteries, supplying a high energy and power density, providing the range and acceleration required for modern vehicles.

1.1.1 Overview

Lithium ion batteries (LIBs) are a family of rechargeable (or 'secondary') batteries commonly used to power portable electronic devices such as mobile telephones and laptop computers, owing to their high capacity and energy density, good life cycle, absence of the memory effect and minimal self-discharge when not in use (in contrast to nickel-metal hydride batteries). It is important to note the difference between primary lithium batteries and secondary lithium ion batteries: primary lithium batteries are not rechargeable and employ lithium metal as the anode, whereas secondary lithium ion batteries employ a low potential lithium ion insertion anode and a high potential insertion cathode with reversible redox reactions.

The low mass and large negative reduction potential of lithium metal (Li^+/Li^0 -3.045 V E°) enables a relatively high power density when Li species are employed in an electrochemical cell - values for lithium ion battery voltages are reported in comparison to the Li^+/Li^0 couple, not the standard reduction potential. Due to such advantages of LIBs, there is much interest to further improve the power and energy density of current technologies and expand into their application in EVs. Unfortunately there are also numerous challenges limiting the use of LIBs in EVs, the most important being safety concerns due to the explosion risks of the organic components.

Commercial LIBs comprise a number of connected electrochemical cells, which consist of an anode, cathode and a non-aqueous electrolyte, separated by a diaphragm (Figure 1.1.1). The electrodes are externally connected to complete the circuit of electrons, which do work on the load. The most common commercial battery comprises a $LiCoO_2$ cathode and a graphite anode. Typically the electrolyte is

composed of organic liquids such as alkyl carbonates, with dissociated lithium salts such as $LiPF_6$, to enable lithium ion transfer between the electrodes.

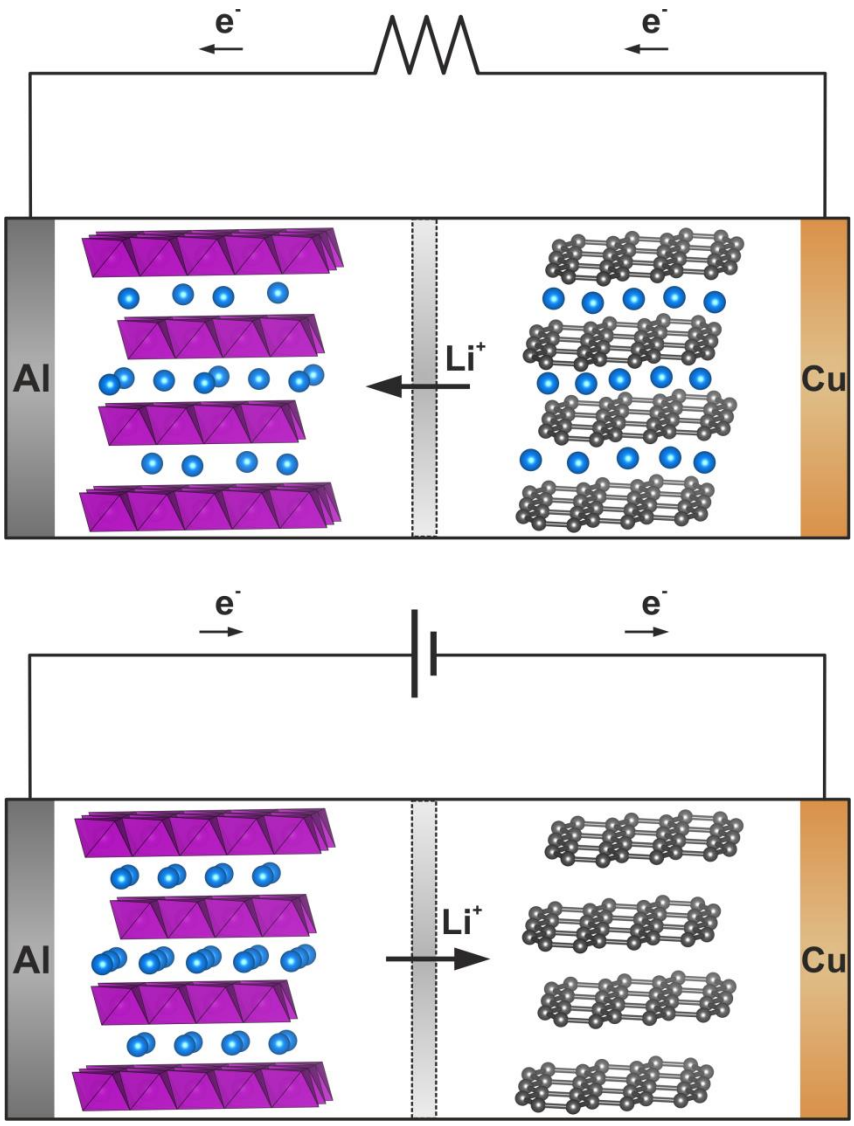

Figure 1.1.1: Schematic of a typical lithium ion cell during discharge (*top*) and charge (*bottom*). The positive insertion electrode (cathode, *left*) is represented by $LiCoO_2$ showing the CoO_6 polyhedra (*purple*) and lithium ions (*blue*). The negative insertion electrode (anode, *right*) is represented by graphite. Arrows indicate the flow of Li^+ through the electrolyte and separator (*centre*); and flow of electrons through the external circuit and aluminium and copper current collectors

Upon discharging (*i.e.* battery use), lithium ions deintercalate from the anode and one electron per Li^+ is donated ultimately to the cathode. The potential difference between

the cathode and anode determines the operating voltage of the cell. The lithium ions diffuse through the electrolyte to lithiate the cathode and the electrons create a current through the external circuit (Figure 1.1.1, *top*). The cathode material contains at least one transition metal which is reduced on discharge, allowing the incorporation of one lithium ion into the structure per electron accepted by the transition metal ion. Overall, on battery discharge the anode is oxidised and the cathode is reduced. Reversible chemical reactions occur at both the anode and cathode as lithium is deintercalated/intercalated and electrons are lost/gained, and structural changes occur.[2] Rechargeable batteries are charged upon the application of a controlled over-potential from an external power source, causing electrons and lithium ions to flow back from the cathode to the anode, where they combine to form lithium metal which intercalates into the porous anode structure (Figure 1.1.1, *bottom*).

Both the anode (Section 1.2.2) and cathode (Section 1.3) require good electronic conductivity, with electrons able to flow freely throughout the electrodes *via* external current collectors. The electrolyte (Section 1.2.3) must be an electronic insulator, otherwise the cell will short-circuit. The cathode, anode and electrolyte must enable facile lithium ion diffusion throughout the materials, with minimal volume and structural change of the electrodes occurring on (de)intercalation of lithium. Since the electrolyte wets the surface of both electrodes, the electrolyte must be adequately stable to minimise detrimental side reactions with electrodes.

1.1.2 Electrochemistry

The open-circuit voltage (V_{OC}) of a lithium-ion cell is determined by the difference in electrochemical potential between the two electrodes when no external load is connected. When the difference between the chemical potentials of the anode and cathode is high, the cell will have a higher voltage and hence a greater power output.

However, to ensure electrochemical stability, the redox energies of the electrodes must lie within the stability window of the electrolyte (E_g), which is defined as the energy separation between the highest occupied molecular orbital (HOMO) and lowest unoccupied molecular orbital (LUMO) of the electrolyte (Figure 1.1.2). Liquid electrolytes wet both the anode and the cathode so this thermodynamic stability is imperative for a battery with a long lifetime.

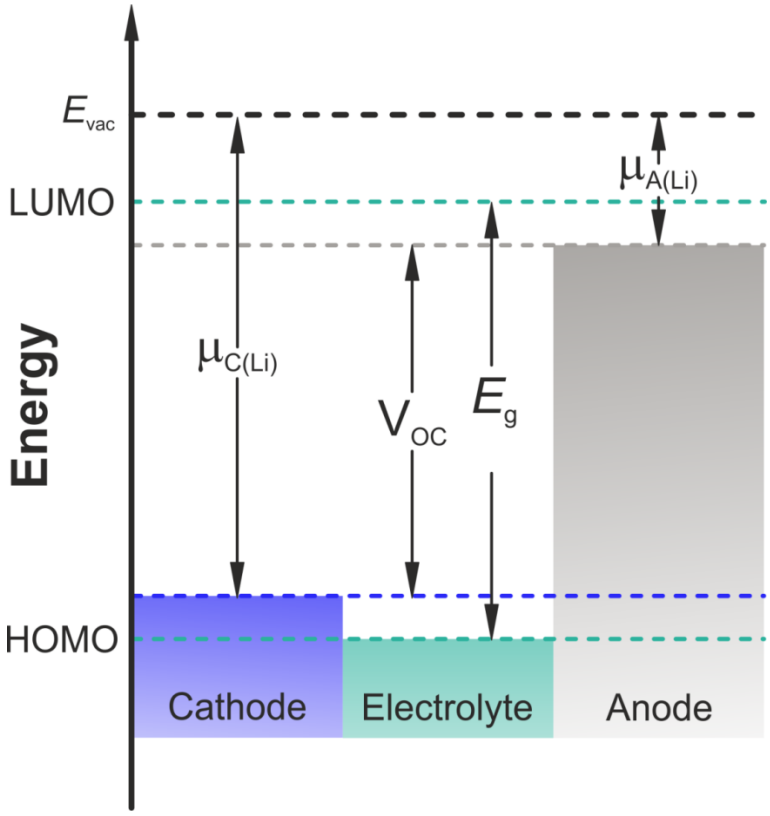

Figure 1.1.2: Energy diagram of a typical lithium-ion cell, representing the positions of the lithium chemical potentials of the anode and cathode with respect to the energy gap of the electrolyte

The lithium chemical potential of the cathode ($\mu_{C(Li)}$) should lie above the HOMO of the electrolyte, otherwise it will oxidise components in the electrolyte and degrade the battery. The lithium chemical potential of the anode ($\mu_{A(Li)}$) should lie below the LUMO of the electrolyte to prevent reduction of the electrolyte components. For organic carbonate based electrolytes which are currently used commercially, the

oxidative and reductive potentials are ~4.7 V and 1 V *vs*. Li^+/Li^0, respectively.[3] The open-circuit voltage can therefore be represented by the following equation:

$$V_{OC} = \frac{(\mu_{A(Li)} - \mu_{C(Li)})}{e}$$

where *e* is the elementary charge.[4]

The stored charge of a lithium-ion battery is referred to as the capacity, values of which are typically reported in mA·h (milliampere hour) for consumers, which indicates the charge transferred at the rated voltage as over time. Since 1 C (coulomb) is equivalent to 1 A·s (ampere second), 1 mA·h is equivalent to 3.6 C. In battery literature, the specific capacity is most often reported normalised to the active mass of the host material in units of mA·h g^{-1}; the rest of the mass of the cell is not included in order to effectively compare values. The theoretical capacity of a material can be calculated based on the molar mass of the fully lithiated host material and the maximum amount of lithium that can be extracted per formula unit. In reality however, the practical reversible specific capacity of these insertion electrodes in operation is lower than the theoretical capacity, the primary reason being not all lithium ions can be extracted reversibly at under standard operating conditions. The specific energy is often reported in W·h kg^{-1}, (or as a function of volume), which takes into account the operating voltage of the battery. Therefore, increasing the voltage and capacity of lithium ion batteries will increase the power output which is necessary for their application in EVs. The capacity and voltage of LIBs has not yet reached its practical limit, with improvement of current state-of-the-art technologies possible through examination and development of the structure-property relationships of the materials constituting the electrochemical cell, whilst maintaining compatibility of the different components.

1.2 Lithium Ion Battery Components

1.2.1 Solid-Electrolyte Interphase (SEI)

The operation of lithium ion batteries results in the formation of a solid-electrolyte interphase (SEI) layer on the surfaces of the electrodes, an effect which is more prevalent at the anode where lithium ions are reduced. The components of the liquid electrolyte are reduced at the surface of the anode on charging, forming deposits of Li-containing salts. These reduction products form a passivating layer, known as the interphase, between the electrolyte and surface of the electrodes, enabling diffusion of lithium ions through this layer but is insulating to electrons, whilst protecting the electrodes from further oxidative attack from the electrolyte and prolonging battery life upon further cycling.[5] This is a particularly important consideration for graphite based anodes where the reduction potential lies below the stability window of the electrolyte. The inner SEI layer (in direct contact with the electrode surface) is thought to be very thin and compact, comprising mostly of inorganic lithium salts and the porous outer SEI layer (in direct contact with the electrolyte) is much thicker, mostly composed of organic lithium salts.[6] Formation of the SEI layers results in the irreversible consumption of lithium ions and loss of capacity compared to the first charge cycle,[7] which continually deposits over the life cycle of the cells resulting in gradual loss of capacity.[8] Thermal decomposition of the SEI at a graphitic anode can easily occur above 120 °C and contribute considerably to the onset of thermal runaway.[9] Some electrolyte additives are intended to improve the thermal stability of the lithiated graphite anode and SEI layer.[10]

At the cathode component, oxidation of the electrolyte can occur and form SEI on the cathode surfaces, particularly in high voltage LIBs where charging above ~4.5 V

exceeds the stability window of conventional non-aqueous liquid electrolytes.[11,12] For effective analysis of the species involved during battery cycling, it is important to consider the surface chemistry of the insertion electrodes in comparison to the bulk processes.

Safety concerns are apparent with all LIBs, particularly with lithium metal oxide cathodes, due to the possibility of gas release during operation at elevated temperatures or overcharging or over-discharging; or the possibility of internal short circuiting. For example, metal oxide cathodes may release oxygen gas during overcharging, the SEI layer can thermally decompose to release gases and the liquid electrolyte can evolve gas at the anode during reduction processes.[13] These exothermic reactions may result in a process known as 'thermal runaway', as heat and gases accumulate inside the cells which eventually rupture and explode, consuming the flammable liquid electrolyte. Numerous safety features are employed to prevent such failures, but are not always successful – clearly this is not a viable option for electric vehicles and larger batteries.[14]

1.2.2 Anode

Graphite is the most commonly used commercial anode material (also referred to as the negative electrode), due to its low cost, stability, excellent life cycle and low reduction potential of ≤ 0.25 V *vs.* Li^+/Li^0.[3] However the chemical potential of graphite lies below the LUMO of typical carbonate-based electrolytes, resulting in reduction of the electrolyte by graphite anodes upon charging. One lithium ion can intercalate per six carbon atoms (LiC_6), sitting between the layers of graphene, which limits its theoretical capacity to 372 $mA{\cdot}h\ g^{-1}$.[15] The rate of lithium ion diffusion within graphite is rapid parallel to the basal plane, but slow perpendicular to these planes hence diffusion is limited across grain boundaries.[16] The limitations of graphitic carbon

anodes has led to the investigation of nanostructured carbon such as graphene nano-sheets (2-D), carbon nanotubes (1-D) and C_{60}, whereby the larger surface area and dimensionality result in greater initial capacities and improved conductivity. The additional cost of synthesis and rapid reduction of carbonate-based electrolytes due to this large surface area currently limit their commercial viability.[17,18]

Lithium metal would be an ideal anode due to its high theoretical capacity of 3860 mA·h g^{-1},[19] low density and lowest negative electrochemical potential without the need for synthesis of pre-lithiated cathodes.[20] The use of lithium metal anodes has yet to be realised commercially, mainly due to the safety hazards this technology currently poses (in addition to limited lithium resources). During repeated charge and discharge cycles of these cells, lithium dendrites have a tendency to grow from the anode and can penetrate the SEI layer and separator, which can eventually result in short circuiting as the anode makes contact with the cathode. The use of carbonaceous materials as anodes avoids this problem due to intercalation within the structure, providing good safety and longevity for these LIBs.

To improve the overall cell capacity without compromising on safety, some attention has been focused on the development of silicon anodes, which in its fully lithiated state forms $Li_{15}Si_4$ enabling a maximum theoretical capacity of 3579 mA·h g^{-1}.[21] The primary disadvantage with the use of silicon anodes is the ~300% volume expansion that occurs upon complete lithiation, in contrast with ~10% expansion with graphite.[22] Anodic volume changes upon cell cycling are problematic and can lead to irreversible capacity loss due to electrode pulverisation, which in turn leads to mechanical stress. Mechanical stress can cause the cell to fracture, exposing the anode to the electrolyte thus consuming both components, in addition to loss of electrical contact through the anode decreasing the conductivity. Nanostructuring of silicon-based anode materials,

such as the use of nanowires or porous structures, has been shown to considerably minimise the effects of volume expansion upon lithiation, but can reduce contact between the particles and affect rate capability.[23-25]

Low voltage spinel structures, in particular $Li_4Ti_5O_{12}$ (or $Li_{4/3}Ti_{5/3}O_4$ in the $A[B_2]X_4$ spinel notation) have also been demonstrated as lithium ion battery anodes.[26] Lithiation of the cubic spinel $Li_4Ti_5O_{12}$ anode upon charging results in the rock-salt type $Li_7Ti_5O_{12}$ structure with a theoretical specific capacity of 168 mA·h g^{-1} at a voltage of 1.5 V *vs*. Li^+/Li^0. The change from the spinel to rock-salt structure is due to the migration of the lithium ions occupying the tetrahedral 8*a* sites in the spinel to octahedral 16*c* sites in the rock-salt upon lithiation; this structural evolution displays minimal volume change (~0.2%) which is advantageous to reduce mechanical stress in battery systems.[27] Lithium-containing spinel anodes have the advantages of facile and inexpensive synthesis and stable cyclability with long lifetimes, but possess modest power outputs and limited ionic and electronic conductivity (which can be improved by carbon-coating, nanostructuring *etc*.) and therefore are more suitable to stationary battery storage systems.[28]

1.2.3 Electrolyte

The electrolyte must have high Li-ion conductivity, fast Li-ion diffusion and negligible electronic conductivity; however liquid electrolytes undergo reactions at the surface of the electrodes consuming the components, particularly at elevated temperatures or during overcharging. The main concern with the use of non-aqueous liquid electrolytes in electric vehicles is the flammability and volatility of organic solvents, which can under extreme operating conditions result in accelerated reaction with the electrodes leading to release of heat and gas and eventually may result in fire and explosion. It is clear this is not an acceptable possibility in EVs, so many research groups are focusing

on development of non-flammable solid electrolytes with an equally wide operating voltage window such as polymers,[29] or glass/ceramic Li^+ conductors.[30] On the other hand, others are developing electrolyte additives to improve the voltage window,[31] minimise capacity-reducing parasitic reactions with the cathode,[32] or make the electrolytes more flame retardant.[33] However it is worth noting that these electrolyte additives tend to lead to decreased ionic conductivity.[34] Room temperature ionic liquids are being considered as alternative electrolytes, owing to their low volatility, low flammability, good stability and high ionic conductivity.[35] Unfortunately lithium ion diffusivity is limited due to their high viscosity, hence limiting the rate of charge and discharge.[36]

1.3 Lithium Ion Battery Cathodes

The cathode component of a lithium ion electrochemical cell (the positive electrode during discharge) must reversibly and rapidly react with lithium *via* intercalation and deintercalation, triggered by the facile reduction and oxidation of a transition metal centre. The material must be a good electronic conductor to aid the redox reaction of the transition metals and complete the circuit for the electrons to do useful work. Upon lithiation and delithiation there should be minimal volume change of the host structure to avoid cell damage and loss of particle contact which can increase impedance. To enable a cell with high power, the cathode should have a large discharge capacity and a high redox potential of the transition metal couple which would result in a higher open circuit voltage. The cathode should also have a long cycle life, good thermal and chemical stability and ideally be composed of environmentally benign, non-toxic, inexpensive and abundant materials with the ability to be recycled.

1.3.1 Rock-Salt Structure Family

Many lithium metal oxides are known to adapt rock-salt superstructures, whereby ions occupy octahedral coordination sites and the total number of cations is equal to the number of anions whilst maintaining electroneutrality. The basic NaCl rock-salt structure possesses a cubic close-packed (*ccp*, or face-centred cubic, *fcc*) array of anions (Cl^-), whereby the cations (Na^+) fully occupy the interstitial octahedral sites and the tetrahedral sites remain vacant. This results in cations that are octahedrally coordinated to six anions and *vice versa*, with the $NaCl_6$ (or $ClNa_6$) octahedra sharing common edges in a three-dimensional array (Figure 1.3.1).[37]

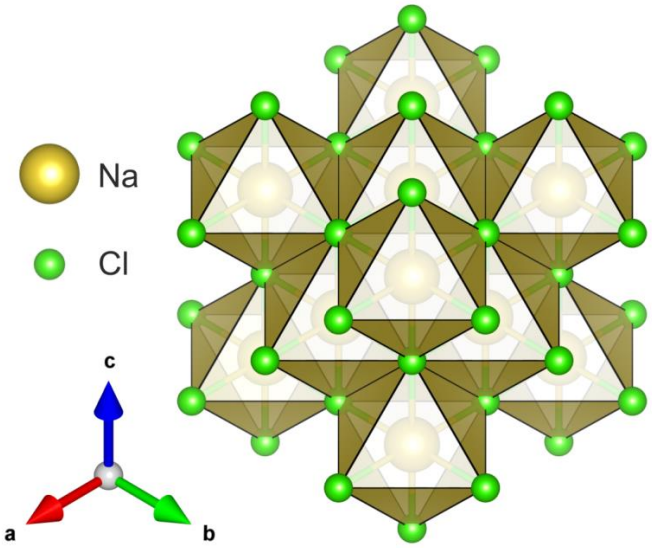

Figure 1.3.1: Representation of the [111] plane in the NaCl rock-salt structure

For ternary alkali metal (A^+) – transition metal (M^{n+}) oxides that can adopt rock-salt type superstructures, general formulae of the form $AM^{(III)}O_2$, $A_2M^{(IV)}O_3$ and $A_5M^{(VII)}O_6$ are capable of possessing fully occupied alkali metal layers (AO^-).[38] For ternary oxides possessing these formulae, Pauling's rule of electroneutrality around each oxide anion is obeyed, that is the sum of the electrovalencies of the nearest- neighbour is equal to

the charge on the anion hence it is possible to preserve electroneutrality around the local oxygen environment.[39]

The α-$NaFeO_2$ structure (of the general AMO_2 formula) is an ordered derivative of the rock-salt structure, whereby the sodium ions and iron (III) ions occupy crystallographically distinct octahedral sites within a close-packed oxide array. This forms, in the ideal structure, fully occupied NaO_2 layers alternating with FeO_2 layers perpendicular to the [111] rock-salt equivalent plane in an -ABC-ABC- stacking scheme; also referred to as O3 stacking (where O indicates octahedral coordination of cations and 3 indicates the stacking period).[40] This layered structure is thermodynamically favoured due to the large difference in ionic radii of Na^+ (1.02 Å) and Fe^{3+} (high-spin 0.645 Å) in octahedral coordination environments. Such layered structures are often adopted when the general formula is AMO_2 where *A* is an alkali metal (such as Na^+, Li^+) and *M* is a trivalent metal ion (such as Fe^{3+}, Co^{3+}) with a sufficient difference in ionic radii. Cations of similar ionic radii are more likely to mix and disorder, such as Li^+ and Ni^{3+} as observed during synthesis and cycling of $LiNiO_2$.[41] In AMO_2 rock-salt structures, the octahedral coordination environment around oxide anions can be 'clustered' as close together as possible in a *fac*-coordination environment (where three ions of the same type occupy one face of the octahedron) as occurs in α-$NaFeO_2$ and $LiCoO_2$ (Figure 1.3.2, *top*). Alternatively, cations of the same type can arrange in a *mer*-coordination environment as far apart as possible (occupying one meridian of the octahedron) as in γ-$LiFeO_2$ (Figure 1.3.2, *bottom*). The coordination adopted depends on lattice energy and polarising power of the M^{3+} cations.[42] As a consequence of the structure adopted by γ-$LiFeO_2$, both Li^+ and Fe^{3+} ions are present in every close-packed oxygen layer. Other examples of

compounds adopting the γ-$LiFeO_2$ structure type include NaMO_2 (M = Ln^{3+}) and Li_2MXO_4 (M = Mg, Mn, Co, Zn; X = Zr, Hf).

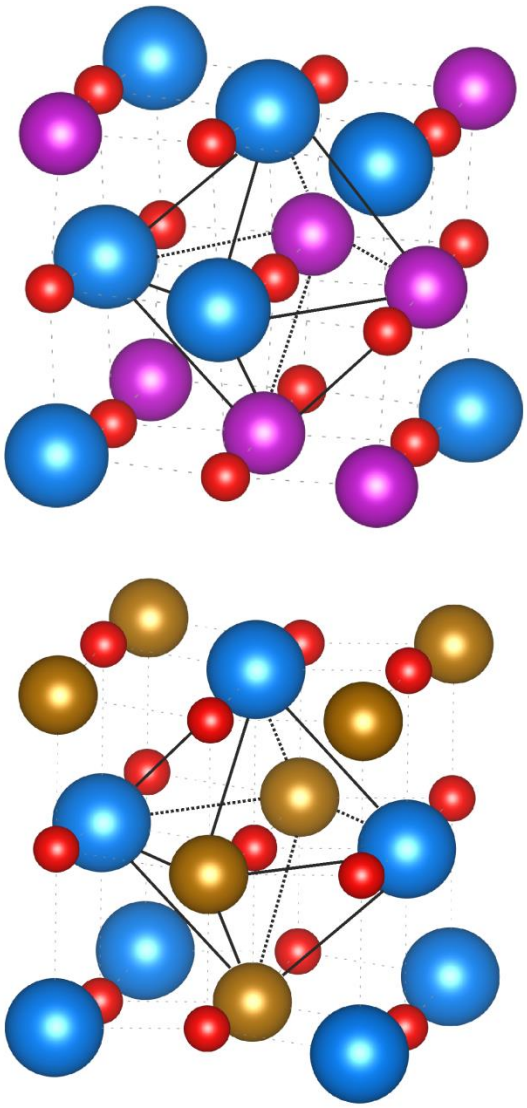

Figure 1.3.2: Representation of clustered oxygen (*red spheres*) *fac*-coordination environment in $LiCoO_2$ (*top*) and dispersed *mer*-coordination environment in γ-$LiFeO_2$ (*bottom*)

Li_2SnO_3 is an example of the A_2MO_3 rock-salt superstructure type, which can adopt two structures, both of which can be thought of as $Li[Li_{1/3}Sn_{2/3}]O_2$. The high temperature rhombohedral α-Li_2SnO_3 possesses fully occupied Li layers alternating with a disordered mixed cation layer and is isostructural with α-$NaFeO_2$ and $LiCoO_2$. Alternatively the Sn and Li cations in the mixed cation layer can order into distinct

crystallographic sites resulting in the lower symmetry monoclinic β-Li_2SnO_3 structure, which is isostructural with Li_2MnO_3.[43] In A_2MO_3 structure types, the *M* cations can coordinate in either a *cis* or *trans* octahedral coordination environment around O^{2-}, depending on whether maximising the *M*-*M* cation distance or their alignment into layers is more thermodynamically stable within the structure.[39]

Of the A_5MO_6 composition where *A* = Li (or Na) and *M* = Re or Os, the M^{7+} ions are fully ordered in one crystallographic site within the mixed cation layer (Figure 1.3.3, *top*), alternating with fully occupied lithium layers, similar to Li_2MnO_3 (space group (abbreviated S.G.) *C*2/*m*). Likewise, although it does not strictly adhere to the A_5MO_6 formula, $Li_3Ni_2TaO_6$ can be thought of in a similar way. The Ta^{5+} ions are ordered over one octahedral site, while Li^+ and Ni^{2+} are disordered over the remaining cation sites (Figure 1.3.3, *bottom*), adopting the orthorhombic *Fddd* space group. Other structural analogues include $Li_3M^{(II)}M^{(V)}O_6$ where $M^{(II)}$ = Ni, Mg, Co and $M^{(V)}$ = Nb, Sb, Ta.

Of course Li-containing rock-salt superstructures are not strictly limited to the general formulae described above. Some cation combinations do not adhere to the electroneutrality rule around each oxide anion, or other factors such as Jahn-Teller distortion and *M*-O bond polarisation influence the ordering adopted.[42] For example, Li_3NbO_4 possesses Nb_4O_{16} tetramers, forming a body-centred cubic lattice.[44] Li_4WO_5 and Li_4MoO_5 can adopt a disordered cubic rock-salt structure, or a fully ordered triclinic ($P\bar{1}$) structure which possesses fully occupied lithium layers.[45-47]

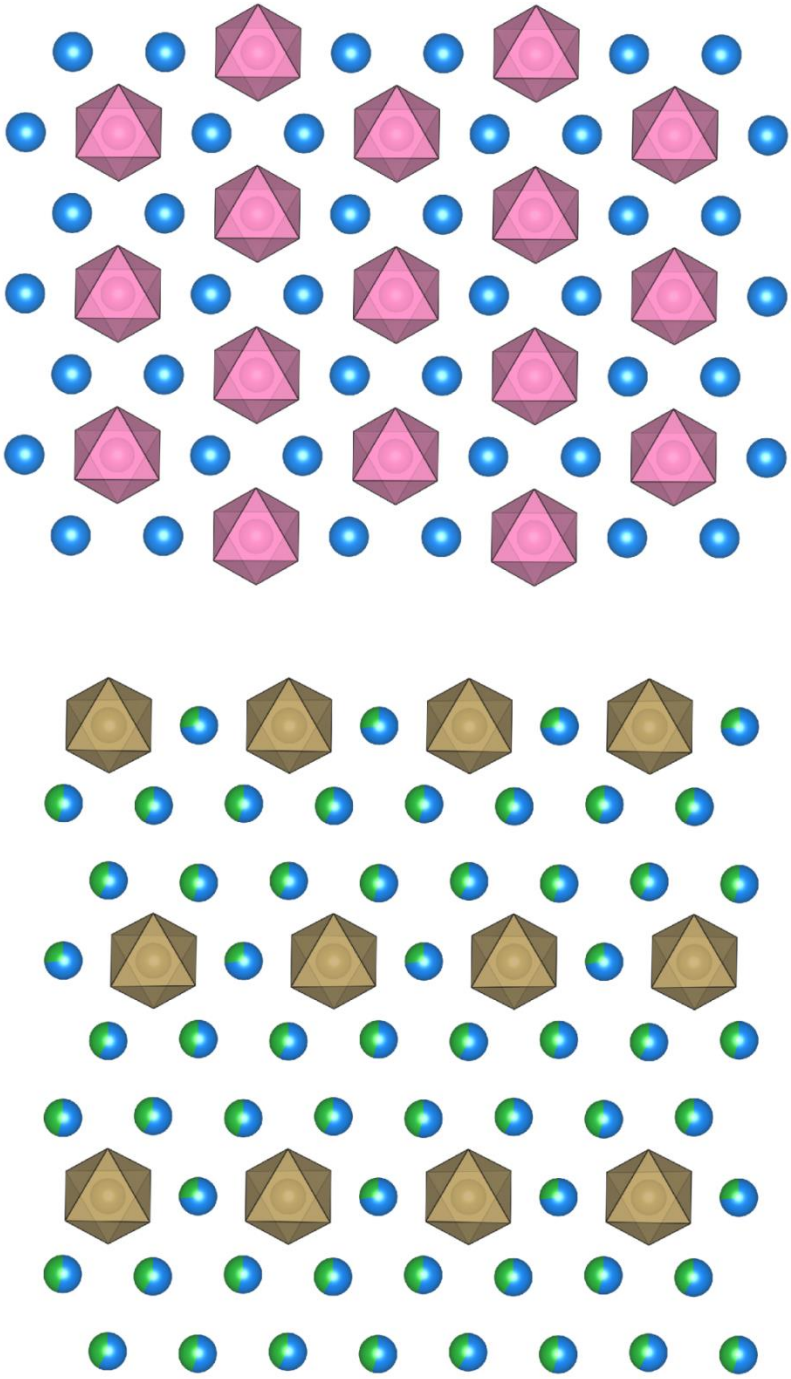

Figure 1.3.3: Representation of ordering of Re octahedra (*pink*) in Li_5ReO_6 (*top*) and Ta octahedra (*gold*) in $Li_3Ni_2TaO_6$ (*bottom*) between close-packed oxygen layers

1.3.2 Lithium Metal Oxide Cathodes

Lithium cobalt oxide, $LiCoO_2$, as a lithium ion battery cathode was first reported by Goodenough and eventually commercialised (coupled with a graphitic anode) by Sony corporation in 1991.[48] The high energy density, high operating voltage, good cyclability and relatively facile manufacture of these electrochemical cells lead to their ubiquitous use in portable electronic devices; however it is unsuitable for EV applications primarily due to safety concerns, in addition to the expense of cobalt metal. The theoretical specific capacity for a $LiCoO_2$/graphite cell is 280 mA·h g^{-1} based on the removal of all lithium ions from the cathode by full reversible oxidation of Co^{3+} to Co^{4+}. However, the practical and reversible specific capacity of $LiCoO_2$ is limited at 140 mA·h g^{-1} as only 0.5 Li^+ can be safely extracted per cobalt ion during oxidation of Co^{3+} to Co^{4+}, creating an average bulk oxidation state of $Co^{3.5+}$ when fully charged. The delithiated form of the cathode, $Li_{0.5}CoO_2$, is a less stable structure and can evolve oxygen at elevated temperatures according to the following equation:[49]

$$Li_{0.5}CoO_2 \rightarrow \frac{1}{2}LiCoO_2 + \frac{1}{6}Co_3O_4 + \frac{1}{6}O_2$$

$LiCoO_2$ adopts the rhombohedral $R\bar{3}m$ space group, comprised of fully occupied cobalt layers alternating with fully occupied lithium layers along the *c*-axis, which is of the α-$NaFeO_2$ structure type (Figure 1.3.4).

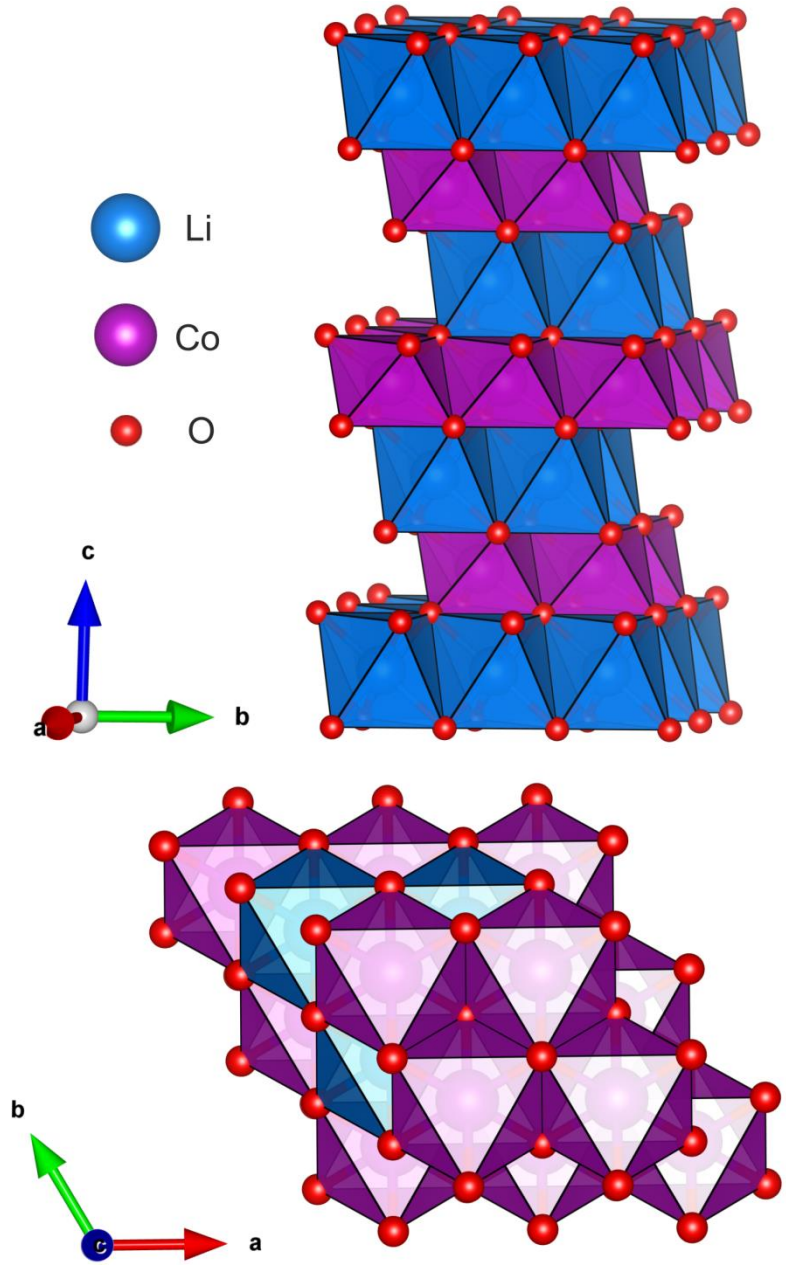

Figure 1.3.4: Representation of the $LiCoO_2$ structure showing the alternating layers of lithium and cobalt octahedra (*top*). Representation of the cation and anion ordering in the rock-salt [111] planes (*bottom*)

Lithium ion batteries employing $LiCoO_2$ as the cathode were commercialised in preference to $LiNiO_2$; despite the higher practical capacity of $LiNiO_2$ (~150 $mAh \cdot g^{-1}$) and reduced cost and toxicity of nickel in comparison to cobalt.[50] This is due in part to the difficult synthetic preparation of the layered $R\bar{3}m$ $LiNiO_2$ structure, often

contaminated with domains of the more thermodynamically stable and disordered cubic $Fm\bar{3}m$ polymorph.[51] Additionally, during battery operation Ni^{3+} ions are able to hop to the Li^+ sites *via* the tetrahedral sites,[52] disordering the layered structure and hence blocking Li^+ diffusion channels.[53] Such problems are not present in $LiCoO_2$ which therefore has greater structural stability and hence better cyclability.[54]

Another example of a commercialised layered lithium metal oxide cathode is $LiNi_{0.8}Co_{0.15}Al_{0.05}O_2$ (NCA), utilising both the nickel and cobalt as redox active centres to deliver capacities of ≤ 200 mA·h g^{-1}. In comparison to $LiCoO_2$, the reversible capacity is greater as the structure does not evolve oxygen until 0.7 Li^+ have been removed from the structure, as well as nickel being more cost-effective and lower toxicity than cobalt. The presence of a small amount of redox inactive Al^{3+} ions within the transition metal layer provide thermal stability to the structure and minimise the migration of Ni^{3+} ions from the transition metal layer to the Li^+ plane.[55]

$LiMn_2O_4$ crystallises into the spinel structure with $Fd\bar{3}m$ space group; it utilises inexpensive and environmentally benign manganese and is safer than $LiCoO_2$. Spinel structures have the general formula AB_2O_4 whereby the *A* cations (Li^+ in this instance) occupy tetrahedral coordination sites and the *B* cations (Mn^{3+}) occupy the octahedral sites within a *ccp* array of oxide anions (Figure 1.3.5). This framework enables three-dimensional, facile transport of lithium ions throughout the structure due to corner sharing tetrahedra and octahedra. Although $LiMnO_2$ adopts a layered α-$NaFeO_2$ structure, it is not a commercially viable cathode material due to irreversible transformation to the spinel $LiMn_2O_4$ phase upon delithiation.[56]

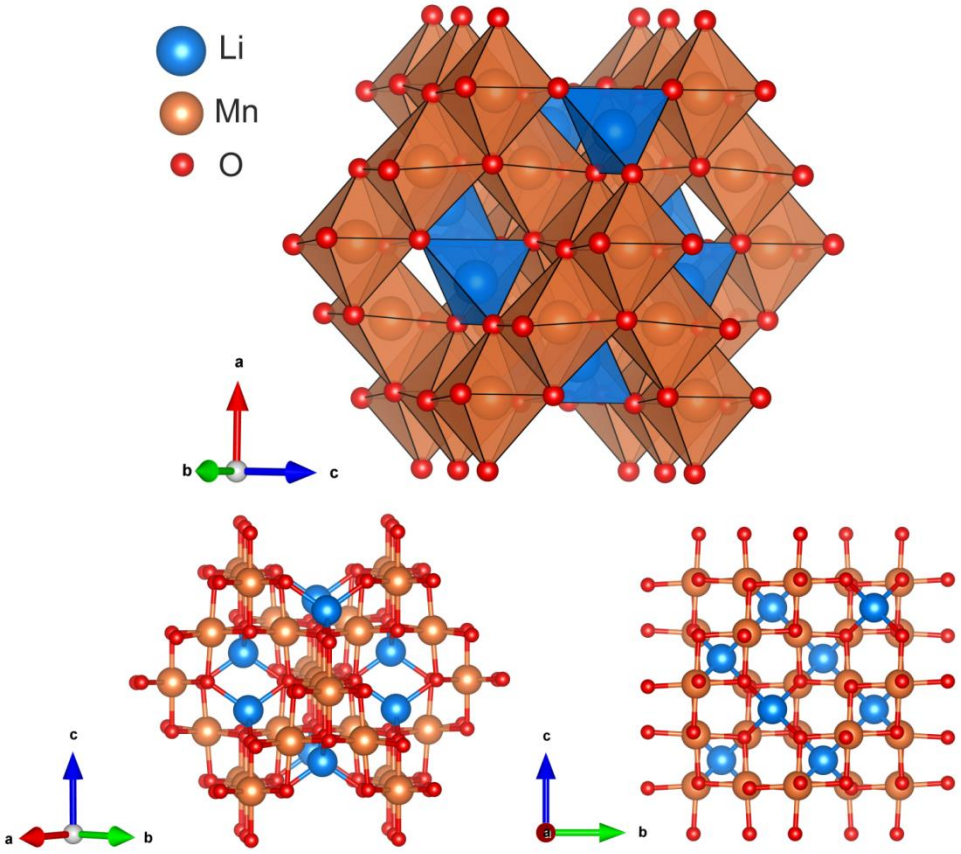

Figure 1.3.5: Representation of cubic spinel structure of $LiMn_2O_4$ showing the LiO_4 tetrahedra and MnO_6 octahedra (*top*) and bonding framework (*bottom*)

The practical specific capacity of $LiMn_2O_4$ is typically 120 mA·h g^{-1} operating at ~4 V *vs.* Li^+/Li^0, however this material suffers considerably from capacity fading, particularly when cycled above 55 °C.[57,58] This capacity fading is a result of the disproportionation of Mn^{3+} ions from the spinel structure into Mn^{4+} and Mn^{2+} ions, a reaction which is facilitated by the presence of a small amount of HF in the electrolyte creating an acidic environment. Mn^{2+} will then dissolve in the electrolyte, resulting in a disordered cathode structure; and Jahn-Teller distortion can also lead to structural instability.[59] Substitution of a quarter of the manganese cations for nickel results in $LiNi_{0.5}Mn_{1.5}O_4$, retaining the spinel structure and improving the cyclability compared to $LiMn_2O_4$ by stabilising the structure against dissolution. The presence of redox active nickel means there is an additional voltage plateau at 4.7 V *vs.* Li^+/Li^0, however

the theoretical capacity is still relatively low at 147 mA·h g^{-1}. In addition, this material is prone to the formation of cubic disordered $Li_xNi^{(II,III)}_{1-x}O$ which degrades the electrochemical performance.[60]

Based on the advantages and disadvantages associated with single transition metal redox centres of the form Li*M*O_2 (*M* = Ni, Mn, Co), this has led to a solid solution approach to mixed metal oxides of the form $LiNi_xMn_yCo_zO_2$ (where $x + y + z = 1$; known as NMCs), retaining the layered α-$NaFeO_2$ type structure. These materials such as $LiNi_{1/3}Mn_{1/3}Co_{1/3}O_2$ exhibit a high redox potential and capacity mostly associated with $Ni^{2+/3+/4+}$ redox. The manganese ions remain in the +4 oxidation state throughout cycling, acting to stabilise the structure against transformation to a spinel-like phase and eliminates the problems associated with Jahn-Teller distortion of Mn^{3+}. Cobalt, in the +3 oxidation state, provides good rate capability and is thought to minimise cation mixing of transition metals onto Li^+ sites during cycling.[61]

$LiNi_{1/3}Mn_{1/3}Co_{1/3}O_2$ (often denoted as NMC333) exhibits a reversible discharge capacity of 150 mA·h g^{-1} at a cut-off charge voltage of 4.2 V, or up to 200 mA·h g^{-1} when charged up to 4.6 V.[62,63] Unfortunately delithiated NMC structures are reactive and have been shown to exhibit facile conversion from layered to spinel to inactive disordered rock-salt phases (originating at the cathode surface), particularly at elevated temperatures, which is exacerbated when charged to higher voltages (despite the additional capacity obtained).[64,65] The structural transitions are due to cation mixing of Ni, Co and Mn into the depleted lithium layers in an attempt to stabilise the delithiated structure (commonly observed in $LiNiO_2$); which can for example be alleviated by incorporating stabilising dopants such as Zr^{4+}.[66]

Since the nickel redox is responsible for the majority of the capacity, increasing the nickel content (*e.g.* $LiNi_{0.8}Mn_{0.1}Co_{0.1}O_2$; NMC881) increases the available capacity, but also encourages structural degradation. The increased proportion of highly reactive Ni^{4+} promotes side reactions with electrolytes at the cathode surface, and can also reduce back to Ni^{2+} with accompanying oxygen gas release in the delithiated structure (to maintain charge neutrality) which also results in rapid capacity fading.[67]

The ratio of transition metal cations, presence of dopants and tuning the synthesis and processing of layered NMC cathodes have been extensively studied to improve the electrochemical properties with a view to producing a safer, cheaper and higher capacity cathode than $LiCoO_2$.[68]

1.3.3 Lithium-Rich Layered Oxide Cathodes

The concept of lithium-rich layered oxides originated from the research of Thackeray and Rossouw,[69] who used acid to leach Li_2O from the layered rock-salt type Li_2MnO_3 to obtain a layered electrochemically active structure $Li_{0.36}Mn_{0.91}O_2$. Cell cycling of the obtained cathode produced a lithiated structure determined as $Li_{1.09}Mn_{0.91}O_2$, which can also be denoted as $0.2Li_2MnO_3{\cdot}0.8LiMnO_2$, exhibiting promising electrochemical behaviour.[70] From this work, other lithium-rich layered oxides of the general formula $xLi_2MnO_3{\cdot}1\text{-}xLiMO_2$ (*M* = Ni, Mn, Co *etc*.) have been widely researched in recent years, displaying initial discharge capacities exceeding 280 $mA{\cdot}h\ g^{-1}$ where NMCs are composited with Li_2MnO_3, due to the additional available lithium.[71] The Li_2MnO_3 component can be electrochemically activated with respect to lithium ion insertion by charging to 4.5 V,[72] whereby manganese remains in the +4 oxidation state but some lattice oxide 'oxidises' to molecular O_2 gas to maintain charge neutrality following Li^+ extraction. This electrochemical activation removes almost all of the Li^+ from the Li_2MnO_3 component to form a layered λ-MnO_2 structure

into which a proportion of the extracted lithium can reversibly intercalate upon cycling; in addition to the cationic redox of the Li*M*O_2 component. Unfortunately, these Li-rich layered oxides utilising Li_2MnO_3 currently suffer from poor cycling performance due to low rate capabilities,[73] a huge irreversible capacity loss in the first cycle and voltage decay due to conversion to cubic spinel phases as a result of cation migration.[74]

Due to the involvement of oxygen during the first cycle of *x*Li_2MnO_3·1-*x*Li*M*O_2 cathodes, research into the viability of reversible redox of lattice oxide (O^{2-}) has garnered increasing research in recent years. Alternative materials to the *x*Li_2MnO_3·1-*x*Li*M*O_2 composites are desirable to access the cumulative cationic and anionic redox processes to enable high discharge capacities in lithium-rich materials, without the problems associated with structural transformations over continued battery use.

The layered lithium-rich rock-salt superstructure of $Li_{1.20}Mn_{0.54}Ni_{0.13}Co_{0.13}O_2$ (or in the composite notation, $0.5Li_2MnO_3{\cdot}0.5LiNi_{1/3}Mn_{1/3}Co_{1/3}O_2$) exhibits a capacity over 200 mA·h g^{-1}, but with significant voltage fade during cycling and a high irreversible capacity loss.[75] Investigation of the redox mechanisms involved during cycling were examined using *in-operando* X-ray absorption spectroscopy, concluding that nickel and cobalt are involved in the cationic redox, but the capacity obtained exceeds the theoretical capacity calculated from solely cationic redox.[76] The source of additional capacity was determined as reversible oxidation of lattice oxide, not just irreversible oxidation to O_2 gas, found to occur following cation oxidation in the core of the particles using high-angle annular dark-field scanning transmission electron microscopy (HAADF-STEM).[77]

Investigation into Li_2RuO_3-based systems (since Li_2RuO_3 is structurally analogous to Li_2MnO_3), determined that the species involved during reversible anionic redox were most likely peroxo or superoxo-type species, referred to as $(O\text{-}O)^{n-}$ or O_2^{n-} since the value of $n = 1,2$ or 3.[78,79] The anionic redox can therefore be considered as the reversible partial oxidation of lattice oxide to peroxo/superoxide species, which accompanies lithium loss from the structure to maintain charge neutrality in rock-salt superstructures.

Furthermore, the synthesis of Li_4FeSbO_6 was targeted by McCalla *et al.*,[80] with a view to developing a material that solely exhibits the anionic redox as a means of obtaining capacity. This material can be considered a structural analogue of the layered Li_2MnO_3 structure, with Mn^{4+} replaced by $^1/_2Fe^{3+}$ and $^1/_2Sb^{5+}$.[81] During charging of this material, the oxidation of Fe^{3+} to Fe^{4+} was observed with simultaneous formation of O_2^{n-} species, with rapid evolution of oxygen gas when charged up to 5 V. The reversibility of the anionic redox was poor over continued cycling up to 4.25 V due to loss of oxygen gas from the structure, resulting in destruction of the cathode material from these structural changes, determined from *in-operando* XRD and Mössbauer spectroscopy.[80]

To date, layered lithium-rich materials exhibit low structural stabilities towards oxygen removal following electrochemical activation by charging to high potentials. The excess of lithium in these structures is thought to enable such anionic redox processes to be accessed,[82] in addition to strong metal *nd* and oxygen 2*p* orbital interactions.[83] Thus far however, the cycling reversibility of materials exhibiting both cationic and anionic redox processes has been poor due to the release of the oxide anions from the cathode structures as O_2 gas,[84] or irreversibly reacting with the carbonate-based electrolytes resulting in rapid capacity fade.[78] These Li-rich layered

structures and the factors controlling the anionic redox stability are discussed in more detail in Chapters 3-5.

1.3.4 Disordered Lithium-Rich Cathodes

In stoichiometric layered LIB cathode materials such as $LiCoO_2$, NMCs *etc*., fully occupied lithium layers are required, migration of the transition metal cations into the lithium layers following delithiation. Cation disordering increases the impedance of the cathode material as the transition metals can block the one-dimensional Li^+ ion diffusion channels and result in capacity fading (as mentioned in Section 1.3.2). However, it was recently shown through a combination of computational and empirical methods that a cathode possessing disordering of cations can still reversibly cycle when the composition is rich in lithium (*i.e.* the ratio of Li^+ to transition metal ions is >1). Such behaviour was exhibited in $Li_{1.211}Mo_{0.467}Cr_{0.3}O_2$, whereby an alternative lithium-ion percolation network was determined; but only when an excess of lithium is present.[82]

1.3.5 Polyanionic Insertion Compounds

Lithium ion battery cathodes comprising of three-dimensional ionically conducting polyanionic (XO_4^{n-}) frameworks and transition metals have been intensively researched in recent years, following the successful commercial development of the ordered olivine-type lithium iron phosphate ($LiFePO_4$) cathode.[85] Utilising such polyanions in the synthesis of LIB cathodes, instead of simple O^{2-} anions such as in $LiCoO_2$, is an approach to increase the operating voltage of the cells due to the inductive effect within *M*-O-*X* bonds. The difference in electronegativity between the O and *X* anions gives the covalent O-*X* bonds ionic character, with the degree of ionic character dependent on the identity of *X*. In comparison to metal oxide systems, the enhanced ionic character of the O-*X* bonds strengthens them and therefore decreases

the energy of the *M*-O bonds within the *M*-O-*X* linkages. In other words, the separation between the bonding and antibonding orbitals of the *M*-O bond is increased, lowering the redox potential of the transition metal.[86,87] Decreasing the redox potential of the active transition metal couple *vs.* Li^+/Li^0 will increase the discharge voltage of the cell and hence increase the power density of the battery, with a versatile selection of transition metal and anion combinations possible. These three-dimensional frameworks provide long-term electrochemical and thermal stability to the cathode, potentially eliminating the possibility of oxygen evolution under abusive conditions and are therefore thought to be considerably safer than lithium metal oxide cathodes such as $LiCoO_2$ and $LiMn_2O_4$.[88] However, polyanionic cathodes are known to have poor electronic conductivity (which can be somewhat alleviated by homogenous carbon coating) and a low specific capacity due to additional electrochemically inactive mass of the polyanions increasing the overall mass of the cathode component.[89,90]

Lithium iron phosphate has a theoretical specific capacity of 170 mA·h g^{-1} at a voltage of 3.45 V *vs.* Li^+/Li^0, with the extraction of lithium from $LiFePO_4$ driven by the oxidation of Fe^{2+} to Fe^{3+}, which occurs in a two-phase reaction:

$$LiFePO_4 - xLi^+ - xe^- \rightarrow xFePO_4 + (1-x)LiFePO_4$$

The presence of the electronegative phosphate groups allows the redox potential of the $Fe^{2+/3+}$ couple to be increased due to the inductive effect, in comparison to a metal oxide structure (for example, the redox energy of $Fe^{2+/3+}$ in Fe_2O_3 is <2.5 V *vs.* Li^+/Li^0).[91]

The crystal structure of $LiFePO_4$ adopts an ordered olivine structure of the form M_2XO_4 crystallising in the orthorhombic space group *Pnma* (Figure 1.3.6). Oxide ions are

ordered in a distorted hexagonal close-packed (*hcp*) array, with Li^+ and Fe^{2+} occupying half of the crystallographically distinct octahedral coordination sites, and P^{5+} on one-eighth of the tetrahedral sites. The olivine structure is a hexagonal analogue of the spinel structure, but $LiFePO_4$ adopts the olivine structure due to the small radius of P^{5+} ions and the two different sized octahedral sites enabling the accommodation of two ions of different size and charge (Li^+ and Fe^{2+}).[85]

Lithium ions diffuse through the structure upon battery operation through one-dimensional channels, formed by edge-sharing chains of LiO_6 octahedra along the *b*-axis (LiO_6 octahedra are not pictured in Figure 1.3.6 for clarity). The distorted FeO_6 octahedra share corners in the *bc* plane and each shares edges with two LiO_6 octahedra; the PO_4 tetrahedra bridge the FeO_6 layers by sharing one edge with FeO_6 and two edges with LiO_6 octahedra.

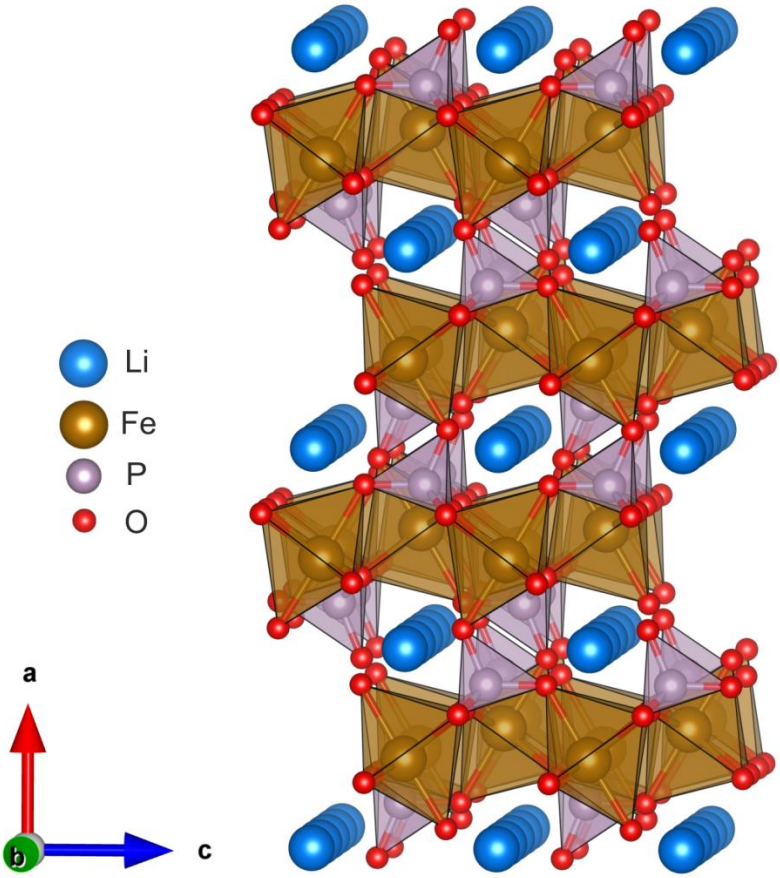

Figure 1.3.6: Representation of the olivine-type structure of $LiFePO_4$, showing the one-dimensional Li^+ channels along the *b*-axis

The three-dimensional bonding network of electronically insulating phosphate groups improves the voltage of this material, but also acts to isolate the redox active metal centres, resulting in poor electronic conduction ($\sigma \sim 10^{-9}$ S cm^{-1} in pristine, uncoated $LiFePO_4$).[92] The fully delithiated structure $Fe^{III}PO_4$ retains the *Pnma* space group, with a small decrease in volume compared to the lithiated structure, attributed to the strongly bonded three-dimensional structure and resulting in a LIB cathode that shows good reversibility and minimal mechanical stress upon cycling.

The diffusion of lithium ions through the one-dimensional channels is considered rapid, in fact it is the hindered electronic conductivity within the structure that is responsible for the slow rates of charge and discharge.[93] However, the material must

be made extremely pure as these Li^+ diffusion channels can easily be blocked by the presence of impurities such as Fe_2P. Nanostructuring of this material by tuning synthetic methods and coating the particles with conductive carbon has led to improvements of the rate capability of this material by improving electronic conductivity.[13,94-96]

Due to the previously mentioned inherent safety concerns of lithium metal oxides, $LiFePO_4$ is commonly used in current electric vehicle technology. It also utilises low cost, abundant and environmentally benign iron as the redox active metal, and shows good thermal and chemical stability, which are critical considerations for large capacity systems such as EVs. However the energy density of $LiFePO_4$ is lower in comparison to $LiCoO_2$; it possesses a lower operating voltage due to the $Fe^{2+/3+}$ redox couple at 3.45 V *vs*. Li^+/Li^0 (occurring in a two-phase reaction), hindered electronic and ionic conduction and a lower volumetric capacity.[97]

Other lithium metal phosphates adopt the ordered olivine-type structure, such as $LiMnPO_4$, $LiCoPO_4$ and $LiNiPO_4$. The high average discharge potential of the Co and Ni olivines make them desirable targets in the development of high-voltage LIB cathodes (4.8 and ~5.1 V *vs*. Li^+/Li, respectively),[98] however current commercial liquid electrolyte technology is not yet stable to such high operating voltages over a large number of cycles.

In addition to phosphates ($LiMPO_4$), other examples of polyanion groups employed for cathode synthesis (allowing the tuning of transition metal redox potentials depending on the electronegativity of the polyanionic clusters) include pyrophosphates ($Li_2MP_2O_7$), fluorophosphates (Li_2MPO_4F), sulfates ($LiMOSO_4$), fluorosulfates ($LiMSO_4F$),[99] silicates (Li_2MSiO_4), borates ($LiMBO_3$) and those based on the

NASICON-type structure ($Li_3M_2(PO_4)_3$). It is apparent that in some of these structures more lithium ions are available for extraction per transition metal, but this would require increasingly higher voltage to increase the oxidation state of the transition metal centre: the operating window (*i.e.* region of electrochemical stability) of current commercial liquid electrolytes is limited to about 4.7 V,[100] in addition to a considerable proportion of the mass being electrochemically inactive and compromising volumetric capacity.

1.4 Summary and Future Directions

The capacity of lithium-ion battery cathodes has been determined as the major current limitation on the development of higher power batteries. The ideal lithium ion insertion cathode material is of low mass, with the capability for a number of lithium ions per redox active metal centre to be incorporated into the material. Electron conductivity and lithium ionic conductivity throughout both electrode materials should be rapid to ensure good rate capability. Within a fully charged cell, the lithiated anode (negative electrode) requires a high oxidation potential *vs.* Li^+/Li^0, *i.e.* a low voltage; and the delithiated cathode a low oxidation potential. The structure should be sufficiently stable upon (de)lithiation, with minimal volume change on the removal or insertion of lithium during cycling in order to minimise mechanical stress and ensure good reversibility of the cell. Stability of the electrodes over a wide operating voltage and chemical stability towards the electrolyte is fundamental for long cell lifetimes. From a commercial aspect, the synthesis of these materials should be simple and use low cost methods of production, in addition to low cost, abundant and non-toxic materials.

The lithium ion diffusion kinetics throughout the cathode depends on the crystal structure and the dimensionality of the diffusion of lithium ions within the structure,

hence detailed structural characterisation is required to effectively assess new compounds as potential LIB cathodes.

Lithium-ion batteries are generally thought to be reaching their limitations in terms of their power density. Due to the high charge density and large negative reduction potential of lithium metal, rechargeable battery technologies based on Li-air and Li-sulfur reactions are emerging avenues for the storage of electrical energy.[101,102]

1.5 Aims of Thesis

The aims of this thesis are primarily to synthesise and characterise new compounds for lithium-ion battery cathode applications. The most promising emerging class of materials are lithium-rich rock-salt type oxides, where the involvement of lattice oxide in a reversible redox reaction enables the additional extraction of lithium, in addition to the cationic redox. To date, the instability of the anionic redox in such Li-rich materials has prevented their commercial viability, generally due to the detrimental structural transformations and associated release of molecular oxygen, which degrades the overall electrochemical performance. Detailed characterisation of the structures of Li-rich cathodes has therefore proved imperative to understanding their electrochemical properties.

Within this thesis, the synthesis and structural and electrochemical characterisation of new Li-rich rock-salt type oxides are reported, with the properties being correlated to their crystal structure. Particular attention has been focused on the incorporation of tungsten into LIB cathode materials, which has thus far been unexplored. The primary aim has been to improve the energy density of lithium ion batteries through the extraction of additional capacity, with accessing and stabilising anionic redox in Li-rich materials being the most viable way of achieving this.

In addition, the viability of flame spray pyrolysis as a method of processing known LIB cathodes is explored as a potential means to improve the Li^+ and electronic diffusion kinetics, through the production of nanoparticles.

1.6 References

1. T. Placke, R. Kloepsch, S. Dühnen and M. Winter, *J. Solid State Electrochem.*, 2017, **21**, 1939-1964.
2. J. M. Tarascon and M. Armand, *Nature*, 2001, **414**, 359-367.
3. S. J. An, J. Li, C. Daniel, D. Mohanty, S. Nagpure and D. L. Wood, *Carbon*, 2016, **105**, 52-76.
4. J. B. Goodenough and K.-S. Park, *J. Am. Chem. Soc.*, 2013, **135**, 1167-1176.
5. E. Peled, *J. Electrochem. Soc.*, 1979, **126**, 2047-2051.
6. P. Verma, P. Maire and P. Novák, *Electrochim. Acta*, 2010, **55**, 6332-6341.
7. S. Zhang, M. S. Ding, K. Xu, J. Allen and T. R. Jow, *Electrochem. Solid-State Lett.*, 2001, **4**, A206-A208.
8. T. Yoshida, M. Takahashi, S. Morikawa, C. Ihara, H. Katsukawa, T. Shiratsuchi and J.-i. Yamaki, *J. Electrochem. Soc.*, 2006, **153**, A576-A582.
9. V. Agubra and J. Fergus, *Materials*, 2013, **6**, 1310-1325.
10. W. G. Qu, E. Dorjpalam, R. Rajagopalan and C. A. Randall, *ChemSusChem*, 2014, **7**, 1162-1169.
11. E. Peled and S. Menkin, *J. Electrochem. Soc.*, 2017, **164**, A1703-A1719.
12. N. S. Choi, J. G. Han, S. Y. Ha, I. Park and C. K. Back, *RSC Adv.*, 2015, **5**, 2732-2748.
13. A. W. Golubkov, D. Fuchs, J. Wagner, H. Wiltsche, C. Stangl, G. Fauler, G. Voitic, A. Thaler and V. Hacker, *RSC Adv.*, 2014, **4**, 3633-3642.
14. P. G. Balakrishnan, R. Ramesh and T. Prem Kumar, *J. Power Sources*, 2006, **155**, 401-414.
15. T. D. Bogart, A. M. Chockla and B. A. Korgel, *Curr. Opin. Chem. Eng.*, 2013, **2**, 286-293.
16. K. Persson, V. A. Sethuraman, L. J. Hardwick, Y. Hinuma, Y. S. Meng, A. van der Ven, V. Srinivasan, R. Kostecki and G. Ceder, *J. Phys. Chem. Lett*, 2010, **1**, 1176-1180.
17. L. W. Ji, Z. Lin, M. Alcoutlabi and X. W. Zhang, *Energy Environ. Sci.*, 2011, **4**, 2682-2699.

18. S. L. Candelaria, Y. Y. Shao, W. Zhou, X. L. Li, J. Xiao, J. G. Zhang, Y. Wang, J. Liu, J. H. Li and G. Z. Cao, *Nano Energy*, 2012, **1**, 195-220.
19. W. Xu, J. Wang, F. Ding, X. Chen, E. Nasybulin, Y. Zhang and J.-G. Zhang, *Energy Environ. Sci.*, 2014, **7**, 513-537.
20. A. Zhamu, G. Chen, C. Liu, D. Neff, Q. Fang, Z. Yu, W. Xiong, Y. Wang, X. Wang and B. Z. Jang, *Energy Environ. Sci.*, 2012, **5**, 5701-5707.
21. M. N. Obrovac and L. Christensen, *Electrochem. Solid-State Lett.*, 2004, **7**, A93-A96.
22. D. Billaud, E. McRae and A. Hérold, *Mater. Res. Bull.*, 1979, **14**, 857-864.
23. L. Ji, Z. Lin, M. Alcoutlabi and X. Zhang, *Energy Environ. Sci.*, 2011, **4**, 2682-2699.
24. C. K. Chan, H. Peng, G. Liu, K. McIlwrath, X. F. Zhang, R. A. Huggins and Y. Cui, *Nat. Nanotechnol.*, 2008, **3**, 31-35.
25. J. Cho, *J. Mater. Chem.*, 2010, **20**, 4009-4014.
26. E. Ferg, R. J. Gummow, A. de Kock and M. M. Thackeray, *J. Electrochem. Soc.*, 1994, **141**, L147-L150.
27. F. Wang, L. J. Wu, C. Ma, D. Su, Y. M. Zhu and J. Graetz, *Nanotech.*, 2013, **24**, 8.
28. T. Yuan, Z. Tan, C. Ma, J. Yang, Z.-F. Ma and S. Zheng, *Adv. Energy Mater.*, 2017, **7**, 1601625-n/a.
29. F. B. Dias, L. Plomp and J. B. J. Veldhuis, *J. Power Sources*, 2000, **88**, 169-191.
30. E. Quartarone and P. Mustarelli, *Chem. Soc. Rev.*, 2011, **40**, 2525-2540.
31. A. F. Liu, in *Applied Materials and Technologies for Modern Manufacturing, Pts 1-4*, eds. L. Zheng, S. Skuroda, H. Liu, B. Du, J. Wei and Y. Zhao, Trans Tech Publications Ltd, Stafa-Zurich, 2013, vol. 423-426, pp. 503-506.
32. J. C. Burns, N. N. Sinha, G. Jain, H. Ye, C. M. VanElzen, W. M. Lamanna, A. Xiao, E. Scott, J. Choi and J. R. Dahn, *J. Electrochem. Soc.*, 2012, **159**, A1095-A1104.
33. Y. E. Hyung, D. R. Vissers and K. Amine, *J. Power Sources*, 2003, **119**, 383-387.
34. X. L. Yao, S. Xie, C. H. Chen, Q. S. Wang, J. H. Sun, Y. L. Li and S. X. Lu, *J. Power Sources*, 2005, **144**, 170-175.
35. T. Sato, T. Maruo, S. Marukane and K. Takagi, *J. Power Sources*, 2004, **138**, 253-261.
36. F. Cheng, J. Liang, Z. Tao and J. Chen, *Adv. Mater. (Weinheim, Ger.)*, 2011, **23**, 1695-1715.

37. A. R. West, in *Basic Solid State Chemistry*, ed. A. R. West, John Wiley & Sons Inc., England, 2nd edn., 1999, ch. 1.

38. P. Ganguly, T. N. Venkatraman, P. R. Rajamohanan and S. Ganapathy, *J. Phys. Chem. B*, 1997, **101**, 11099-11105.

39. J. Hauck, *Acta Crystallogr. Sect. A*, 1980, **36**, 228-237.

40. L. Croguennec, C. Pouillerie and C. Delmas, *J. Electrochem. Soc.*, 2000, **147**, 1314-1321.

41. P. Kalyani and N. Kalaiselvi, *Sci. Tech. Adv. Mat.*, 2005, **6**, 689-703.

42. G. C. Mather, C. Dussarrat, J. Etourneau and A. R. West, *J. Mater. Chem.*, 2000, **10**, 2219-2230.

43. T. Takayama, A. Kato, R. Dinnebier, J. Nuss, H. Kono, L. S. I. Veiga, G. Fabbris, D. Haskel and H. Takagi, *Phys. Rev. Lett.*, 2015, **114**, 077202.

44. K. Ukei, H. Suzuki, T. Shishido and T. Fukuda, *Acta Cryst Sect. C*, 1994, **50**, 655-656.

45. R. Hoffmann and R. Hoppe, *Z. Anorg. Allg. Chem.*, 1989, **573**, 157-169.

46. P. Tabero and A. Frackowiak, *J. Therm. Anal. Calorim.*, 2017, **130**, 311-318.

47. G. Blasse, *Z. Anorg. Allg. Chem.*, 1964, **331**, 44-50.

48. K. Mizushima, P. C. Jones, P. J. Wiseman and J. B. Goodenough, *Mater. Res. Bull.*, 1980, **15**, 783-789.

49. D. D. MacNeil and J. R. Dahn, *J. Electrochem. Soc.*, 2001, **148**, A1205-A1210.

50. T. Ohzuku, A. Ueda, M. Nagayama, Y. Iwakoshi and H. Komori, *Electrochim. Acta*, 1993, **38**, 1159-1167.

51. Z. Lu, X. Huang, H. Huang, L. Chen and S. Joop, *Solid State Ionics*, 1999, **120**, 103-107.

52. M. G. S. R. Thomas, W. I. F. David, J. B. Goodenough and P. Groves, *Mater. Res. Bull.*, 1985, **20**, 1137-1146.

53. J. W. Fergus, *J. Power Sources*, 2010, **195**, 939-954.

54. Y. Zhang and C.-Y. Wang, *J. Electrochem. Soc.*, 2009, **156**, A527-A535.

55. N. Leifer, O. Srur-Lavi, I. Matlahov, B. Markovsky, D. Aurbach and G. Goobes, *Chem. Mater.*, 2016, **28**, 7594-7604.

56. Y. I. Jang, B. Huang, Y. M. Chiang and D. R. Sadoway, *Electrochem. Solid-State Lett.*, 1998, **1**, 13-16.

57. R. Koksbang, J. Barker, H. Shi and M. Y. Saïdi, *Solid State Ionics*, 1996, **84**, 1-21.

58. J. Cho, *Solid State Ionics*, 2001, **138**, 267-271.

59. L. Yang, M. Takahashi and B. Wang, *Electrochim. Acta*, 2006, **51**, 3228-3234.

60. R. Santhanam and B. Rambabu, *J. Power Sources*, 2010, **195**, 5442-5451.

61. F. Schipper, E. M. Erickson, C. Erk, J.-Y. Shin, F. F. Chesneau and D. Aurbach, *J. Electrochem. Soc.*, 2017, **164**, A6220-A6228.

62. O. Tsutomu and M. Yoshinari, *Chem. Lett.*, 2001, **30**, 642-643.

63. N. Yabuuchi and T. Ohzuku, *J. Power Sources*, 2003, **119-121**, 171-174.

64. S.-M. Bak, E. Hu, Y. Zhou, X. Yu, S. D. Senanayake, S.-J. Cho, K.-B. Kim, K. Y. Chung, X.-Q. Yang and K.-W. Nam, *ACS Appl. Mater. Interfaces*, 2014, **6**, 22594-22601.

65. S.-K. Jung, H. Gwon, J. Hong, K.-Y. Park, D.-H. Seo, H. Kim, J. Hyun, W. Yang and K. Kang, *Adv. Energy Mater.*, 2014, **4**, 1300787-n/a.

66. F. Schipper, M. Dixit, D. Kovacheva, M. Talianker, O. Haik, J. Grinblat, E. M. Erickson, C. Ghanty, D. T. Major, B. Markovsky and D. Aurbach, *J. Mater. Chem. A*, 2016, **4**, 16073-16084.

67. F. Lin, I. M. Markus, D. Nordlund, T.-C. Weng, M. D. Asta, H. L. Xin and M. M. Doeff, *Nat. Commun.*, 2014, **5**, 3529.

68. S.-L. Wu, W. Zhang, X. Song, A. K. Shukla, G. Liu, V. Battaglia and V. Srinivasan, *J. Electrochem. Soc.*, 2012, **159**, A438-A444.

69. M. H. Rossouw and M. M. Thackeray, *Mater. Res. Bull.*, 1991, **26**, 463-473.

70. M. H. Rossouw, D. C. Liles and M. M. Thackeray, *J. Solid State Chem.*, 1993, **104**, 464-466.

71. M. M. Thackeray, S. H. Kang, C. S. Johnson, J. T. Vaughey and S. A. Hackney, *Electrochem. Commun.*, 2006, **8**, 1531-1538.

72. D. Mohanty, S. Kalnaus, R. A. Meisner, K. J. Rhodes, J. Li, E. A. Payzant, D. L. Wood Iii and C. Daniel, *J. Power Sources*, 2013, **229**, 239-248.

73. H. Yu and H. Zhou, *J. Phys. Chem. Lett*, 2013, **4**, 1268-1280.

74. E.-S. Lee and A. Manthiram, *J. Mater. Chem. A*, 2014, **2**, 3932-3939.

75. H. Koga, L. Croguennec, P. Mannessiez, M. Ménétrier, F. Weill, L. Bourgeois, M. Duttine, E. Suard and C. Delmas, *J. Phys. Chem. C*, 2012, **116**, 13497-13506.

76. H. Koga, L. Croguennec, M. Ménétrier, P. Mannessiez, F. Weill, C. Delmas and S. Belin, *J. Phys. Chem. C*, 2014, **118**, 5700-5709.

77. C. Genevois, H. Koga, L. Croguennec, M. Ménétrier, C. Delmas and F. Weill, *J. Phys. Chem. C*, 2015, **119**, 75-83.

78. M. Sathiya, K. Ramesha, G. Rousse, D. Foix, D. Gonbeau, A. S. Prakash, M. L. Doublet, K. Hemalatha and J. M. Tarascon, *Chem. Mater.*, 2013, **25**, 1121-1131.

79. M. Sathiya, G. Rousse, K. Ramesha, C. P. Laisa, H. Vezin, M. T. Sougrati, M. L. Doublet, D. Foix, D. Gonbeau, W. Walker, A. S. Prakash, M. Ben Hassine, L. Dupont and J. M. Tarascon, *Nat. Mater.*, 2013, **12**, 827-835.

80. E. McCalla, M. T. Sougrati, G. Rousse, E. J. Berg, A. Abakumov, N. Recham, K. Ramesha, M. Sathiya, R. Dominko, G. Van Tendeloo, P. Novák and J.-M. Tarascon, *J. Am. Chem. Soc.*, 2015, **137**, 4804-4814.

81. E. McCalla, A. Abakumov, G. Rousse, M. Reynaud, M. T. Sougrati, B. Budic, A. Mahmoud, R. Dominko, G. Van Tendeloo, R. P. Hermann and J.-M. Tarascon, *Chem. Mater.*, 2015, **27**, 1699-1708.

82. J. Lee, A. Urban, X. Li, D. Su, G. Hautier and G. Ceder, *Science*, 2014, **343**, 519-522.

83. E. McCalla, A. M. Abakumov, M. Saubanère, D. Foix, E. J. Berg, G. Rousse, M.-L. Doublet, D. Gonbeau, P. Novák, G. Van Tendeloo, R. Dominko and J.-M. Tarascon, *Science*, 2015, **350**, 1516-1521.

84. E. McCalla, A. S. Prakash, E. Berg, M. Saubanère, A. M. Abakumov, D. Foix, B. Klobes, M.-T. Sougrati, G. Rousse, F. Lepoivre, S. Mariyappan, M.-L. Doublet, D. Gonbeau, P. Novak, G. Van Tendeloo, R. P. Hermann and J.-M. Tarascon, *J. Electrochem. Soc.*, 2015, **162**, A1341-A1351.

85. A. K. Padhi, K. S. Nanjundaswamy and J. B. Goodenough, *J. Electrochem. Soc.*, 1997, **144**, 1188-1194.

86. B. C. Melot and J. M. Tarascon, *Acc. Chem. Res.*, 2013, **46**, 1226-1238.

87. C. Liu, Z. G. Neale and G. Cao, *Mater. Today*, 2016, **19**, 109-123.

88. C. Masquelier and L. Croguennec, *Chem. Rev. (Washington, DC, U. S.)*, 2013, **113**, 6552-6591.

89. K. Zaghib, A. Mauger and C. M. Julien, *J. Solid State Electrochem.*, 2012, **16**, 835-845.

90. K. Zaghib, A. Mauger, J. B. Goodenough, F. Gendron and C. M. Julien, *Chem. Mater.*, 2007, **19**, 3740-3747.

91. A. Manthiram, *Electrochem. Soc. Interface*, 2009, **18**, 44.

92. P. S. Herle, B. Ellis, N. Coombs and L. F. Nazar, *Nat. Mater.*, 2004, **3**, 147-152.

93. D. Morgan, A. Van der Ven and G. Ceder, *Electrochem. Solid-State Lett.*, 2004, **7**, A30-A32.

94. C. Delacourt, P. Poizot, S. Levasseur and C. Masquelier, *Electrochem. Solid-State Lett.*, 2006, **9**, A352-A355.

95. N. Meethong, H.-Y. S. Huang, W. C. Carter and Y.-M. Chiang, *Electrochem. Solid-State Lett.*, 2007, **10**, A134-A138.

96. L.-X. Yuan, Z.-H. Wang, W.-X. Zhang, X.-L. Hu, J.-T. Chen, Y.-H. Huang and J. B. Goodenough, *Energy Environ. Sci.*, 2011, **4**, 269-284.

97. L. Yu, Q. Liu and H. Wang, *Ionics*, 2009, **15**, 689-692.

98. M. Hu, X. Pang and Z. Zhou, *J. Power Sources*, 2013, **237**, 229-242.

99. G. Rousse and J. M. Tarascon, *Chem. Mater.*, 2013, **26**, 394-406.

100. K. Xu, *Chem. Rev. (Washington, DC, U. S.)*, 2004, **104**, 4303-4418.

101. P. G. Bruce, L. J. Hardwick and K. M. Abraham, *MRS Bulletin*, 2011, **36**, 506-512.

102. E. M. Erickson, E. Markevich, G. Salitra, D. Sharon, D. Hirshberg, E. de la Llave, I. Shterenberg, A. Rosenman, A. Frimer and D. Aurbach, *J. Electrochem. Soc.*, 2015, **162**, A2424-A2438.

Chapter 2: Experimental Methods

2.1 Synthesis

The primary method of synthesis used for the preparation of target materials was the solid state method, whereby high temperatures and long reaction times result in thermodynamic products. These conditions are required in order to overcome the high kinetic diffusion barriers associated with ionic diffusion through solids, which is usually a slow process. A number of cycles of sintering and grinding materials is often required to obtain phase pure samples with good homogeneity. Powdered starting materials are used with well-defined compositions and purity, often requiring drying before weighing (~200 °C overnight within this work). For small scale exploratory synthesis (of the order of ~1 g of product), hand grinding of the solid precursors in an agate pestle and mortar is sufficient to reduce particle size and ensure good homogeneity of the reaction mixture, with the optional addition of organic solvents (acetone or ethanol) to aid mixing where necessary, before pressing into pellets. For preparation of larger amounts of sample (such as for neutron powder diffraction), mechanical milling was employed to ensure good homogeneity and decrease particle size with comparison to hand grinding. The starting materials were weighed out and added to zirconia milling pots, with a number of 10 mm diameter zirconia spheres and isopropanol. The precursors were milled using a Fritsch Pulverisette planetary mill operating at 350 rpm, for at least 1 hr total milling time. The resulting slurry was dried in a crystallising dish on a stirrer hotplate to remove the isopropanol, and the mixed powder recovered and hand ground to avoid sedimentation before pelletising.

Pressing the reactants into pellets enhances contact between particles to aid ionic diffusion, in addition to minimising the loss of any volatile reactants and contact with the crucible and was employed for all sintering steps within this work. An important consideration for the preparation of lithium-containing materials is the volatilisation of lithium to form Li_2O, which occurs rapidly at ~900 °C and above. For this reason, a molar excess of lithium precursors is often included to compensate for any lithium loss at these high reaction temperatures. Also, where precursors are deemed to be volatile in the preparation of pellets, a sacrificial powder can be employed to surround the pellet and maintain the required stoichiometric ratio within the pellet. The sample containers used within this work were alumina crucibles, occasionally requiring a lining of platinum foil to avoid reaction with the crucible. The primary focus of this work is the synthesis of lithium metal oxides, where sintering in a muffle furnace employing a static air atmosphere were the most commonly employed conditions. It is also possible to adjust the oxygen partial pressure during reactions by reaction in a tube furnace with a dynamic flow of gas (such as argon) to control the oxygen content and oxidation states of metal ions. The details of reaction conditions are reported in the following chapters.

The use of flame spray pyrolysis (FSP) as a synthetic method is discussed in detail in Chapter 6. This method involves the using of liquid precursors sprayed into a flame, causing rapid product formation, which are then deposited on an unreactive surface. The rapid reaction time results in nano-sized particles, which is desirable for some lithium-ion battery cathodes whereby the diffusion kinetics are hindered by slow diffusion from the bulk to the surface and across grain boundaries.

2.2 Powder Diffraction

Powder diffraction is a widely used analytical technique for the structural characterisation of polycrystalline materials. The diffraction of X-rays, neutrons or electrons on a powder sample can afford valuable information about the three-dimensional arrangement of atoms in crystals in a non-destructive manner with minimal additional sample preparation.

2.2.1 Powder X-Ray Diffraction (PXRD)

Crystalline solids possess long-range ordering of atoms in three-dimensional periodic arrays, with interatomic distances spanning ~0.5-2.5 Å. The diffraction of X-rays from crystalline solids is possible due to the interatomic distances being comparable to the wavelength of X-rays, 0.1-100 Å. The scattering of X-rays from the electron cloud of an atom is directly proportional to the number of electrons in that atom or ion. For this reason, it can be difficult to distinguish lighter atoms which have a smaller scattering factor, or distinguish between atoms or ions with similar atomic numbers (*Z*). Within this thesis, three laboratory X-ray diffractometers were used for data collection, depending on the required X-ray source (Cu, Co or Mo anode) and whether Bragg-Brentano or Debye-Scherrer geometry was preferred.

The Bragg-Brentano focusing method, also referred to as reflection geometry, employs flat specimens of crystalline powders continuously rotating on a flat sample plate (Figure 2.2.1). Focusing of the X-ray source allows good resolution of data and peak intensities. The diffraction angle, 2θ is defined as the angle between the incident and diffracted X-ray beam. The X'Pert PANalaytical diffractometer uses a cobalt anode for the X-ray source (Co $K\alpha_1$ = 1.78896 Å), used in Bragg-Brentano geometry within this thesis.

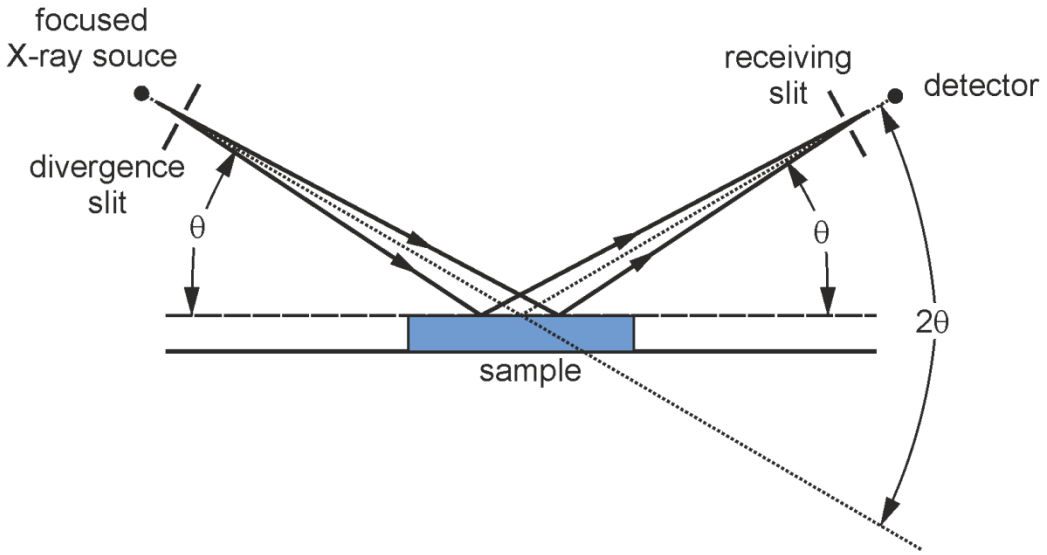

Figure 2.2.1: Labelled diagram of PXRD collection in Bragg-Brentano geometry

The Debye-Scherrer (or transmission) geometry is used in the Bruker D8 diffractometers, using a copper (Cu $K\alpha_1$ = 1.540596 Å) or molybdenum (Mo $K\alpha_1$ = 0.7093 Å) anode as the radiation source. The sample is either loaded in a flat holder encased with a thin transparent film, or within a transparent capillary (Figure 2.2.2).

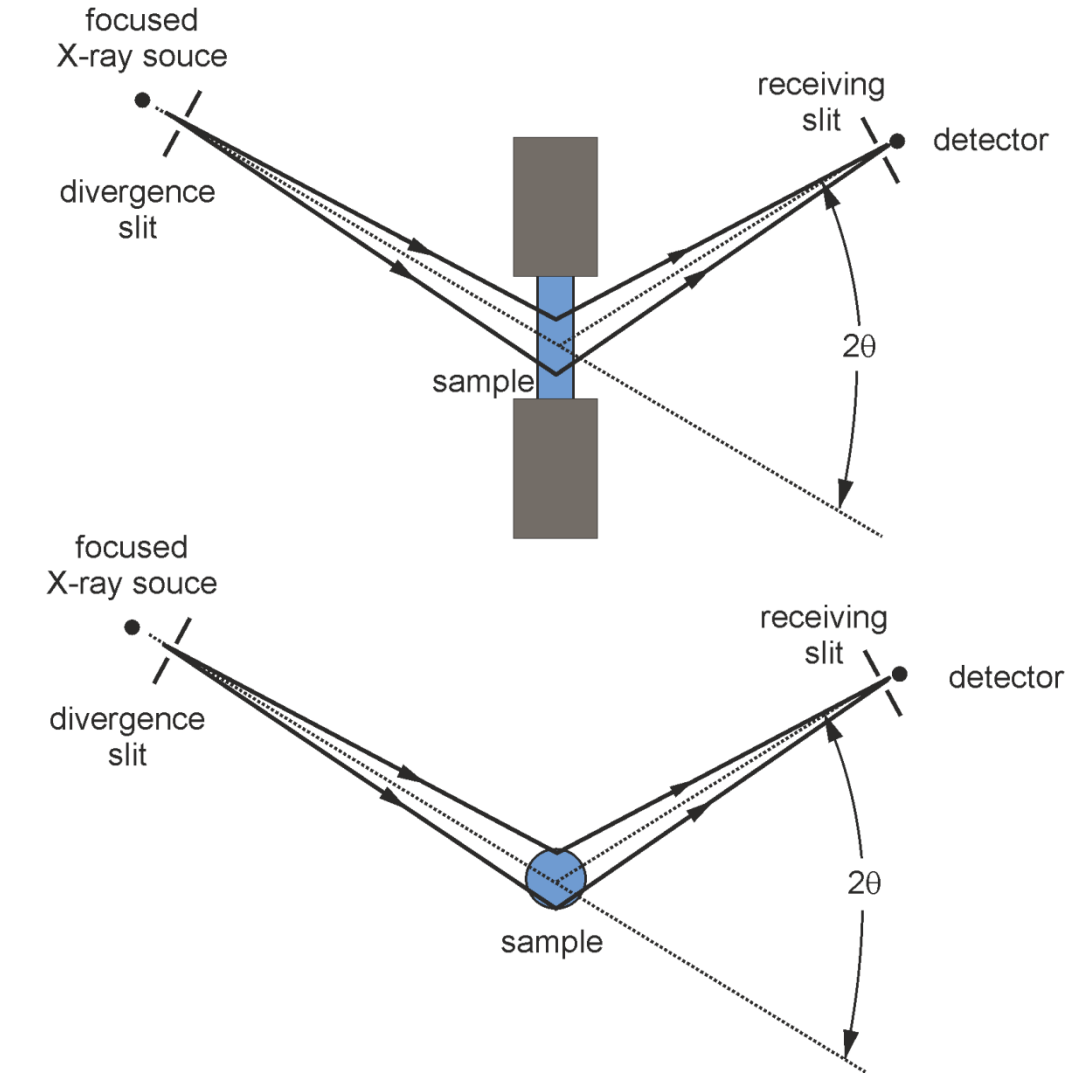

Figure 2.2.2: Labelled diagram of PXRD collection in Debye-Scherrer geometry, using a rotating transmission foil stage (*top*) or capillary (*bottom*)

Additionally, for high resolution and high-angle data, PXRD was performed on the I11 beamline at the Diamond synchrotron at the Rutherford Appleton Laboratory (Oxfordshire, UK). This beamline employs a wide-angle position sensitive detector (PSD) for rapid data acquisition and time-resolved analysis, or five multi-analysing crystal (MAC) devices for high-resolution measurements in Debye-Scherrer geometry.

2.2.2 Neutron Powder Diffraction (NPD)

Neutrons are scattered by the nucleus of atoms (whereas X-rays are scattered by electrons), meaning the scattering length (*b*) is dependent on the isotopes present rather than varying with *Z*. This makes NPD a somewhat complementary analytical technique to PXRD, where lighter elements such lithium and oxygen interact more strongly with neutrons. In addition, there is effectively no form factor for the interaction of neutrons with the nucleus (with the exception of magnetic cations), as the nucleus is a point scatterer compared to the wavelength of the incident neutron radiation. As a result, the intensity of the NPD patterns does not decrease with decreasing interatomic spacings and high-quality data at low *d*-spacings can be obtained.

Neutron powder diffraction data was used for structural characterisation in Chapter 3. High-resolution time-of-flight (TOF) neutron powder diffraction data were collected at room temperature using the HRPD (high-resolution powder diffraction) instrument at the ISIS facility at the Rutherford Appleton Laboratory (Oxfordshire, UK). The samples used for NPD were synthesised using ^{7}Li-enriched Li_2CO_3 to minimise neutron absorption by ^{6}Li, using a vanadium canister as the sample holder. Three databanks were utilised for data collection employing the backscattering detector at 168°, and detectors positioned at 90° and 30° relative to the incident neutron beam (bank 1, 2 and 3 respectively) in order to obtain high-resolution data at short *d*-spacings (0.3 Å) from the backscatter detector, and lower resolution data at higher *d*-spacings (16.5 Å). The data were collected at room temperature.

2.2.3 Structural Refinement from Powder Diffraction

Powder diffraction patterns contain information about the crystal structure of crystalline materials based on the positions and intensities of diffraction peaks. The peak positions are determined by Bragg's law, dependent on the wavelength of the incident radiation and the spacing between lattice planes (d_{hkl}). The peak intensities (I_{hkl}) for a given reflection are proportional to the square of the structure factor (F_{hkl}), which in turn is dependent on the atomic positions and the scattering factor of that atom. The shape and width of the diffraction peaks (with the inherent peak profile of the diffractometer accounted for) and oscillations in the background of the diffractogram contain detailed information about the local structure of crystallites.

Through determination of peak positions, the lattice parameters and Bravais lattice can be deduced by the assignment of Miller indices (*hkl*) to each peak, known as indexing. Pawley and Le Bail refinements are methods used for refining the size and shape of the unit cell using least squares analysis and does not include refinement of atomic positions. The Rietveld method includes the atomic structure in the refinement of the model, $y_{i(calc)}$, to experimental diffraction data, $y_{i(obs)}$, using the non-linear least squares method. Structure solution using the Rietveld method allows the simultaneous refinement of structural parameters: fractional coordinates of the atomic sites, the scattering factor of the atomic sites, atom occupancies and atomic displacement parameters. For the solution of an unknown structure, it is important that the lattice parameters, peak profile and zero shift have been established and the background modelled (typically using a polynomial function such as Chebyshev polynomials) before introducing the structural model to refine in a systematic way. Following each iteration, whereby the structural model is refined to fit the observed data, the statistical parameters representing the quality of the fit (*R*-factors) should be

considered, with lower values representing a better fit. However, it is possible to over fit the data and the user should ensure the structural model remains chemically sensible.

The non-linear least squares function which is being minimised during a Rietveld refinement is given by:

$$S_y = \sum_i w_i \left\{ y_{i(\mathrm{obs})} - y_{i(\mathrm{calc})} \right\}^2$$

$$\text{where weight for each observation, } w_i = \frac{1}{\sigma_i^2}$$

From this the weighted profile *R*-factor, R_{wp}, can be established as:

$$R_{wp} = 100\% \times \left[\frac{\sum_i w_i \left\{ y_{i(\mathrm{obs})} - y_{i(\mathrm{calc})} \right\}^2}{\sum_i w_i \left\{ y_{i(\mathrm{obs})} \right\}^2} \right]^{1/2}$$

The expected *R*-factor, R_{exp}, provides the best possible value for R_{wp}, with a lower number representing higher quality of data:

$$R_{exp} = 100\% \times \left[\frac{(N - P)}{\sum_i w_i \left\{ y_{i(\mathrm{obs})} \right\}^2} \right]^{1/2}$$

where N = number of observations; P = number of parameters

The value of the weighted *R*-factor can be compared that for the expected *R*-factor for Rietveld and Pawley or Le Bail refinements to monitor convergence of the calculated to observed data after each iteration cycle. The parameter χ represents the 'goodness of fit' and is reported as χ^2 whose value is dependent on R_{wp} and R_{exp}:

$$\chi^2 = \left(\frac{R_{wp}}{R_{exp}}\right)^2$$

The value for R_{wp} should never be less than R_{exp} for a good structural model, likewise χ^2 should never be less than one. These *R*-factors and goodness of fit allow statistical comparisons to the quality of the structural model.[1]

Throughout this work, Topas Academic V5 was used as the primary refinement software.[2] Combined Rietveld refinements allow the use of SXRD and NPD data simultaneously to solve crystal structures and were employed in Chapter 3.

2.3 Electron Microscopy

Electron microscopes use a beam of accelerated electrons, focused using electromagnetic condenser lenses, to image materials in an evacuated environment. The de Broglie wavelength of a beam of electrons is about one thousand times shorter than that of a photon of visible light, meaning the resolution of electron microscopes is one thousand times higher than an optical microscope.

2.3.1 Scanning Electron Microscopy (SEM)

The use of scanning electron microscopy allows the imaging of the surface of solid materials, providing topographical information for the determination of particle morphology and allowing estimation of particle size. A focused beam of electrons is used to scan the surface of a solid sample and interact with it as the electron beam slightly penetrates the surface. This results in the emission of secondary and backscattered electrons which are detected and an image is produced with the brightness dependent on the current collected.[3] A low accelerating voltage is typically used for imaging.

Within this thesis, SEM was performed using a Hitachi S-4800 Field-Emission Scanning Electron Microscope and the samples were sputter-coated with gold nanoparticles to aid conduction of electrons.

2.3.2 Energy Dispersive X-Ray (EDX) Spectroscopy

Scanning and transmission electron microscopy can be coupled with EDX to provide detailed compositional information about a sample using an X-ray detector: as the focused electron beam interacts with the sample X-rays are also generated, with an energy specific to the atoms contained in the specimen. The X-rays are emitted as the interacting electron beam excites a core electron to create a hole and an electron in a higher energy level falls down to fill the hole, emitting an X-ray of quantised energy characteristic of that atom. These X-rays are detected and counted to give a quantitative count of the elements present in the sample. Unfortunately, this technique has its limitations: lithium cannot currently be detected by EDX as the X-rays produced are of too low energy to be detected and other elements with $Z < 11$ are difficult to detect and quantify. A higher accelerating voltage is used for SEM-EDX, typically 10 – 30 kV, allowing the bulk composition of the sample to be measured due to penetration of the electron beam beyond the surface. It has the capability of visually mapping the quantity of certain elements over a defined area.

2.3.3 Transmission Electron Microscopy (TEM)

Transmission electron microscopy affords a higher resolution to SEM, whereby a focused beam of electrons is transmitted through and interacts with the sample to produce a number of different secondary signals such as backscattered electrons, Auger electrons and X-rays of characteristic wavelengths. TEM allows the observation of bulk structural features of crystalline materials such as dislocations and grain boundaries, and can be used in the analysis of multiphasic samples due to

the high resolution. In addition to imaging, various chemical analyses can also be performed by detection of secondary signals.

Within this thesis, TEM-EDX was performed using a JEOL 2000FX instrument equipped with an EDX spectrometer. A small amount of powder from each sample was well ground and dispersed in ethanol and deposited onto a copper TEM grid with thanks to Dr Marco Zanella and Dr Timothy Johnson.

2.4 Inductively Coupled Plasma Optical Emission Spectroscopy (ICP-OES)

The ICP and optical spectrometer provide a quantitative elemental analytical technique. Plasma, typically argon, is generated using a radio frequency generator and is used for the atomisation and excitation of the electrons in the sample, resulting in ionisation. The electrons emit characteristic, quantised wavelengths of light as the electrons return to lower energy states. The multiple optical emission lines from the plasma pass into the spectrometer *via* a diffraction grating which separates the incoming light into element-specific wavelengths. A corresponding detector measures the intensity of light for each wavelength, proportional to the concentration of that element in the sample. This has the advantage over EDX for the compositional analysis of LIB cathode materials as lithium can be detected and quantified. It also currently requires liquid samples, typically achieved using microwave-assisted digestion with concentrated acids and hydrogen peroxide within this work.

2.5 Electrochemical Behaviour

2.5.1 Coin Cell Assembly

Electrochemical testing of materials as lithium-ion battery cathodes was performed in the Stephenson Institute for Renewable Energy (SIRE) at University of Liverpool, UK with thanks to Dr Nicholas Drewett, Filipe Braga Noguiera and Jose Coca-Clemente (Hardwick group) for supplying the data. Coin cells (CR2025) were assembled in an argon-filled glove box using 1 M $LiPF_6$ dissolved in ethylene dicarbonate/dimethyl carbonate (BASF) 1:1 by volume as the electrolyte, impregnated onto a glass fibre separator (Whatman) (Figure 2.5.1).

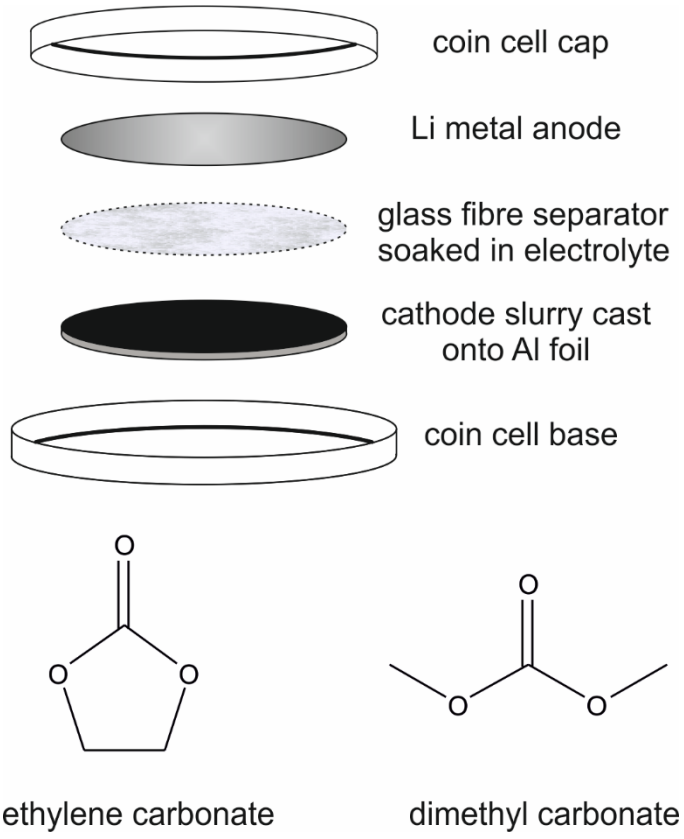

Figure 2.5.1: Schematic diagram of coin cell assembly for cathode testing (*top*) and representation of the alkyl carbonates used for the electrolyte (*bottom*)

The composite electrodes were fabricated by casting a homogenous mixture of well-ground or ball-milled active cathode material: Super C carbon: polyvinylidene fluoride binder (Kynarflex, Arkema) (typically 80:10:10 by wt) onto an aluminium foil current collector using solvent etching. This results in a layer of cathode ~10-35 μm thick on aluminium foil, cut to 10 mm diameter disks to form the cathode of the coin cell, and a lithium metal counter electrode completes the cell. Electrochemical characterization of the cyclability was carried out at 30 °C using a Maccor Series 4200 battery cycler. A check of the open circuit voltage (OCV) using a voltmeter ensures that the coin cell will function and has not short-circuited. A number of *ex-situ* analytical techniques were employed for analysis of the electrochemical behaviour of lithium-ion battery cathodes as detailed in Chapter 4.

2.5.2 Galvanostatic Cycling of Coin Cells

Galvanostatic cycling involves cycling of coin cells at a constant temperature over a defined voltage range with a constant current rate (C-rate). A C-rate of 1C is defined as the current required for the full discharge of the cell in one hour (which can be estimated by calculating the theoretical capacity). Charge-discharge curves represent the charge and discharge capacities with respect to the voltage. For testing of the long term cycling stability of a battery, coin cells are charged and discharged a number of times and the capacity is monitored over a number of cycles. The capacity retention, also known as cyclability, is usually given as a percentage of the initial capacity over a given number of cycles.

2.5.3 Rate Capability Measurements

Increasing the C-rate during battery cycling indicates how much capacity can be extracted during fast charging or discharging. During the rate capability measurements presented in this thesis, the C-rate is incrementally increased for a

number of cycles to assess the capacity retention and overall capacity extraction. The rate capability depends on the lithium ion and electronic conduction kinetics, hence the performance at higher rates indicates whether either of these factors is limiting the overall electrochemical performance of the cathode.

2.5.4 X-Ray Absorption Near Edge Structure (XANES) Spectroscopy

X-ray absorption spectroscopy (XAS) encompasses XANES and EXAFS (extended X-ray absorption fine structure). It requires a tunable X-ray source, such as that from a synchrotron, to probe the valence states and local bonding environments of various elements near to their characteristic absorption edges. The absorption edges arise from the excitation of a core electron to a higher energy level by incident X-rays. For example, the K-edge absorption is defined as the excitation of a 1*s* level electron to the lowest lying *p* orbital. The tungsten L_3-edge is a result of the excitation from $2p_{3/2}$ to $5d_{3/2}$ and $5d_{5/2}$ states.[4]

The active cathode material ($Li_{4.15}Ni_{0.85}WO_6$, 80% wt) was hand ground with Super C carbon (10% wt) and PVDF binder (10% wt) and a number of coin cells were assembled as detailed in Section 2.5.1. The coin cells were charged and discharged to specified voltages to obtain various levels of lithiation and disassembled in an argon-filled glovebox. The cathode casts were heat-sealed in polyethylene(PE)-lined aluminium foil bags (Sigma Aldrich) in a glovebox to prevent exposure to air and moisture. $NiWO_4$ was prepared *via* solid state synthesis to act as a Ni^{2+} and W^{6+} standard. Additionally, $LiNiO_2$ was prepared as a Ni^{3+} standard using sol-gel synthesis and annealing under a dynamic O_2 atmosphere. WO_2 (99.99%, Sigma Aldrich) served as the W^{4+} standard and WO_3 (99.995%, Sigma Aldrich) as an additional W^{6+} standard. The standards for XANES analysis were prepared by hand grinding an appropriate mass of each material (10-24 mg) with a

cellulose binder (Sigma Aldrich) until homogeneous and pressed into pellets using a 13 mm pellet die.

The X-ray absorption spectra were measured at the B18 beamline at Diamond Light Source (Oxfordshire, UK) in transmission configuration. XANES spectroscopy was used for analysis of the nickel and tungsten oxidation states, near the Ni K- and W L_3-edges (Chapter 4). Thanks to Professor Alan Chadwick and Dr Giannantonio Cibin for their assistance with this experiment. XANES data were processed using the Athena software.[5]

2.5.5 X-Ray Photoelectron Spectroscopy (XPS)

The use of XPS allows the oxidation states of elements in a sample to be determined. It relies on the photoelectric effect, whereby core electrons absorb the energy from incident X-ray photons of sufficient energy to cause the photon to be emitted from the material. The kinetic energy of these emitted photoelectrons is measured by the detector and the binding energy of the electrons can be determined. The binding energy of the core electrons depends on *Z*, with the binding energy increasing with increasing oxidation state. The magnitude of the chemical shift in binding energy compared to that of known oxidation states is used to analyse the binding energy of the core electrons in the sample and the oxidation states of elements present. In addition, since the detector counts the number of photoelectrons emitted in a given time, XPS can also be used for the quantification of elements in a sample. XPS is a surface sensitive analytical technique (due to the low inelastic mean free path of photoelectrons), requiring an ultra-high vacuum environment for detection of photoelectrons, with the surface often treated with argon sputtering to remove impurities.

XPS experiments were performed in a standard ultra-high vacuum surface science chamber consisting of a PSP Vacuum Technology electron energy analyser (angle integrating ± 10°) and a dual anode Mg (Kα = 1253.6 eV) X-ray source. The base pressure of the system was 2×10^{-10} mbar, with hydrogen as the main residual gas in the chamber. Calibration of the spectrometer was achieved using Au $4f_{7/2}$ energy level (83.9 eV). The XPS spectra were fitted using Voigt functions after Shirley background removal with an overall resolution of 0.2 eV. This technique was applied to determine the oxidation states of lithium (1*s*), nickel (2*p*), tungsten (4*f*) and oxygen (1*s*) in $Li_{4.15}Ni_{0.85}WO_6$ (Chapter 4). Thanks to Jose Coca-Clemente (SIRE, University of Liverpool) for providing this data.

2.5.6 Hard X-Ray Photoelectron Spectroscopy (HAXPES)

This analytical technique requires a synchrotron source to provide a high photon flux of tunable energies. For analysis of lithium-ion battery cathode materials, this has the advantage over XPS in that it is much less surface sensitive with a penetration depth of ~10-15 nm, due to a high flux of hard X-rays.[6] This is particularly useful for LIB materials due to the presence of the SEI layer present on electrode surfaces that have been electrochemically cycled, instead allowing the bulk oxidation states to be analysed in a similar way to XPS. HAXPES was employed in Chapter 4 for the analysis of the oxygen oxidation states (O 1*s*) in the bulk of the cathode material.

HAXPES data was collected on the P09 beamline of the Petra III synchrotron (DESY, Hamburg) with thanks to Dr Andrei Hloskovsky.

2.6 References

1. B. H. Toby, *Powder Diffr.*, 2012, **21**, 67-70.
2. A. A. Coelho, *Coelho Software*, 2007.
3. K. C. A. Smith and C. W. Oatley, *Br. J. Appl. Phys.*, 1955, **6**, 391.
4. U. Jayarathne, P. Chandrasekaran, A. F. Greene, J. T. Mague, S. DeBeer, K. M. Lancaster, S. Sproules and J. P. Donahue, *Inorg. Chem.*, 2014, **53**, 8230-8241.
5. B. Ravel and M. Newville, *J. Synchrotron Radiat.*, 2005, **12**, 537-541.
6. B. Pal, S. Mukherjee and D. D. Sarma, *J. Electron Spectrosc. Relat. Phenom.*, 2015, **200**, 332-339.

Chapter 3: Synthesis and Characterisation of $Li_{4+x}M_{1-x}WO_6$ Rock-Salts

3.1 Introduction

Lithium metal oxide cathode materials of the form $LiMO_2$ (such as $LiCoO_2$) are derivatives of the rock-salt structure type, with lithium layers separating layers of (MO_6) octahedra. Similarly, Li_2MnO_3 can be thought of as $Li[Li_{1/3}Mn_{2/3}]O_2$ in the $LiMO_2$ notation, possessing a cubic close-packed oxide array with ordered layers of Li and Mn octahedra separated by fully occupied lithium layers (see Chapter 5).[1] Based on the Li_2MnO_3 structure, substitution of Mn^{4+} for two different metal centres (where the sum of the oxidation states of these metals is equal to +4 to retain charge neutrality) can result in ordered rock-salt type superstructures. The general formula can therefore be considered as $Li_2M_{0.5}M'_{0.5}O_3$, or $Li_4MM'O_6$ where the sum of the oxidation states of the two metal centres is equal to +8. Reported examples include Li_4MTeO_6 ($M^{(II)}$ = Co, Ni, Cu, Zn)[2, 3] and Li_4MSbO_6 ($M^{(III)}$ = Al, Cr, Ga, Fe, Mn).[4-6] These structures retain the close-packed arrangement of oxygen ions with octahedrally coordinated metals forming an ordered 'honeycomb' array, separated by a fully occupied lithium layer (Figure 3.1.1). Alternatively, rock-salt superstructures with a composition of the form $Li_3M_2M'O_6$ (*e.g.* $M^{(II)}$ = Co, Ni, Mg; $M'^{(V)}$ = Nb, Ta) have been found to adopt a different ordering of cations,[7] whereby the pentavalent metal cations are fully ordered but the divalent metal cations and lithium ions are disordered, meaning the distinct fully occupied Li-layers are no longer present (see Chapter 1).[8, 9] The large

difference between the valence states of *M* and *M'* drives the cation ordering in such materials.

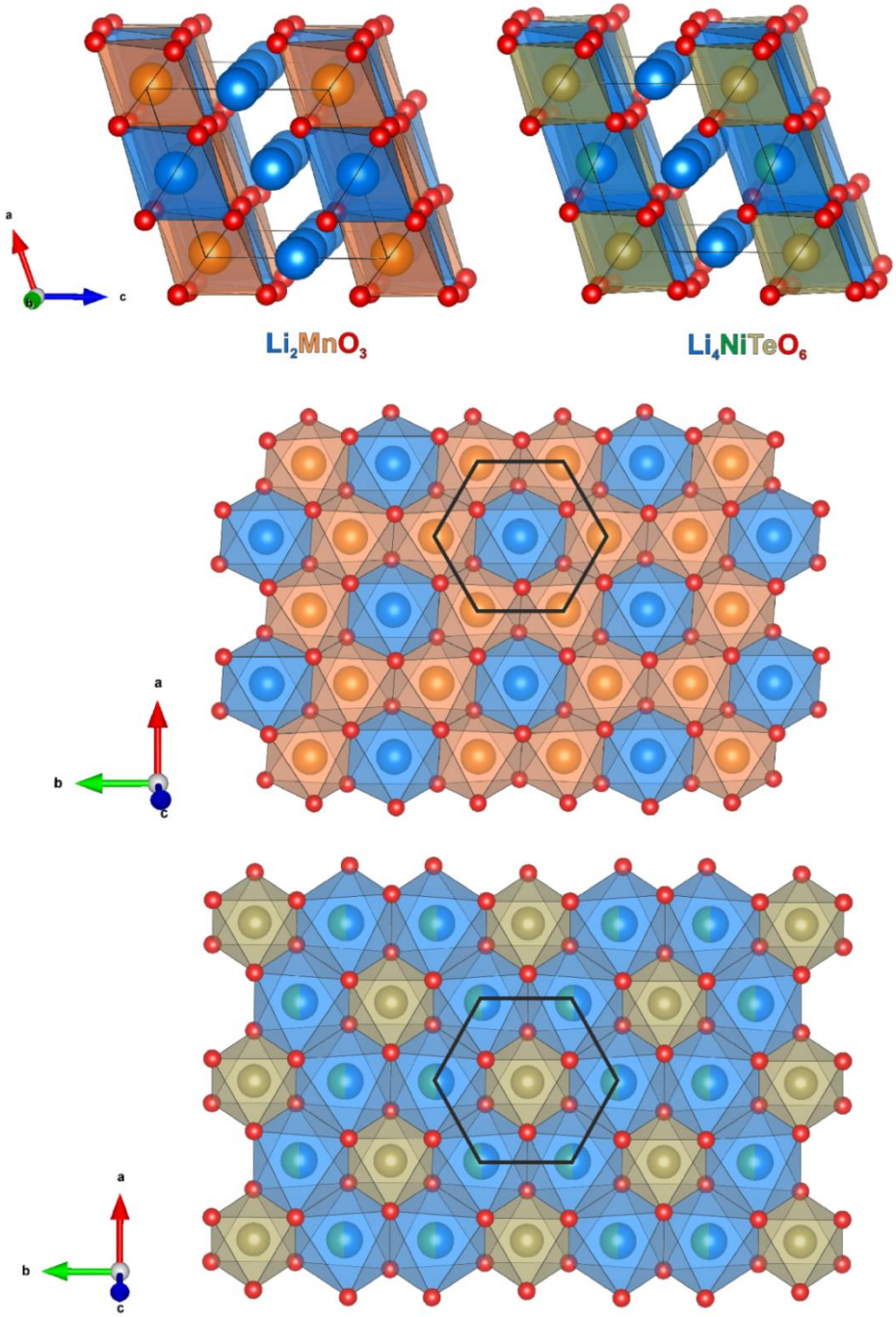

Figure 3.1.1: Comparison of structures of Li_2MnO_3 and Li_4NiTeO_6 (S.G. *C*2/*m*) viewed along the [010] direction (*top*) and visualisation of honeycomb ordering in mixed metal layers viewed along the [111] axis of the cubic rock-salt sub-cell (*bottom*). Li represented by *blue* spheres, O by *red* spheres, Mn by *orange* spheres, Te by *gold* spheres, Ni by *green* spheres

Few of these Li-containing rock-salt superstructures have been investigated for their electrochemical activity as Li-ion battery cathodes, despite the high lithium content (*i.e.* the ratio of Li: transition metal >1) and incorporation of transition metal ions with multiple accessible oxidation states. This is perhaps due to the presence of high-valency heavy metal cations which are cation redox inactive (such as Te^{6+}, Mo^{6+}, Ta^{5+}). In particular, the accessibility of the two-electron $Ni^{4+/2+}$ redox process enables high capacities to be achieved, where two Li ions are able to reversibly deintercalate from the structure upon cycling due to this redox couple.[10, 11]

The $Ni^{4+/2+}$ redox has been utilised in Li_4NiTeO_6 and Li_4NiMoO_6 (which can be considered as the binary system $0.5Li_4MoO_5{\cdot}0.5NiO$), with $[M^{VI}O_6]^{6-}$ moieties exhibiting an inductive effect on the nickel ions and raising the oxidation potential in comparison to $LiNiO_2$.[12, 13] Li_4NiTeO_6 was determined to have fully occupied Li layers (Figure 3.1.1), exhibiting a reversible specific capacity of 110 mA·h g^{-1}, with oxidation of $Ni^{2+} \rightarrow Ni^{4+}$ occurring at 4.2 V *vs.* Li^+/Li^0. On the other hand, Li_4NiMoO_6 was determined to have full ordering of the Mo sites, but lithium and nickel site mixing was observed, hence no fully occupied lithium layers were observed. The specific capacity of Li_4NiMoO_6 was also ~110 mA·h g^{-1} when cycled between 2.5-4.1 V. However, when the voltage window was extended from 1.5-4.8 V, an additional redox process was observed contributing to an increased overall capacity, but with a rapid reduction in capacity over subsequent cycles. This capacity degradation was attributed to an irreversible phase transition due to migration of Mo^{6+} ions. The origin of the additional redox process activated at high voltage and appearing at ~2 V discharge was not conclusively identified, but most likely due to the anionic redox process as observed in the structurally analogous Li_4FeMoO_6 system by X-ray absorption spectroscopy.[14] The anionic redox processes involves the evolution of oxygen from

the structure upon charge, thought to cause 'oxidation' to peroxo-type species ($2O^{2-} \rightarrow O_2^{n-}$ where n = 1, 2 or 3) enabling additional lithium extraction by comparison to solely cationic redox,[15, 16] and is discussed in more detail in Chapter 4.

The motivation behind this project was to synthesise binary systems between NiO and Li_4WO_5, to create new lithium-rich rock-salt superstructures, with an initial target composition of Li_4NiWO_6 to function as a lithium-ion battery cathode material. The electrochemical activity of the rock-salt type Li_4WO_5 itself has not been reported to date, but is expected to be inactive due to the $5d^0$ electronic configuration, hence there are no electrons present in the conduction band (similar to Li_4MoO_5 or Li_3NbO_4). However, metal substitution with a $3d^n$ metal (Ni^{2+} [Ar]$3d^8$ in this case) is expected to donate electrons to the conduction band enabling Li^+ ion and electronic conductivity.[14] Nickel is chosen as the electrochemically active transitional metal ion with the ability to employ the Ni^{4+}/Ni^{2+} redox couple to drive Li deintercalation, with W^{6+} providing electroneutrality and structural stability to the rock-salt based structure and allowing the influence of a $5d^0$ metal on the electrochemical properties to be investigated. The use of 5*d* transition metals within LIB electrodes to date is unreported, likely due to the high relative atomic mass. Additionally, a magnesium analogue (of target composition $Li_{4.08}Mg_{0.90}W_{1.02}O_6$) was synthesised for structural comparison.

3.2 Experimental Methods

3.2.1 Synthesis of Li_4NiWO_6

Samples were synthesised *via* ceramic synthesis using Li_2CO_3 (99.997%, Sigma Aldrich), NiO (99.999%, Sigma Aldrich) and WO_3 (99.995%, Sigma Aldrich). The powders were pre-dried overnight at 250° C prior to synthesis and combined in a pestle and mortar in a stoichiometric ratio of Li:Ni:W (4:1:1). The reactants were hand ground in an agate pestle and mortar, where the reaction was completed on a less than 1 g scale. In situations where more sample was required, for neutron powder diffraction experiments for example, to ensure homogenous mixing the reagents were first milled using a planetary mill (350 rpm) using 10 mm diameter zirconia balls and isopropanol as the milling media for a total of 2 h. The milled samples were then dried using a crystallising dish on a stirrer hotplate and the resulting milled powder hand ground in a pestle and mortar. A 10 or 13 mm diameter pellet of approximately half of the mixed reactants was pressed by applying uniaxial pressure of 1-2 tons, with the remaining precursor mixture surrounding the pellet in the alumina crucible to serve as a sacrificial powder, in order to minimise the effects of Li_2O volatilisation. The final synthetic conditions used for this materials was two firings in air using a box furnace at 1000 °C for 24 h (48 h in total) at a heating and cooling rate of 5 °C min^{-1}. The pellet was ground and re-pressed and the sacrificial powder was ground separately between firings. This stoichiometric ratio of Li:Ni:W resulted in a pale green powder and PXRD data were obtained for phase identification.

3.2.2 Synthesis of $Li_{4.1}Ni_{0.9}WO_6$

A non-stoichiometric analogue was synthesised as above but using a 12% molar excess of lithium carbonate (4.4:1:1 molar ratio of Li:Ni:W). Initially the target was also the Li_4NiWO_6 phase, with a 12% molar lithium excess added to compensate for any

lithium that may be volatilised as Li_2O at these high synthetic temperatures. This synthesis afforded a dark brown/black powder which first appeared phase pure by lab PXRD. Upon further analysis using synchrotron PXRD, NPD and TEM-EDX, a small amount of impurity of the form $Li_xNi_{1-x}O$ was detected.

3.2.3 Synthesis of Solid Solution Series $Li_{4.1+x}Ni_{0.9-x}WO_6$

The presence of a cubic $Li_xNi_{1-x}O$ impurity phase in the material described in Section 3.3.2 provided evidence of a solid solution of the form $Li_{4.1+x}Ni_{0.9-x}WO_6$, whereby the rock-salt structure is maintained (*i.e.* the total number of cations is still equal to the number of anions) and the charge neutrality is retained by the increase in the average oxidation state of nickel with increasing Li content. These materials were synthesised as above, with the inclusion of a 10% molar excess of lithium, in the appropriate ratio of starting materials for the series $Li_{4.1+x}Ni_{0.9-x}WO_6$ where x = 0.0, 0.05, 0.10, 0.15, 0.20 and 0.25.

3.2.4 Synthesis of $Li_{4.08}Mg_{0.90}W_{1.02}O_6$

Samples were synthesised *via* ceramic synthesis using Li_2CO_3 (99.997%, Sigma Aldrich), MgO (99.995%, Sigma Aldrich) and WO_3 (99.995%, Sigma Aldrich). The powders were pre-dried overnight at 250° C prior to synthesis and combined in a pestle and mortar with target composition of $Li_{4.08}Mg_{0.90}W_{1.02}O_6$. The required molar ratio of Li:Mg:W was eventually determined to be 4.51:0.95:1 (see Section 3.9). The reactants were hand ground in an agate pestle and mortar pressed into a pellet by applying uniaxial pressure of 1-2 tons to the powder within a 13 mm diameter pellet die. The pellets were fired three times at 900 °C for 24 h (72 h in total) at a heating and cooling rate of 5 °C min^{-1}, with hand grinding of the pellet in between firings.

3.2.5 Powder X-Ray Diffraction

For the initial collection of powder X-ray diffraction in the laboratory, a Phillips X'pert PANalytical diffractometer (Co $K\alpha_1$ radiation, λ = 1.788960 Å) in Bragg-Brentano geometry. This instrument was also used in determination of the lattice parameter trend on the $Li_{4.1+x}Ni_{0.9-x}WO_6$ series ($0 \leq x \leq 0.25$) by including highly crystalline silicon (99.999%, Alfa Aesar) in the sample (1:4 by mass) as an internal standard. High-resolution synchrotron powder diffraction data (SXRD) were collected at the I11 beamline at Diamond Light Source at the Harwell Science and Innovation Campus in Oxfordshire, UK. Five multi-analyser crystal (MAC) detectors (λ = 0.82588(1) Å) were employed for the Rietveld refinement data, whereby the samples were loaded into borosilicate capillaries of 0.1 mm internal diameter, mounted on a capillary spinner during data collection in Debye-Scherrer geometry for a total of 90 minutes.

3.2.6 Neutron Powder Diffraction

For the neutron powder diffraction (NPD) experiments, synthesis of Li_4NiWO_6 and $Li_{4.1}Ni_{0.9}WO_6$ was repeated (as detailed in Sections 3.2.1 and 3.2.2) scaled up to 4 g of product, using $^7Li_2CO_3$ (99% ^{7}Li atom, Sigma Aldrich, dried at 250 °C overnight) as the lithium source. The enrichment of the sample with the ^{7}Li isotope (negative neutron scattering length) was used to enable greater contrast between Ni, W and O (positive neutron scattering length), with minimal positive scattering arising from the ^{6}Li isotope (7.5% natural abundance).[17] High-resolution time-of-flight (TOF) neutron powder diffraction data were collected on the HRPD instrument at the ISIS facility (Oxfordshire, UK) whereby the samples were loaded into vanadium canisters for data collection at room temperature. Three databanks were utilised for data collection employing the backscattering detector, and detectors positioned at 90° and 30° relative to the incident neutron beam (bank 1, 2 and 3 respectively) in order to obtain high

resolution data at short *d*-spacings from the backscatter detector and lower resolution data at higher *d*-spacings. The data were corrected for sample absorption, accounting for the presence of 1% ^{6}Li.

3.2.7 Compositional Analysis

Inductively coupled plasma optical emission spectroscopy (ICP-OES) was employed for compositional analyses. Separate solutions of the powders were obtained using microwave dissolution by adding approximately 10 mg of the material to a mixture of 10 mL H_2SO_4 (> 95%, Fisher Scientific), 2 mL HNO_3 (70%, Fisher Scientific) and 2 mL H_2O_2 solution (30%, BDH). The mixture was made up to 100 mL with deionized water and ~20 mL of H_2O_2 solution to prevent the precipitation of tungsten oxides.[18]

Transmission electron microscopy-energy dispersive X-ray spectroscopy (TEM-EDX) was performed using a JEOL 2000FX instrument equipped with an EDAX spectrometer. A small amount of powder from each sample was dispersed in ethanol and deposited on a copper TEM grid. Up to forty particles were chosen at random to determine the Ni and W composition within the powders, with correction factors applied from suitable reference compounds.

3.3 Identifying Related Phases

During the initial exploratory synthesis of $Li_{4+x}Ni_{1-x}WO_6$ compounds, the molar excess of lithium and inclusion or omission of a sacrificial powder during synthesis were found to be crucial to control for separation of the two phases. The two separate phases are indicated in green (Li_4NiWO_6, as reported in Section 3.4) and in black ($Li_{4.1}Ni_{0.9}WO_6$, as reported in Section 3.5) as shown in Figure 3.3.1.

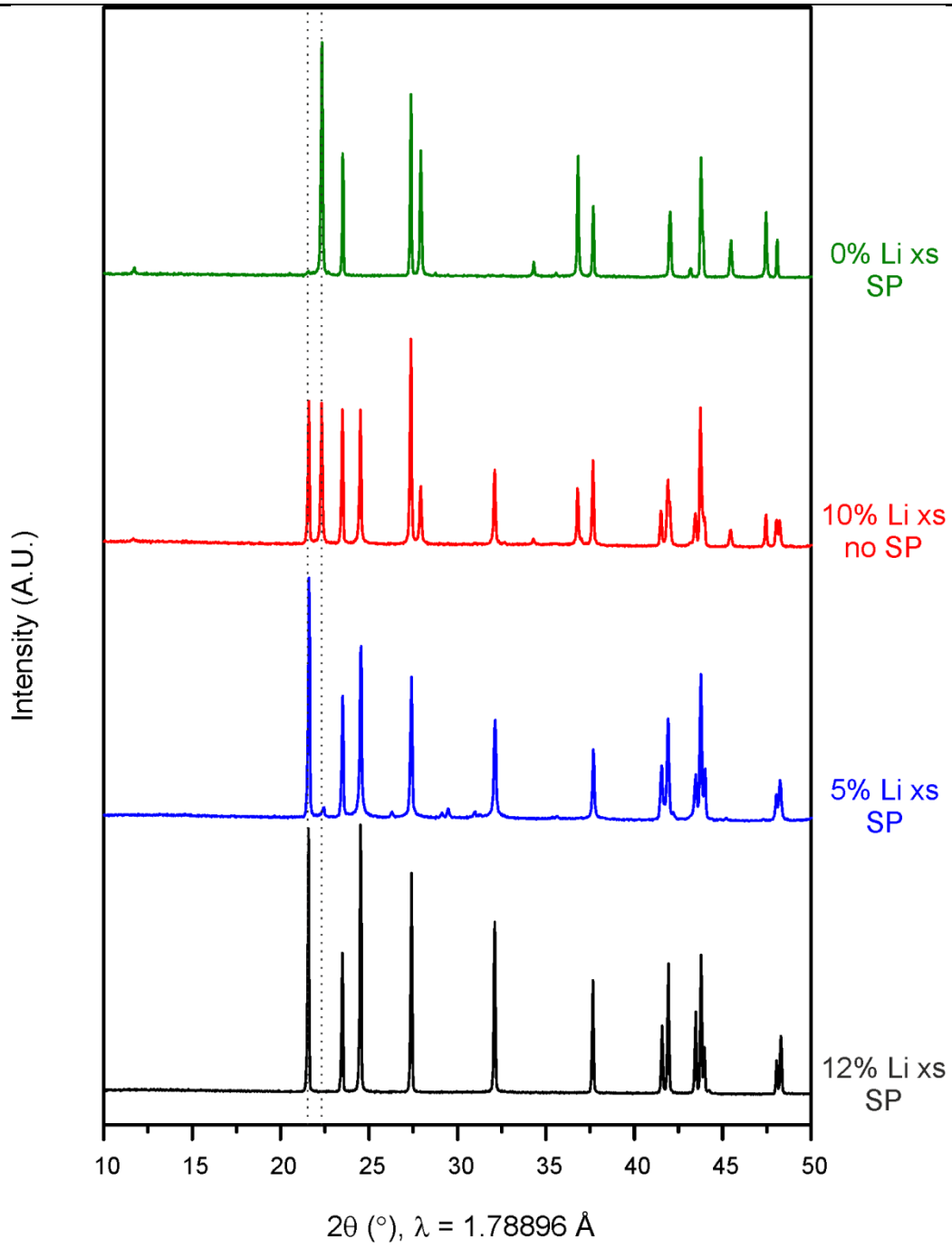

Figure 3.3.1: PXRD of targeting Li_4NiWO_6 from adjustment of molar Li excess and inclusion or omission of a sacrificial powder (SP/no SP) as indicated on the *right*. The dashed lines represent the positions of the first most intense Bragg reflections corresponding to each of the two different phases

When targeting the previously unreported Li_4NiWO_6 (4:1:1 Li:Ni:W plus excess Li) phase under the same firing conditions (as reported in Section 3.2.1 and Section 3.2.2),

inclusion of 10% molar excess ('10% Li xs') of lithium but without use of a sacrificial powder ('no SP') resulted in a similar proportion of both phases, as shown in red. Reduction of the lithium excess to 5% but including a sacrificial powder of the same composition (as shown in blue) greatly reduced the proportion of the green Li_4NiWO_6 phase. The inclusion of 12% molar excess plus a sacrificial powder gave a brown-black powder with no evidence of any peaks belonging to the green Li_4NiWO_6 phase, which was determined to have the composition $Li_{4.1}Ni_{0.9}WO_6$ plus a small amount of cubic $Li_xNi_{1-x}O$ impurity (as discussed in Section 3.5). These results indicated that the two separate phases are closely related in energy, with the structure obtained dependent on the lithium and nickel content.

3.4 Structural Characterisation of Li_4NiWO_6

3.4.1 Compositional Analysis

Analysis of this material by ICP-OES gave a composition of $Li_{4.01(5)}Ni_{1.00(2)}W_{0.99(1)}$ which is consistent with the target 4:1:1 stoichiometry. The ratio of Ni:W was determined from TEM-EDX was 0.9(3):1, however due to large standard deviation, seven of the 39 measurements were discarded as outliers and the central population was determined as Ni:W 0.98(4):1 (Figure 3.4.1). The elemental analysis therefore determined that the global composition of the sample could be restrained to the target composition, Li_4NiWO_6.

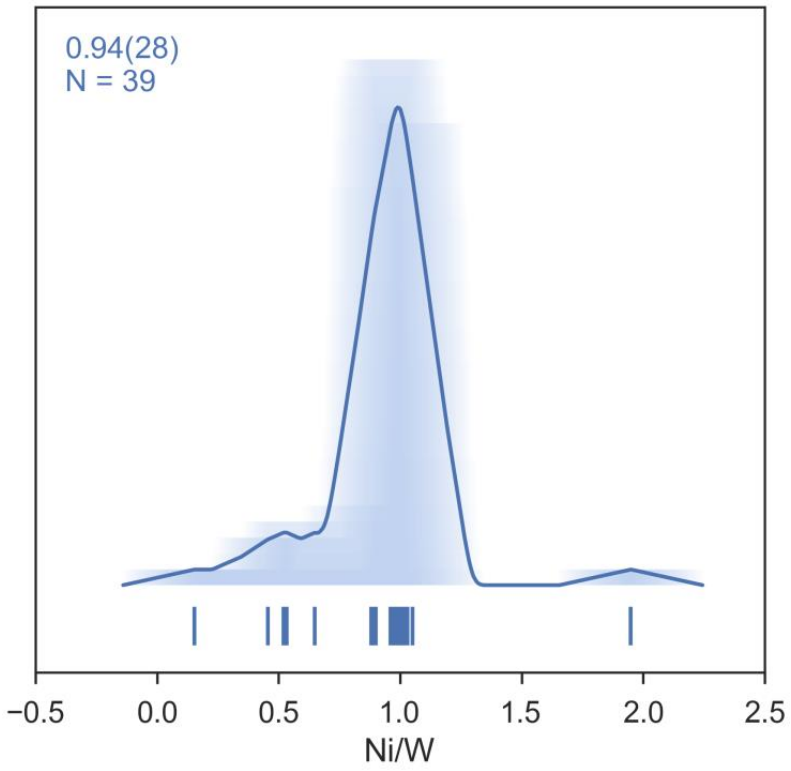

Figure 3.4.1: Average shifted histogram of TEM-EDX distribution of Ni/W in Li_4NiWO_6, showing the majority of particles possessing a Ni/W ratio ~1. Some of the lower Ni/W values were discarded as outliers

3.4.2 Phase and Unit Cell Determination of Li_4NiWO_6

Phase identification of laboratory PXRD data of the Li_4NiWO_6 material did not yield any matches to known binary, ternary or quaternary oxides of lithium, nickel or tungsten by using the 'Search & Match' feature in the X'Pert Highscore software. A Le Bail fit was performed in Topas using the unit cell of Li_4NiTeO_6 as a model (space group *C*2/*m*, a = 5.1584(1) Å, b = 8.8806(1) Å, c = 5.1366(1) Å, β = 110.24°),[12] which proved that this material adopts a different crystal structure to Li_4NiTeO_6. Because no known phases could be identified in the sample it was determined that a new structure was obtained, requiring structural characterisation by first determining the unit cell and space group of the material. Using good quality laboratory PXRD data from the X'Pert PANalytical diffractometer, the background was graphically fitted using the

GSAS software, which was then input into the Topas Rietveld refinement software, in addition to setting up instrument parameters. The first ~40 diffraction peaks (up to $2\theta \approx 55°$) were fitted and their 2θ positions and intensities systematically refined until a satisfactory model of the data was obtained. In some instances the width of some peaks modelled to the diffraction data were too narrow and the intensity too high, which indicated there were two or more overlapping reflections which were then included in the peak fitting. The occurrence of these split peaks indicated that the cell is most likely to be monoclinic and not orthorhombic. All peaks were modelled using a single peak profile which was allowed to refine, fitting most of the peaks well. The refined peak positions and intensities were then auto-indexed using the Topas software, generating a ranked list of possible lattice parameters and space groups for the phase based on the accurate peak positions obtained from the peak fitting. Triclinic Bravais lattices were excluded from indexing.

Initially the solutions from indexing of the pattern suggested approximate lattice parameters of a = 5.849 Å, b = 17.585 Å, c = 5.112 Å, $\beta = 110.3°$ with the candidate space groups (from lowest to highest symmetry) of $P2$, $P2_1$, Pc and $P2_1/c$. These lattice parameters and space groups were then fitted to the pattern one by one using Le Bail extraction, resulting in an equally good fit for all four space groups. Since $P2_1/c$ is the highest symmetry space group of these options, initially this was chosen as the space group. However it can be seen from the Le Bail fit that this afforded a high number of reflections of zero intensity, suggesting a higher symmetry space group would be more appropriate (Figure 3.4.2).

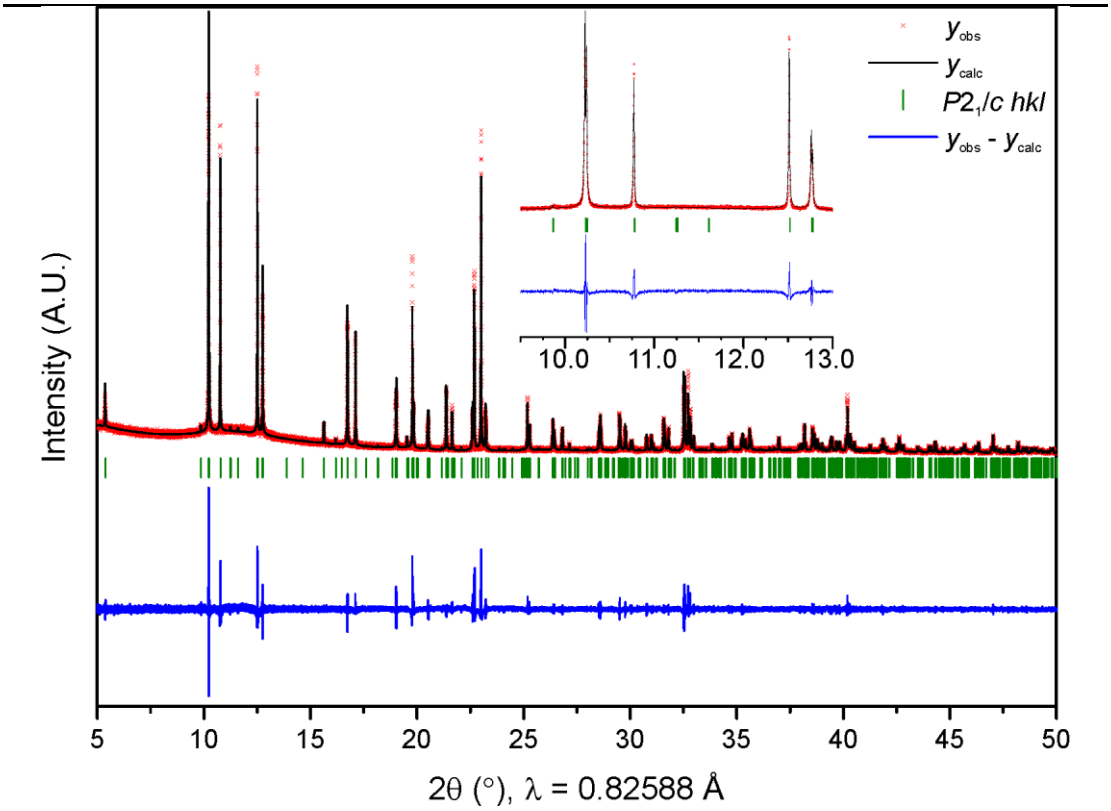

Figure 3.4.2: Le Bail fit of Li_4NiWO_6 synchrotron MAC PXRD data to $P2_1/c$ space group setting;

R_{wp} = 9.03%, R_{exp} = 4.74%, χ^2 = 3.63

By observation of the reflection condition $h + k = 2n$, a *C*-centred lattice was confirmed for this material, with systematic absences consistent with either the *Cc* or *C*2/*c* space group. The material was assigned the higher symmetry *C*2/*c* space group for the refinements. Modelling the experimental data using Le Bail fitting to both the $P2_1/c$ and *C*2/*c* space group resulted in similar values for the fitting parameters, with both giving a large difference between the observed and calculated data (Figure 3.4.2 and Figure 3.4.3, respectively). These misfits are attributed to a single peak shape model being insufficient to model the data in either space group, as was observed during peak fitting and indexing of the powder pattern.

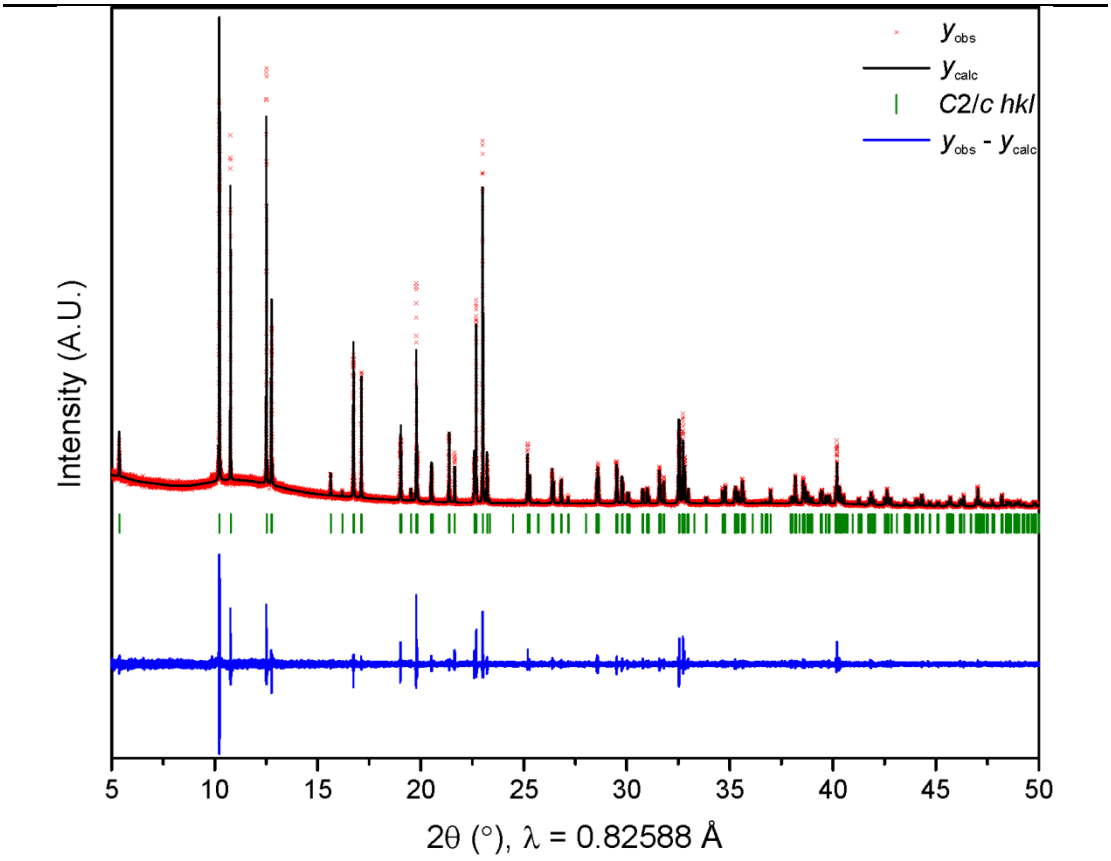

Figure 3.4.3: Le Bail fit of Li_4NiWO_6 synchrotron MAC PXRD data to *C*2/*c* space group setting; R_{wp} = 9.95%, R_{exp} = 4.74%, χ^2 = 4.41

Regions of peak broadening between *C*2/*c* peaks were observed in the SXRD data, contributing significant intensity which could not be fitted appropriately using the single phase model. This broadening between peaks, in addition to the peak shape model being insufficient, suggested an additional more disordered phase would need to be included to establish a chemically sensible structural model for this new material.

With help from Dr John Claridge and Dr Matthew Dyer, it was noted that the lattice parameters obtained for the *C*2/*c* model are a monoclinic distortion of the orthorhombic unit cell of the rock-salt $Li_3Ni_2TaO_6$ (a = 5.9073 Å, b = 8.4259 Å, c = 17.7329 Å, V = 882.64 Å^3).[8] The *C*2/*c* (Z = 4) space group is an isomorphic subgroup of *Fddd* (Z = 8) and therefore possess the same asymmetric unit cell, with

the *C*2/*c* cell being less symmetric and hence more ordered. The *C*2/*c* unit cell was transformed to the related orthorhombic *Fddd* cell using the axes transformation (**-a**, **a** + **2c**, **b**) (Figure 3.4.4). From this transformation, the unique axis *b*' in the monoclinic setting becomes the *c* axis in the orthorhombic setting, with the new orthorhombic unit cell volume being twice that of the monoclinic cell.

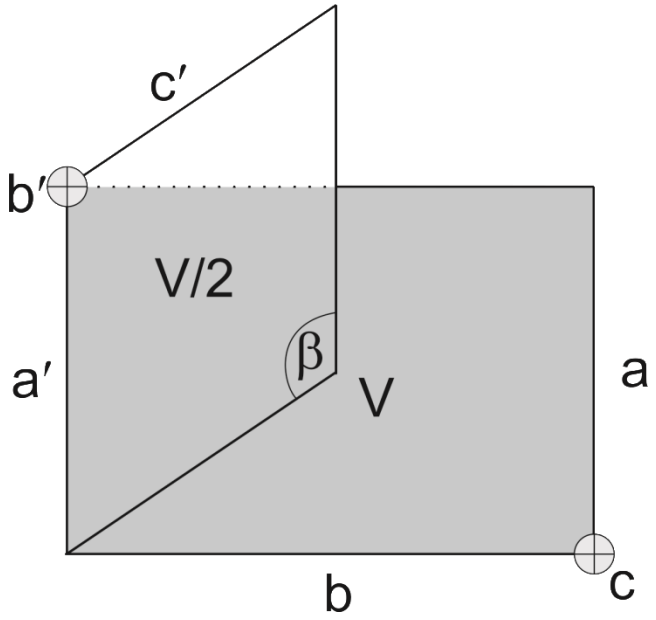

Figure 3.4.4: Relationship between the *C*2/*c* monoclinic cell (of dimensions *a', b', c',* β) and *Fddd* orthorhombic unit cell (of dimensions *a*, *b*, *c*, and volume *V* shown in *grey*)

A further Le Bail fit was then performed using both the Li_4NiWO_6 *C*2/*c* phase and the *Fddd* phase, with both sets of lattice parameters allowed to refine (Figure 3.4.5). Due to the related cell symmetry between these two phases, the inclusion of the *Fddd* cell was determined to sufficiently model the peak shapes and the regions of broadening between *C*2/*c* reflections (Figure 3.4.6). It has not been distinguished whether a separate disordered orthorhombic phase is present (as it has not yet been experimentally isolated, and all of the Bragg reflections in the neutron diffraction data could be accounted for using the *C*2/*c* cell only). The broadening between peaks could

also be due to either regions of order and disorder within one *C*2/*c* phase, or one phase containing a significant volume fraction of domain boundaries. Separate Le Bail refinements were performed on the SXRD (R_{wp} = 7.00%, R_{exp} = 4.74%, χ^2 = 2.18) and all three NPD databanks (R_{wp} = 2.80%, R_{exp} = 1.88%, χ^2 = 2.22).

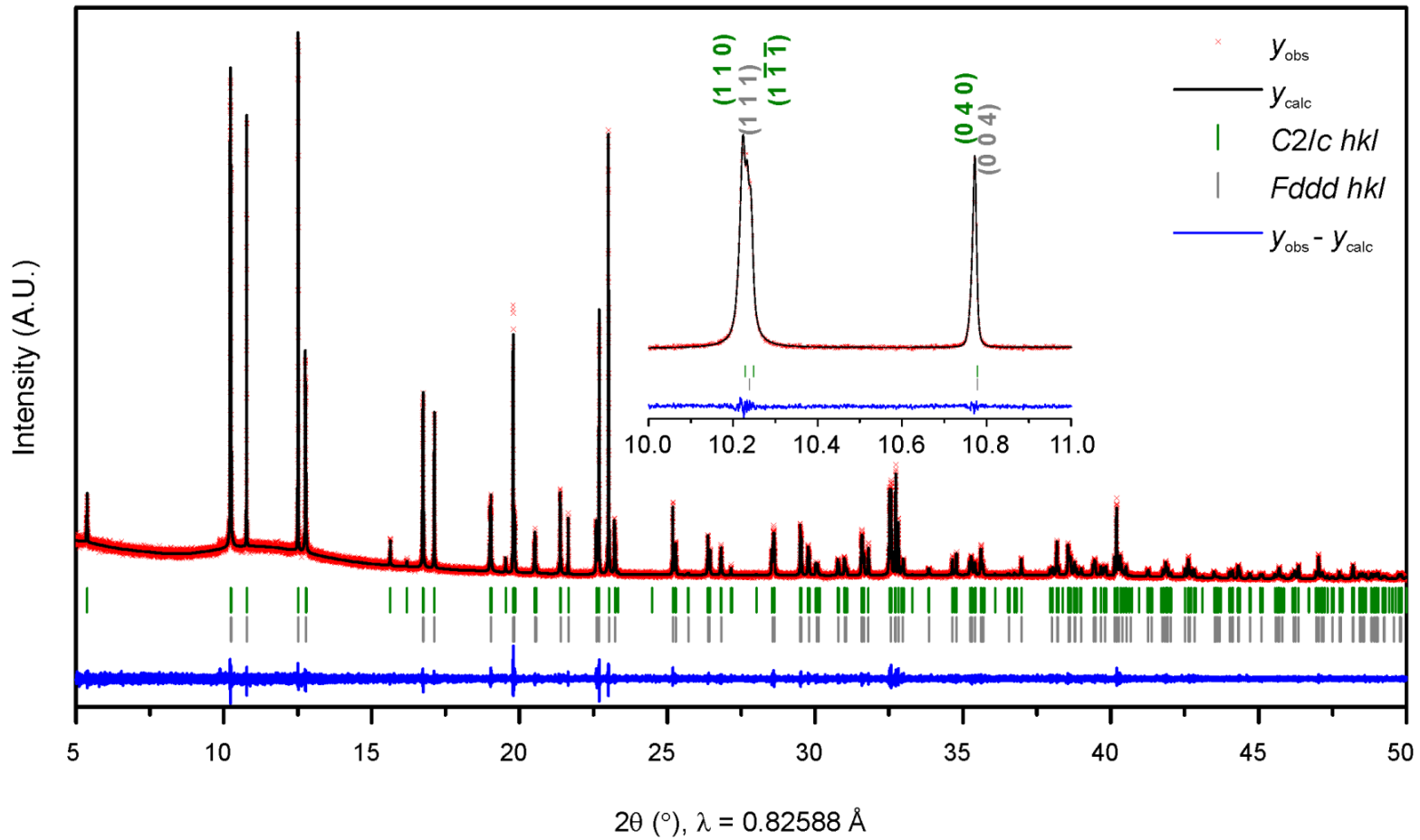

Figure 3.4.5: Two phase Le Bail fit of Li_4NiWO_6 synchrotron MAC PXRD data. R_{wp} = 7.00%, R_{exp} = 4.74%, χ^2 = 2.18. *Inset*: labelled indices of two first intense peaks showing *C*2/*c* phase (*green*) and *Fddd* phase (*grey*)

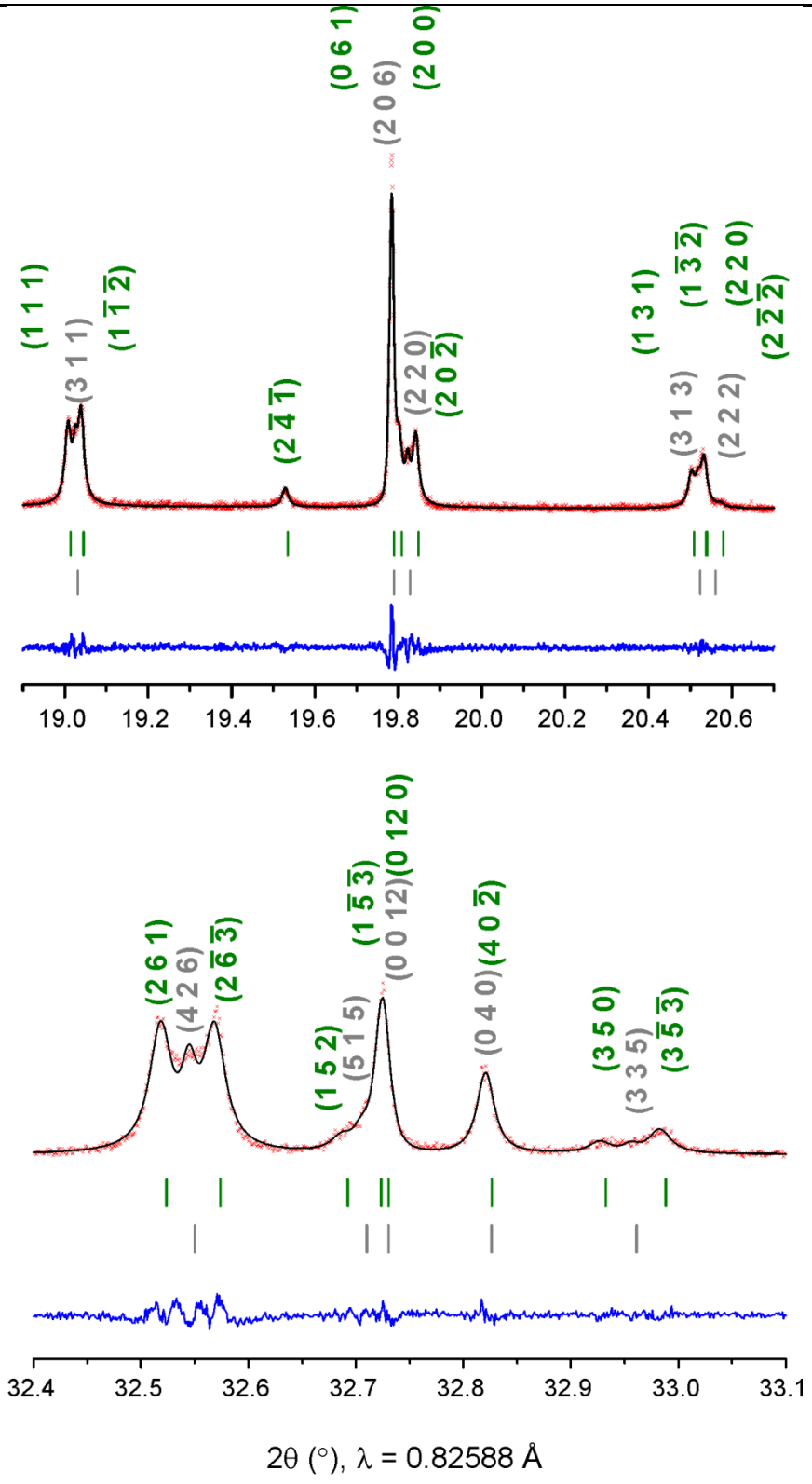

Figure 3.4.6: Examples of broadening and overlap between *C*2/*c* peaks (Miller indices labelled *green*, corresponding to *green tick marks*) and *Fddd* peaks (labelled *grey*) from the Le Bail fit

3.4.3 Rietveld Refinement of Li_4NiWO_6

Using the ISODISTORT programme,[19] the atomic structure of $Li_3Ni_2TaO_6$ was reduced in symmetry to *C*2/*c* using the axes matrix transformation (**-a**, **c**, ½ **a** + ½ **b**) with an origin shift of (¼, ¼, ½) to generate a *C*2/*c* starting structural model. Initially a Rietveld refinement was performed on the SXRD data using only the *C*2/*c* structural model to partly refine the atomic positions.[20, 21] Using this, the structural model for the Li_4NiWO_6 *Fddd* model was obtained by applying the inverse transformation mentioned above, and both phases were included for the Rietveld refinement. Both phases are related by the same ordering pattern of the tungsten sites.

The unit cell of the *C*2/*c* majority phase was determined to be a = 5.84579(10) Å, b = 17.58769(35) Å, c = 5.109138(9) Å, β = 124.768(1)°, V = 431.506(2) Å^3. Constraints were applied to the *C*2/*c* phase whereby the overall occupancy of each site was restrained to equal one, given the rock-salt structure with no vacancies. The secondary *Fddd* phase was restrained during the Rietveld refinement (due to the assumptions made about the composition and overlapping reflections with the *C*2/*c* phase) by fixing the atomic positions (obtained from the refinement of the transformed *C*2/*c* model), with the lattice parameters fixed to the values determined from the Le Bail fit to the SXRD (a = 5.8453(9) Å, b = 8.397(11) Å, c = 17.5894(10) Å, V = 863.3(15) Å^3). The fully occupied tungsten site was assigned the special position (Wyckoff site 8*a*) and the remaining three cation sites were assumed to each comprise $^4/_5$Li and $^1/_5$Ni, with a total occupancy of each site equal to one. Only the phase fraction was allowed to refine and comprised 11.8(6) wt% of the sample. The global composition of the sample was constrained to Li_4NiWO_6 as determined from compositional analysis.

Rietveld refinements were performed on the SXRD data to determine the electron density of the metal sites and atomic positions (Figure 3.4.7). Following this, refinements were performed on the NPD data using the same structural models to aid location of lithium and oxide ions (Figure 3.4.8). Finally, a combined Rietveld refinement was employed using the two data sets to determine the crystal structure. The final refined structural parameters are given in Table 3.4.1.

Table 3.4.1: Structural parameters of Li_4NiWO_6 (*C*2/*c*; *a* = 5.84579(10) Å, *b* = 17.58769(35) Å, *c* = 5.109138(9) Å, β = 124.768(1)°, *V* = 431.506(2) Å^3) from combined Rietveld refinement. Numbers in parentheses represent 1σ

atom	site	*x*	*y*	*z*	occupancy	B_{iso} (Å^2)
W1	4*e*	0	0.37057(2)	1/4	0.9526(17)	0.172(5)
Li1	4*e*	0	0.37057(2)	1/4	0.0475(17)	0.172(5)
Ni2	4*e*	0	0.54179(6)	1/4	0.5690(17)	0.172(5)
Li2	4*e*	0	0.54179(6)	1/4	0.4230(19)	0.172(5)
W2	4*e*	0	0.54179(6)	1/4	0.0080(10)	0.172(5)
Li3	4*e*	1/2	0.53982(13)	1/4	0.7238(11)	0.172(5)
Ni3	4*e*	1/2	0.53982(13)	1/4	0.2763(11)	0.172(5)
Li4	4*e*	0	0.20578(23)	1/4	0.9109(12)	0.172(5)
Ni4	4*e*	0	0.20578(23)	1/4	0.0891(12)	0.172(5)
Li5	4*e*	-1/2	0.37581(22)	1/4	0.9367(20)	0.172(5)
W5	4*e*	-1/2	0.37581(22)	1/4	0.0385(84)	0.172(5)
Ni5	4*e*	-1/2	0.37581(22)	1/4	0.0249(18)	0.172(5)
Li6	4*e*	0	0.28696(22)	3/4	0.9582(12)	0.172(5)
Ni6	4*e*	0	0.28696(22)	3/4	0.0418(12)	0.172(5)
O1	8*f*	-0.26962(29)	0.12391(6)	0.20946(18)	1	0.674(8)
O2	8*f*	-0.23445(26)	0.29770(6)	0.25257(30)	1	0.674(8)
O3	8*f*	0.76454(22)	0.45312(6)	0.25033(24)	1	0.674(8)

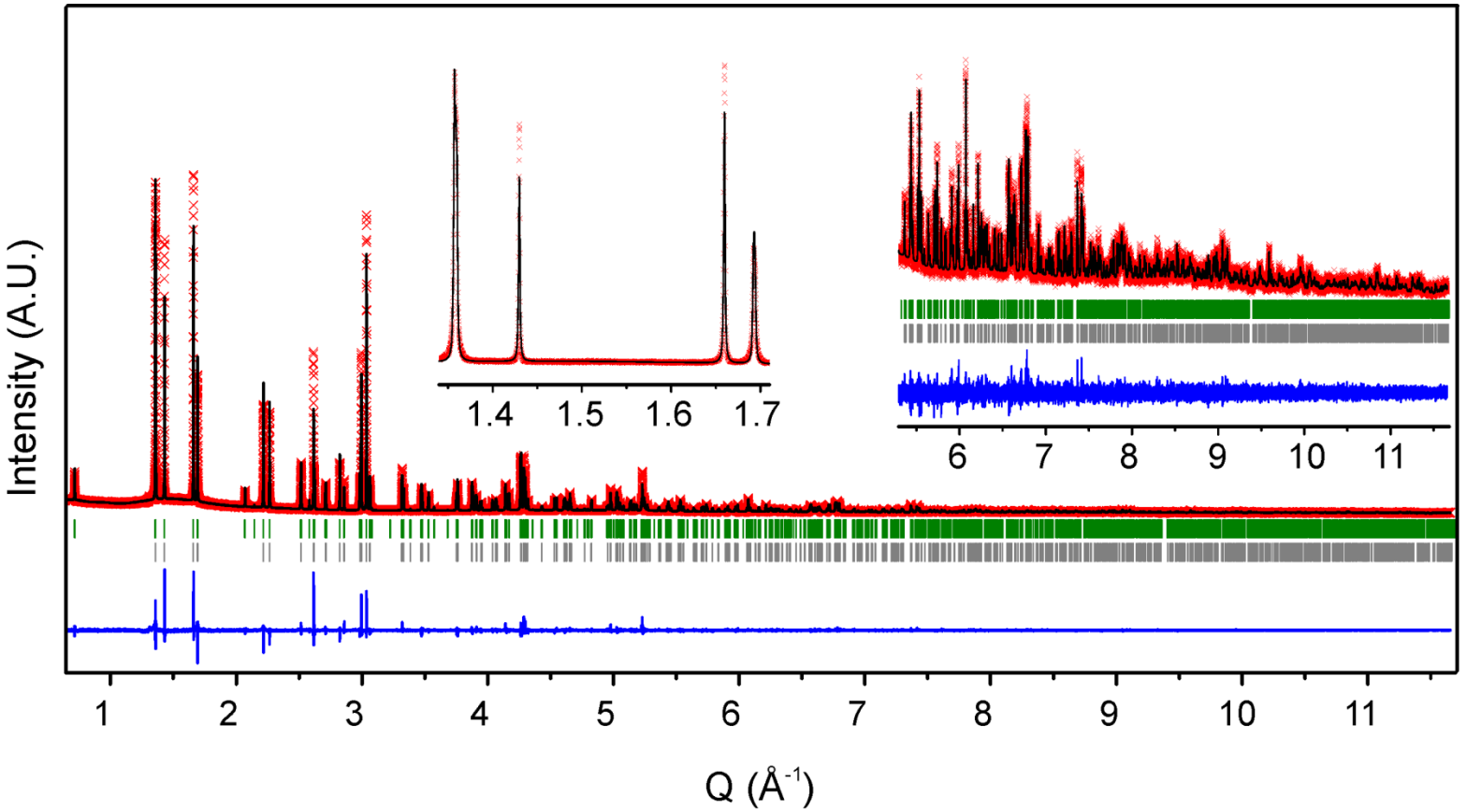

Figure 3.4.7: SXRD pattern for the combined Rietveld refinement of Li_4NiWO_6 (λ = 0.82588(1) Å); R_{wp} = 8.57%, R_{exp} = 4.74%, χ^2 = 3.27; *green* ticks indicate *C*2/*c* phase, *grey* ticks indicate *Fddd* phase

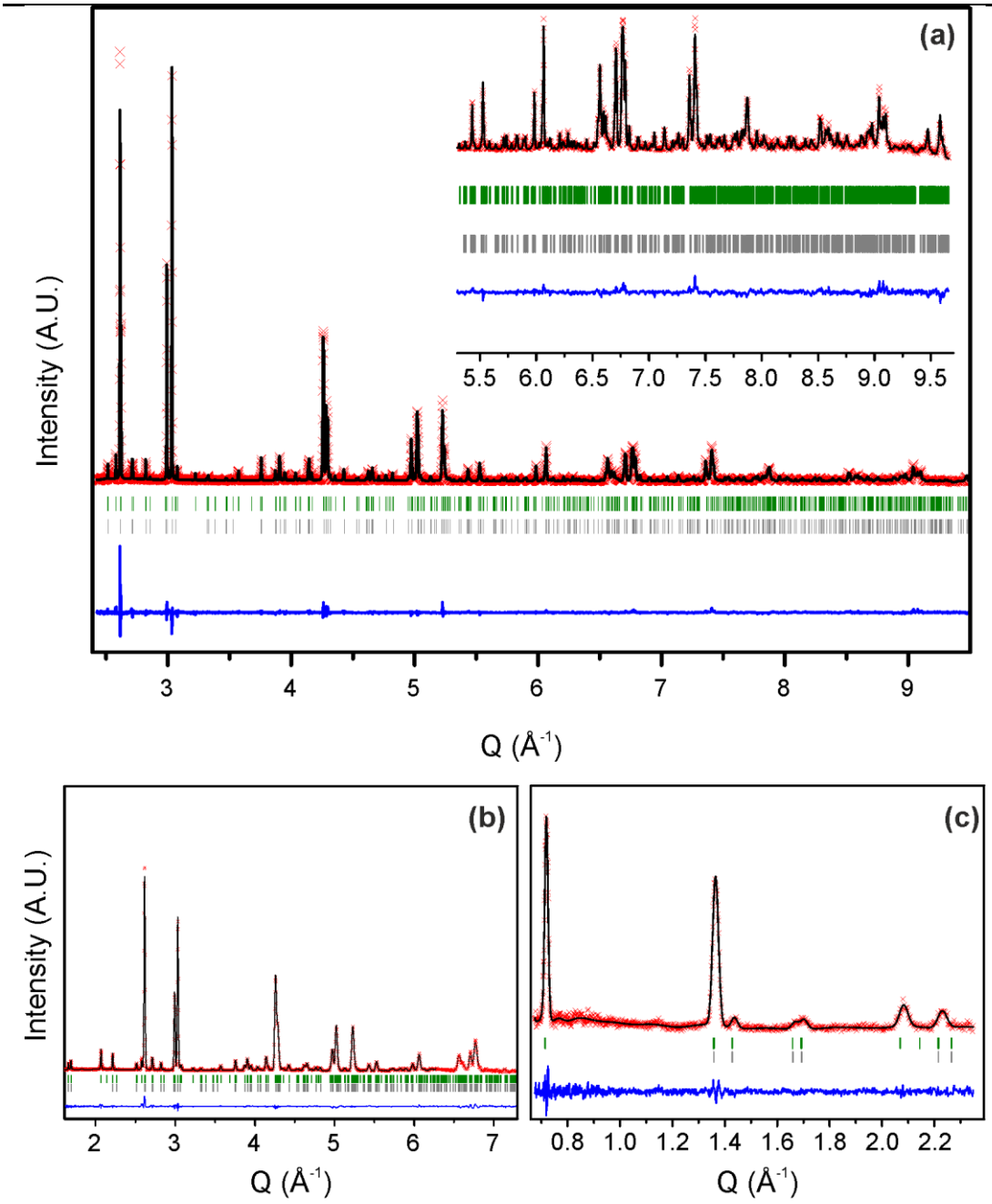

Figure 3.4.8: NPD patterns from the HRPD instrument for the combined Rietveld refinement of Li_4NiWO_6; (*a*) backscattered bank 1; R_{wp} = 4.94%, R_{exp} = 2.71%, χ^2 = 3.32; (*b*) bank 2 90° detector; R_{wp} = 3.11%, R_{exp} = 1.11%, χ^2 = 7.89; (*c*) bank 3 30° detector; R_{wp} = 7.44%, R_{exp} = 6.54%, χ^2 = 1.29; green ticks indicate *C*2/*c* phase, *grey* ticks indicate *Fddd* phase

3.4.4 Crystal Structure of Li_4NiWO_6

The refined crystal structure of the *C*2/*c* polymorph of Li_4NiWO_6 was determined to comprise edge-sharing octahedra with partial cation order (Figure 3.4.9).

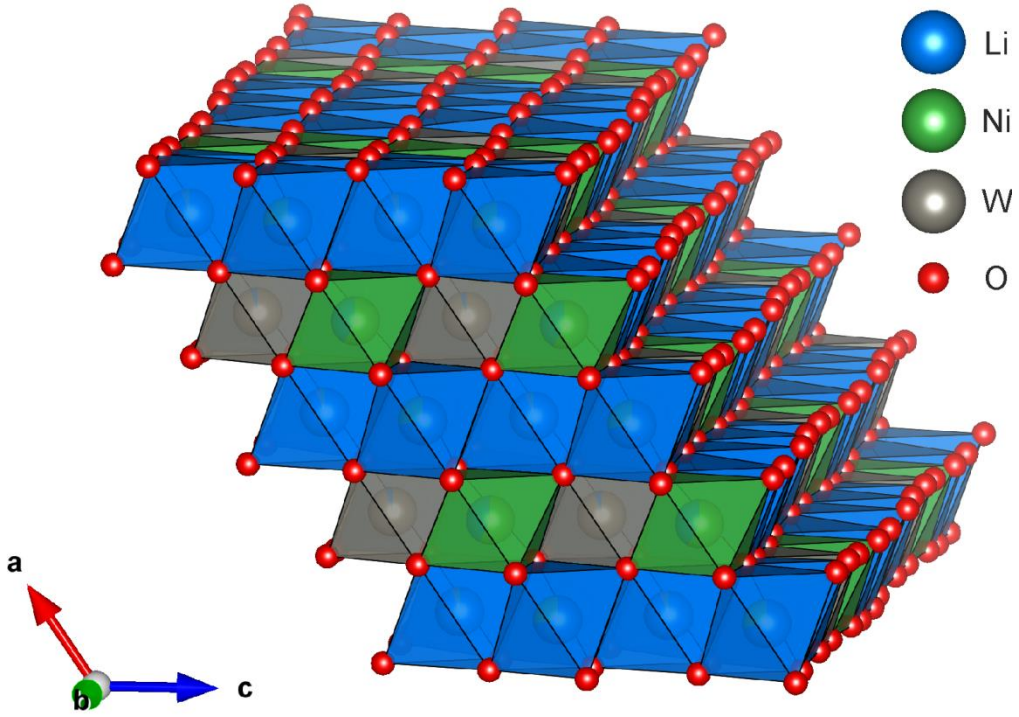

Figure 3.4.9: Representation of the structure of Li_4NiWO_6 (*C*2/*c* polymorph) viewed along the [010] direction

The combination of SXRD and NPD data for the Rietveld refinement allowed the extent of cation order at each of the six metal sites to be identified. No fully occupied lithium layers were determined to be present within this structure. The tungsten ions were not fully ordered, with 4.8% lithium occupying the tungsten site and the remaining 4.8% tungsten distributed between two of the remaining five cation sites. The nickel ions, calculated to be Ni^{2+} based on a fully occupied rock-salt structure, are ordered amongst the other five metal sites with 57% of the Ni^{2+} located on one site. No metal sites were found to be fully occupied with Li^+. The *C*2/*c* phase observed for Li_4NiWO_6 can be thought of as a monoclinic distortion of the archetype $Li_3Ni_2TaO_6$

(S.G. *Fddd*) based on the same ordering pattern of the almost fully occupied W sites *cf.* Ta (Figure 3.4.10).

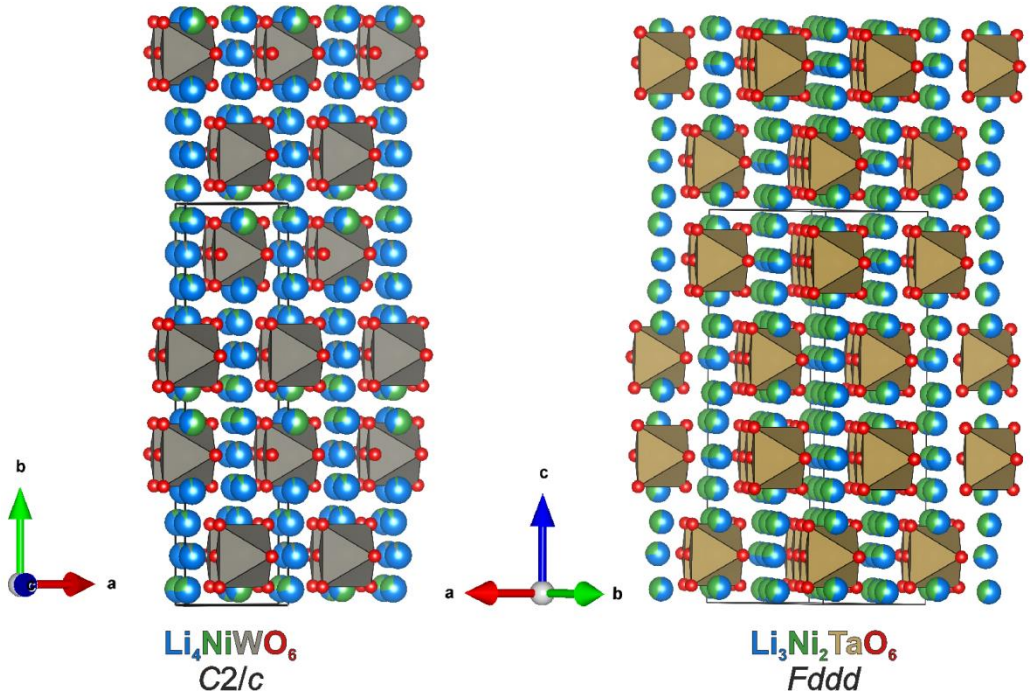

Figure 3.4.10: Representation of the WO_6 ordering in Li_4NiWO_6 (*left*) and TaO_6 ordering in $Li_3Ni_2TaO_6$ (*right*); both viewed perpendicular to the long axis of the unit cell

Li_4NiWO_6 possesses a single mixed cation octahedral layer (containing Li, Ni and W), stacked as to maximize the distance between W^{6+} within each layer and between layers (Figure 3.4.11), which is analogous to $Li_3Ni_2TaO_6$. Both $Li_3Ni_2TaO_6$ and Li_4NiWO_6 structures exhibit a six-layer repeat sequence of close-packed oxygens in the (026) lattice planes of the $Li_3Ni_2TaO_6$ archetype, which correspond to the (061) lattice planes of the *C*2/*c* cell (Figure 3.4.12); based on the matrix transformation given in Section 3.4.2.

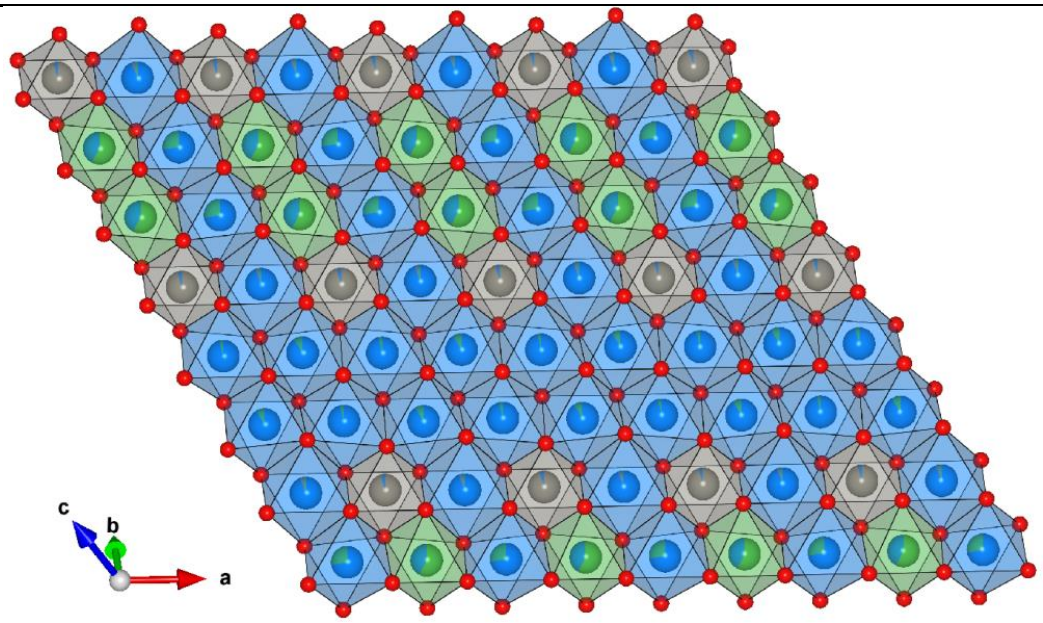

Figure 3.4.11: Representation of the octahedral layer in Li_4NiWO_6 (*C*2/*c*), viewed along the [111] axis of the cubic rock-salt sub-cell

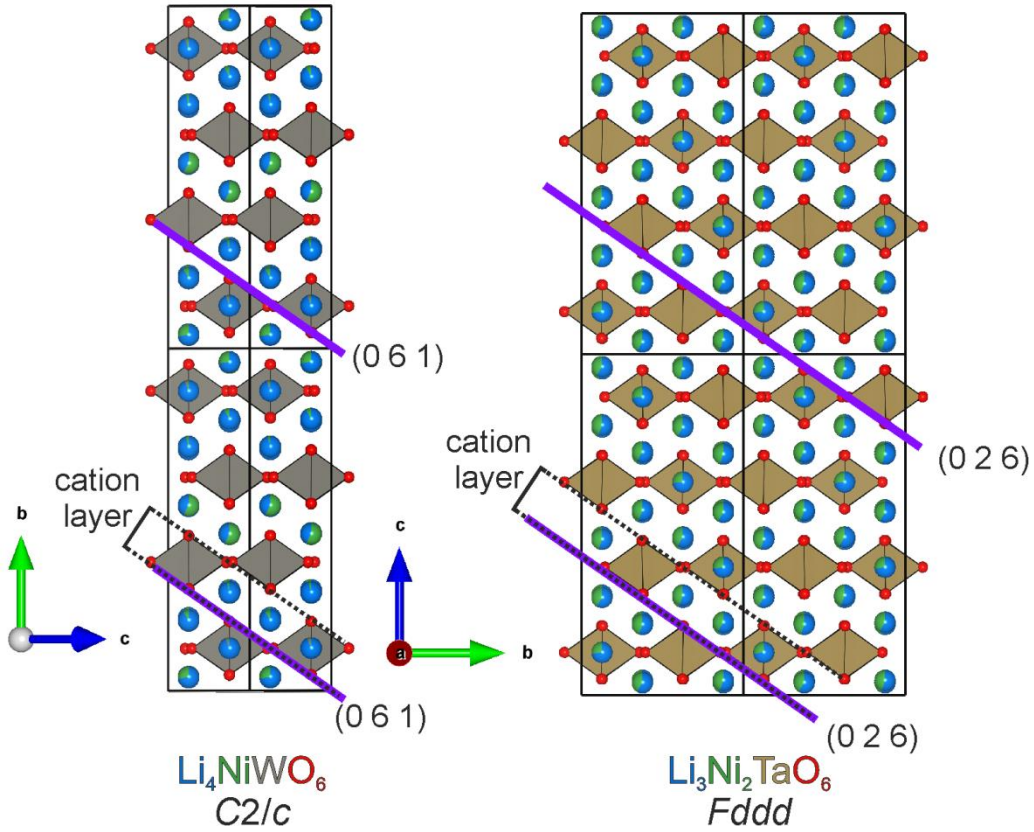

Figure 3.4.12: Representation of the repeating mixed cation layers in Li_4NiWO_6 (*left*) and $Li_3Ni_2TaO_6$ (*right*) with the (061) planes (026) planes marked in *purple*

Li_4NiWO_6 (*C*2/*c*) has six distinct cation sites with different amounts of cation ordering, and three fully occupied anion sites (Table 3.4.1). The related *Fddd* phase, which was included to model the peak broadening in the Rietveld refinement, has four distinct cation sites and two anion sites in the unit cell (Figure 3.4.13).

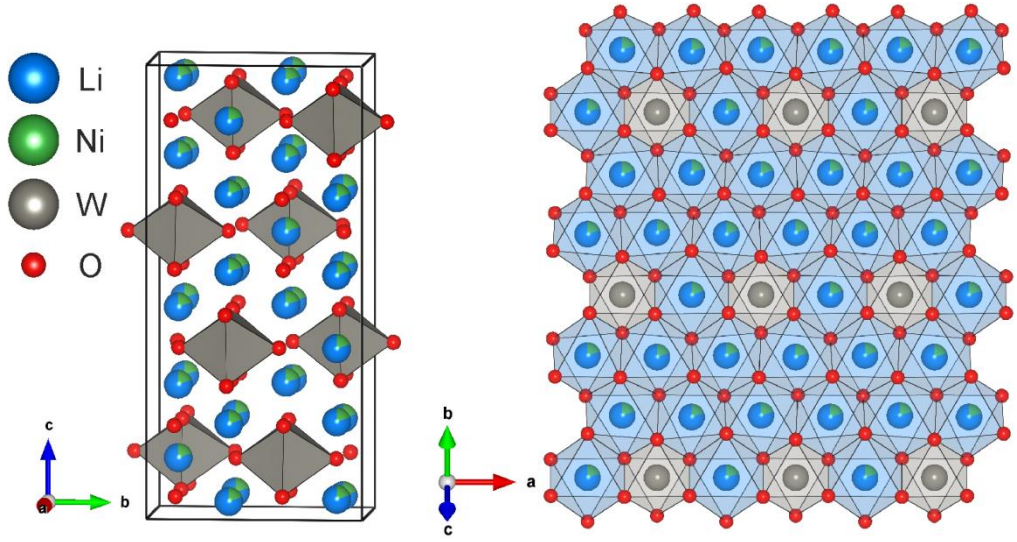

Figure 3.4.13: Representation of the *Fddd* polymorph of Li_4NiWO_6 showing the 4:1 Li:Ni mixed cation sites (*left*) and ordering of the tungsten sites in the octahedral layer (*right*)

The d^0 configuration of W^{6+} leads to asymmetric distortion towards one edge of the $[WO_6]^{6-}$ octahedra as a result of second-order Jahn-Teller effects.[22, 23] These displacements occur in opposing directions along [010] and [0$\bar{1}$0] axes, resulting in no overall dipole in the material (Figure 3.4.14). Such displacement is absent in the less ordered *Fddd* analogue, whereby the tungsten sites are located at the centroid of the octahedra at Wyckoff site 8*a* (which has point symmetry 222 and thus no dipole).

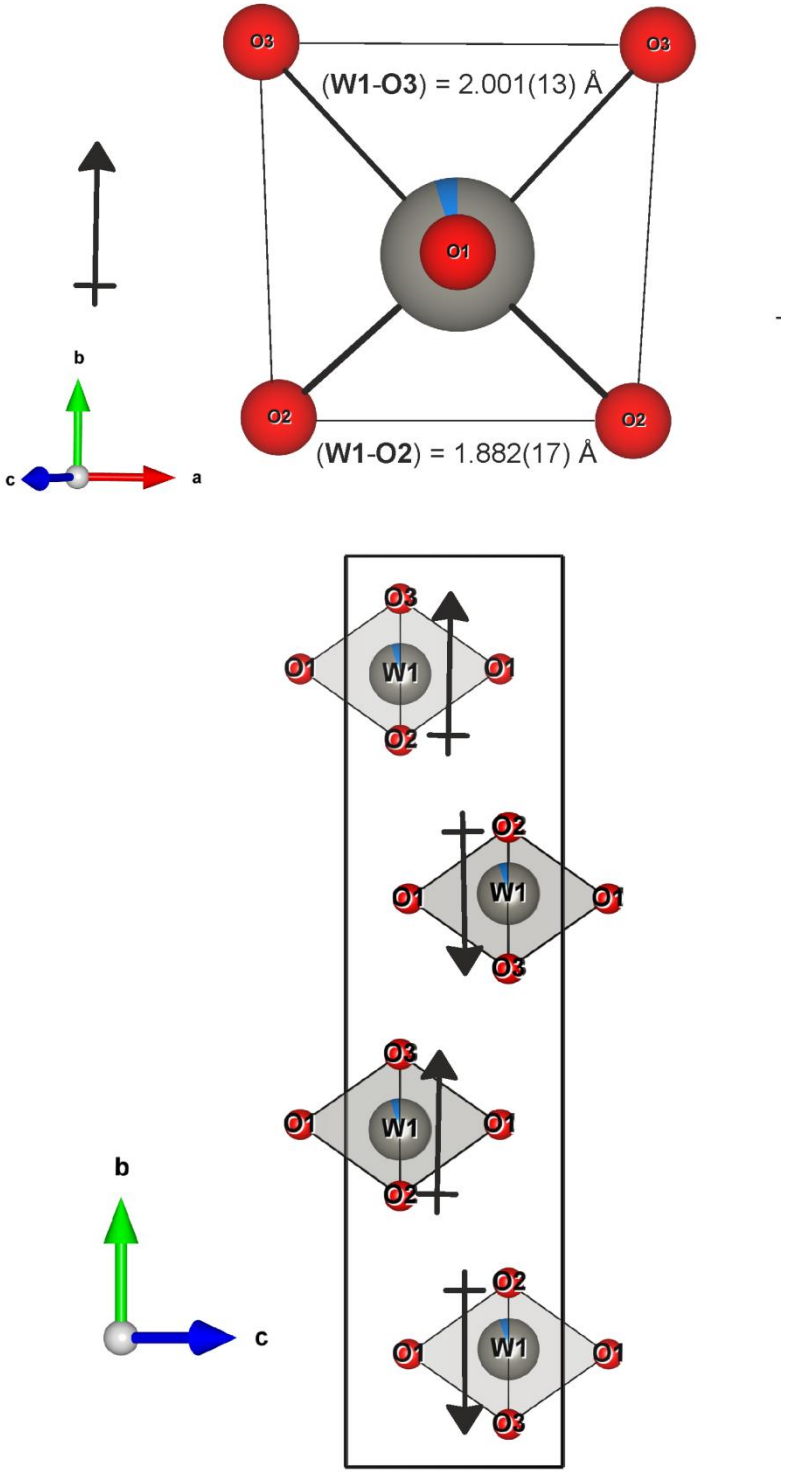

Figure 3.4.14: Octahedral coordination environment of the tungsten W1 site showing the difference in (W1-O2) and (W1-O3) bond lengths and resulting dipole direction; where (W1-O1) bond lengths = 1.931(14) Å (*top*); and opposing directions of polarity within the lattice (*bottom*)

The bond valence sums (BVS) were calculated for each atomic site to give an estimate of the oxidation states of each element within the refined structure, according to Equation 3.4.1.[24] The *M*-O (*R*) bond lengths were obtained from the Rietveld refinement, with R_0 and *b* being the empirically determined bond valence parameters from literature sources (Table 3.4.2).[25]

$$\text{bond valence} = e^{\left(\frac{(R_0 - R)}{b}\right)}$$

Equation 3.4.1: Bond valence sum

The octahedral bond length distortion, Δ, was calculated according to Equation 3.4.2, where r_i are the individual *M*-O bond lengths and *r* is the average *M*-O bond length.[26]

$$\Delta = \frac{1}{6} \cdot \sum \{(r_i - r)/r\}^2$$

Equation 3.4.2: Octahedral bond length distortion

Bond angle variance, δ, was also calculated according to the following equation, where θ_i are the O-*M*-O bond angles and *n* is the number of bonds (≠180°) which is 12 in an octahedron:

$$\delta = \sum \left[(\theta_i - 90)^2/(n - 1)\right]$$

Equation 3.4.3: Octahedral bond angle variance

As shown in Table 3.4.2, all of the MO_6 octahedra in the *C*2/*c* structure were found to be considerably distorted, which in addition to the greater cation ordering means this monoclinic configuration is adopted as the majority polymorph. The bond valence values are not in good agreement with the oxidation values expected within this

structure, which may be due to the constraints applied to both *C*2/*c* and *Fddd* models during the Rietveld refinement. Additionally, the distortion parameters obtained apply to the averaged powder structure, and not representative of local coordination environments and any disorder present within the material.

Table 3.4.2: Average *M*-O bond lengths and bond valence sums (BVS) for each atom from refined structure of Li_4NiWO_6 (*C*2/*c*) where numbers in parentheses represent 1σ and the assumed valence states are Li(1), Ni(2) and W(6). The bond length distortion (Δ) and angle variance (δ) from the ideal octahedral configuration are also reported

atom	BVS	average *M*-O bond length (Å)	Δ (×10^4)	δ
W1	5.72(14)	1.938(60)	6.417	5.420
Li1	1.69(4)			
Ni2	3.85(3)	2.082(18)	0.513	23.820
Li2	1.137(8)			
W2	2.00(1)			
Li3	1.03(2)	2.120(45)	3.050	20.140
Ni3	1.81(3)			
Li4	1.09(2)	2.097(36)	1.999	27.661
Ni4	1.92(3)			
Li5	1.03(4)	2.13(12)	20.699	17.955
W5	3.47(15)			
Ni5	1.80(8)			
Li6	0.99(1)	2.132(30)	1.310	25.128
Ni6	1.75(2)			

3.5 Structural Characterisation of $Li_{4.1}Ni_{0.9}WO_6$

3.5.1 Compositional Analysis

Elemental analysis of the sample synthesized with excess Li revealed a global composition of $Li_{4.02(5)}Ni_{1.00(2)}W_{0.98(1)}$ by ICP-OES. Elemental analysis of this material by TEM-EDX revealed two different phases were likely present due to two distinct distributions: a W-rich, Ni-poor phase (Ni:W ratio of 0.92(6):1) and a lower proportion of a Ni-rich, W-poor phase (Figure 3.5.1). Normalising to a total of six cations and based on 70% of the population out of 36 particles sampled from the EDX data, the majority phase composition was estimated as $Li_{4.1}Ni_{0.9}WO_6$. The remaining 30% is attributed to a nickel-rich phase, later determined to be $Li_{0.3}Ni_{0.7}O$.

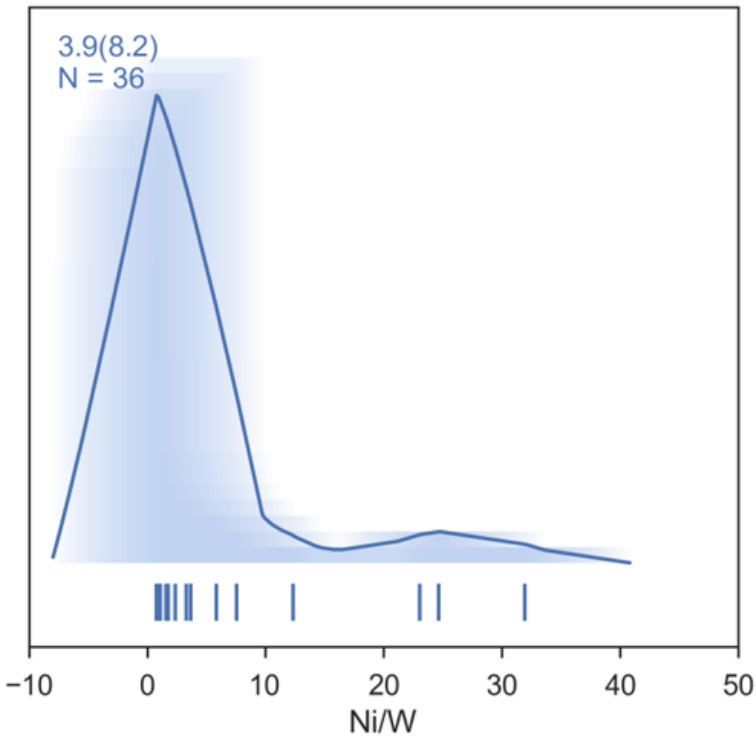

Figure 3.5.1: Average shifted histogram of TEM-EDX showing a broad distribution of Ni/W in $Li_{4.1}Ni_{0.9}WO_6$ and the presence of a nickel rich phase (high Ni/W ratio)

3.5.2 Phase and Unit Cell Determination of $Li_{4.1}Ni_{0.9}WO_6$

Initially peak fitting was performed on laboratory PXRD data based on the Li_4NiTeO_6 cell (a = 5.158 Å, b = 8.881 Å, c = 5.137 Å, β = 110.24°)[12] which adopts the $C2/m$ space group, which accounted for all of the Bragg reflections. Taking the systematic absences into consideration the candidate space groups for this structure were $C2/m$, $C2$ and Cm. Le Bail fitting was performed on the SXRD data (R_{wp} = 14.23%, R_{exp} = 11.36%, χ^2 = 1.57) and the refined lattice parameters were used for the Rietveld refinement.

Separate Le Bail fits were also performed on the three banks of NPD data (R_{wp} = 2.58%, R_{exp} = 1.86%, χ^2 = 1.93), which allowed the identification of a small amount of cubic impurity of the form $Li_xNi_{1-2x}^{2+}Ni_x^{3+}O$, the Bragg reflections of which mostly overlap with the main phase in the SXRD. This is also consistent with the TEM-EDX data which suggested a Ni-rich phase was present. The structure of Li_4NiTeO_6 was used as a structural model to begin the Rietveld refinement on the SXRD and NPD data sets. The lattice parameters were allowed to refine to different values for the SXRD and NPD data to account for any temperature differences during sample collection. The lattice parameters of the cubic impurity $Li_xNi_{1-2x}^{2+}Ni_x^{3+}O$ phase were refined, but the atomic positions and occupancies were not. Due to the low weight percent of this phase present in the sample, an accurate composition of this impurity could not be determined by Rietveld refinement. The volume of the unit cell of this phase was consistent with a composition of $Li_{0.3}Ni_{0.7}O$ based on a previous study of this system reported by Goodenough *et al.*,[27] hence the composition of this phase was fixed to these values.

A Rietveld refinement was performed using the Li_4NiTeO_6 as a model for the atomic positions and the lattice parameters obtained for Le Bail fitting in the *C*2/*m* space group setting. This Rietveld model in *C*2/*m* gave a poor fit to the SXRD (R_{wp} = 15.55%, R_{exp} = 11.36%, χ^2 = 1.87) and NPD (R_{wp} = 3.84%, R_{exp} = 1.86%, χ^2 = 4.29) in comparison to the Le Bail fit. The space group was reduced in symmetry to *Cm*, which is a non-centrosymmetric space group: this involves moving the tungsten site off-centre thereby removing the two-fold rotation axis symmetry operation, maintaining the total number of cation sites at four but doubling the number of anion sites from two (Wyckoff sites 8*j* and 4*i*, point symmetry 1 and *m* respectively) to four (sites 4*b* and 2*a*, point symmetry 1 and *m*, respectively).

As with Li_4NiWO_6, initially Rietveld refinement was performed separately on the high resolution SXRD (R_{wp} = 14.38%, R_{exp} = 11.36%, χ^2 = 1.60) and NPD (R_{wp} = 3.44%, R_{exp} = 1.86%, χ^2 = 3.44) data, and then combined for the final refinement for elucidation of the structure. The unit cell parameters were determined to be: a = 5.113747(23) Å, b = 8.791326(40) Å, c = 5.093213(23) Å, β = 110.1564(12)°, V = 214.950(2) $Å^3$. The atomic coordinates were refined independently for all sites, with the total occupancy of each site being restrained to one and no global compositional restraint. Thermal parameters were constrained to refine to the same value for the cation sites and a separate value for the four oxide sites. The refined composition of the *Cm* phase was found to be $Li_{4.099(4)}Ni_{0.896(3)}W_{1.005(3)}O_6$ with the average oxidation state of nickel calculated to be +2.11 based on a rock-salt structure with no vacancies. This Ni/W ratio is consistent with the majority of particles sampled by TEM-EDX. The final fitting parameters for the combined SXRD and NPD Rietveld refinement are R_{wp} = 8.03%, R_{exp} = 6.12%, χ^2 = 1.73, in good agreement with the equivalent Le Bail fit (R_{wp} = 7.72%, R_{exp} = 6.12%, χ^2 = 1.59).

Unlike related Li-rich rock-salt superstructures such as Li_4NiTeO_6 and Li_2MnO_3, none of the cation sites were fully occupied with Li^+, with nickel ions disordered over the three of the four cation sites. The composition of the impurity phase was fixed to $Li_{0.3}Ni_{0.7}O$, based on the cell volume matching this composition from the solid solution series $Li_xNi_{1-2x}^{2+}Ni_x^{3+}O$ ($Fm\bar{3}m$, a = 4.11835(7) Å), comprising 2.7(2) wt% of the sample.[27] The global cation composition (accounting for the atomic percentage of the impurity phase) from Rietveld refinement was $Li_{4.135(5)}Ni_{1.009(4)}W_{1.000(3)}$, in good agreement with the composition determined from ICP-OES. The final refined structure parameters are given in Table 3.5.1.

Table 3.5.1: Structural parameters of $Li_{4.1}Ni_{0.9}WO_6$ (*Cm*; *a* = 5.113747(23) Å, *b* = 8.791326(40) Å, *c* = 5.093213(23) Å, β = 110.1564(12)°, *V* = 214.950(2) Å^3) from combined Rietveld refinement. Numbers in parentheses represent 1σ

atom	site	*x*	*y*	*z*	occupancy	B_{iso} (Å^2)
W1	2*a*	0	0	0	0.9911(18)	0.75(10)
Li1	2*a*	0	0	0	0.0089(18)	0.75(10)
Li2	4*b*	0	-0.3326(2)	0	0.7129(12)	0.75(10)
Ni2	4*b*	0	-0.3326(2)	0	0.2818(9)	0.75(10)
W2	4*b*	0	-0.3326(2)	0	0.0054(8)	0.75(10)
Li3	2*a*	1/2	0	1/2	0.9191(17)	0.75(10)
Ni3	2*a*	1/2	0	1/2	0.0774(8)	0.75(10)
W3	2*a*	1/2	0	1/2	0.0036(10)	0.75(10)
Li4	4*b*	1/2	0.3182(4)	1/2	0.8726(5)	0.75(10)
Ni4	4*b*	1/2	0.3182(4)	1/2	0.1274(5)	0.75(10)
O1	4*b*	0.2326(24)	0.1554(5)	0.2372(17)	1	0.794(3)
O2	4*b*	0.2667(23)	-0.3438(5)	-0.2346(17)	1	0.794(3)
O3	2*a*	0.2688(23)	1/2	0.2199(17)	1	0.794(3)
O4	2*a*	0.7329(23)	1/2	0.7642(17)	1	0.794(3)

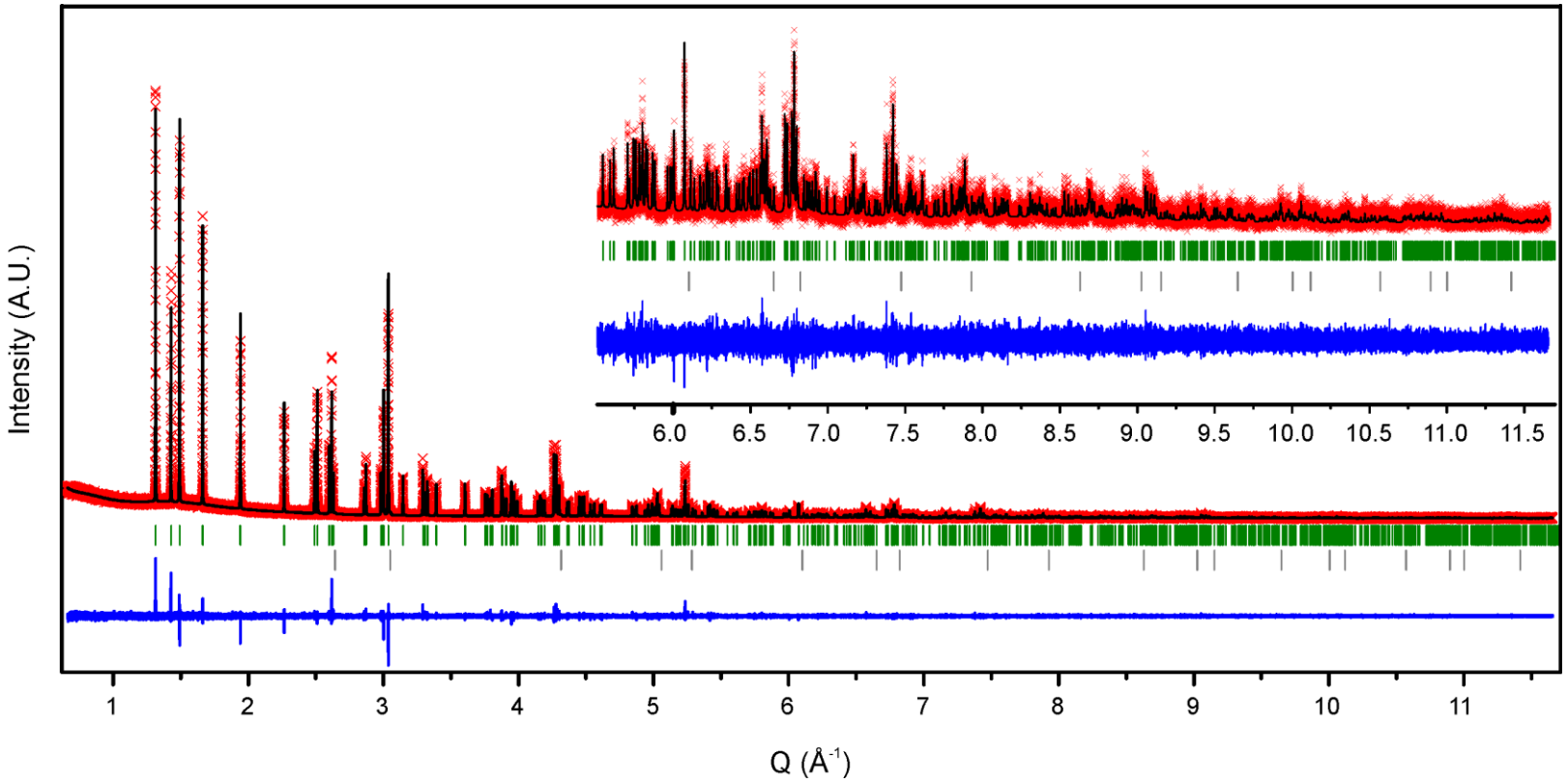

Figure 3.5.2: SXRD pattern for the combined Rietveld refinement of $Li_{4.1}Ni_{0.9}WO_6$ (λ = 0.82588(1) Å); R_{wp} = 14.38%, R_{exp} = 11.36%, χ^2 = 1.60; *green* ticks indicate *Cm* phase, *grey* ticks indicate cubic $Li_{0.3}Ni_{0.7}O$ impurity

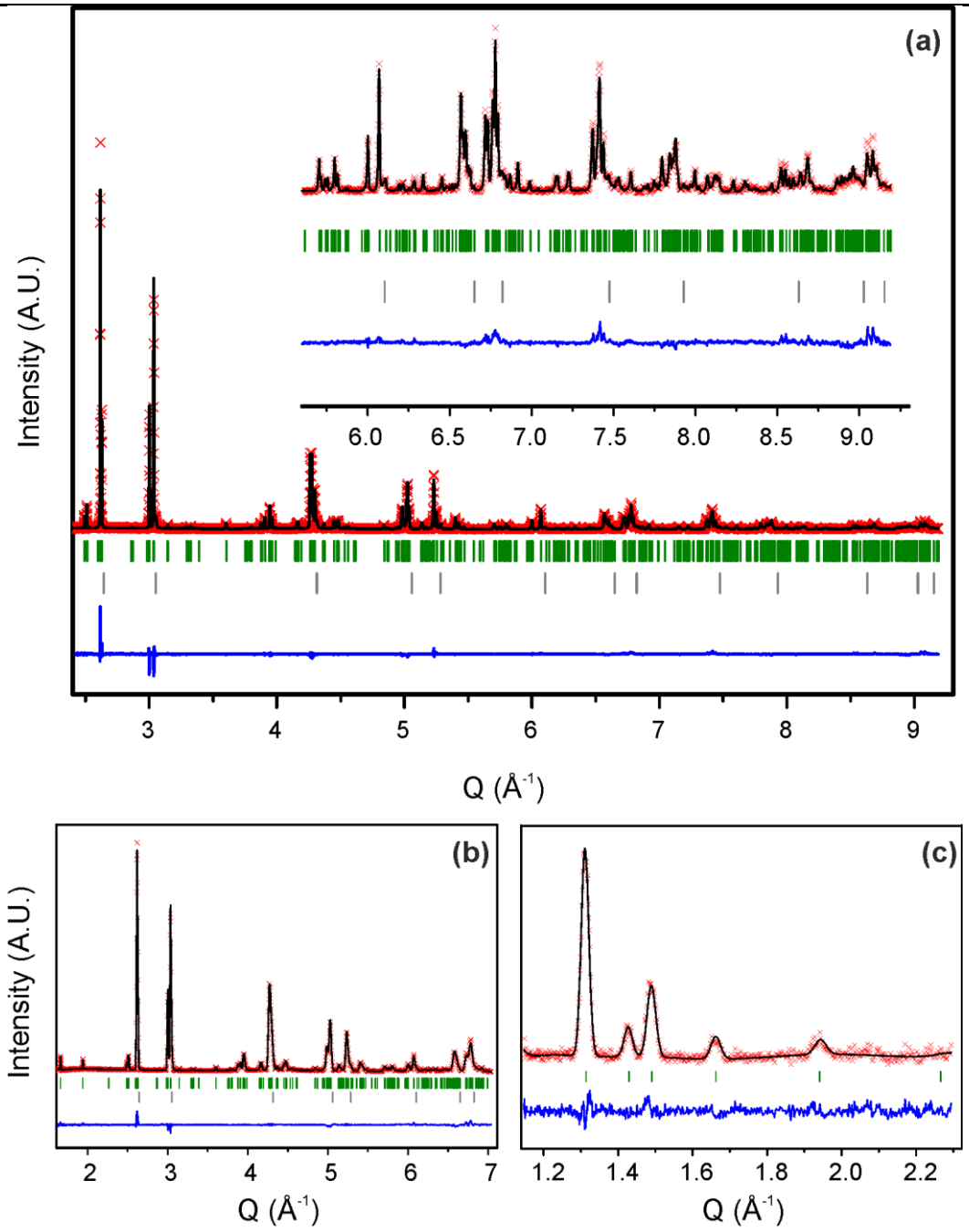

Figure 3.5.3: NPD patterns from the HRPD instrument for the combined Rietveld refinement of $Li_{4.1}Ni_{0.9}WO_6$; (*a*) backscattered bank 1; R_{wp} = 4.82%, R_{exp} = 2.77%, χ^2 = 3.03; (*b*) bank 2 90° detector; R_{wp} = 2.58%, R_{exp} = 1.15%, χ^2 = 5.08; (*c*) bank 3 30° detector; R_{wp} = 7.30%, R_{exp} = 6.24%, χ^2 = 1.37; *green* ticks indicate *Cm* phase, *grey* ticks indicate cubic $Li_{0.3}Ni_{0.7}O$ impurity

3.5.3 Crystal Structure of $Li_{4.1}Ni_{0.9}WO_6$

$Li_{4.1}Ni_{0.9}WO_6$ adopts a monoclinic structure with two distinct types of octahedral layers (Figure 3.5.4), with similar unit cell parameters as the archetypal Li_5ReO_6 rock-salt superstructure. In the Li_5ReO_6 structure, the ReO_6 octahedra are fully ordered and isolated from each other by adopting a two layer structure whereby LiO_6 octahedra surround ReO_6 in a honeycomb arrangement forming one layer, alternating with fully occupied Li layers. In the case of $Li_{4.1}Ni_{0.9}WO_6$, all four cation sites were determined to be fully occupied, with each displaying partial cation ordering. $Li_{4.1}Ni_{0.9}WO_6$ was not found to possess a fully occupied lithium layer, attributed to the similar ionic radius of Ni^{2+} and Li^{+} (Figure 3.5.5). Interestingly, W^{6+} was not found to be fully ordered, with <1% Li mixing on the tungsten site, and the remaining tungsten distributed on two of the three remaining cation sites.

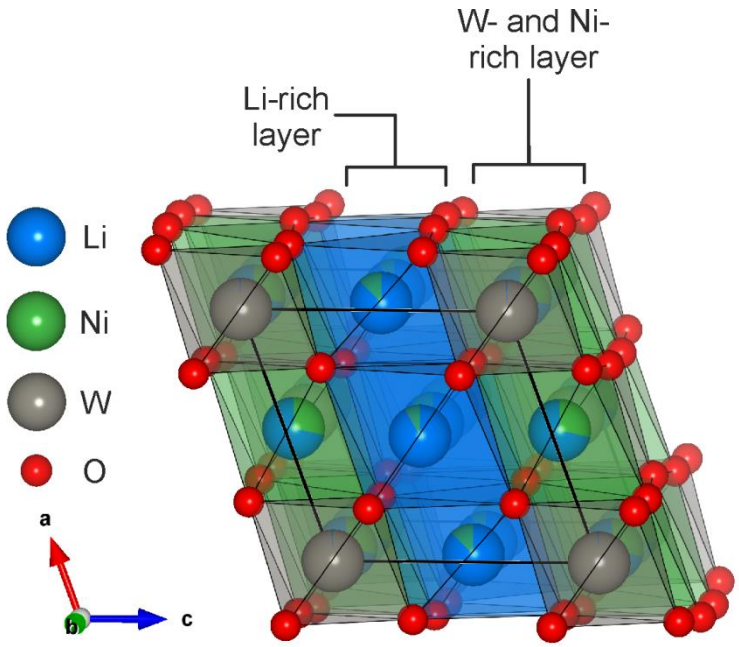

Figure 3.5.4: Representation of the $Li_{4.1}Ni_{0.9}WO_6$ unit cell structure as determined from combined Rietveld refinement

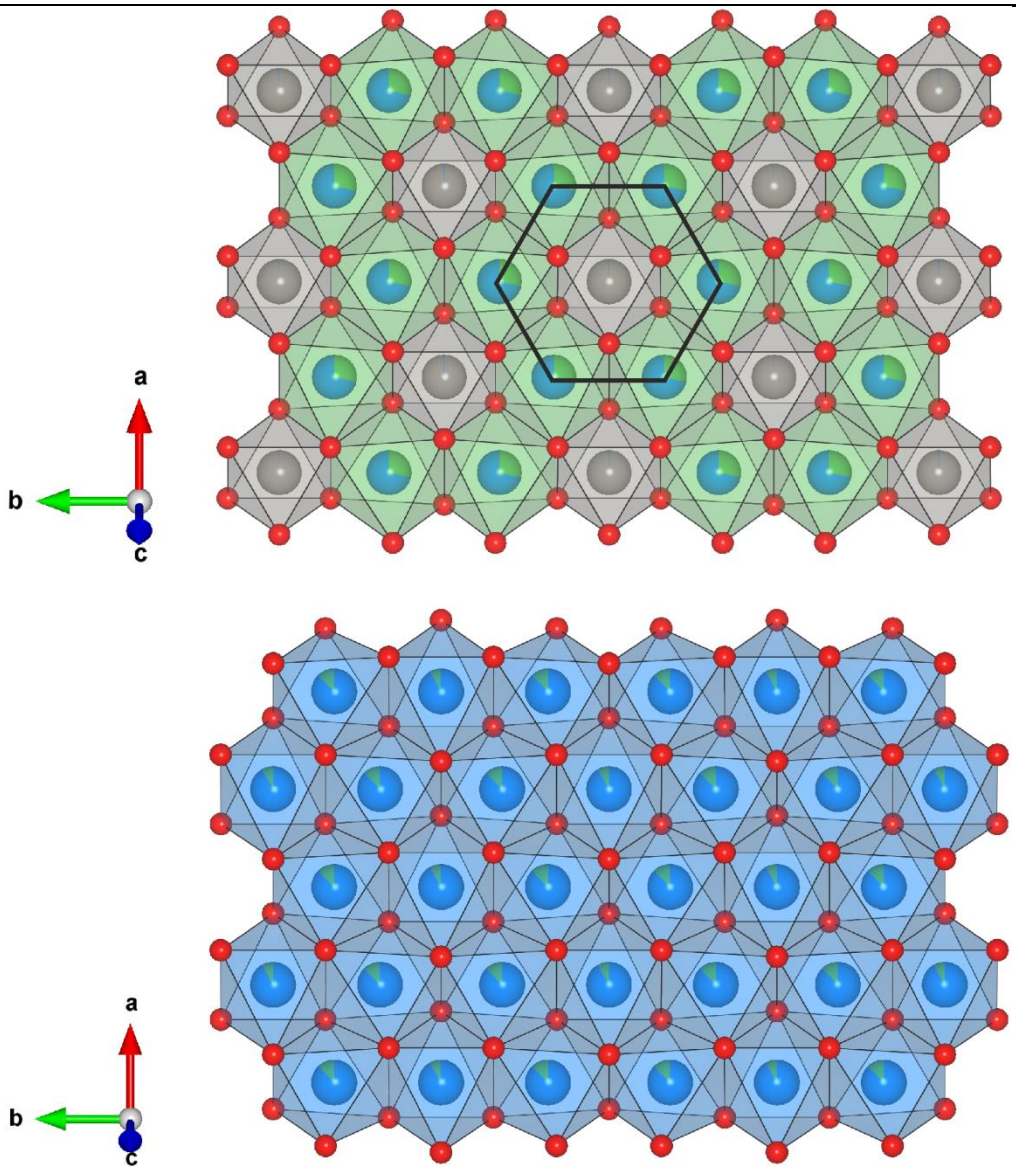

Figure 3.5.5: Representation of the two types of layering in $Li_{4.1}Ni_{0.9}WO_6$: W- and Ni-rich layer and honeycomb ordering pattern around WO_6 (*top*) and Li-rich layer (*bottom*) viewed along the [111] axis of the cubic rock-salt sub-cell

The ordering of tungsten matches that of rhenium in the Li_5ReO_6 structure (Figure 3.5.6), whereby WO_6 octahedra are surrounded by Ni-rich octahedra in one layer in a honeycomb-type ordering, separated by a Li-rich layer in the (002) plane.

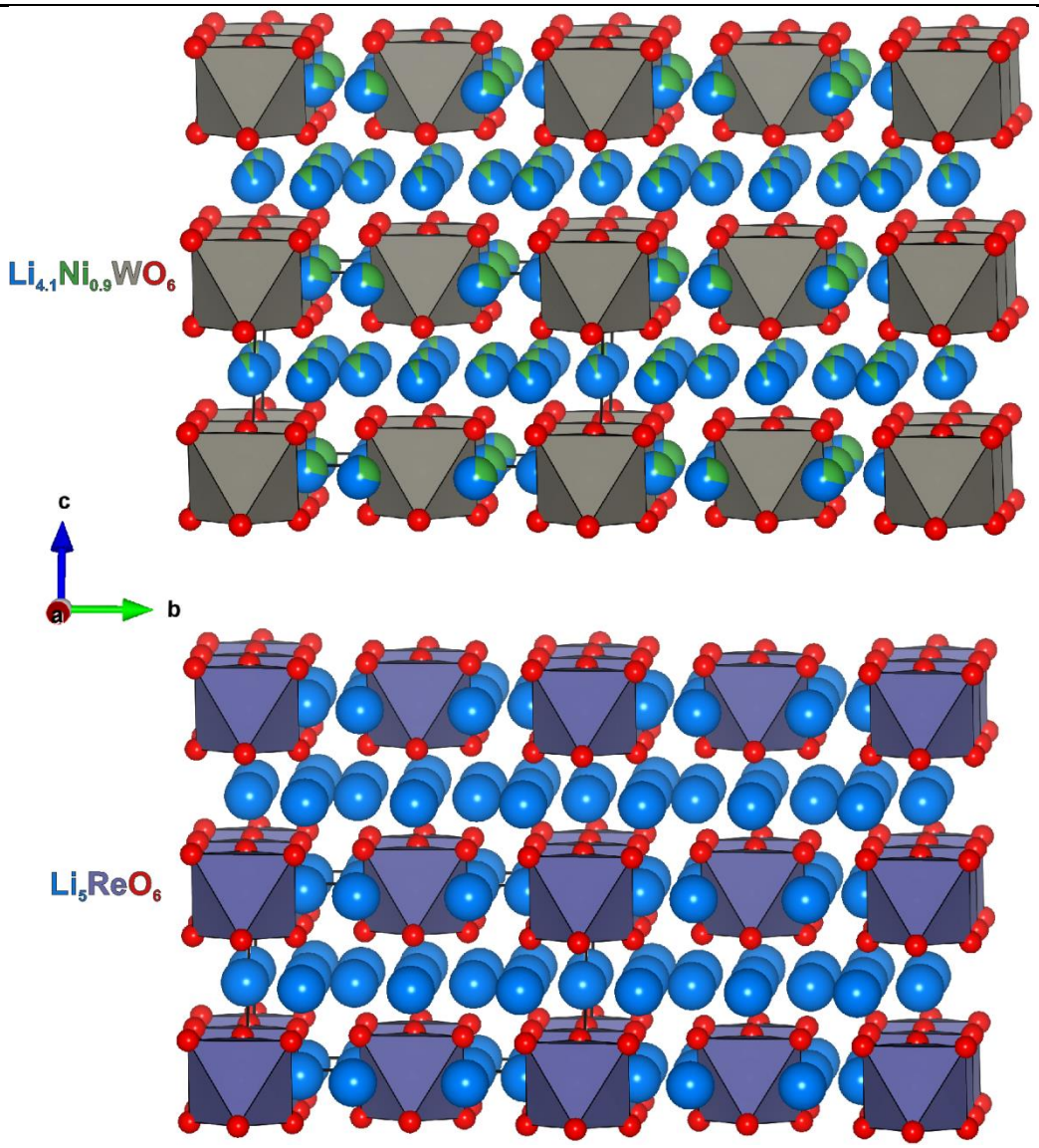

Figure 3.5.6: Representation of the ordering of WO_6 octahedra in $Li_{4.1}Ni_{0.9}WO_6$ (*top*) and ReO_6 octahedra in Li_5ReO_6 (*bottom*)

The reduction in symmetry to *Cm* from *C*2/*m* space group (*C*2/*m* is the space group adopted in related ordered rock-salt type materials such as Li_5ReO_6,[28] Li_2MnO_3,[29] Li_4NiTeO_6 *etc*.)[12] is a result of the displacement of W^{6+} ions towards one apex of the $[WO_6]^{6-}$ octahedra (Figure 3.5.7). The W1-O3 bond length is shorter than W1-O4, and these oxygen atomic sites are also the apical oxygens for the most lithium-rich octahedral site labelled Li3, hence the tungsten ions are displaced towards the Li3 site

(Table 3.5.1). Since the displacement occurs in the same direction, this propagates throughout the lattice resulting in an overall permanent dipole in the [101] direction and a loss of the two-fold rotation symmetry operation in the as-synthesised material, hence losing the inversion centre. This is because W is moved off the special position (Wyckoff position 2*a*) in the *C*2/*m* model (with 2/*m* site symmetry operations) to the 2*a* site in the *Cm* structure, with mirror symmetry only.[22, 30]

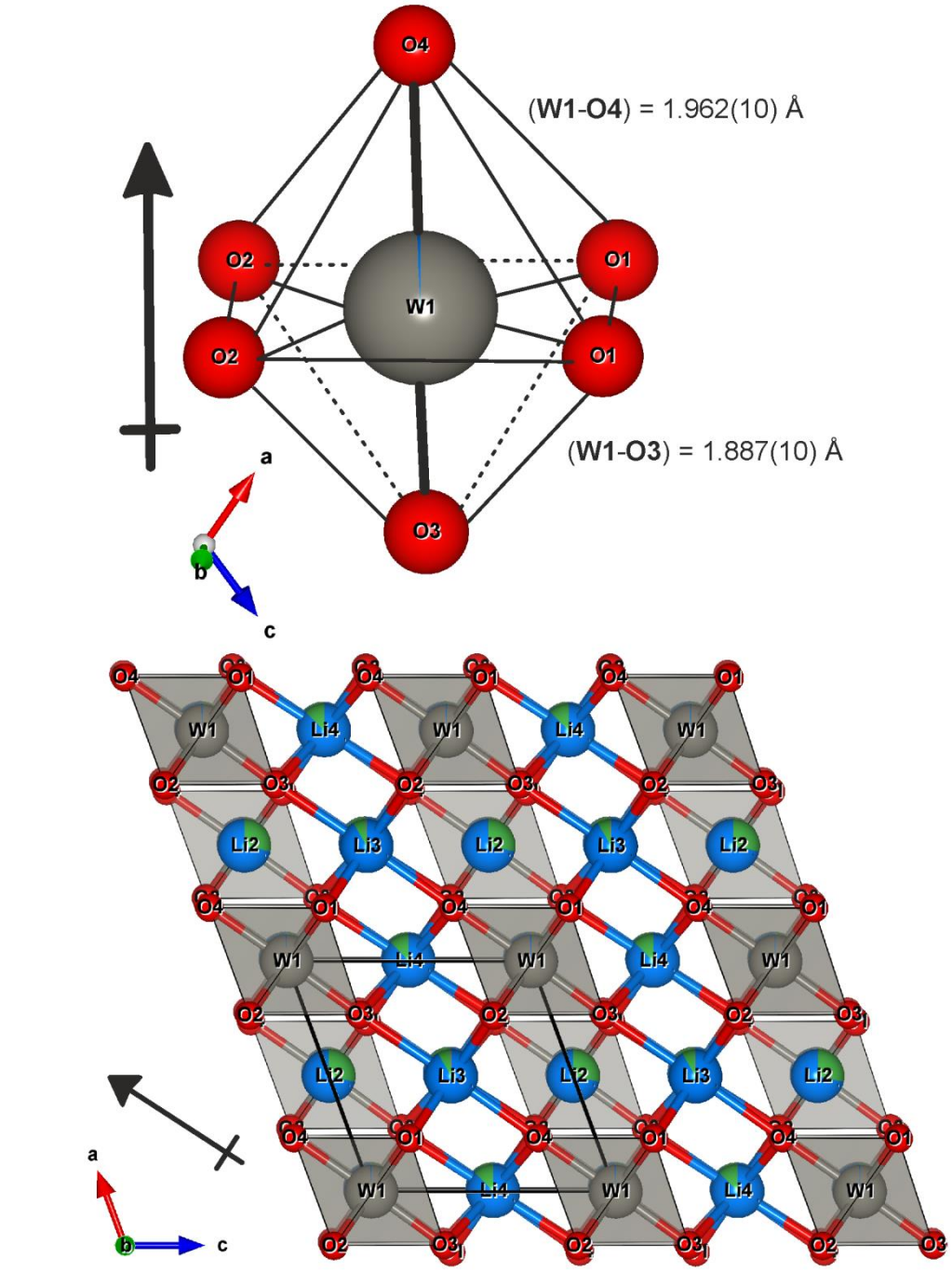

Figure 3.5.7: Octahedral coordination environment of the tungsten W1 site showing the difference in W-O axial bond lengths and resulting dipole direction; where equatorial (W1-O1) and (W1-O2) bond lengths = 1.937(7) Å (*top*); and direction of polarity within the lattice (*bottom*)

The bond valence sums (for both Ni^{2+} and Ni^{3+}) and octahedral distortion parameters were calculated as detailed in Section 3.4.4 and reported in Table 3.5.2. In particular the bond valence states for nickel differ considerably from expected, which is attributed to the mixed charge valences and extensive site mixing observed from the Rietveld refinement. The polar W1 site was not determined to have the greatest bond length or angle distortion, but since it distorts towards Li3 this may explain why the Li3 site is considerably distorted from octahedral geometry.

Table 3.5.2: Average *M*-O bond lengths and bond valance sums (BVS) for each atom from refined structure of $Li_{4.1}Ni_{0.9}WO_6$ (*Cm*) where numbers in parentheses represent 1σ. The bond length distortion (Δ) and angle variance (δ) from the ideal octahedral configuration are also reported

assumed valence state	atom	occupancy	BVS	average *M*-O bond length (Å)	Δ (×10⁴)	δ
6	W1	0.9911(18)	5.76(7)	1.933(2)	1.348	0.191
1	Li1	0.0089(18)	1.70(2)			
1	Li2	0.7129(12)	1.13(1)	2.085(21)	0.850	27.544
2	Ni2	0.2818(9)	1.99(2)			
3	Ni2	0.2818(9)	2.43(2)			
6	W2	0.0054(8)	3.82(4)			
1	Li3	0.9191(17)	1.02(4)	2.13(10)	18.664	18.720
2	Ni3	0.0774(8)	1.79(7)			
3	Ni3	0.0774(8)	2.19(9)			
6	W3	0.0036(10)	3.44(14)			
1	Li4	0.8726(5)	1.01(2)	2.127(42)	3.303	31.825
2	Ni4	0.1274(5)	1.78(3)			
3	Ni4	0.1274(5)	2.18(4)			

3.6 Comparison of the $Li_{4+x}Ni_{1-x}WO_6$ Structures

Both Li_4NiWO_6 and $Li_{4.1}Ni_{0.9}WO_6$ structures were found to crystallise in monoclinic space groups, adopting a rock-salt superstructure with a fully occupied *ccp* oxide array with edge-sharing octahedra. Partial cation order was determined in both structures. The site mixing of Li^+ and Ni^{2+} is not uncommon, and has been observed in a number of materials such as $LiNi_{1/3}Mn_{1/3}Co_{1/3}O_2$, $LiNiO_2$ and Li_4NiMoO_6 due to similar ionic radii (Li^+ = 0.76 Å, Ni^{2+} = 0.69 Å).[13, 31, 32] Surprisingly, considering its high charge, perfect ordering for W^{6+} ions was not observed in either of the as-synthesised materials: a small amount of W^{6+} (0.60 Å) and Li^+ site mixing was observed through a combination of SXRD and NPD refinement. In both materials, displacement of W^{6+} within the $[WO_6]^{6-}$ octahedra was observed, attributed to second-order Jahn-Teller effects,[33] which are widely reported other W^{6+} oxides such as WO_3, Bi_2WO_6, $BaTeW_2O_9$ and $NaLaMgWO_6$.[22, 23, 34, 35] In Li_4NiWO_6, the bond length between W1 and both O2 sites is shorter than the remaining four W-O bonds, resulting in a displacement of the tungsten ion off-centre towards an apex of the WO_6 octahedra. Such displacement occurs in opposing directions along the [010] axis resulting in an apolar material overall (Figure 3.4.14). In $Li_{4.1}Ni_{0.9}WO_6$, one axial W-O bond is shorter, resulting in displacement towards an apex of the WO_6 octahedra, which propagates throughout the lattice in the [101] direction, suggesting the material will possess an overall polarity (Figure 3.5.7).

No reports of other structures with similar lattice parameters to *C*2/*c* Li_4NiWO_6 could be found through searching of the cell symmetry in the Inorganic Crystal Structure Database (ICSD) or within relevant literature. Likewise a large number of compounds

with compositions related to $Li_{4.1}Ni_{0.9}WO_6$ with similar unit cell parameters are reported, but none thus far have been determined to adopt the *Cm* space group.

By comparison of the ordering pattern for the tungsten sites, $Li_{4.1}Ni_{0.9}WO_6$ can be thought of as a polar analogue of Li_5ReO_6. For Li_4NiWO_6, both the *C*2/*c* and *Fddd* models adopt the same tungsten site ordering as tantalum in the $Li_3Ni_2TaO_6$ archetype (Figure 3.4.10). The difference in the ordering of the majority tungsten sites is that $Li_{4.1}Ni_{0.9}WO_6$ has tungsten located in alternating close-packed oxygen layers (Figure 3.5.5), whereas Li_4NiWO_6 has tungsten located in every layer (Figure 3.4.11, Figure 3.4.12), without honeycomb-type ordering around WO_6 octahedra. The absence of fully occupied lithium layers in $Li_{4.1}Ni_{0.9}WO_6$ is attributed to Li^+/Ni^{2+} cation site mixing. The related structure of Li_4CuTeO_6 was reported in the literature to crystallise in the *C*2/*m* space group, with Li and Cu ordered in the honeycomb array around TeO_6 octahedra. In this structure cation mixing of Cu^{2+} and Li^+ in between the layers containing Te was determined, in addition to a small amount of Cu (6%) reported to occupy the Te crystallographic site.[2]

All refined structures and their archetypes can be thought of as the general rock-salt superstructure A_5MO_6 formula (see Chapter 1), whereby the overall structure is electroneutral and the electroneutrality around each oxygen site is preserved.[7] For example, in Li_4NiWO_6, the average coordination around oxygen would be $OLi^{I}_4Ni^{II}W^{VI}$, (where $Li_4Ni = A_5$ and $W = M$) therefore the sum of the electrovalence around each oxide anion is equal to +2 according to Equation 3.6.1 where z = charge and n = coordination number.

$$\sum \frac{z}{n} = \left(4_{\mathrm{Li}} \times \frac{1}{6}\right) + \left(1_{\mathrm{Ni}} \times \frac{2}{6}\right) + \left(1_{\mathrm{W}} \times \frac{6}{6}\right) = 2$$

Equation 3.6.1: Electrovalence sums around octahedral oxide in Li_4NiWO_6

The same is true for the $Li_{4.1}Ni_{0.9}WO_6$ formula where the average charge state of nickel is calculated to be +2.11. Within rock-salt superstructures of this general formula, this means no *M* cations (W^{6+}) can be coordinated to the same oxygen ion, thus isolating the highly charged *M* ions. Consequentially, the ordering of the *A* and *M* cations therefore depends on whether it is more energetically favourable to align the MO_6 into layers, as occurs in Li_5ReO_6, and in $Li_{4.1}Ni_{0.9}WO_6$ where the W and majority Ni reside in alternating layers (Figure 3.5.5, Figure 3.5.6); or maximising the distance between all *M* cations as occurs in $Li_3Ni_2TaO_6$ and Li_4NiWO_6 (Figure 3.4.10, Figure 3.4.12)

The distances between the W^{6+} sites in both structures is approximately the same between and within the layers (5.1-5.2 Å), maximising the distance between the highly charged $5d^0$ ions hence minimising the electrostatic repulsion,[9] suggesting that there is very little difference in energy between the two structures. A greater degree of ordering of the nickel ions was observed in Li_4NiWO_6 (*C*2/*c*) whereby more than half the nickel ions are located on one of the six cation sites, in contrast to $Li_{4.1}Ni_{0.9}WO_6$ (*Cm*) where the nickel ions are more evenly distributed, with the majority located within the honeycomb layer containing the tungsten ions. The adoption of a different crystal structure from alteration of the metal ratios is primarily attributed to the presence of Ni^{3+} ions (0.56 Å) driving the cation ordering.[7, 36] The rock-salt type $Li_2Ni_2TeO_6$ has been reported to crystallise into the honeycomb-ordered *C*2/*m* space group and more disordered orthorhombic *Fddd* space group depending on the synthetic method,[37] (with Li_5ReO_6 and $Li_3Ni_2TaO_6$ archetypal structures, respectively) which

supports the conclusion that the $Li_{4+x}Ni_{1-x}WO_6$ structures have similar formation enthalpies.

3.7 Solid Solution Series $Li_{4.1+x}Ni_{0.9-x}WO_6$

The emergence of the $Li_{0.3}Ni_{0.7}O$ impurity with the sample with refined composition $Li_{4.1}Ni_{0.9}WO_6$ provided evidence of a solid solution of the form $Li_{4.1+x}Ni_{0.9-x}WO_6$, whereby the rock-salt structure is retained upon increasing values of x as Ni^{2+} is substituted for Li^+. The average oxidation state of nickel therefore increases to maintain a total cation charge of +12 per formula unit, hence maintaining an electroneutral rock-salt superstructure. These materials were synthesised with a 10% molar excess of lithium (a reduction from 12% for the original synthesis reported for $Li_{4.1}Ni_{0.9}WO_6$) to minimise the formation of the cubic impurity phase but maintain a lithium-rich composition.

The lattice parameters for each member of the solid solution were refined by Le Bail fitting of laboratory PXRD (Figure 3.7.1) using the Topas software, with the lattice parameters of the internal silicon standard fixed (S.G. $Fd\bar{3}m$, a = 5.43053(7) Å). All members of the solid solution were determined to adopt the *Cm* structure.

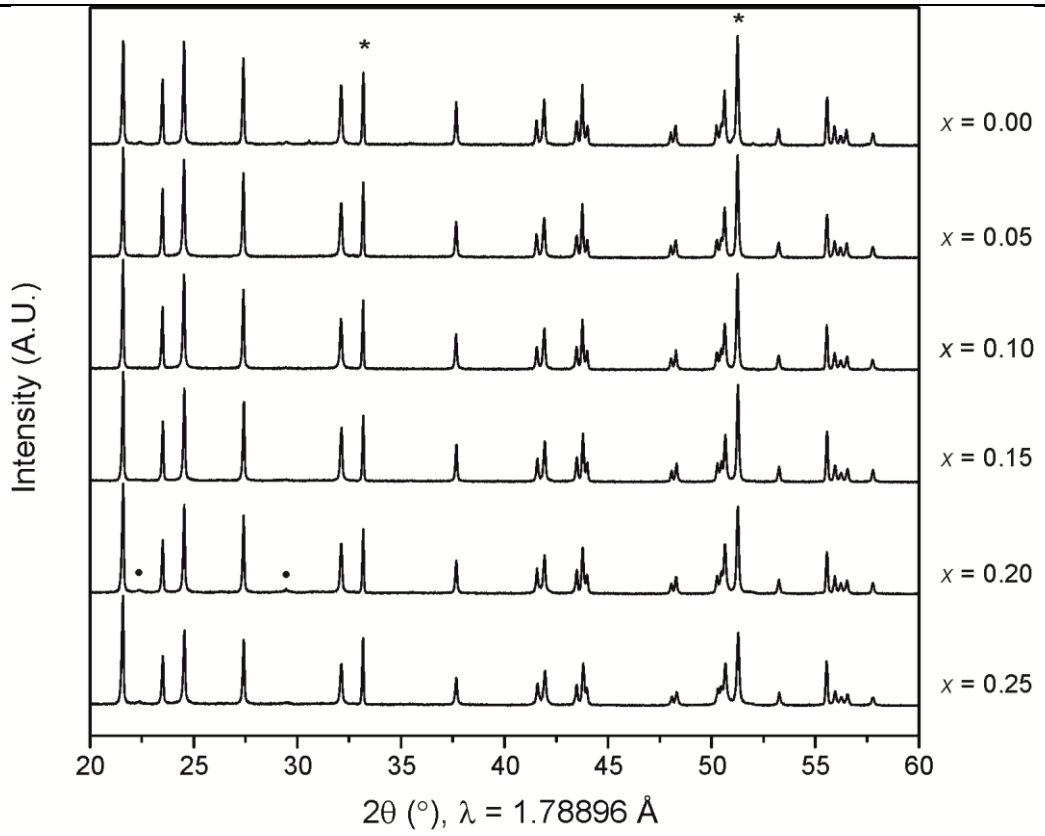

Figure 3.7.1: PXRD of members of solid solution series $Li_{4.1+x}Ni_{0.9-x}WO_6$ with nominal values of *x* listed on the *right*. * indicates Si peaks, ● indicates impurity (likely Li_4WO_5)

Impurity peaks which correspond to Li_4WO_5 ($P\bar{1}$) appear at values of $x > 0.20$ indicating the limit of purity lies between nominal values of $0.15 \leq x \leq 0.20$. Additionally in the $x = 0.00$ sample, low intensity reflections corresponding to Li_4NiWO_6 are visible, verifying that the two structures are very closely related in energy and largely dependent on the Li/Ni ratio. It was found that the lattice parameters decrease monotonically with increasing values of *x*, obeying Vegard's law (Figure 3.7.2).

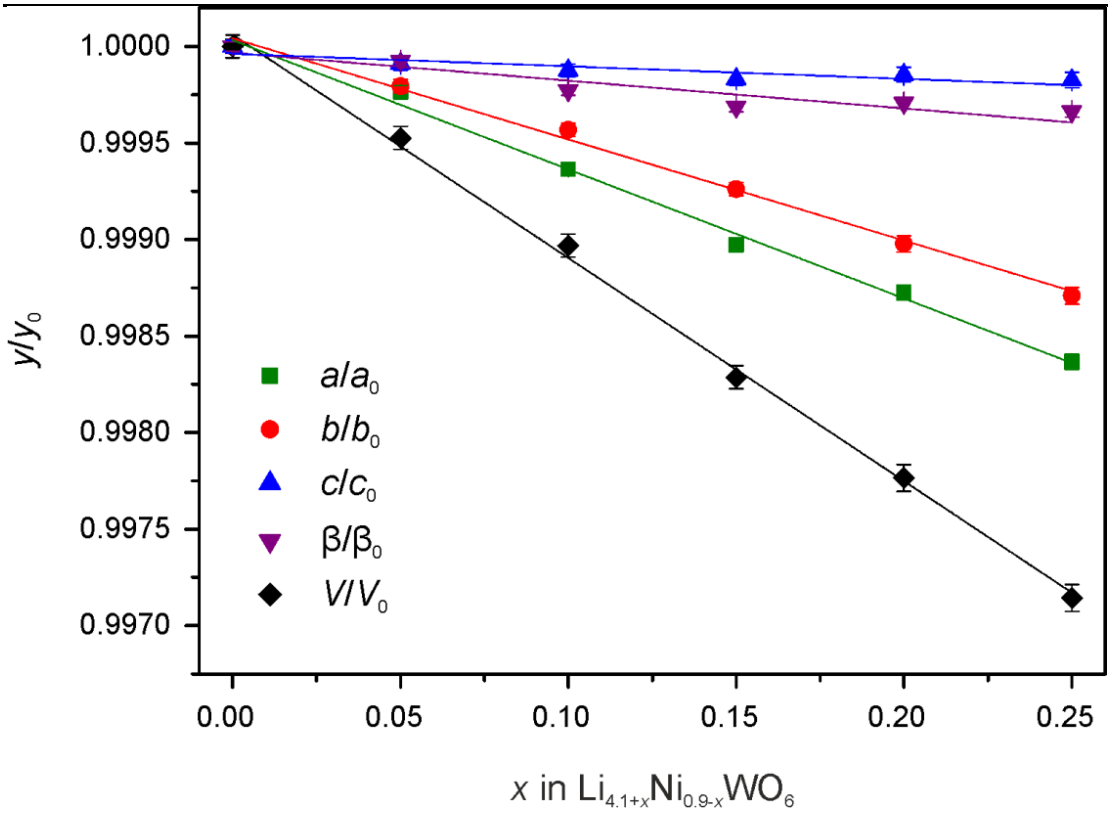

Figure 3.7.2: Trend in lattice parameters for the doping series of nominal composition $Li_{4.1+x}Ni_{0.9-x}WO_6$ (reported as a fraction of the $x = 0.00$ sample). Error bars represent 3σ

This lattice parameter trend is comparable to the $Li_xNi_{1-2x}^{2+}Ni_x^{3+}O$ series,[38] whereby the unit cell volume decreases linearly with increasing values of x. This is due to the substitution of Ni^{2+} (0.69 Å) for smaller and more highly charged Ni^{3+} (0.56 Å), and Li^+ (0.76 Å). In this case we see a similar trend, whereby the average increase in the oxidation state of nickel with increasing x results in a decrease in cell volume, despite an increase in Li^+ which has a slightly larger ionic radius than Ni^{2+}.

3.8 $Li_{4.15}Ni_{0.85}WO_6$

From the solid solution series, the material with nominal composition $Li_{4.15}Ni_{0.85}WO_6$ (x = 0.05) was chosen for further electrochemical study, which is discussed in detail in Chapter 4 due to the high lithium content and phase purity determined from SXRD.

A Rietveld refinement was performed using synchrotron MAC data of $Li_{4.15}Ni_{0.85}WO_6$ using the structural model obtained from the refinement of $Li_{4.1}Ni_{0.9}WO_6$ (Figure 3.8.1). Since NPD data was not collected for this material, the sum of the occupancies of each crystallographic site was restrained to equal one, assuming a rock-salt structure with no vacancies, with the occupancies of only two point scatterers able to be refined at each cation site. The final calculated composition from Rietveld refinement ($Li_{3.983(9)}Ni_{1.02(7)}W_{0.997(6)}O_6$) is not in full agreement with the elemental analysis from ICP-OES ($Li_{4.19(8)}Ni_{0.82(1)}W_{0.99(4)}$) due to the constrains applied to the mixed cation sites. The refined lattice parameters were determined to be a = 5.11475(4) Å, b = 8.79311(7) Å, c = 5.09298(4) Å, β = 110.1594(5)°, V = 215.022(3) $Å^3$.

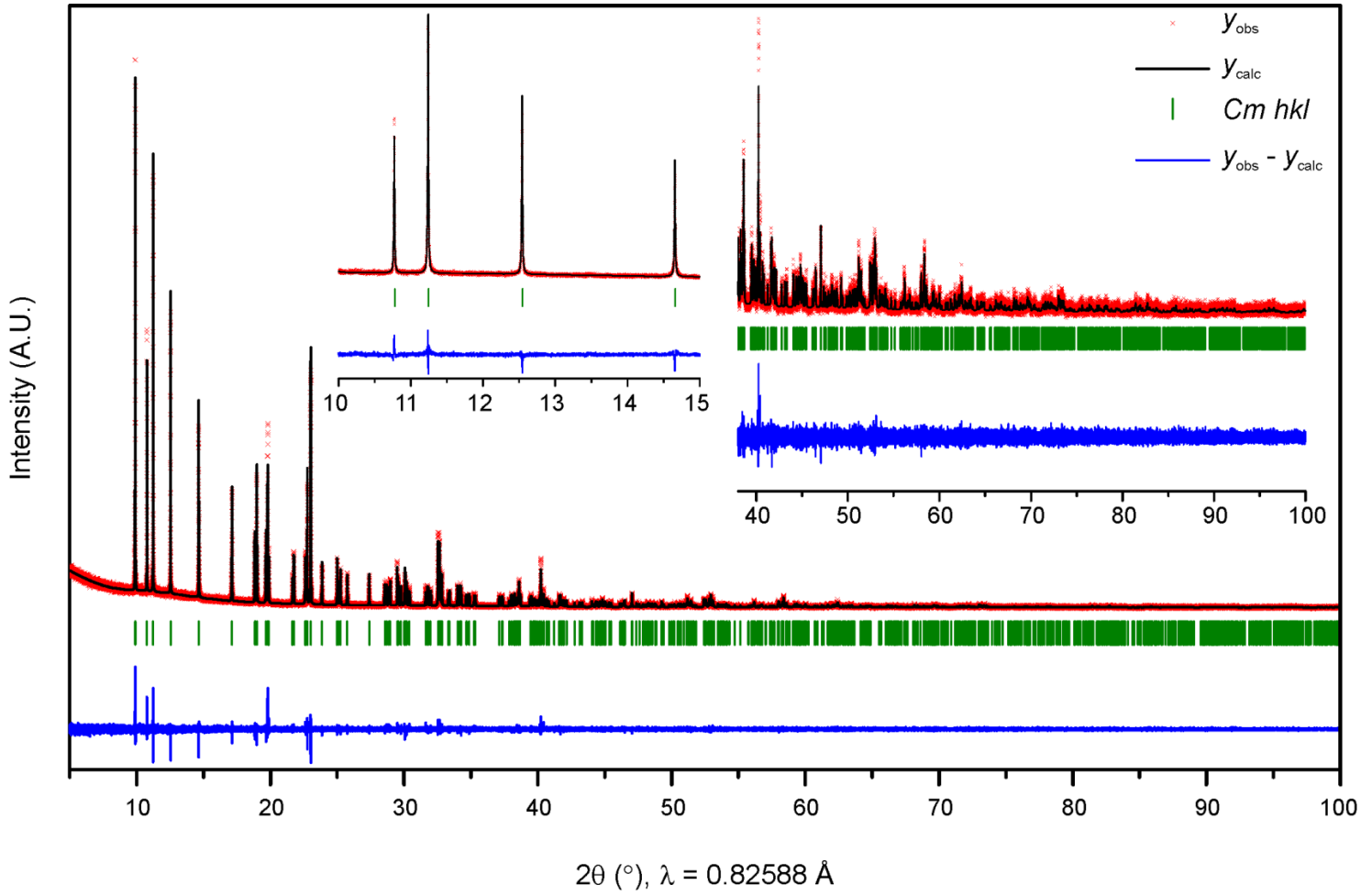

Figure 3.8.1: Rietveld refinement of SXRD (MAC) data of $Li_{4.15}Ni_{0.85}WO_6$; R_{wp} = 15.65%, R_{exp} = 12.21%, χ^2 = 1.64

The structural refinement proves it is an analogue of the $Li_{4.1}Ni_{0.9}WO_6$ *Cm* structure, with similar unit cell parameters and honeycomb ordering of Li/Ni cations around the WO_6 octahedra (Figure 3.8.2) but a varying Li and Ni content. The average nickel oxidation state is calculated to be +2.18, with the largest amount of nickel located within the tungsten layer. A degree of cation mixing was observed for each site (Table 3.8.1), meaning this structure also does not possess fully occupied lithium layers.

Table 3.8.1: Structural parameters of $Li_{4.15}Ni_{0.85}WO_6$ (*Cm*; a = 5.11475(4) Å, b = 8.79311(7) Å, c = 5.09298(4) Å, β = 110.1594(5)°, V = 215.022(3) Å^3) from SXRD Rietveld refinement. Numbers in parentheses represent 1σ

atom	site	*x*	*y*	*z*	occupancy	B_{iso} (Å^2)
W1	2*a*	0	0	0	0.997(6)	0.74(1)
Li1	2*a*	0	0	0	0.003(6)	0.74(1)
Li2	4*b*	0	-0.3330(2)	0	0.658(3)	0.74(1)
Ni2	4*b*	0	-0.3330(2)	0	0.342(3)	0.74(1)
Li3	2*a*	1/2	0	1/2	0.906(2)	0.74(1)
Ni3	2*a*	1/2	0	1/2	0.094(2)	0.74(1)
Li4	4*b*	1/2	0.3306(5)	1/2	0.878(2)	0.74(1)
Ni4	4*b*	1/2	0.3306(5)	1/2	0.122(2)	0.74(1)
O1	4*b*	0.230(2)	0.1440(9)	0.229(2)	1	0.25(6)
O2	4*b*	0.270(2)	-0.3311(9)	-0.228(2)	1	0.25(6)
O3	2*a*	0.252(3)	0.5	0.216(3)	1	0.25(6)
O4	2*a*	0.715(3)	0.5	0.763(3)	1	0.25(6)

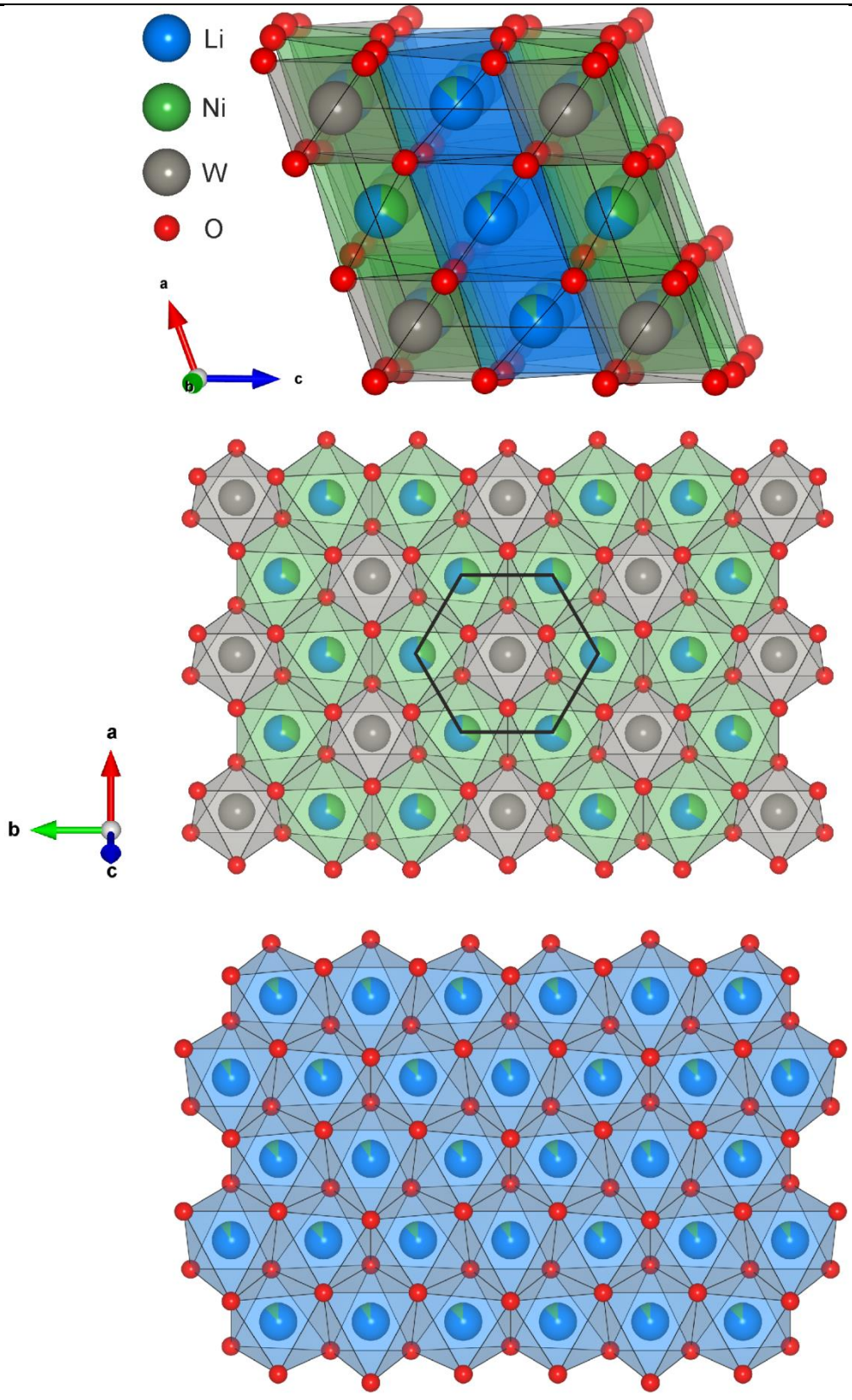

Figure 3.8.2: Representation of the unit cell structure of $Li_{4.15}Ni_{0.85}WO_6$ (*top*), the W and Ni-rich layer displaying honeycomb ordering around WO_6 (*middle*) and the Li-rich layer (*bottom*)

3.9 $Li_{4.08}Mg_{0.90}W_{1.02}O_6$

A number of variations on the Li:Mg:W ratio were explored in an attempt to get a phase pure lithium-rich Mg analogue of $Li_{4.1}Ni_{0.9}WO_6$. Based on the assumption that the material would be a no-vacancy rock-salt superstructure, possible electroneutral stoichiometries include Li_4MgWO_6 and $Li_{4.08}Mg_{0.90}W_{1.02}O_6$ since the cation oxidation states of lithium, magnesium and tungsten are not expected to deviate from +1, +2 and +6, respectively. Both target compositions maintain Pauling's rule of electroneutrality around each oxide anion (as demonstrated for Li_4NiWO_6 in Section 3.6), therefore it can be predicted that they would likely adopt similar cation ordering patterns to $Li_3Ni_2TaO_6$ or Li_5ReO_6 rock-salt archetypes. Initial attempts at targeting the Li_4MgWO_6 composition did not result in a phase pure sample; however the majority of the Bragg reflections could be indexed to an *Fddd* cell with similar lattice parameters to $Li_3Ni_2TaO_6$.

It was found that targeting a stoichiometry of $Li_{4.08}Mg_{0.90}W_{1.02}O_6$ resulted in a phase pure material by PXRD analysis. Elemental analysis was performed on this sample by ICP-OES confirming a composition of $Li_{4.10(8)}Mg_{0.893(2)}W_{1.011(3)}$, normalising to a total six cations per formula unit, which agrees within 3σ with the target composition. Through a systematic exploration of numerous ratios of starting reagents and reaction conditions, the required molar ratio of Li:Mg:W reagents was determined to be 4.51:0.95:1. It was found necessary to have a molar excess of MgO, with the Mg content in the product being lower than in the reagent, attributed to drying of the MgO reagent at too low a temperature (see Section 3.2.4). Three firing steps at 900 °C without sacrificial powder were deemed necessary due to the slow reaction kinetics of MgO and to remove any excess lithium, since too high a lithium content resulted in

the formation of an unknown impurity phase (the intensity of the peaks of which decreased upon subsequent firings). From laboratory PXRD all the peaks were determined to index to a *C*2/*m* cell with similar lattice parameters to $Li_{4.1}Ni_{0.9}WO_6$, and further high-resolution SXRD (MAC) data was obtained.

From the Le Bail fit to the SXRD MAC data (Figure 3.9.1), a small number of very low intensity Bragg reflections were identified that do not index to the *C*2/*m* unit cell (*e.g.* at 2θ ~13.5° in Figure 3.9.1, *top left inset*). Additionally, a single pseudo-Voigt peak shape model did not adequately model all of the peaks was as observed during indexing of Li_4NiWO_6 (see Section 3.4.2), which again may indicate the presence of an additional related phase. Attempts to improve the Le Bail fit using related cells were thus far unsuccessful.

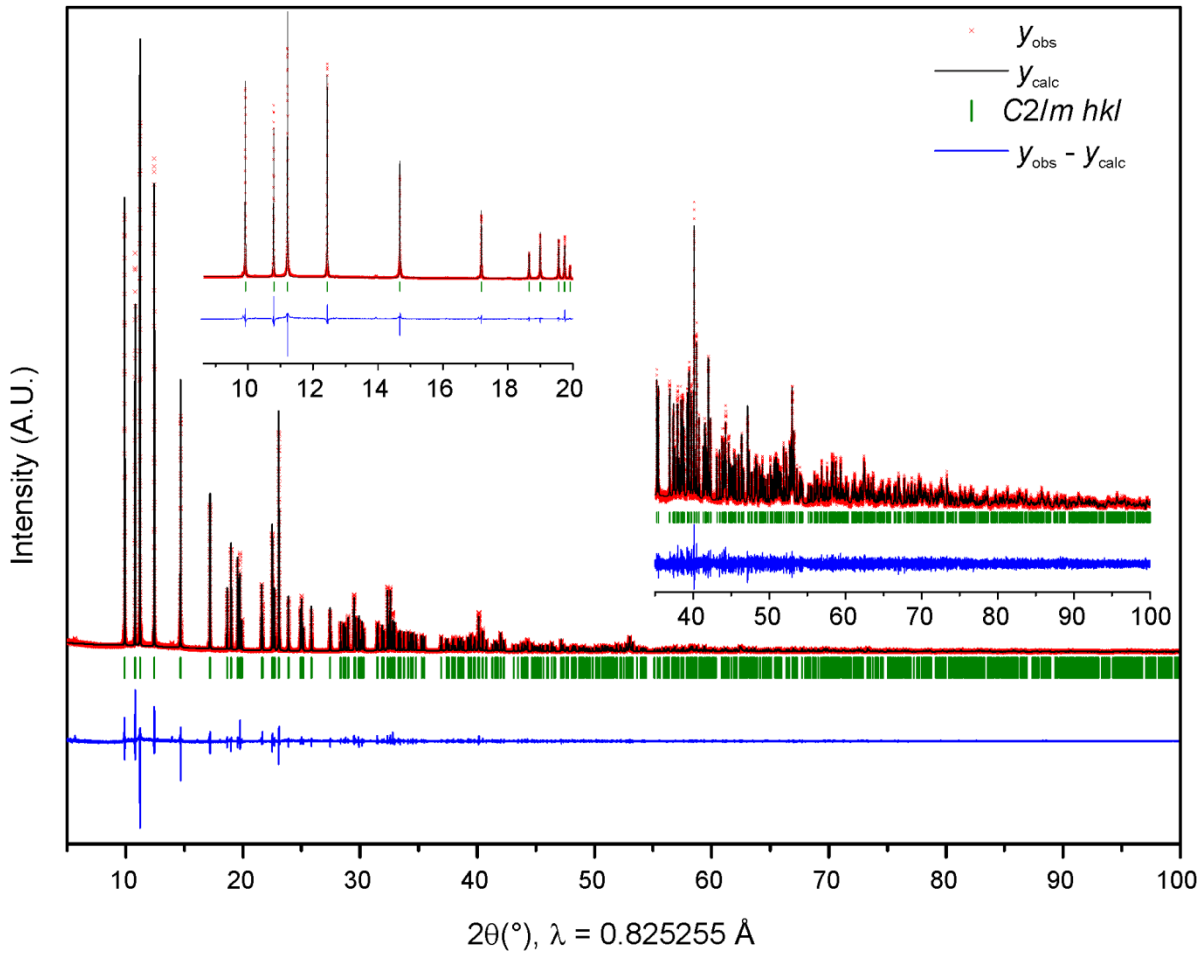

Figure 3.9.1: Le Bail refinement of SXRD (MAC) data of $Li_{4.08}Mg_{0.90}W_{1.02}O_6$; R_{wp} = 11.50%, R_{exp} = 6.07%, χ^2 = 3.59

Following the Le Bail refinement, separate Rietveld refinements were performed on the data using the Li_4NiTeO_6 (*C*2/*m*) and $Li_{4.1}Ni_{0.9}WO_6$ (*Cm*) structural models. Considering the similar ionic radii of octahedrally coordinated Mg^{2+} (0.72 Å) and Li^+ (0.76 Å), one would expect these cations to exhibit site mixing, while the highly charged tungsten is expected to fully order, similar to the Li_5ReO_6 archetype. Powder neutron diffraction data would be required to correctly locate and quantify the amount of lithium in the structure, and aid identification of a likely secondary phase. For this reason the heavy atom site (Wyckoff site 2*a*) was assigned to be fully occupied with tungsten, and the three remaining cation sites were refined as a fraction of magnesium, due to the inaccuracy of identifying lithium using solely X-ray diffraction data. It was found that the *C*2/*m* model (Figure 3.9.2) (R_{wp} = 11.72%, R_{exp} = 6.07%, χ^2 = 3.73, in good agreement with the Le Bail fitting parameters) gave an equally good fit to the data as the non-centrosymmetric *Cm* cell, hence the higher symmetry *C*2/*m* cell was chosen, though ideally this would be confirmed with NPD. The refined lattice parameters were determined to be *a* = 5.15401(2) Å, *b* = 8.77578(1) Å, *c* = 5.10924(2) Å, β = 110.9171(3)°, *V* = 215.864(3) $Å^3$, which are similar to the unit cell parameters of $Li_{4.1}Ni_{0.9}WO_6$.

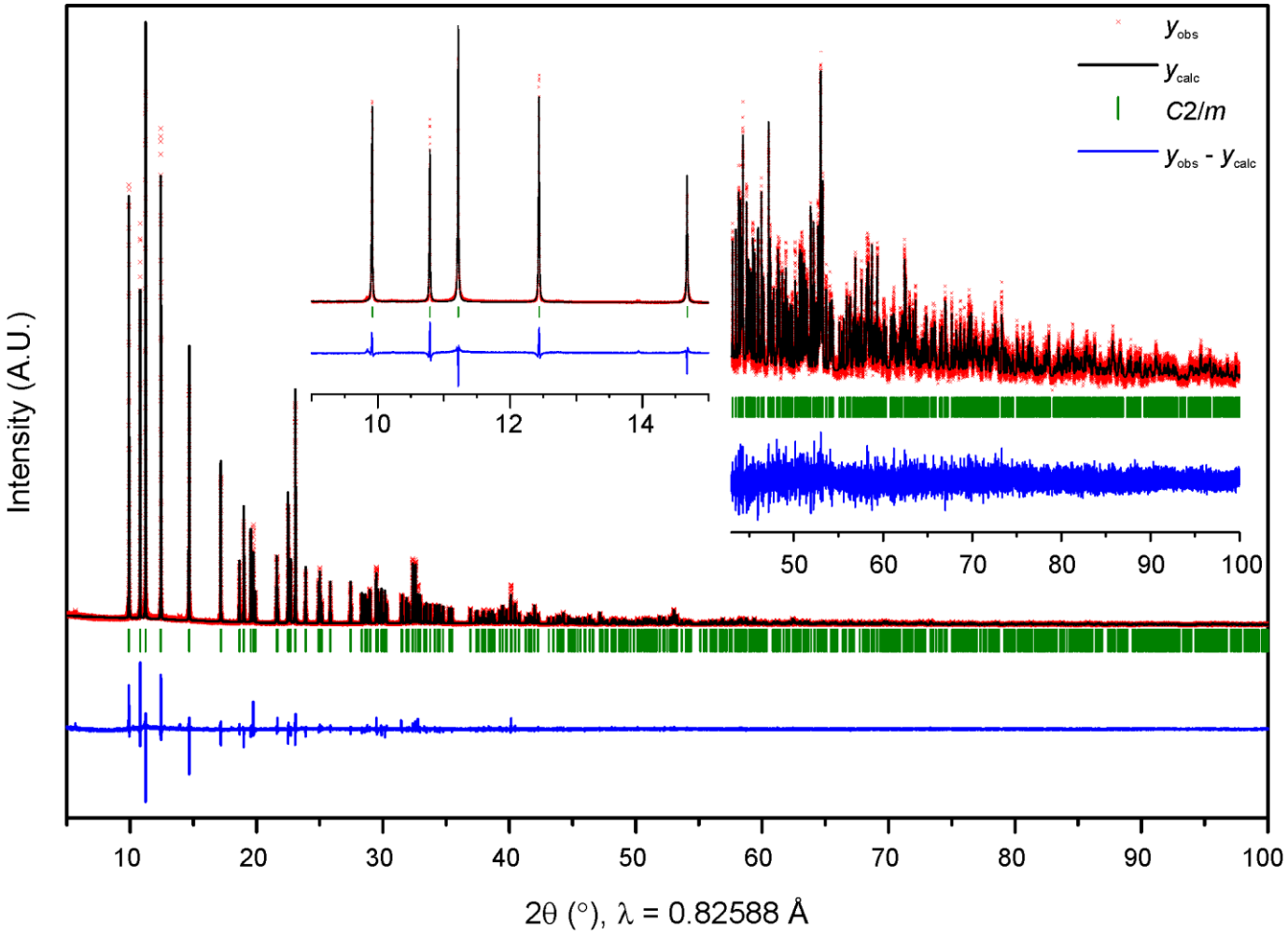

Figure 3.9.2: Rietveld refinement of SXRD (MAC) data of $Li_{4.08}Mg_{0.90}W_{1.02}O_6$; R_{wp} = 11.72%, R_{exp} = 6.07%, χ^2 = 3.73

3.10 Conclusions and Future Work

This work displays the synthesis and structural characterisation of new Li-rich rock-salt type materials of the form $Li_{4+x}Ni_{1-x}WO_6$; with partial cation ordering established by combined Rietveld analysis of high-resolution synchrotron and neutron powder diffraction data. Additionally a new Li-rich magnesium analogue with the formula $Li_{4.08}Mg_{0.90}W_{1.02}O_6$ has been synthesised and characterized using synchrotron data.

For the $Li_{4+x}Ni_{1-x}WO_6$ materials, the omission or inclusion of a molar excess of lithium during synthesis under identical conditions resulted in two distinct materials affording different coloured solids with different PXRD patterns. This suggested two different structures were formed which vary depending on the Li and Ni content of the main phases. By comparison of the ordering of the tungsten sites, it was established that Li_4NiWO_6 crystallised in the *C*2/*c* space group, which is compared to the orthorhombic $Li_3Ni_2TaO_6$ archetype. The material synthesised with an excess of lithium was found to be $Li_{4.1}Ni_{0.9}WO_6$ which crystallised in the non-centrosymmetric *Cm* space group, which is structurally comparable to the Li_5ReO_6 archetype and other known rock-salt superstructures with high lithium content such as Li_2MnO_3 and Li_4NiTeO_6. Due to the similarities in composition, the two new structures are thought to have little difference in their enthalpies of formation, largely depending on the Li:Ni ratio and therefore the average oxidation state of nickel.

Further neutron diffraction data on $Li_{4.15}Ni_{0.85}WO_6$ and $Li_{4.08}Mg_{0.90}W_{1.02}O_6$ would be desirable to allow the refinement of three cations per site, as was discovered in Li_4NiWO_6 and $Li_{4.1}Ni_{0.9}WO_6$. Furthermore, it would be interesting to try and isolate the hypothesised disordered *Fddd* analogue of Li_4NiWO_6, which was included to aid

modelling of the SXRD data, and consequentially obtain a phase pure *C*2/*c* Li_4NiWO_6. This may be achieved by exploration of synthetic temperature, cooling rates such as quenching *vs*. slow cooling or minor adjustments in the cation ratios. For example, fully ordered $LiNiO_2$ has proved difficult to synthesise due to Li^+/Ni^{2+} site mixing, with fully occupied lithium layers necessary for good electrochemical properties in LIB cathodes of the form $LiMO_2$.[32, 39]

The electrochemical testing of $Li_{4.15}Ni_{0.85}WO_6$ (in addition to Li_4NiWO_6 for comparison) is reported in Chapter 4, with the properties being linked back to the structures elucidated from the detailed structural analysis.

3.11 References

1. A. Boulineau, L. Croguennec, C. Delmas and F. Weill, *Chem. Mater.*, 2009, **21**, 4216-4222.
2. V. Kumar, N. Bhardwaj, N. Tomar, V. Thakral and S. Uma, *Inorg. Chem.*, 2012, **51**, 10471-10473.
3. V. B. Nalbandyan, M. Avdeev and M. A. Evstigneeva, *J. Solid State Chem.*, 2013, **199**, 62-65.
4. E. A. Zvereva, O. A. Savelieva, Y. D. Titov, M. A. Evstigneeva, V. B. Nalbandyan, C. N. Kao, J. Y. Lin, I. A. Presniakov, A. V. Sobolev, S. A. Ibragimov, M. Abdel-Hafiez, Y. Krupskaya, C. Jahne, G. Tan, R. Klingeler, B. Buchner and A. N. Vasiliev, *Dalton Trans.*, 2013, **42**, 1550-1566.
5. A. Gupta, V. Kumar and S. Uma, *J. Chem. Sci. (Bangalore, India)*, 2015, **127**, 225-233.
6. N. Bhardwaj, A. Gupta and S. Uma, *Dalton Trans.*, 2014, **43**, 12050-12057.
7. G. C. Mather, C. Dussarrat, J. Etourneau and A. R. West, *J. Mater. Chem.*, 2000, **10**, 2219-2230.
8. J. G. Fletcher, G. C. Mather, A. R. West, M. Castellanos and M. P. Gutierrez, *J. Mater. Chem.*, 1994, **4**, 1303-1305.
9. G. C. Mather, R. I. Smith, J. M. S. Skakle, J. G. Fletcher, M. A. Castellanos R, M. P. Gutierrez, A. R. West, G. C. Mather, R. I. Smith, J. M. S. Skakle, J. G. Fletcher, M. A. Castellanos R, M. P. Gutierrez and A. R. West, *J. Mater. Chem.*, 1995, **5**, 1177-1182.

10. M. Yoshio, T. Konishi, Y. M. Todorov and H. Noguchi, *Electrochemistry*, 2000, **68**, 412-414.

11. J. Cho, Y. Kim and M. G. Kim, *J. Phys. Chem. C*, 2007, **111**, 3192-3196.

12. M. Sathiya, K. Ramesha, G. Rousse, D. Foix, D. Gonbeau, K. Guruprakash, A. S. Prakash, M. L. Doublet and J. M. Tarascon, *Chem. Commun. (Cambridge, U. K.)*, 2013, **49**, 11376-11378.

13. N. Yabuuchi, Y. Tahara, S. Komaba, S. Kitada and Y. Kajiya, *Chem. Mater.*, 2016, **28**, 416-419.

14. T. Matsuhara, Y. Tsuchiya, K. Yamanaka, K. Mitsuhara, T. Ohta and N. Yabuuchi, *Electrochemistry*, 2016, **84**, 797-801.

15. E. McCalla, A. M. Abakumov, M. Saubanère, D. Foix, E. J. Berg, G. Rousse, M.-L. Doublet, D. Gonbeau, P. Novák, G. Van Tendeloo, R. Dominko and J.-M. Tarascon, *Science*, 2015, **350**, 1516-1521.

16. C. L. Zhao, Q. D. Wang, Y. X. Lu, Y. S. Hu, B. H. Li and L. Q. Chen, *J. Phys. D-Appl. Phys.*, 2017, **50**.

17. V. F. Sears, *Neutron News*, 1992, **3**, 26-37.

18. P. C. Murau, *Anal. Chem.*, 1961, **33**, 1125-1126.

19. B. J. Campbell, H. T. Stokes, D. E. Tanner and D. M. Hatch, *J. Appl. Crystallogr.*, 2006, **39**, 607-614.

20. H. M. Rietveld, *Acta Crystallogr.*, 1967, **22**, 151-152.

21. H. M. Rietveld, *J. Appl. Crystallogr.*, 1969, **2**, 65-71.

22. P. S. Halasyamani, *Chem. Mater.*, 2004, **16**, 3586-3592.

23. H.-S. Ra, K. M. Ok and P. S. Halasyamani, *J. Am. Chem. Soc.*, 2003, **125**, 7764-7765.

24. I. D. Brown, in *Bond Valences*, eds. I. D. Brown and K. R. Poeppelmeier, Springer Berlin Heidelberg, Berlin, Heidelberg, 2014, DOI: 10.1007/430_2012_89, pp. 11-58.

25. I. D. Brown, Accumulated Table of Bond Valence Parameters, http://www.iucr.org/resources/data/data-sets/bond-valence-parameters, (accessed September, 2016).

26. R. Shannon, *Acta Crystallogr. Sect. A*, 1976, **32**, 751-767.

27. J. B. Goodenough, D. G. Wickham and W. J. Croft, *J. Phys. Chem. Solids*, 1958, **5**, 107-116.

28. L. R. Morss, E. H. Appelman, R. R. Gerz and D. Martin-Rovet, *J. Alloys Compd.*, 1994, **203**, 289-295.

29. V. Massarotti, M. Bini, D. Capsoni, A. Altomare and A. G. G. Moliterni, *J. Appl. Crystallogr.*, 1997, **30**, 123-127.

30. S.-J. Oh, D. W. Lee and K. M. Ok, *Dalton Trans.*, 2012, **41**, 2995-3000.

31. L. S. Cahill, S. C. Yin, A. Samoson, I. Heinmaa, L. F. Nazar and G. R. Goward, *Chem. Mater.*, 2005, **17**, 6560-6566.

32. T. Ohzuku, A. Ueda and M. Nagayama, *J. Electrochem. Soc.*, 1993, **140**, 1862-1870.

33. R. G. Pearson, *J. Mol. Struct. (Theochem.)*, 1983, **103**, 25-34.

34. A. D. Walkingshaw, N. A. Spaldin and E. Artacho, *Phys. Rev. B*, 2004, **70**, 165110.

35. G. King and P. M. Woodward, *J. Mater. Chem.*, 2010, **20**, 5785-5796.

36. J. C. Knight and A. Manthiram, *J. Mater. Chem. A*, 2015, **3**, 22199-22207.

37. V. Kumar, A. Gupta and S. Uma, *Dalton Trans.*, 2013, **42**, 14992-14998.

38. L. D. Brownlee and E. W. J. Mitchell, *Proc. Phys. Soc. Sect. B*, 1952, **65**, 710.

39. C. Delmas, M. Menetrier, L. Croguennec, I. Saadoune, A. Rougier, C. Pouillerie, G. Prado, M. Grune and L. Fournes, *Electrochim. Acta*, 1999, **45**, 243-253.

Chapter 4: Electrochemical Behaviour of Li-Rich Rock-Salts with Partial Cation Order

4.1 Introduction

Research into Li-rich cathode materials has to date primarily revolved around layered $LiM'O_2$ structures incorporating layered rock-salt type $Li_2M^{(IV)}O_3$ structures (S.G. *C*2/*m* or *C*2/*c*, $M^{(IV)}$ = Mn, Sn, Ru, Ir, Ge, Mo),[1, 2] with the first reported example being $xLi_2MnO_3{\cdot}(1\text{-}x)LiNi_{1/3}Mn_{1/3}Co_{1/3}O_2$ with a capacity of ~220 mA·h g^{-1}. The mechanism responsible for the high capacity (exceeding those obtained from $LiNi_{1/3}Mn_{1/3}Co_{1/3}O_2$ alone, 190-170 mA·h g^{-1})[3] has over recent years been attributed to the role of oxygen within the Li_2MnO_3 domains.

The overall electrochemical extraction of Li^+ from Li_2MnO_3 has been explored experimentally and computationally and is thought to occur as follows: $Li_2MnO_3 \rightarrow 2Li^+ + 2e^- + \lambda\text{-}MnO_2 + O_2$.[4] The extraction of lithium is charge compensated by the removal of electrons from lattice oxygen, forming localised holes on the oxygen ($O^{2-} \rightarrow O^-$), which within this structure are calculated to not be thermodynamically stable, resulting in dimerisation into peroxo (O_2^{2-}) or superoxo (O_2^-) species.[5] The oxygen dimers $(O\text{-}O)^{n-}$ are further oxidised to form molecular oxygen, hence overall oxygen gas is released from the lattice upon delithiation following charging to ≥ 4.5 V. As lithium ions are extracted from the octahedral sites in the fully occupied Li layer, Mn^{4+} ions migrate into the now vacant lithium octahedral sites; the cation migration is facilitated by oxygen dimerisation. Upon re-lithiation, the Li^+ ions

tend to favour the neighbouring tetrahedral interstitial sites, promoting spinel formation primarily at the surface, leading to voltage fade.[6]

Li_2RuO_3 (isostructural with Li_2MnO_3) displays a reversible discharge capacity of ~220 mA·h g^{-1} between 2-4.6 V *vs.* Li^+/Li^0, despite a theoretical capacity based on the $Ru^{4+/5+}$ cationic redox couple of 164 mA·h g^{-1}.[7] The origin of the additional capacity was attributed to the formation and cycling of peroxo-type species (O_2^{2-}) from lattice oxygen, which becomes activated at a higher voltage than the oxidation of $Ru^{4+} \rightarrow Ru^{5+}$. The appearance of O_2^{2-} species was detected using XPS and EELS analysis, resulting in considerable distortion of the RuO_6 octahedra as determined from Ru K-edge EXAFS. Strong hybridisation of the Ru(4*d*) and O(2*p*) orbitals are thought to enable the anionic redox process to occur in addition to cationic redox by stabilisation of peroxo species, an effect which is not observed in Li_2MnO_3.[8] Li_2RuO_3 shows relatively poor capacity retention when charged to high potentials (~4.8 V *vs.* Li^+/Li^0), attributed to extensive distortion of RuO_6 octahedra on delithiation leading to structural instability.[9]

The anionic redox mechanism has been explored further in $Li_2Ru_{1-x}M_xO_3$ rock-salts where *M* = Mn, Sn and Ti. For example, the $Li_2Ru_{0.5}Mn_{0.5}O_3$ structure was determined to possess fully occupied Li layers alternating with $Li_{1/3}Ru_{1/3}Mn_{1/3}$ honeycomb-like layers with stacking faults, exhibiting a reversible capacity ≥ 200 mA·h g^{-1} at 3.6 V *vs.* Li^+/Li^0 (equivalent to the removal of 1.3 moles Li^+).[10] XPS analysis confirmed the reversibility of the anionic redox process (in addition to the reduction of some lattice oxygen to molecular O_2 gas) in addition to the $Ru^{4+/5+}$ cationic redox process. Through DFT calculations, the Ru^{5+} was determined to partially stabilise the hole on O^{2-} (*i.e.* O^-) through strong orbital hybridisation, suppressing (though not eliminating) the

recombination of O^- holes into O_2 gas and promoting reversible anionic redox. Although cycling stability is greater *cf.* Li_2MnO_3, voltage fade associated with cation migration to form a spinel-type structure was still observed, with a large first cycle irreversible capacity loss associated with O_2 gas loss from the oxide lattice.[11]

Conversely, in the $Li_2Ru_{1-x}Sn_xO_3$ system, the larger Sn^{4+} ion ($4d^{10}$, 0.69 Å *cf.* Mn^{4+}; $3d^3$, 0.53 Å) cannot migrate *via* tetrahedral sites to the vacant Li^+ octahedral sites upon delithiation, supressing structural transformation to a spinel-type phase thus minimising voltage fade while displaying a similar capacity to the Ru-Mn analogue. The presence of relatively weak Sn-O bonds is also thought to allow the stabilisation of O^- to condense to $(O\text{-}O)^{n-}$ ligands coordinated to Ru^{5+} with η^2 hapticity therefore re-stabilising the oxygen network.[12] While Li_2SnO_3 alone is not electrochemically active, the introduction of Sn^{4+} into Li_2RuO_3 has been shown to enhance the capacity retention *cf.* Li_2RuO_3 when charged to high potentials.[7, 12]

In contrast to Li_2RuO_3, charging of isostructural α-Li_2IrO_3 results in concomitant oxidation of O^{2-} to O_2^{n-} species and oxidation of Ir^{4+}, corresponding to the removal of one molar equivalent of Li^+. Such behaviour has been observed from a combination of O(1*s*) and Ir(4*f*) XPS, with visualisation of $(O\text{-}O)^{n-}$ dimers achieved using HAADF-STEM.[13] The β-Li_2IrO_3 polymorph (S.G. *Fddd*) also possesses a rock-salt type structure, but with stacking of Li_2Ir layers (as opposed to alternating Li and $Li_{1/3}Ir_{2/3}$ layers in the α-polymorph), resulting in a three-dimensional framework of edge-sharing IrO_6 octahedra.[14] β-Li_2IrO_3 has recently been demonstrated as the first example of simultaneous reversible cationic and anionic redox occurring in a structure without the presence of fully occupied Li-layers in the pristine material.[15]

Investigation into the stabilisation of anionic redox in Li-rich transition metal oxides is an important factor in improving the energy density of Li-ion batteries.[16] Based on extensive studies of layered Li_2MO_3-based systems, the fate of oxygen hole species (O^-, caused by oxidation of lattice oxygen upon charging) effectively depends on the crystal structure of the cathode material. For irreversible anionic redox, O^- can dimerise and oxidise irreversibly to molecular oxygen, resulting in irreversible capacity loss and often accompanied by cationic migration such as in Li_2MnO_3-based cathodes. Alternatively, O^- can directly react with and degrade carbonate-based electrolytes, resulting in rapid degradation of electrochemical performance.[17, 18] Therefore, for the anionic redox to be reversible (*i.e.* $2O^{2-} \leftrightarrow O_2^{n-}$), the O_2^{n-} species must be stabilised and remain coordinated to the metallic framework.[19] Oxygen evolution is supressed when metal-oxygen bonds display covalent character and are therefore strengthened, which commonly occurs using 4*d* or 5*d* metal centres, due to greater *M*4*d*/5*d*-O2*p* orbital hybridisation. This has been attributed to the delocalisation of the oxygen hole across the *M*-O and O-O bonds with covalent character, stabilising the peroxo bond.

Fully ordered Li metal oxides possessing fully occupied lithium layers between transition metal-containing layers were previously thought to be a requirement for highly reversible Li^+ (de)intercalation and good energy density, with minimal structural change during cycling. In these layered rock-salt materials, Li^+ deintercalates from the Li layers by hopping between octahedral sites, *via* tetrahedral sites, which are separate from the transition metal lattice. Through a combination of empirical and computational analytical methods on the Li-rich cation disordered $Li_{1.211}Mo_{0.467}Cr_{0.3}O_2$ system, materials possessing an excess of lithium have been shown to exhibit facile lithium-ion diffusion through an alternative Li-percolation

network, without the need for Li-layers.[20] Capacities of up to 300 mA·h g^{-1} have also been observed in $Li_{1.3}Nb_{0.3}Mn_{0.4}O_2$, a cation disordered lithium-rich rock-salt exhibiting cumulative cationic ($Mn^{3+} \rightarrow Mn^{4+}$) and anionic redox, which utilises Nb^{5+} ($4d^0$) for stabilisation of the redox reaction of lattice oxide ions.[21]

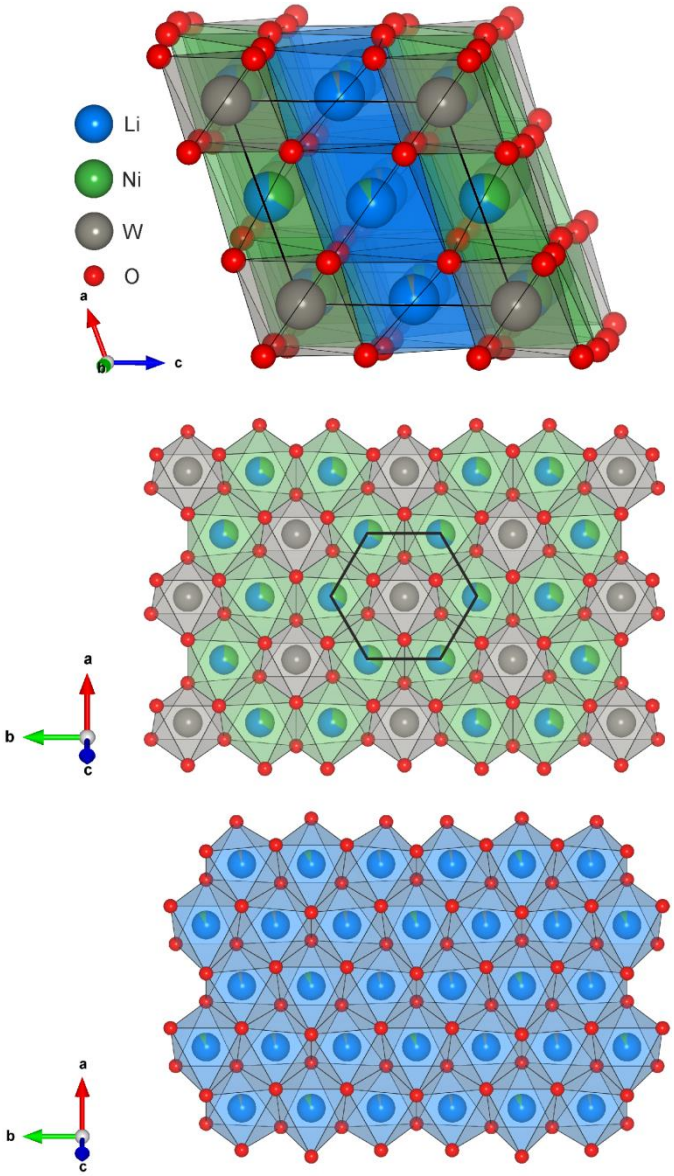

Figure 4.1.1: The rock-salt structure of $Li_{4.15}Ni_{0.85}WO_6$ viewed along the [010] direction (*top*); honeycomb-like ordering around W in the W/Ni-rich layer (*middle*) and the Li-rich mixed Li/Ni layer (*bottom*), viewed down the [111] direction of the equivalent rock-salt sub-cell

As established in Chapter 3, $Li_{4.15}Ni_{0.85}WO_6$ is a lithium-rich rock-salt type cathode exhibiting partial cation ordering, without fully occupied lithium layers. The presence of tungsten within LIB materials is as of yet unreported, most likely as it is expected to remain in the maximum +6 oxidation state at conventional LIB operating voltages and is therefore anticipated to simply increase the overall mass of the cell. The rapid emergence of detailed research over recent years into the observation of cumulative cationic and anionic redox processes within lithium-rich cathodes has determined that fully occupied Li layers are not deemed necessary to access the anionic redox, and the presence of heavy 4*d*/5*d* metals can assist in the stabilisation of this process, primarily attributed to orbital overlap effects. Of course, there are a number of other factors influencing this complicated redox process, such as local coordination environment and cation migration which are difficult to thoroughly explore experimentally in battery materials.[22] Considering numerous reports of stable tungsten peroxo and superoxo species,[23-26] $Li_{4.15}Ni_{0.85}WO_6$ is expected to exhibit cationic redox (from the nickel ions) and stabilisation of the overall structure and the peroxo species (by $5d^0$ W^{6+}) to enhance the reversibility of anionic redox, despite only partial ordering of cations.

The performance of $Li_{4.15}Ni_{0.85}WO_6$ as a Li-ion battery cathode was assessed by electrochemical cycling and *ex-situ* SXRD, XANES and XPS spectroscopy to provide evidence for anionic redox processes being stabilised in this material. Nickel is chosen as the electrochemically active transitional metal ion with the ability to employ the Ni^{4+}/Ni^{2+} redox couple to drive Li^+ deintercalation, with W^{6+} providing electroneutrality and structural stability to the rock-salt based structure and allowing the influence of a $5d^0$ metal on the electrochemical properties to be investigated.

4.2 Experimental Methods

4.2.1 Synthesis of Li-Rich Metal Tungsten Oxides

The synthesis and structural characterisation of materials discussed in this chapter ($Li_{4.15}Ni_{0.85}WO_6$ and Li_4NiWO_6) are discussed in detail in Chapter 3. For $Li_{4.15}Ni_{0.85}WO_6$, the starting materials were mixed using the planetary mill prior to heating to ensure homogenous mixing of the large batch of materials for testing.

4.2.2 Post-Synthetic Ball Milling

Additional processing was necessary in order to successfully cast these cathode materials onto the aluminium current collectors to produce coin cells for testing. The particle size was reduced further by milling in the planetary mill using isopropanol and 5 mm diameter zirconia balls at 350 rpm for 2 h. PXRD before and after this additional milling step confirmed the structure of the material was retained.

4.2.3 Powder X-Ray Diffraction

High resolution synchrotron powder diffraction data (SXRD) were collected at the I11 beamline at Diamond Light Source at the Harwell Science and Innovation Campus in Oxfordshire, UK; thanks to Dr Chui Tang and Dr Sarah Day. A wide-angle position sensitive detector (PSD) was used for collection of $Li_{4.15}Ni_{0.85}WO_6$ *ex-situ* cycled data. Thanks to Dr Michael Pitcher for assistance with analysis of this data.

4.2.4 SEM Imaging

Surface imagining of the particles was achieved using a Hitachi S-4800 Field-Emission Scanning Electron Microscope operating at an accelerating voltage of 5-10 kV. The samples were sputter-coated with gold nanoparticles to aid conduction.

4.2.5 Cathode Coin Cell Testing

Coin cells were assembled as detailed in Chapter 2. Galvanostatic cyclability measurements were carried out between 1-5 V at a C/10 charge/discharge rate (where (where 1C = 100 mA g^{-1}). For the rate capability measurements, initial C-rate was C/10 for the first ten cycles, then the C-rate was adjusted every five cycles to C/4, C/2, 1C, C/10 between 1 and 5 V for 30 cycles in total. The cathode composition was 80% active material, 10% PVDF binder and 10% Super C carbon by weight. Thanks go to Dr Nicholas Drewett, Jose Coca-Clemente and Professor Laurence Hardwick (University of Liverpool) for supplying the electrochemical testing data and assistance with interpretation.

4.2.6 X-Ray Absorption Near Edge Structure (XANES) Spectroscopy

XANES spectroscopy was employed to observe the Ni K-edge (excitation of 1*s* electron) and W L_3-edge (excitation of 2*p* electron) of the cathode of nominal composition $Li_{4.15}Ni_{0.85}WO_6$ after being charged/discharged to certain voltages of the first and second electrochemical cycle. Coin cells were prepared and cycled to appropriate points in the first and second electrochemical cycle, and disassembled in an argon-filled glove box. The electrolyte was washed from the cathode casts, which were subsequently heat-sealed into polyethylene (PE)-lined aluminium foil bags to prevent exposure to air and moisture. Samples were measured in transmission mode at the B18 beamline at Diamond Light Source at the Harwell Science and Innovation Campus in Oxfordshire, UK, with assistance from Dr. Giannantonio Cibin (beamline scientist) and Professor Alan Chadwick (University of Kent, UK).

4.2.7 X-Ray Photoelectron Spectroscopy (XPS)

Ex-situ XPS experiments were performed in a standard ultra-high vacuum surface science chamber consisting of a PSP Vacuum Technology electron energy analyser (angle integrating ± 10°) and a dual anode Mg Kα (1253.6 eV) X-ray source. The base pressure of the system was 2×10^{-10} mbar, with hydrogen as the main residual gas in the chamber. Calibration of the spectrometer for the quantification and analysis of oxidation states of Li(1*s*), Ni(2*p*), W(4*f*) and O(1*s*) was achieved using Au $4f_{7/2}$ energy level (83.9 eV). The XPS spectra were fitted using Voigt functions after Shirley background removal with an overall resolution of 0.2 eV. A transfer chamber allowed loading of the cycled samples in an argon-filled glove box to be transferred to the instrument without exposure to the atmosphere. XPS data was collected at the Stephenson Institute of Renewable Energy, University of Liverpool, by Jose Coca Clemente.

4.2.8 Hard X-Ray Photoelectron Spectroscopy (HAXPES)

The HAXPES technique requires a synchrotron source to obtain hard X-rays. Similar to XPS, it is used to analyse electronic states, however the higher energy of X-rays allows a probing depth into the bulk typically 10-15 nm below the surface. This technique was utilised *ex-situ* to examine the O 1*s* electronic states in the bulk of $Li_{4.15}Ni_{0.85}WO_6$ after being charged/discharged to certain voltages of the first electrochemical cycle. Analysis by HAXPES was performed on the P09 beamline of the Petra III synchrotron at the DESY facility in Hamburg, Germany with assistance from Dr Andrei Hloskovsky.

4.3 Electrochemical Behaviour

Due to the presence of the $Li_{0.3}Ni_{0.7}O$ impurity in the $Li_{4.1}Ni_{0.9}WO_6$ material, additional batches of $Li_{4.15}Ni_{0.85}WO_6$ were synthesised (as reported in Section 3.2.3), which appeared phase pure by PXRD, for cathode testing. Some preliminary electrochemical testing was also performed on the Li_4NiWO_6 phase, but due to the more desirable electrochemical properties of the Li-rich material, further characterisation was performed on $Li_{4.15}Ni_{0.85}WO_6$.

The electrochemical behaviour of these materials was evaluated by galvanostatic cycling of coin cells between 1-5 V and cyclic voltammetry. Firstly, the theoretical specific capacity for each material was calculated, based on a purely cationic redox whereby the nickel is the only redox active metal. Upon charge, it is expected that the average nickel oxidation state will increase (from +2 to +4 in the bulk material) which will drive the deintercalation of one Li^+ ion per electron removed from the redox active metal. The theoretical specific capacity of Li_4NiWO_6 (M_r 366.3 g mol^{-1}) was calculated to be 146 mA·h g^{-1}. For $Li_{4.15}Ni_{0.85}WO_6$, the average bulk oxidation state of nickel was calculated to be +2.18, and accounting for the ratio of Li:Ni in this material, full oxidation to Ni^{4+} corresponds to the removal of 1.55 Li per formula unit. The theoretical specific capacity of $Li_{4.15}Ni_{0.85}WO_6$ was calculated to be 116 mA·h g^{-1} as shown in Equation 4.3.1.

$$M_r\ (Li_{4.15}Ni_{0.85}WO_6) = 358.5\ g\ mol^{-1}$$

$$\text{Faraday constant, } F = e \times N_A = 96485.3\ C\ mol^{-1}$$

$$1.55 \times F = 149263\ C\ mol^{-1}$$

$$3.6\ C \equiv 3.6\ A{\cdot}s \equiv 1\ mA{\cdot}h$$

$$\frac{149263\ C\ mol^{-1}}{3.6\ C} = 41462\ mA{\cdot}h\ (\text{per mol of charge})$$

$$\frac{41462\ mA{\cdot}h}{358.5\ g} = \underline{116\ mA{\cdot}h\ g^{-1}}$$

Equation 4.3.1: Calculation of theoretical specific capacity of $Li_{4.15}Ni_{0.85}WO_6$

Extraction of all lithium from $Li_{4.15}Ni_{0.85}WO_6$ would give a capacity of 310 mA·h g^{-1}.

4.3.1 Capacity and Cyclability of Li_4NiWO_6

Electrochemical testing of Li_4NiWO_6 as a Li-rich cation disordered LIB cathode material was performed at a discharge rate of C/10 between 1-5 V using the coin cell set up. The material was cast without ball-milling post synthesis. The initial discharge capacity was 29 mA·h g^{-1}, increasing to 89 mA·h g^{-1} on the second electrochemical cycle (Figure 4.3.1). This suggests that some extensive structural rearrangement may be occurring during the first cycle, which may be a result of the presence of W^{6+} in every layer of the rock-salt material blocking a proportion of Li^+ diffusion channels. This also may explain why the practical specific capacity is considerably lower than the calculated theoretical capacity based on the removal of two lithium ions per nickel ion. This material displayed a relatively low capacity retention of 60% from the 2nd to 20th cycle.

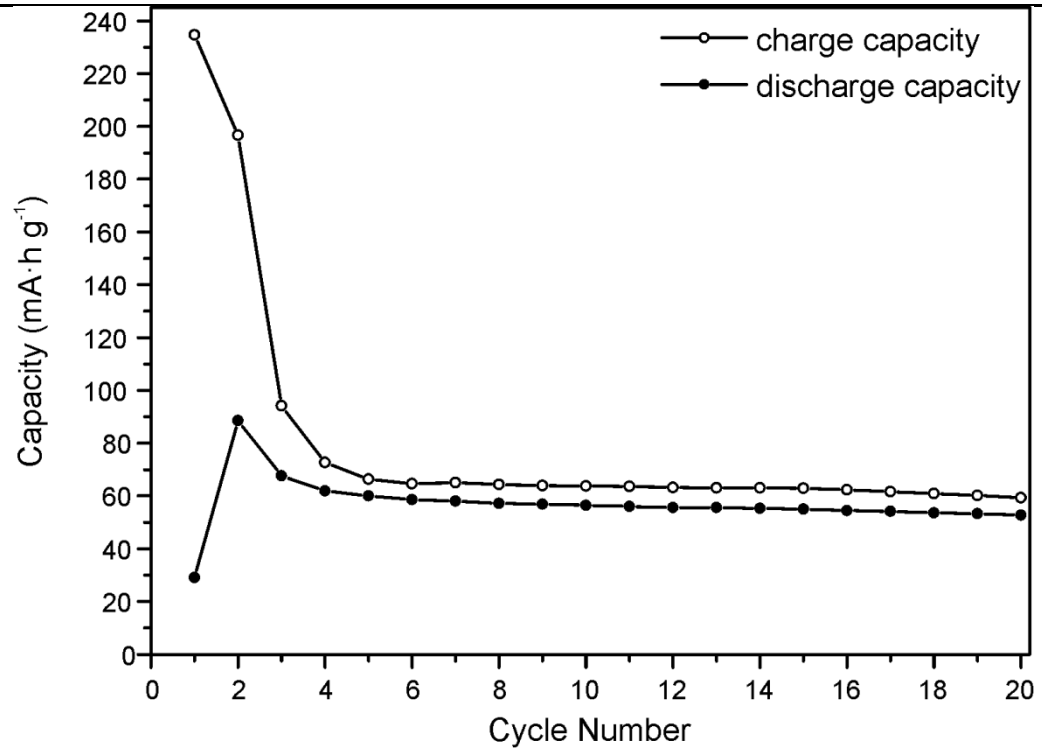

Figure 4.3.1: Galvanostatic cycling of Li_4NiWO_6 (no post synthetic ball milling) over 20 electrochemical cycles between 1-5 V at a C-rate of C/10

Despite the cation disorder, the material still exhibits a reversible capacity, attributed to it being rich in lithium.[20] No further electrochemical testing was undertaken on Li_4NiWO_6.

4.3.2 Cathode Testing of $Li_{4.15}Ni_{0.85}WO_6$ Before Ball Milling

The capacity and cyclability of $Li_{4.15}Ni_{0.85}WO_6$ was tested as a coin cell, cycled galvanostatically between 1-5 V at a discharge rate of C/10. Before the post-synthetic ball-milling process, the material had an initial discharge capacity of 126 mA·h g^{-1}, with considerable irreversible capacity loss observed over the first few cycles. The capacity plateaus to ~91 mA·h g^{-1} on the seventh electrochemical cycle, with remarkable capacity retention of ≥98.5% (*cf*. other reported Li-rich cathodes) between

the 7^{th}-45^{th} cycles (Figure 4.3.2), comparable to the calculated theoretical capacity of 116 mA·h g^{-1}.

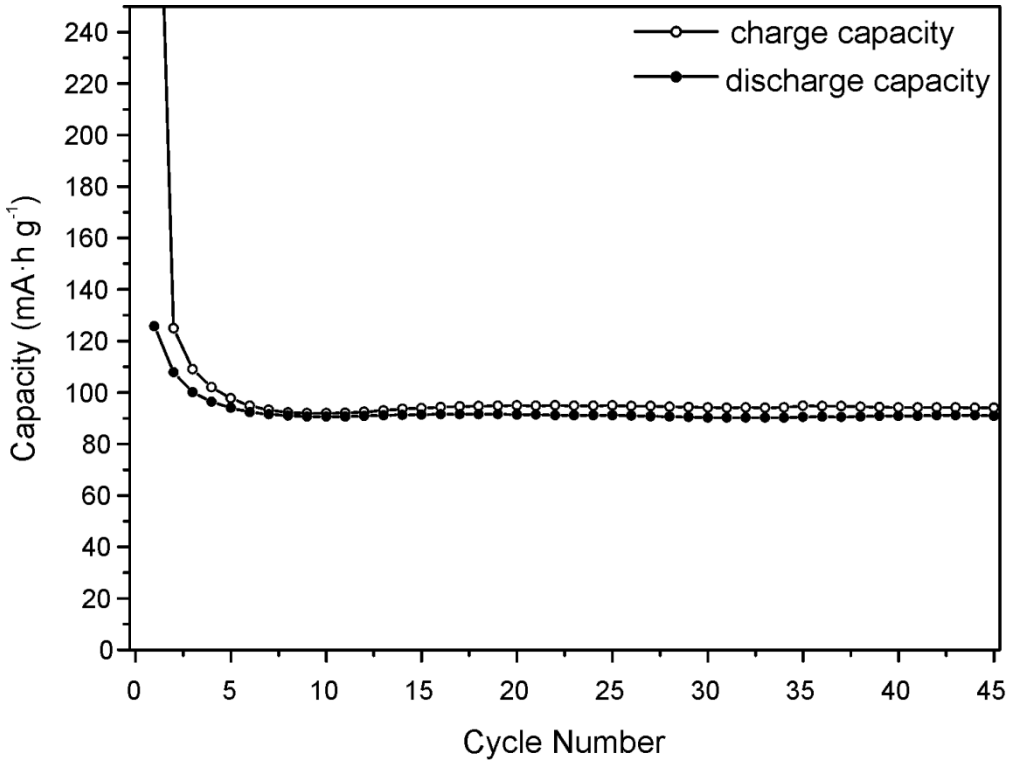

Figure 4.3.2: Galvanostatic cycling of $Li_{4.15}Ni_{0.85}WO_6$ (no post synthetic ball milling) over 45 electrochemical cycles between 1-5 V at a C-rate of C/10

The rate capability of this material was also tested, whereby the discharge rate was increased systematically for five cycles over the same voltage window then returned to the original C/10 discharge rate (Figure 4.3.3). The specific capacity of the material returns to ~91 mA·h g^{-1} after cycling at higher discharge rates, which indicates that although the capacity extracted from the material is lower at higher discharge rates as expected, discharging at higher rates does not irreversibly damage the material or cell components. This material afforded a reasonable rate capability (meaning the capacity extracted at high rates is still reasonable) with good capacity retention, suggesting the

diffusion of lithium ions through the material is not particularly hindered by the cation mixing.

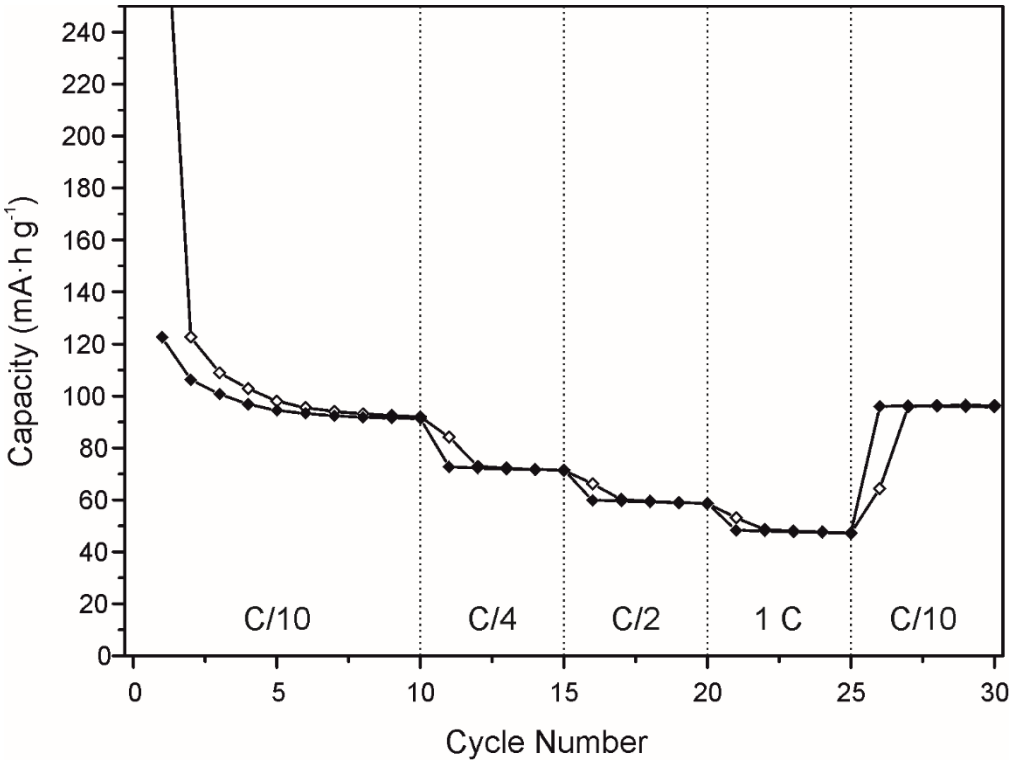

Figure 4.3.3: Rate capability testing of $Li_{4.15}Ni_{0.85}WO_6$ (no post synthetic ball milling), whereby the C-rate was varied as indicated**.** *Open* symbols indicate charge capacity, *filled* symbols indicate discharge capacity

4.3.3 Cathode Testing of $Li_{4.15}Ni_{0.85}WO_6$ After Ball Milling

Before ball-milling of $Li_{4.15}Ni_{0.85}WO_6$, the particle size was found to be typically between 5-20 μm from SEM imaging with a roughened surface composed of smaller particles (Figure 4.3.4).

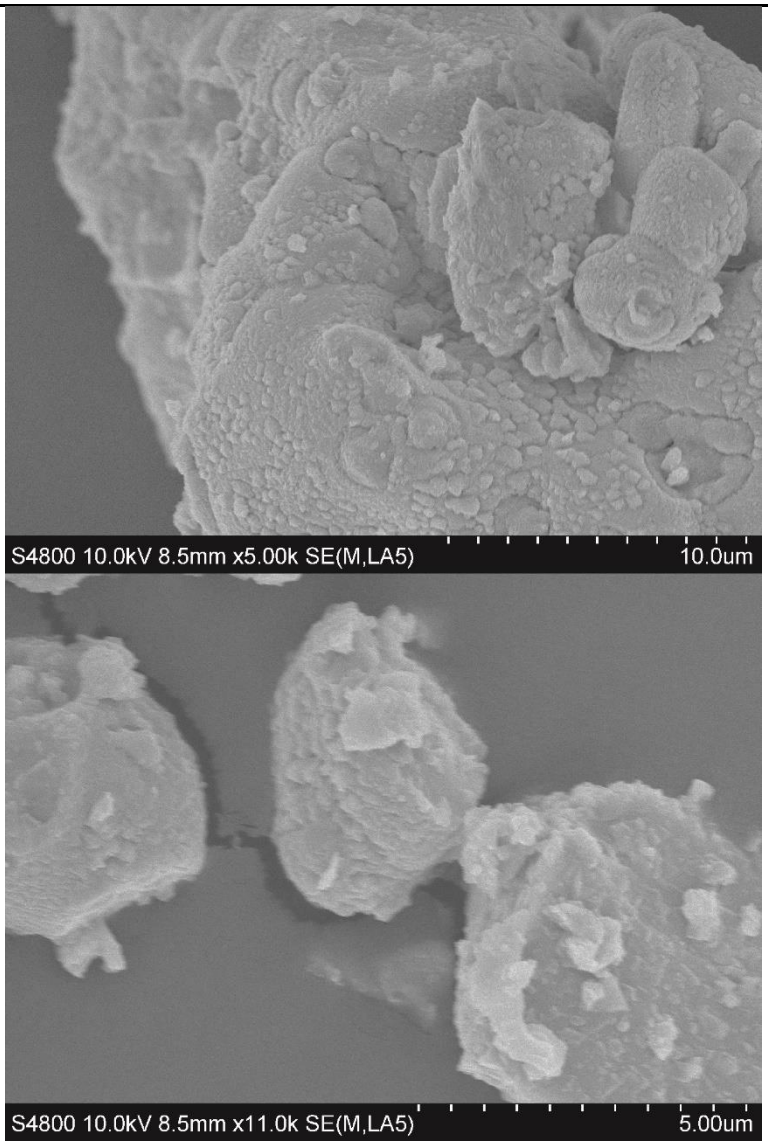

Figure 4.3.4: SEM images of as-synthesised $Li_{4.15}Ni_{0.85}WO_6$ displaying large, micrometre-sized particles

Larger particles are typically obtained by the solid state synthetic route without any additional processing, and usually display poorer Li^+ diffusion kinetics compared to a smaller particle size. The particle size of $Li_{4.15}Ni_{0.85}WO_6$ was reduced by planetary milling of the material to examine the effects on the electrochemical capacity and rate capability as detailed in Section 4.2.2. The particle size and morphology post-milling was examined using SEM imaging (Figure 4.3.5), exhibiting near-spherical grains of

200-300 nm in diameter, aggregated into larger more angular particles up to 5 μm in size.

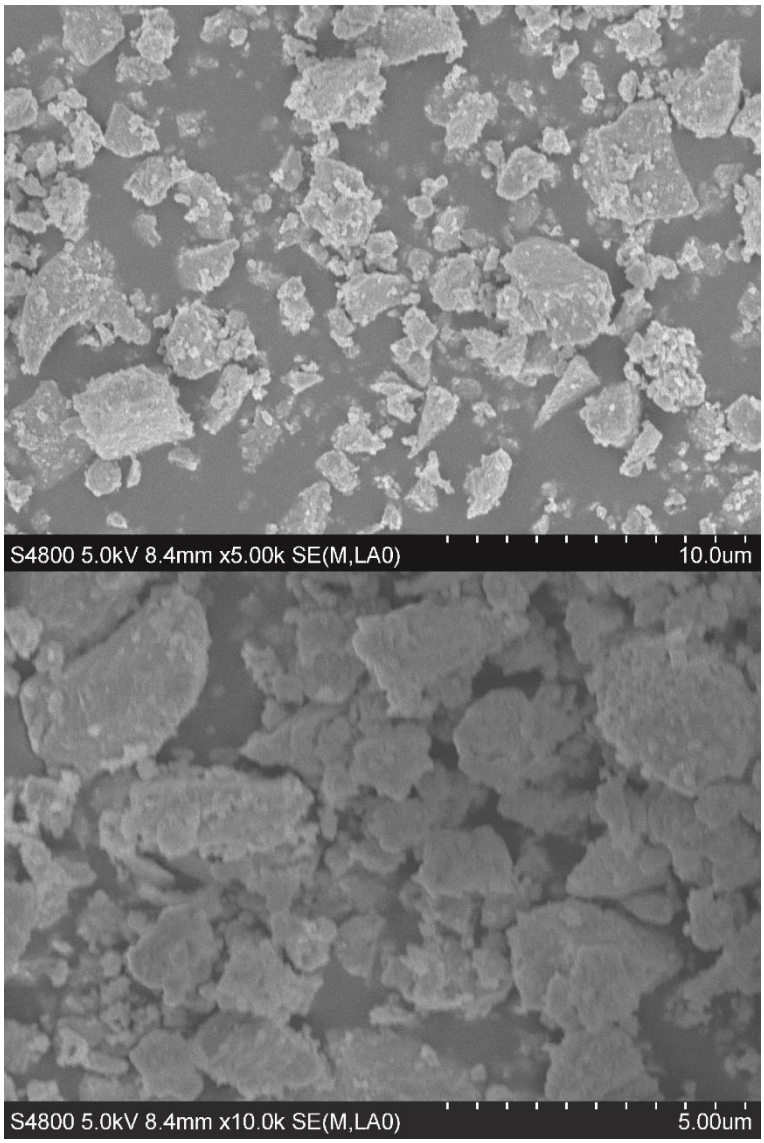

Figure 4.3.5: SEM images of $Li_{4.15}Ni_{0.85}WO_6$ ball-milled post synthesis displaying angular micrometre-sized particles with smaller spherical particles on the surface

The same cathode testing conditions were applied to the milled sample, and it was found that increasing the surface area by reduction of particle size increases the initial discharge capacity by >64%, which most likely indicates that surface reactions are in part responsible for the high capacity of $Li_{4.15}Ni_{0.85}WO_6$. The initial discharge capacity

of the ball-milled material is 202 mA·h g^{-1} (Figure 4.3.6), which is comparable to Li_2MnO_3-NMC composites and $LiNi_{0.8}Co_{0.15}Al_{0.05}O_2$ (NCA).[27, 28] The overall discharge capacity retention over 44 cycles is 59%; however the capacity begins to diminish after ~24 cycles (Figure 4.3.6). The reversible discharge capacity is therefore taken as 173 mA·h g^{-1}, corresponding to 86% capacity retention over 24 cycles, which is a reasonable retention for cycling over an unconventionally wide voltage window (1-5 V).

The considerable difference between the charge and discharge capacity may be indicative of extensive structural rearrangements or side-reactions with the electrolyte, as it suggests more Li^+ is extracted from $Li_{4.15}Ni_{0.85}WO_6$ than is reinserted. The difference in charge/discharge capacities begins to converge after the ~24^{th} cycle, where both begin to rapidly fade, which could indicate structural degradation of the cathode. Galvanostatic cycling indicated that charging to a high potential (5 V) and deep discharge (1 V) was necessary to extract the maximum capacity from this material as shown in Figure 4.3.8. These potentials lie beyond the stability window of the electrolyte (as discussed in Chapter 1), which promotes parasitic reactions with carbonate-based electrolytes causing detriment to the electrochemical performance, which is accelerated with a smaller particle size (see Chapter 6).[29]

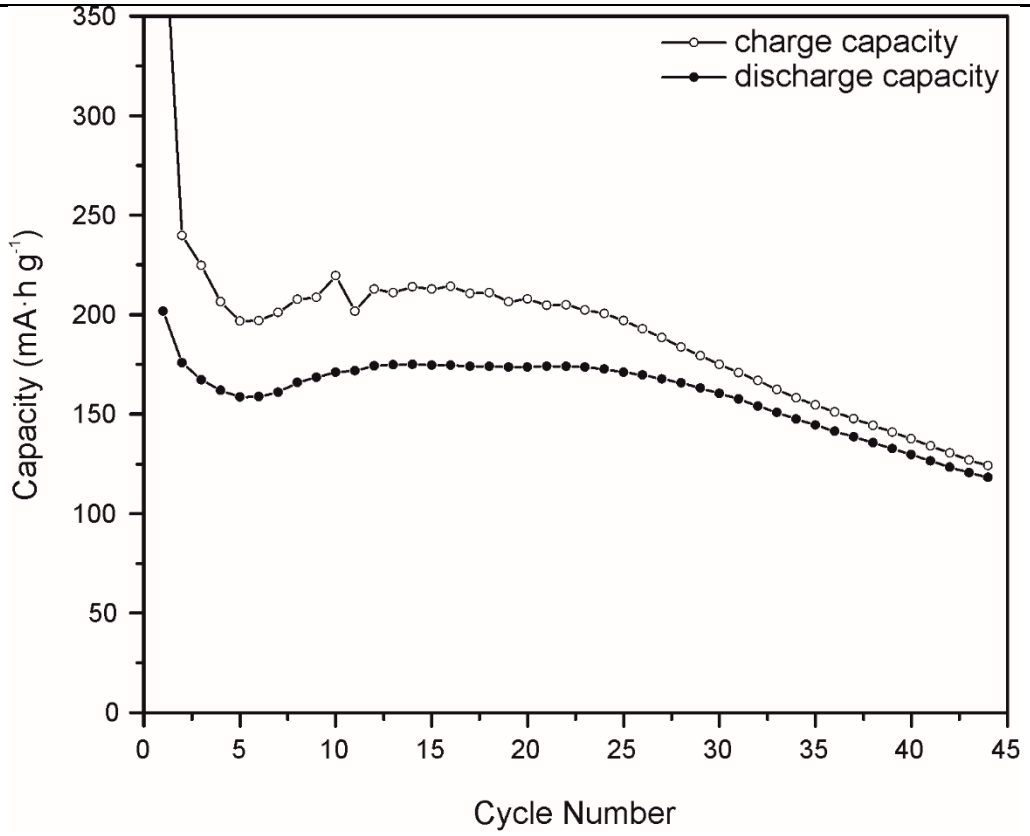

Figure 4.3.6: Galvanostatic cycling of ball-milled $Li_{4.15}Ni_{0.85}WO_6$ over 44 electrochemical cycles between 1-5 V at a C-rate of C/10

Ball-milled $Li_{4.15}Ni_{0.85}WO_6$ shows good capacity retention when discharged at higher C-rates (Figure 4.3.7), and on return to the low discharge rate of C/10, the capacities return to the expected level. The higher C-rates also appear to minimise the difference between the charge and discharge capacities, suggesting improved Li^+ and electronic conduction when discharged using higher currents.

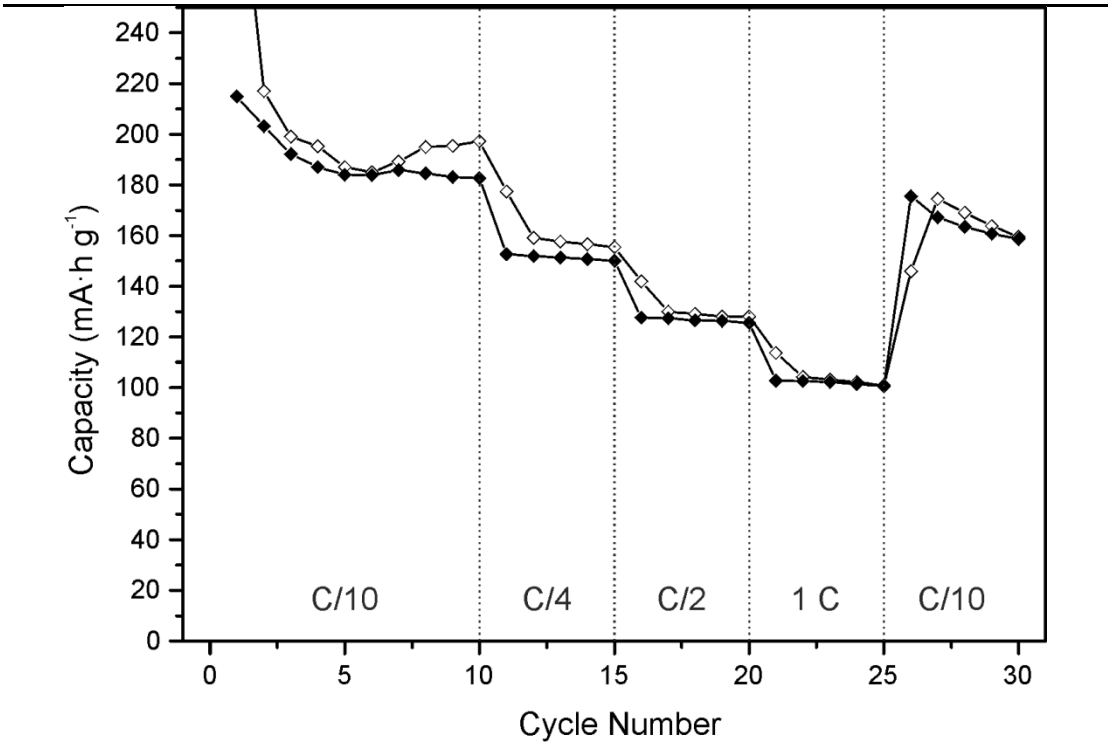

Figure 4.3.7: Rate capability measurements of $Li_{4.15}Ni_{0.85}WO_6$ over 30 cycles with the C-rate varied as indicated. *Open* symbols indicate charge capacity, *filled* symbols indicate discharge capacity

The effect of ball-milling on the rate capability is reported in Table 4.3.1.

Table 4.3.1: Comparison of the rate capability of $Li_{4.15}Ni_{0.85}WO_6$ before (*pre BM*) and after (*post BM*) ball-milling

Rate Capability									
C-rate	**C/10**			**1C**			**C/10**		
	Discharge capacity of n^{th} cycle (mA·h g^{-1})								
	1st	**10th**	**Retention (%)**	**21st**	**25th**	**Retention (%)**	**26th**	**30th**	**Retention (%)**
pre BM	122.6	91.3	74.4	48.2	47.1	97.7	95.9	95.7	99.7
post BM	214.9	182.6	85.0	102.8	100.6	97.8	175.5	158.7	90.4

Reduction of particle size has been shown to enhance the performance of $Li_2MnO_3{\cdot}LiMO_2$ cathode systems due to the slow reaction kinetics for the oxidation of

oxide ions.[30] Here we have demonstrated that reducing the particle size and testing the cathode under the same conditions greatly enhances the capacity, suggesting surface reactions may be play a key role in Li^+ (de)intercalation. Unfortunately, the reduction in particle size also results in a more rapid capacity fade during long cycling. For comparison, the cycling of Li_4NiTeO_6 (which possesses fully occupied Li^+ layers, with the same Te site ordering as W in $Li_{4.15}Ni_{0.85}WO_6$, see Chapter 3) between 2-5 V results in the initial discharge capacity of 110 mA·h g^{-1} diminishing to ~5 mA·h g^{-1} after just 40 cycles.[31] This poor capacity retention of Li_4NiTeO_6 was found to be due to evolution of oxygen gas from the system following additional research into its electrochemical behaviour.[32] The poor electrochemical performance of $LiNiO_2$ as a cathode material is largely a result of capacity fade due to the migration of Ni^{2+} ions into the lithium layers, which blocks the lithium diffusion channels and hinders further deintercalation of lithium upon subsequent cycles.[33] However it has been shown that Li-rich materials displaying partial cation disorder, as was observed in $Li_{4.15}Ni_{0.85}WO_6$ (from the Rietveld refinement of the related $Li_{4.1}Ni_{0.9}WO_6$ material in Chapter 3), the presence of an excess of lithium facilitates the diffusion of lithium ions throughout the material *via* a different Li-ion percolation network.[20] This suggests that the partial cation ordering in $Li_{4.15}Ni_{0.85}WO_6$ is not a significant contributing factor in the observed capacity fading. From here on, the electrochemical characterisation focusses on the post-synthesis ball-milled $Li_{4.15}Ni_{0.85}WO_6$ material due to the superior discharge capacity.

The charge-discharge profiles of numerous cycles were examined to observe the voltages at which plateaus occur which is representative of lithium (de)intercalation (Figure 4.3.8).

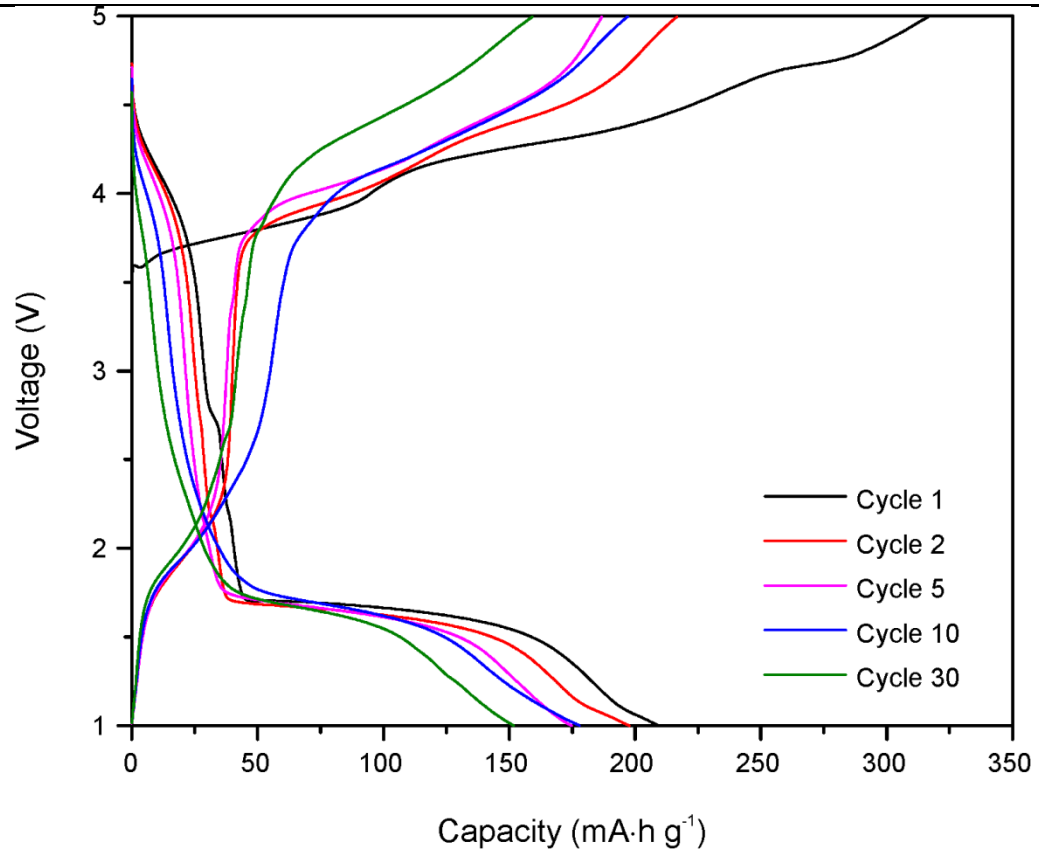

Figure 4.3.8: Galvanostatic charge-discharge profiles (at C/10 C-rate) of selected cycles of $Li_{4.15}Ni_{0.85}WO_6$

A large voltage hysteresis is present in this material, with the majority of lithium extraction occurring ~4 V and reinserting around 1.5 V, resulting in a poor energy density overall, despite the relatively high capacity. This large voltage polarisation indicates a high kinetic barrier towards lithium reinsertion, perhaps due to stabilisation of the oxidised structure *e.g.* through coordination of $(O_2)^{2-}$ dimers to tungsten resulting in $WO_4(O_2)$ moieties.

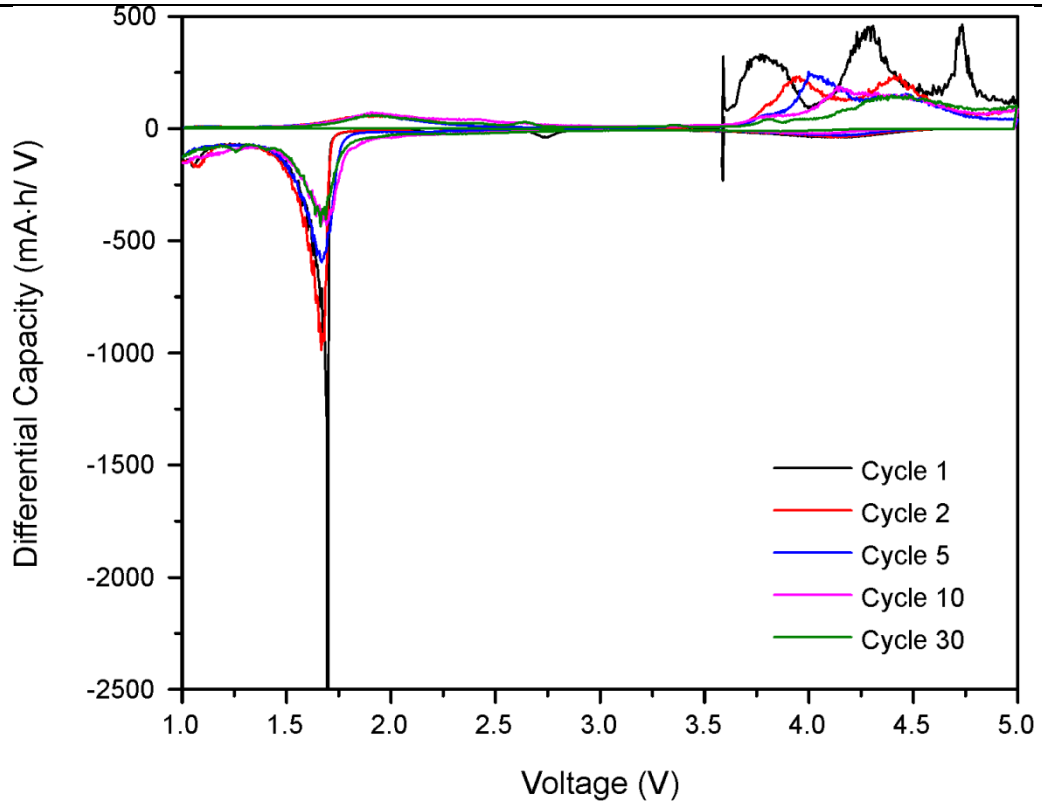

Figure 4.3.9: Differential capacity plots obtained from the charge-discharge profiles of selected cycles of $Li_{4.15}Ni_{0.85}WO_6$

The differential capacity plots clearly display the voltages at which processes contributing to charge/discharge capacity occur (Figure 4.3.9). It can be seen that the first cycle has a very different profile to subsequent cycles, with three distinct Li^+ extraction processes occurring at ~3.7 V, 4.2 V and 4.7 V charge. Upon discharge from 5 V, Li^+ intercalation occurs over the broad voltage range of 4.5-3.5 V discharge, an additional process at 2.8 V discharge and a significant amount of intercalation at ~1.6 V. On the second charge cycle, two Li^+ extraction processes are evident at ~3.9 V and 4.5 V and the process at 2.8 V discharge is no longer present. By the fifth cycle, a broad Li^+ extraction process occurs at ~1.8 V charge. The differential capacity plots suggest a number of different species are responsible for electrochemical activity and the voltages at which these processes occur shift upon subsequent cycling. This voltage

shift indicates the energy required for extraction of lithium ions changes over a number of cycles, which may be indicative of structural rearrangements *via* cationic migration occurring over long cycling.[34]

4.3.4 *Ex-Situ* Analysis

The specific discharge capacity for $Li_{4.15}Ni_{0.85}WO_6$ remains above the theoretical value calculated for a solely cation redox based on the $Ni^{2.18+} \rightarrow Ni^{4+}$ oxidation. For this reason, the mechanisms involved in the (de)intercalation of lithium ions from this material were explored further using a combination of *ex-situ* analyses. Samples were obtained by charging coin cells to the voltages marked on Figure 4.3.10 on the first or subsequent cycle, and the cathode materials were separated for analysis as described in Section 4.2.6.

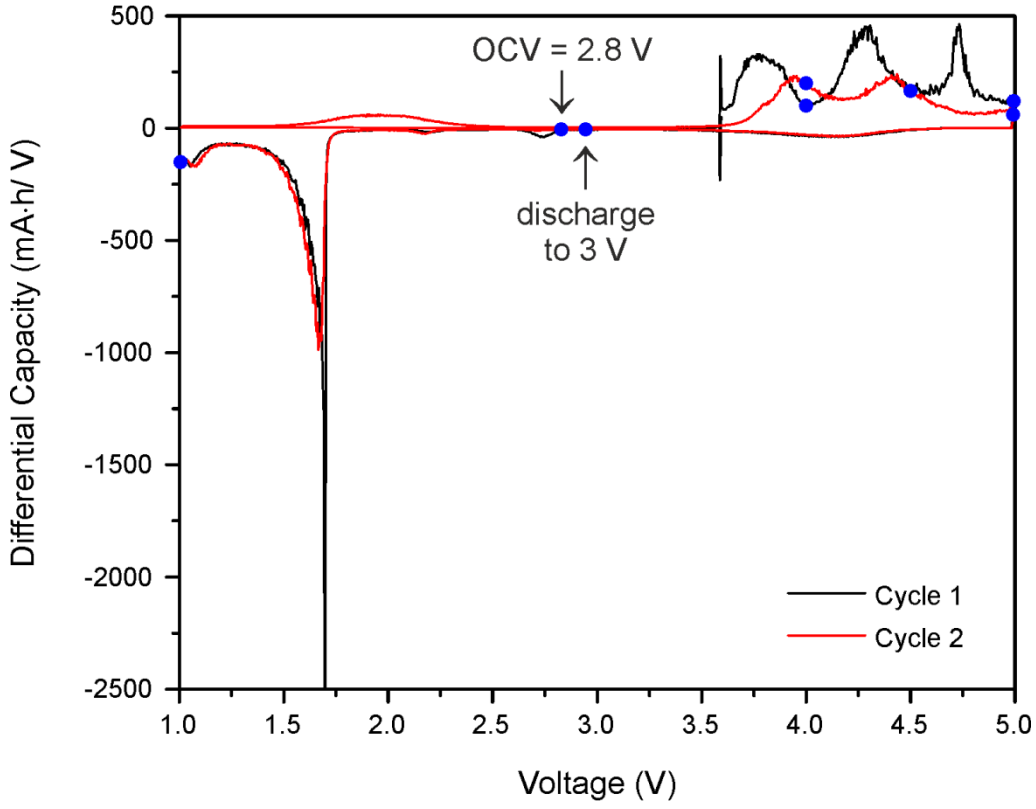

Figure 4.3.10: Differential capacity plots of first and second electrochemical cycle, marking the voltages (●) which were examined for *ex-situ* analysis

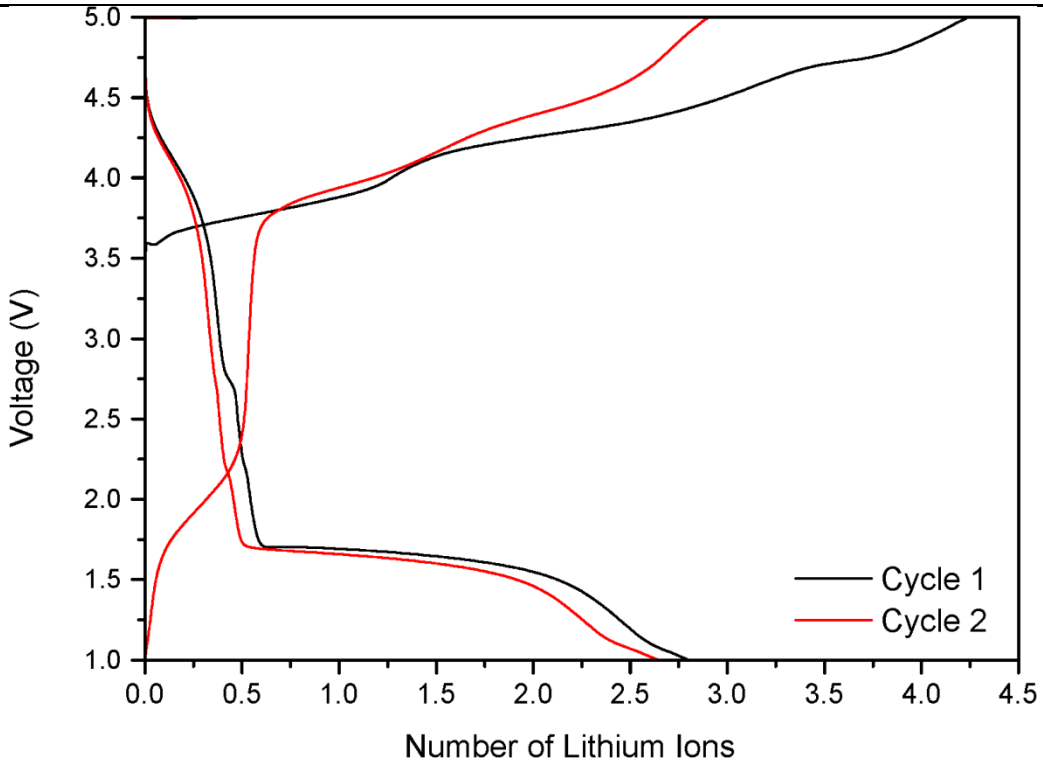

Figure 4.3.11: Charge-discharge profiles for the first and second electrochemical cycles with the specific capacity represented as the number of moles of Li^+ ions per formula unit extracted from (on charge) and reinserted into (on discharge) $Li_{4.15}Ni_{0.85}WO_6$

By equating the capacity observed with the corresponding number of Li^+ ions per formula unit of $Li_{4.15}Ni_{0.85}WO_6$, all of the lithium (4.24 mol) is extracted from the structure upon charging to 5 V, and only 2.8 Li^+ are re-intercalated by the end of the first cycle (Table 4.3.2). It is worth noting that the charge capacity may be slightly greater than the maximum number of Li^+ ions in the material (the as-synthesised material was determined by ICP to have a cation composition of $Li_{4.19(8)}Ni_{0.82(1)}W_{0.99(4)}$ to 1σ, see Chapter 3), which is attributed to capacity contributions from electrolyte and/or anodic side reactions. This means almost a third of lithium ions are irreversibly lost from the cathode during the first charge alone, most likely depositing within the SEI layer at the anode. An irreversible capacity loss of ~1/3 from the first charge to

first discharge capacity is typical of Li-rich layered cathodes, such as $x$$Li_2MnO_3$·(1-$x$)$LiNi_{1/3}Mn_{1/3}Co_{1/3}O_2$ when cycled under similar conditions.[35]

Table 4.3.2: Discharge capacity observed at given voltages in cycle 1 and 2 and equivalent number of moles of Li^+ extracted/reinserted in $Li_{4.15}Ni_{0.85}WO_6$

		Voltage (V)	Capacity (mA·h g^{-1})	Moles Li^+
		OCV	0	0
Cycle 1	charge	4	94.8	1.27
		4.5	222.6	2.98
		5	317	4.24
	discharge	3	28.8	0.38
		1	209.3	2.8
Cycle 2	charge	2.8	39.4	0.53
		4	87.9	1.18
		4.5	172	2.3
		5	217	2.9
	discharge	3	25.1	0.34
		1	197.7	2.64

4.4 *Ex-Situ* XANES Spectroscopy

Ex-situ XANES spectroscopy was employed in order to investigate the valency of the nickel and tungsten ions throughout the first two electrochemical cycles, by analysis of the Ni K-edge and W L_3-edge, in order to elucidate which cationic species were responsible for the Li^+ deintercalation and reinsertion at each voltage plateau. A shift

of the absorption edges to higher energies indicates a higher oxidation state of that element, as greater energy is required for the excitation of a core electron to higher energy states.

4.4.1 Ni K-Edge XANES Spectroscopy

The standards prepared for Ni XANES analysis were $NiWO_4$ (Ni^{2+}) and $LiNiO_2$ (Ni^{3+}) for comparison of the edge energy positions, which arise from the transition of a 1*s* core electron to unoccupied 4*p* states (allowed by the dipole selection rule, $\Delta l = \pm 1$). The pristine material was ball-milled post synthesis and was cast onto the Al foil substrate, referred to as OCV (open circuit voltage) in the figures, with a nominal nickel oxidation state of +2.18. The voltages chosen for *ex-situ* XANES analysis are shown in Figure 4.3.10.

The existence of a pre-edge feature in the XANES spectra is frequently observed for first row transition metals, *i.e.* possessing an unfilled 3*d* orbital.[36] The pre-edge peaks occur at lower energies than the intense edge energies, arising from $1s \rightarrow 3d$ electronic transitions, which are forbidden by the dipole selection rule (since $\Delta l = +2$), but are weakly observed due to unoccupied 3*d*-4*p* orbital hybridisation or quadrupolar coupling.[37] The *p-d* hybridisation can occur as a result of distorted or asymmetric octahedral coordination environments, which was determined for $Li_{4.15}Ni_{0.85}WO_6$ in Chapter 3. As a result of the presence of pre-edge absorptions in the Ni K-edge XANES spectra, quantitative analysis of the nickel oxidation states throughout the first (Figure 4.4.1) and second (Figure 4.4.2) electrochemical cycle was determined to be inaccurate. Where the absorption edge comprises electronic transitions of equal energy, the oxidation states can be determined *via* the second derivative method.[38, 39] This method involves recording the energy whereby the second derivative crosses

zero, *i.e.* the point on the absorption edge of maximum gradient. However, due to pre-edge interference and possibly the presence of mixed valency nickel cations, all spectra were determined to have multiple points where the gradient is at a maximum. Other quantitative measurements employed in the literature for analysis of nickel oxidation states from XANES include comparing the position of the peak maximum as the edge position and using a polynomial calibration curve of the positions of known Ni oxidation states or extracting the edge energies at half the height of the peak maximum.[38, 40, 41] The spectra are displayed with normalised intensities, comprised of the summation of three separate spectra collected for each material.

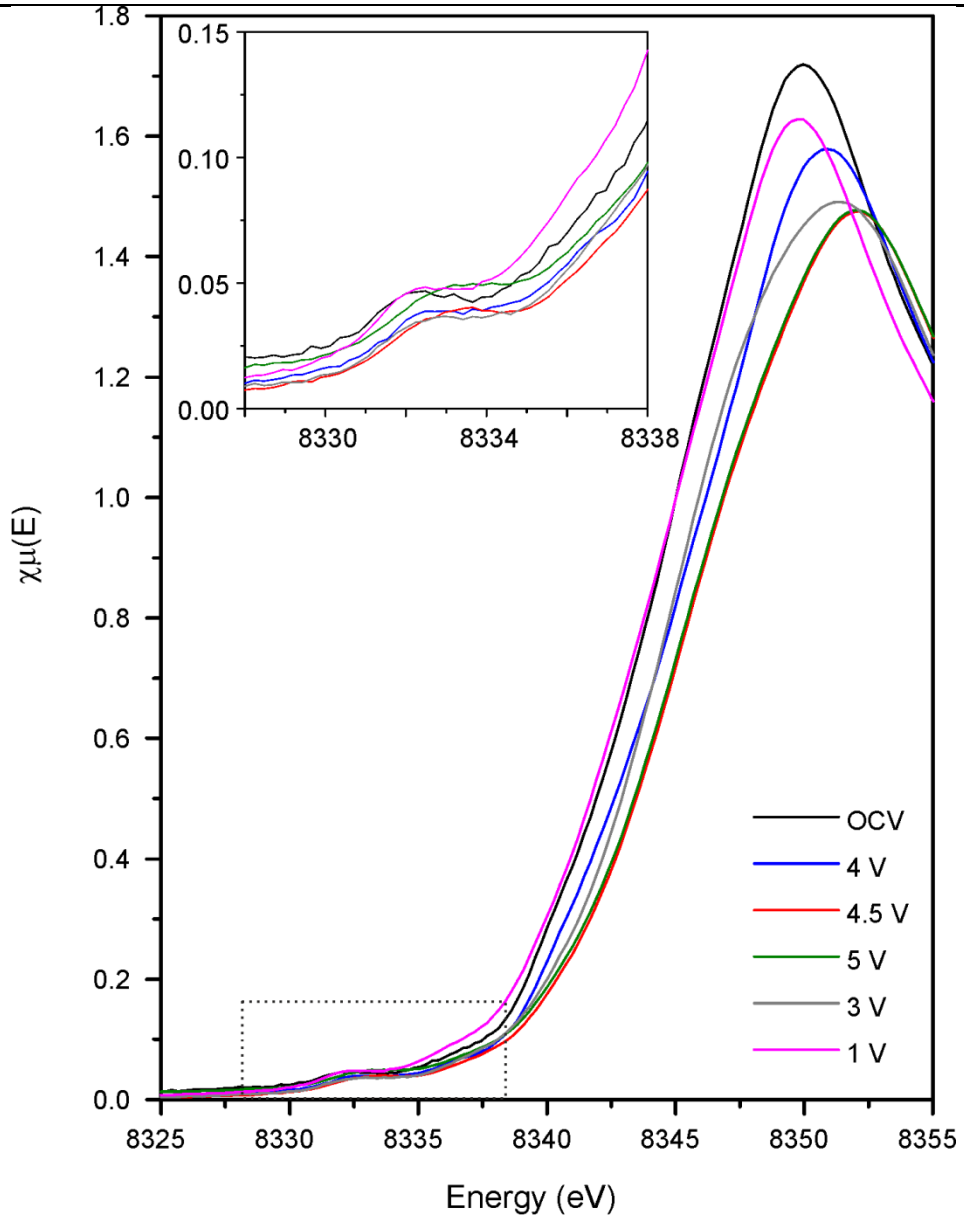

Figure 4.4.1: Ni K-edge XANES spectra of the first electrochemical cycle. *Inset*: expansion of the outlined pre-edge features

By analysis of the edge positions of the overlaid spectra for the first electrochemical cycle, it can be seen that upon charging to 4 V, the edge position shifts to higher energies, hence the nickel oxidation state increases slightly from the pristine material (labelled OCV in Figure 4.4.1), reaching a maximum at 4.5 and 5 V charge. Upon discharge back down to 3 V, the edge position returns to the 4 V charge position, and

upon deep discharge to 1 V, the edge position returns to the pristine oxidation state. The same behaviour can be observed in the pre-edge absorption peaks (Figure 4.4.1, *inset*).

During the second electrochemical cycle, the nickel oxidation states display different behaviour to the first cycle. Upon charging to 2.8 and 4 V, the edge energy does not shift discernibly, but shifts to higher energy upon charging to 4.5 and 5 V (Figure 4.4.2). During discharge to 3 V, the edge position shifts between the maximum oxidation state achieved and the pristine oxidation state, and returns to the pristine state upon full discharge to 1 V. The nickel redox is therefore determined to be reversible.

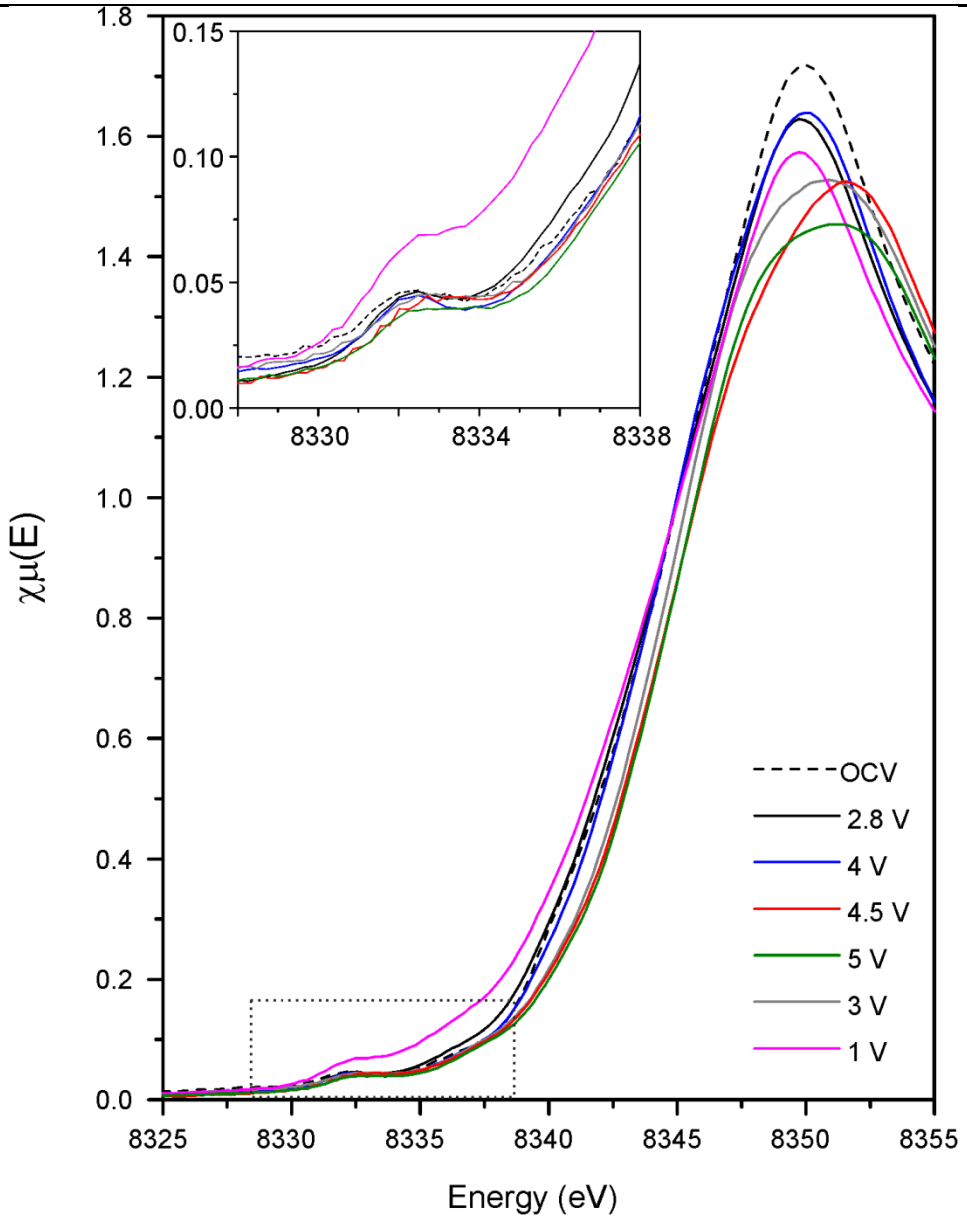

Figure 4.4.2: Ni K-edge XANES spectra of the second electrochemical cycle. *Inset*: expansion of the outlined pre-edge features

The broadening of the peak maxima (particularly evident at voltages of 5 and 3 V in Figure 4.4.2) led to the conclusion that determining nickel oxidation states from the position of the peak maxima was unreliable. Additionally, this may suggest that two distinct oxidation states of nickel are present during electrochemical cycling which are not clearly distinguished by this spectroscopic method. Due to interference from the

pre-edge absorption peaks, taking half the peak maximum height was also deemed ineffective for quantitative analysis of nickel oxidation states.

By comparison of the edge positions to the Ni^{2+} and Ni^{3+} standards, ($NiWO_4$ and $LiNiO_2$, respectively), it can be qualitatively determined that the total average nickel oxidation state does not appear to exceed +3 during charging up to 5 V in either the first or second cycle (Figure 4.4.3).

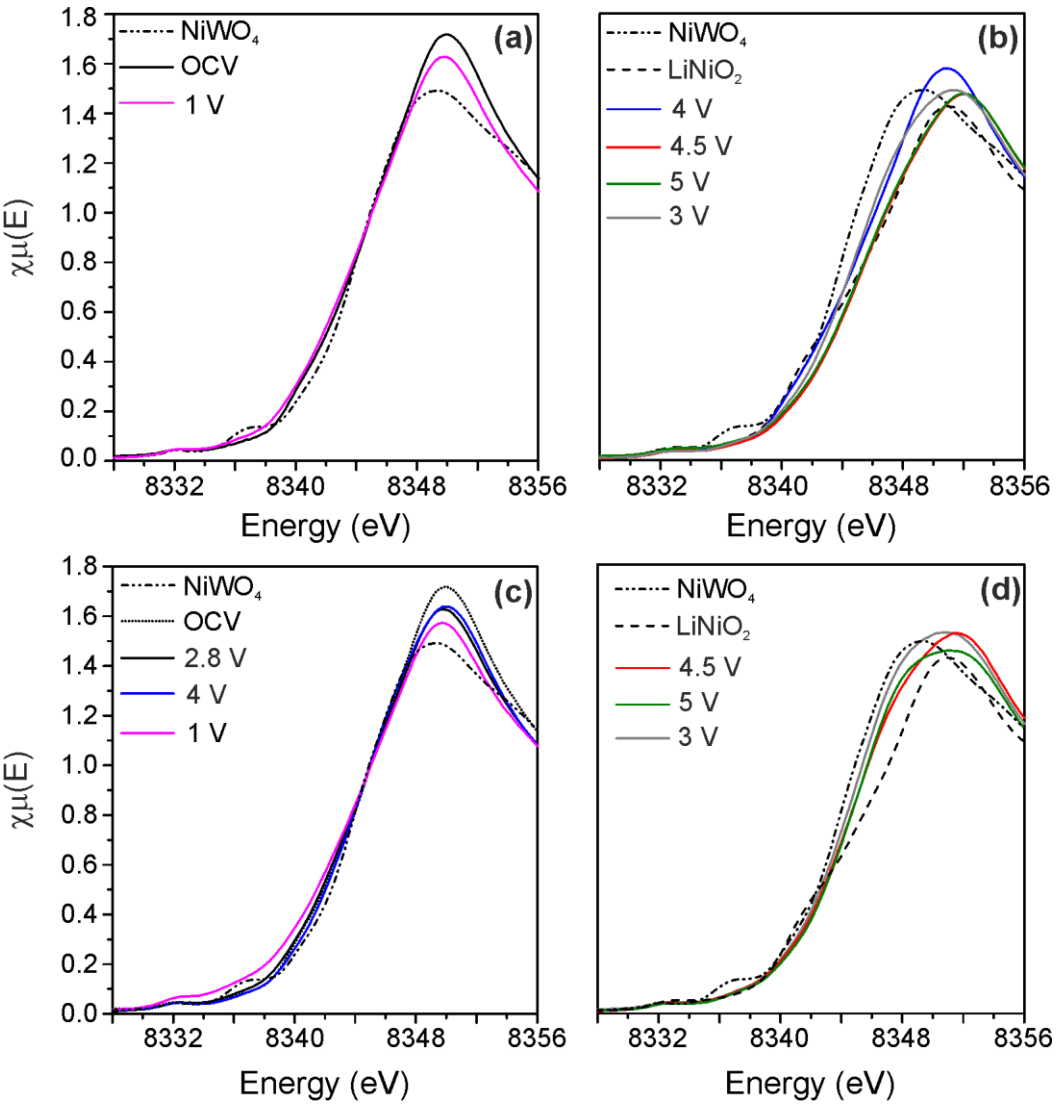

Figure 4.4.3: Ni K-edge XANES spectra compared to Ni^{2+} and Ni^{3+} standards where (a) and (b) show the first cycle; (c) and (d) show the second cycle

The highest oxidation state of nickel in the first cycle at 5 V charge approximately matches the edge position of the Ni^{3+} standard (Figure 4.4.3 (b)). However, on charging to 5 V in the subsequent cycle (Figure 4.4.3 (d)), the edge position lies between the +2 and +3 standard absorption lines and the peak maximum appears broader. In addition, by comparison of Figure 4.4.3 (a) and (c), in the first cycle charge to 4 V the oxidation state shifts above the pristine oxidation state, whereas in the second cycle no discernible energy shift is observed, despite there being an extraction of capacity (hence Li^+ extraction) observed at 4 V charge on cycle 2 (Figure 4.3.10). Considering that nickel was observed on three of the four distinct cation sites in $Li_{4.15}Ni_{0.85}WO_6$ (see Chapter 3), it is possible that on subsequent electrochemical cycles, some Ni oxidises to +3 whereas some remain +2 depending on the local bonding environment. The differences between the XANES spectra of the two cycles provides further evidence that an irreversible structural transformation is occurring on the first electrochemical cycle.

It is likely that the $Ni^{2+/3+}$ oxidation is being stabilised in this material, therefore the $Ni^{3+/4+}$ oxidation is not accessible when charged up to 5 V. This is possibly due to the inductive effect of electronegative $[WO_6]^{6-}$ octahedra, resulting in an increased voltage required to oxidise the nickel ions;[31, 42, 43] this effect is responsible for the relatively high potential of the $Ni^{2+/3+}$ oxidation in $LiNiPO_4$ (5.2 V *vs*. Li/Li^+).[44] $Li_{4.15}Ni_{0.85}WO_6$ provides a rare example of the average oxidation state of nickel being considerably less than +4 after charging to 5 V for electrochemical delithiation in an oxide.[31, 45] Considerable oxidation of carbonate-based electrolytes is expected when charging cells to 5 V, however it is possible that the inaccessibility of the $Ni^{3+/4+}$ redox could partly minimise the electrolyte oxidation.[46] The $LiNi_{0.5}Mn_{1.5}O_4$ and $LiMn_{0.5}Ni_{0.5}O_2$ cathodes also show good cyclability when cycled to high potentials, attributed to

surface effects caused by the presence of Ni ions in the structures;[47, 48] effects which may also be present in $Li_{4.15-x}Ni_{0.85}WO_6$.

4.4.2 W L_3-Edge XANES Spectroscopy

The tungsten standards used were WO_2 (W^{4+}) and $NiWO_4$ (W^{6+}) and WO_3 (W^{6+}) (as discussed in Chapter 2) for comparison of the edge energy positions (Figure 4.4.4). Due to the absence of pre-edge features in the W L_3-edge XANES spectra, the edge energies were analysed using the second derivative method. Unlike the Ni K-edge XANES data, the W L_3-edge did not exhibit any significant shift in energy throughout the first two electrochemical cycles, meaning tungsten remains in the +6 oxidation state in the bulk of the material, as expected (Figure 4.4.5, Figure 4.4.6).

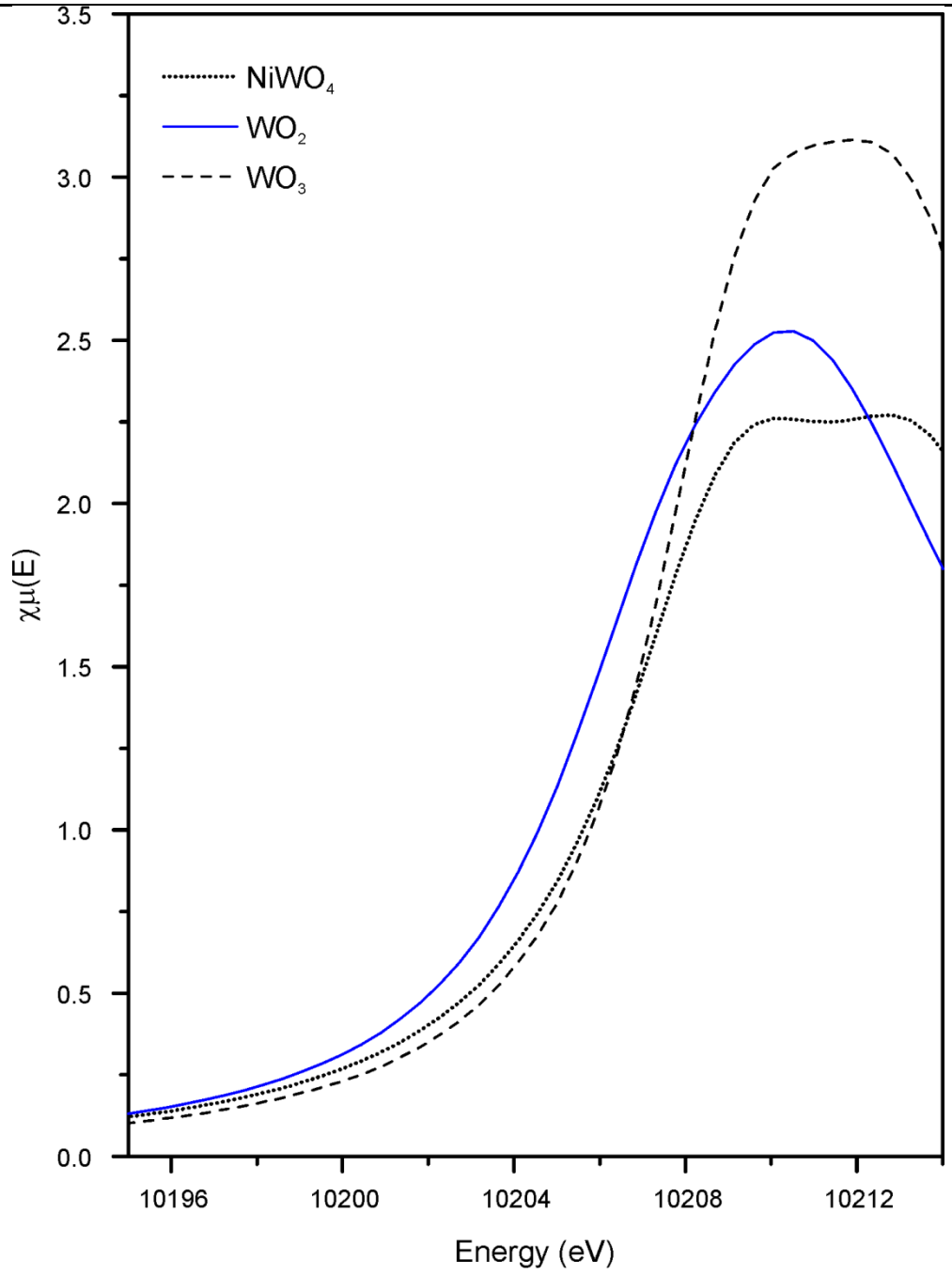

Figure 4.4.4: W L_3-edge XANES spectra of tungsten standards

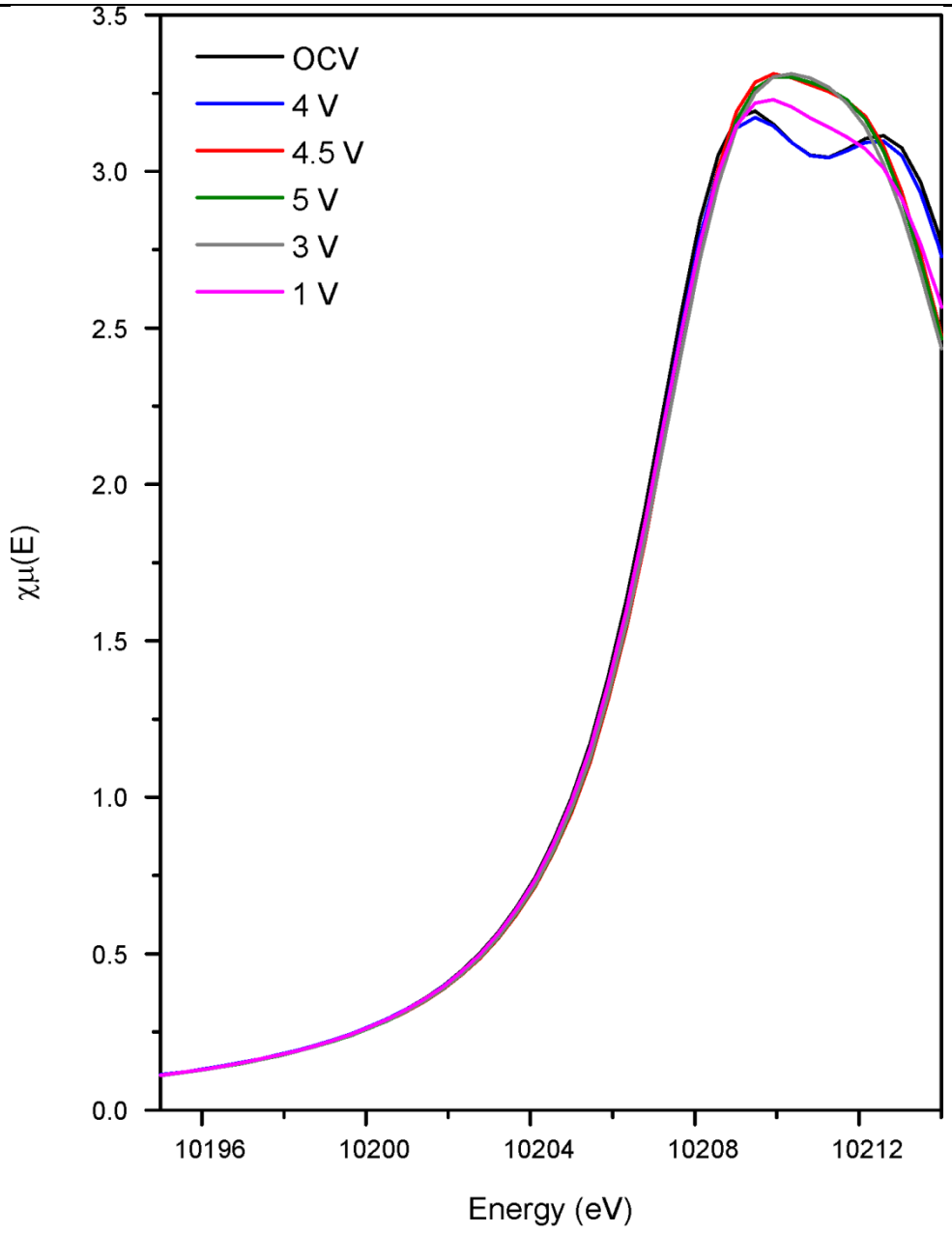

Figure 4.4.5: W L_3-edge XANES spectra of the first electrochemical cycle

However, in the extended X-ray absorption fine structure (EXAFS) region above the W L_3-edge data, a double peak can be seen in the uncycled material and the 4 V charged material. Upon further charging beyond 4 V, this double peak coalesces and does not return back to its initial shape at the end of the first cycle. This suggests up until 4 V charge, the tungsten retains its initial local coordination environment, which does not return upon discharge back to 1 V. A similar double peak shape is also

observed in the $NiWO_4$ standard W L_3-edge XANES (Figure 4.4.4), which is reported to possess four short and two long W-O distances through XANES and EXAFS analysis.[49] The variation in peak shape in the EXAFS region for $Li_{4.15-x}Ni_{0.85}WO_6$ provides evidence for irreversible structural changes occurring during the first electrochemical cycle, most likely due to distortion of the WO_6 octahedra. This coalesced peak shape is maintained during the second cycle and the W L_3-edge position remained constant.

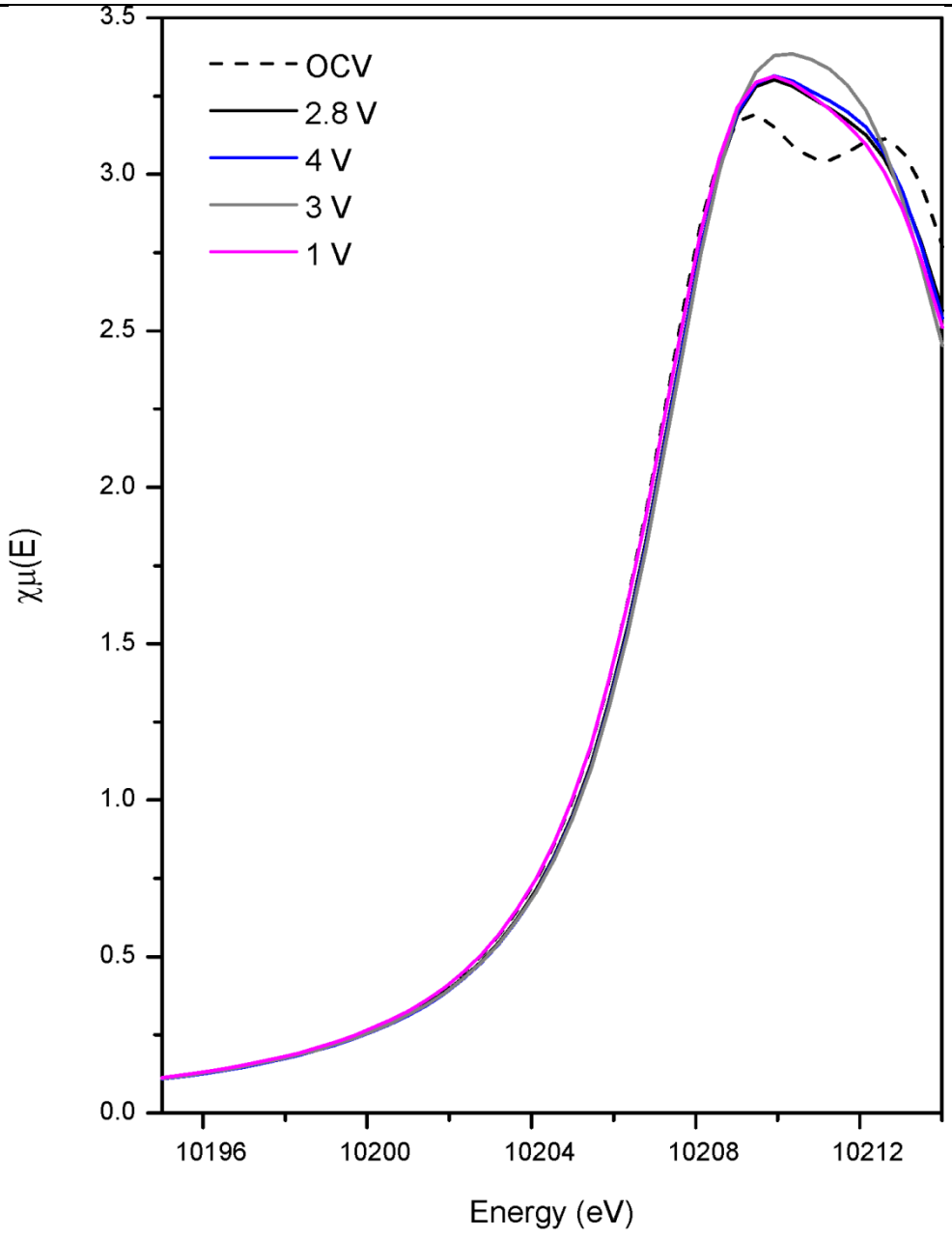

Figure 4.4.6: W L_3-edge XANES spectra of the second electrochemical cycle

It can therefore be concluded that no oxidation or reduction of tungsten is occurring during electrochemical cycling between 1-5 V; hence nickel is the only redox active metal cation within $Li_{4.15}Ni_{0.85}WO_6$.

4.5 Structural Evolution during Electrochemical Cycling

4.5.1 *Ex-Situ* SXRD

The samples prepared for the XANES experiments were retained within the sealed PE-lined foil packages for structural analysis using synchrotron data collection. A diffraction pattern of an empty foil package was obtained to confirm the reflections not arising from the cathode material. The PXRD have been plotted using a logarithmic *y*-scale due to the high intensity of the aluminium substrate peaks from the cathode coin cell casts (Figure 4.5.1). The aluminium foil substrate peaks were used to align the data from each cycle. By comparison to the PE-polymer peaks, the reflections of the rock-salt phases decrease in intensity and broaden, suggesting some local rearrangements accompanying the deintercalation and subsequent re-intercalation of Li^+ are likely to have occurred. The PXRD did not show any evidence of NiO_2, which is formed when charging $LiNiO_2$ above 4 V *vs.* Li/Li^+, indicating the new phase formed is stable to charging to 5 V.[50] The phase fractions were estimated by comparison of the ratios of the intensity of the most intense Bragg reflection for each phase with assistance from Dr Michael Pitcher.

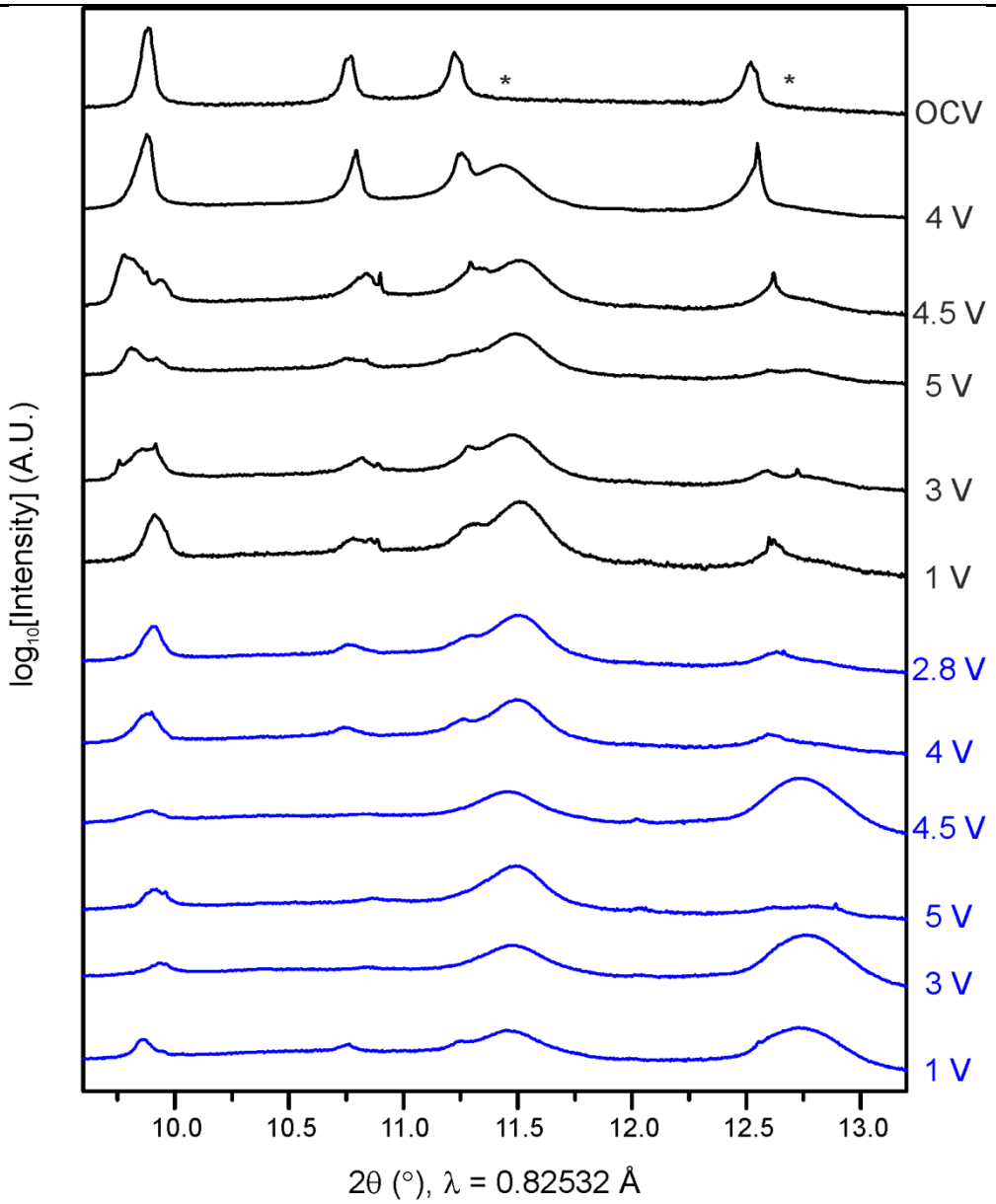

Figure 4.5.1: *Ex-situ* SXRD of cathode casts charged/discharged to voltages indicated on the *right*. First cycle data are represented in *black*, second cycle data represented in *blue*. Broad peaks marked with (*) indicate reflections arising from PE-lined Al foil bags

With reference to Figure 4.5.2, the pristine material (denoted OCV) consists of the single-phase *Cm* rock-salt structure (Phase 0), which transforms to two related rock-salt phases upon the first charge by 4.5 V (Phase 1 and Phase 2). The reflections of Phase 1 and of Phase 2 can be fit to the parent Phase 0 *Cm* unit cell.

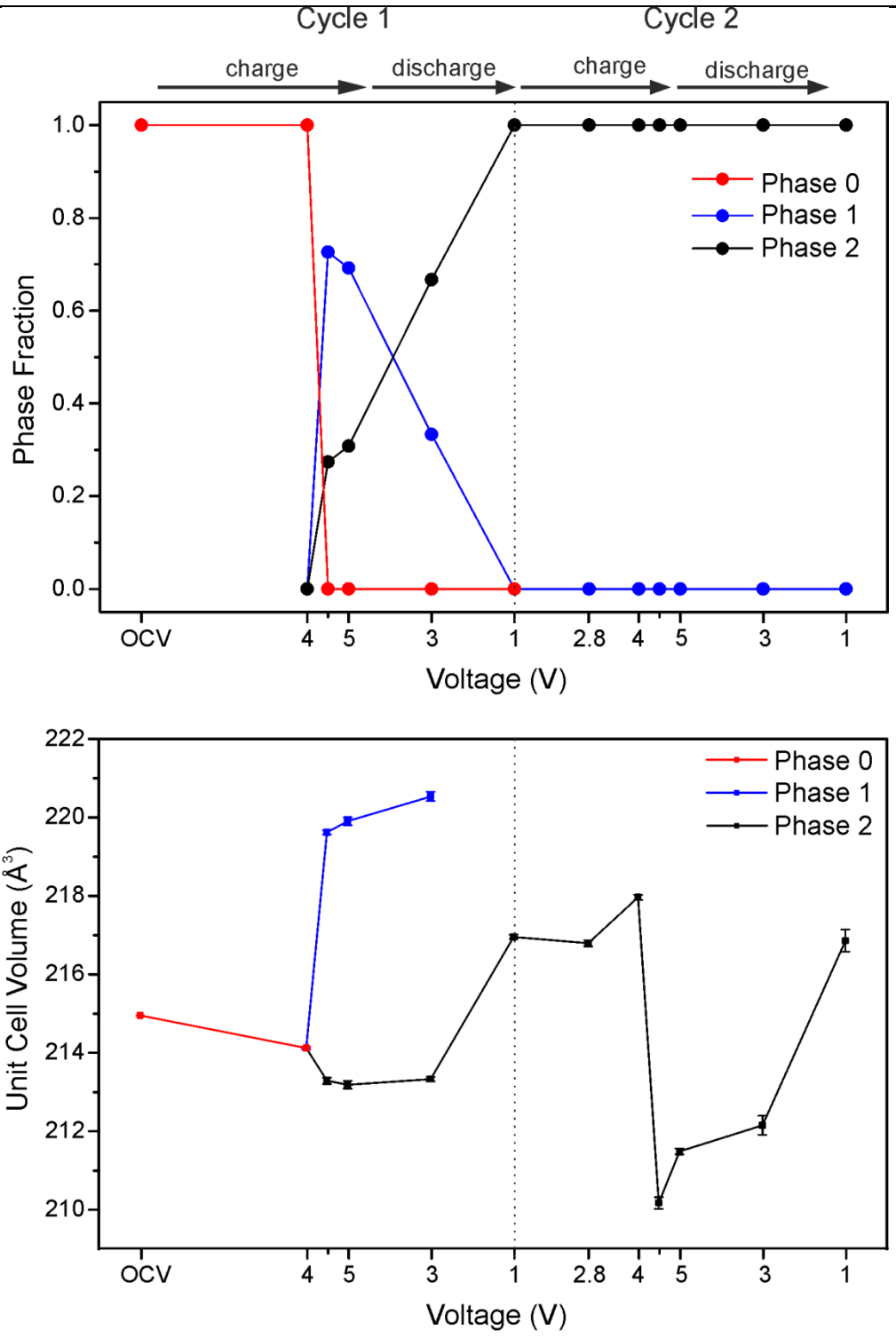

Figure 4.5.2: Variation of phase fractions (*top*) and unit cell volume of phases (*bottom*) with voltage (error bars represent 3σ from Pawley refinements)

The fraction of Phase 1 diminishes throughout the first cycle as it converts into Phase 2, with only Phase 2 being present at the end of the first cycle.

The second electrochemical cycle was found to only contain Phase 2, which cycles reversibly. As a result, neither Phase 0 nor Phase 1 are recovered, confirming the irreversible structural evolution occurring during the first electrochemical cycle. During the second cycle, the unit cell volume of the stable Phase 2 rapidly decreases from 4 to 4.5 V charge. From the Ni XANES data collected for the second cycle (Figure 4.4.3), an increase in the nickel oxidation state is also observed in this region. The decrease in the cell volume could be due removal of lithium ions causing contraction, with possible accompanying cation migration of nickel ions.[51, 52] A similar decrease in unit cell volume upon delithiation was also observed in the structurally related Li_4NiTeO_6 system.[32] In addition to Li^+/Ni^{2+} site mixing observed in the preparation and cycling of $LiNiO_2$, for example, the migration of Ni^{3+} ions to vacated Li^+ octahedral sites has also been observed during the cycling of nickel-rich NMC materials such as $LiNi_{0.6}Mn_{0.3}Co_{0.1}O_2$, whereby Ni^{2+} oxidises to Ni^{3+} on charge.[53]

Due to peak broadening effects accompanying cation migrations and possible oxygen transformations, it is difficult to fully analyse the delithiated structures *via* this method.

4.6 Evidence for Anionic Redox Processes

From the XANES and cycling data, although definitive values for the oxidation states of nickel could not be determined, the cation oxidation was not determined to be the sole source of lithium extraction from $Li_{4.15}Ni_{0.85}WO_6$. Even if full oxidation of $Ni^{2.18+} \rightarrow Ni^{4+}$ was occurring, as calculated in Equation 4.3.1, this would only account for 116 mA·h g^{-1} of the discharge capacity. Experimentally, a reversible discharge

capacity of ~173 mA·h g^{-1} is observed meaning there must be additional reversible (de)intercalation of lithium which is not directly from redox action of the nickel or tungsten cations. As discussed in Section 4.1, the most likely source of additional capacity is from involvement of oxide anions within the structure of the cathode. Further analysis was therefore performed in an attempt to verify the presence of anionic redox in this Li-rich material with partial cation ordering.

4.6.1 XPS

X-ray photoelectron spectroscopy was employed *ex-situ* to evaluate the oxidation states of Li, Ni, W and O throughout the first and second electrochemical cycles of $Li_{4.15}Ni_{0.85}WO_6$ (collected on the same charged/discharged samples as the XANES data (Figure 4.3.10). The oxidation state of tungsten was found to remain in the +6 oxidation state throughout the first two cycles, which is in full agreement with the W XANES data (Figure 4.4.5, Figure 4.4.6). No lithium was detected in the samples charged to 5 V after subsequent discharge to 3 V in both cycles; however the charge-discharge profile *vs*. the number of Li^+ ions (de)intercalated (Figure 4.3.11) indicates a small amount Li^+ has reinserted at 3 V discharge. This may not have been detected by XPS either because such a small amount of Li^+ cannot be detected, or Li^+ has re-intercalated into the cathode beneath the surface. The oxygen 1*s* XPS spectra are displayed in Figure 4.6.1, with the positions of the binding energies for O^{2-} and O_2^{2-} (peroxide) indicated.

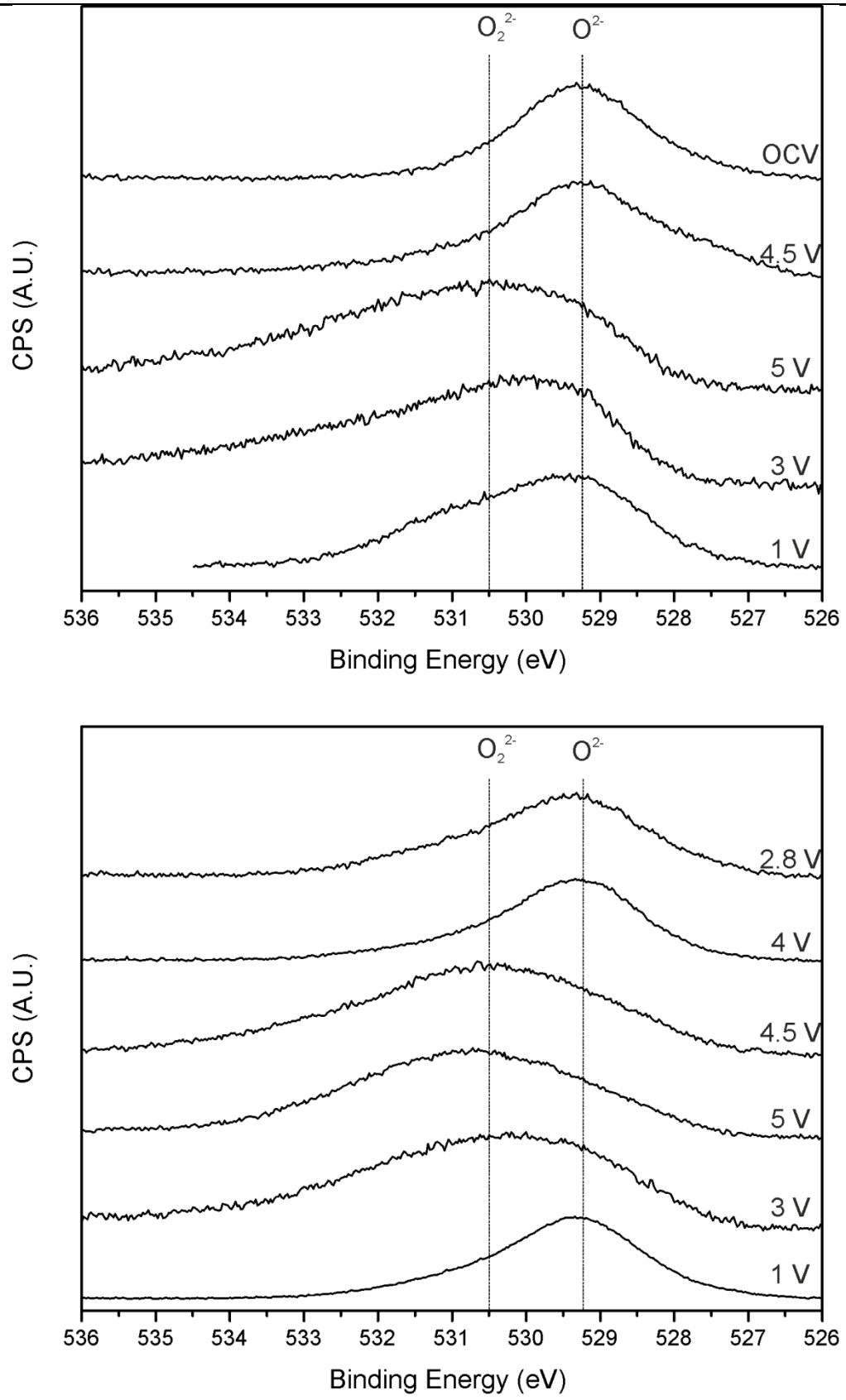

Figure 4.6.1: XPS O1*s* spectra for first (*top*) and second (*bottom*) electrochemical cycle with the voltages of $Li_{4.15-x}Ni_{0.85}WO_6$ indicated on each spectrum

The oxygenated species were approximately quantified by fitting the spectra using Voigt functions and comparing the relative areas. The proportion of each species has been presented in Figure 4.6.2 with comparison to the average oxygen oxidation state. The average oxidation state of oxygen generally increases upon charge and return to O^{2-} at the end of each cycle (~529.3 eV). This behaviour indicates a loss of electrons from some of the oxide ions in the $Li_{4.15}Ni_{0.85}WO_6$ structure, to form peroxo-type species, accompanied by Li^+ deintercalation for charge balance. Oxygen returns to the -2 oxidation state at the end of each cycle, providing evidence for reversible anionic redox processes. As expected, the proportion of peroxo species (~530.4 eV) increases with the increase in oxygen oxidation state, with evidence of a greater proportion of peroxides in the second cycle. The exact nature of the peroxo species has not yet been determined *e.g.* whether $(O_2)^-$, $(O_2)^{2-}$, $(O_2)^{3-}$ or a combination are present.[54] The species present in the broad region above the binding energy for peroxide have therefore been labelled as 'other'.

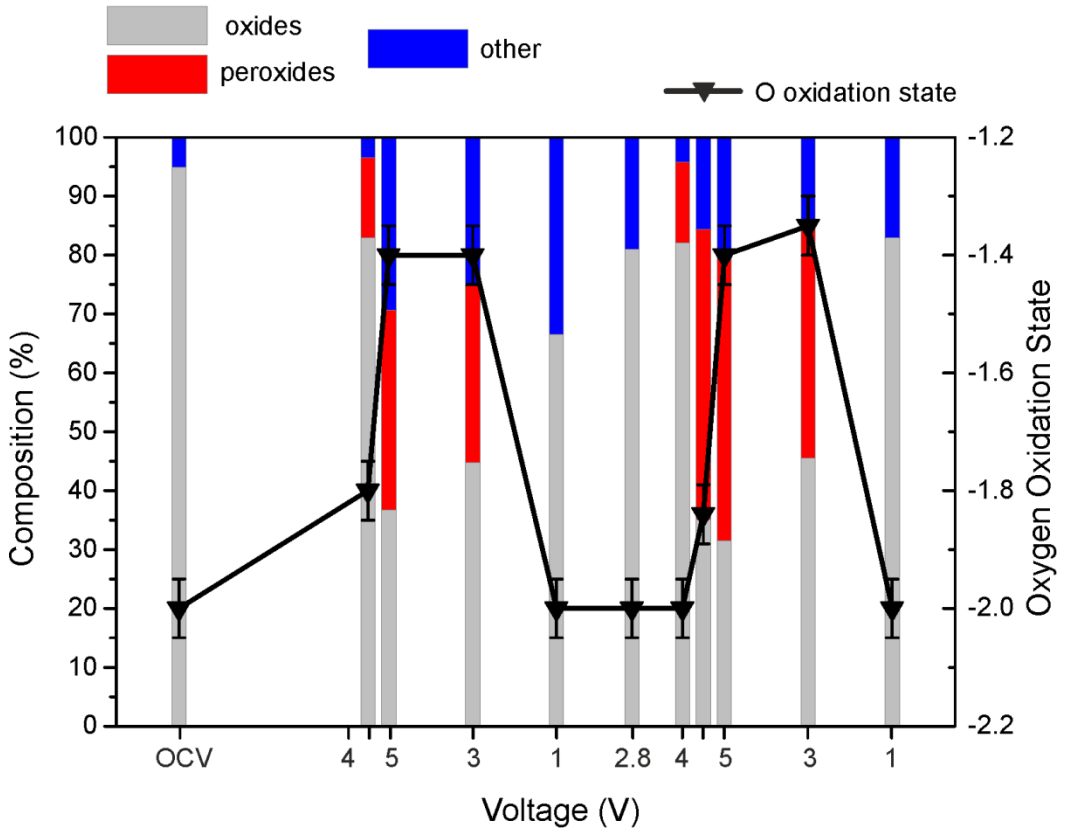

Figure 4.6.2: Stacked bar chart representing the quantities of oxygen species at voltages throughout the first and second electrochemical cycle as detected from XPS (*left y*-axis) and overlaid average oxygen oxidation state (*right y*-axis)

The oxidation states of nickel and oxygen throughout the first two cycles were quantified (Figure 4.6.3). The variation of nickel oxidation states is in agreement with those established from *ex-situ* XANES spectroscopy (Figure 4.4.3). As predicted, the nickel oxidation state does not exceed +3 upon charging to 5 V, and returns to the oxidation state observed in the uncycled sample (OCV) at the end of each cycle, confirming the reversibility of the nickel redox observed by XANES.

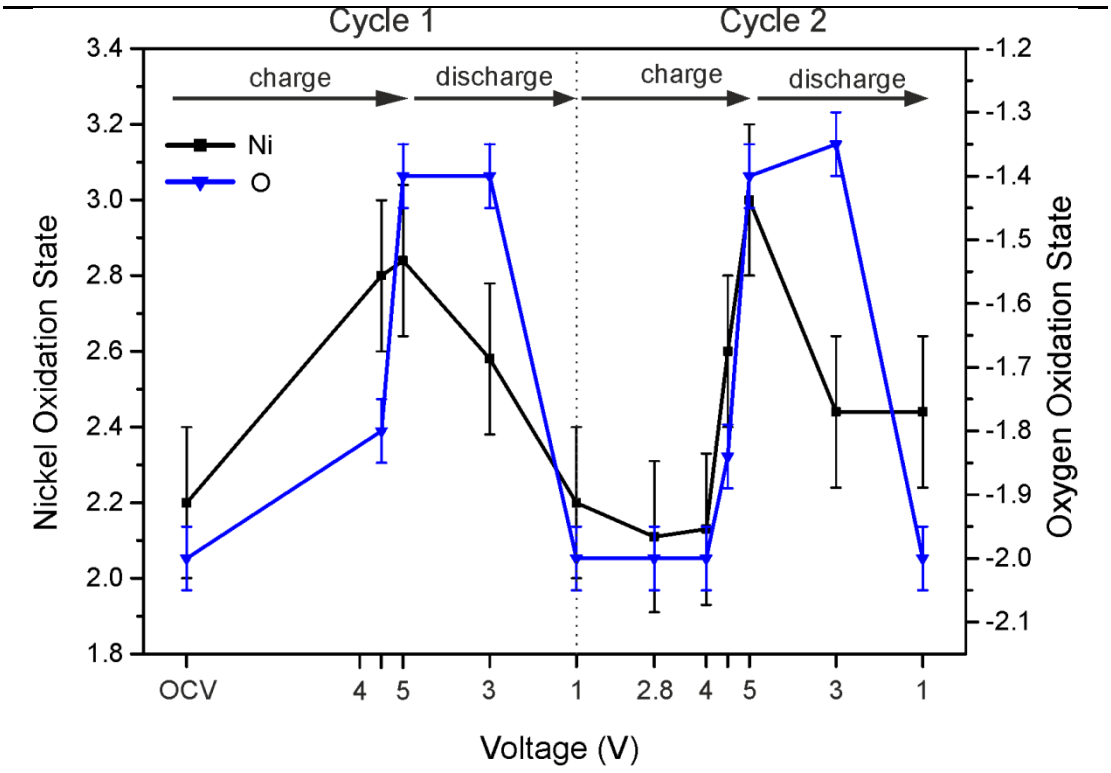

Figure 4.6.3: Variation of nickel (*black*) and oxygen (*blue*) oxidation states with voltage over the first two electrochemical cycles as determined by *ex-situ* XPS. Error bars represent 3σ

On discharge to 3 V the nickel has been reduced to $2.6(2)^{+}$ (*i.e.* approximately half the nickel is reduced by 3 V) and is fully reduced back to $2.2(2)^{+}$ by 1 V; however the peroxo-type species are not reduced until discharged below 3 V (and return to O^{2-} upon discharge to 1 V). It is therefore most likely that the large feature observed in the differential capacity plots at ~1.6 V discharge are due to the reduction of O_2^{n-} species back to $2O^{2-}$ within the lattice, accompanying Li^{+} reinsertion. Due to the low voltage at which this reduction occurs, it suggests that the peroxo-species are considerably stabilised, predicted to coordinate to the W^{6+} ions. From the W-XANES spectra, upon the first cycle charge to 4.5 V there is a permanent local W cation site structural rearrangement occurring in tandem with oxidation of nickel and oxygen, which is also the voltage at which two new phases were detected from the *ex-situ* SXRD (Figure 4.5.1, Figure 4.5.2).

The removal of electrons from $Ni^{2.18+}$ and O^{2-} appears to occur simultaneously on charging based on the estimated oxidation states from XPS, although it is possible that oxidation of nickel occurs at the surface prior to the bulk. By comparison to the edge energy shifts observed in Ni-XANES data and the differential capacity plots of the first two cycles, which are more representative of the bulk material, the estimated redox species responsible for Li^+ (de)intercalation at each voltage can be assigned (Figure 4.6.4, labelled **A**-**F**).

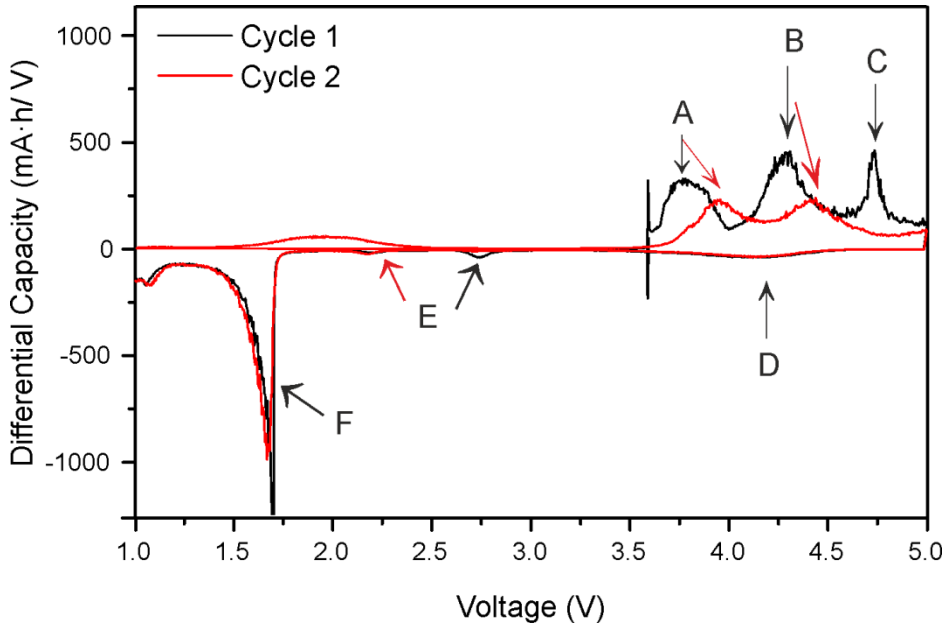

Figure 4.6.4: Points of reactions responsible for Li^+ (de)intercalation labelled **A-F** on the differential capacity plots of cycle 1 and 2

Based on the XPS analysis, the feature labelled **A** is estimated as the oxidation of lattice oxides, $O^{2.00(5)-} \rightarrow O^{1.45(5)-} + 0.55(5)\ Li^+ + 0.55\ e^-$, which shifts to a higher voltage on cycle 2. Point **B** is assigned as the oxidation of $Ni^{2.2(2)+} \rightarrow Ni^{3.0(2)+} + 0.82\ Li^+ + 0.82\ e^-$ which also occurs at a higher voltage on cycle 2. The sharp peak in the first cycle at ~4.7 V (labelled **C**) is attributed to oxidation of the electrolyte resulting in SEI formation at the electrode surfaces (primarily at the anode). This peak is no longer

present in the second cycle, meaning the electrolyte should not considerably oxidise further, as the Li-permeable SEI layer acts to protect the electrolyte from further oxidative attack at the cathode. The reduction of Ni^{3+} on discharge is thought to occur in two steps at points **D** ($Ni^{3.0(2)+} \rightarrow Ni^{2.6(2)+}$) and **E** ($Ni^{2.6(2)+} \rightarrow Ni^{2.2(2)+}$). Since the pristine structure was determined to have nickel located on three distinct crystallographic sites (see Chapter 3), the energy required for oxidation/reduction at each site will vary, which may explain why the nickel reduction steps (**D** and **E**) has been determined to occur at different voltages. Point **F** is assigned the reduction of peroxo-like species back to lattice oxide ($O^{1.45(5)-} \rightarrow O^{2-}$) occuring at ~1.6 V on discharge.

4.6.2 HAXPES

Since XPS is a surface-sensitive analytical technique, hard-X-ray photoelectron spectroscopy (HAXPES) was employed to observe whether peroxo-like species were present in the bulk of delithiated $Li_{4.15}Ni_{0.85}WO_6$, and minimise the observation of surface species (Figure 4.6.5). Peak fitting and extraction of the oxidation states/quantification of species requires additional alignment due to charging, but the observed broadening of the peaks is indicative of formation of O_2^{n-} species.[55]

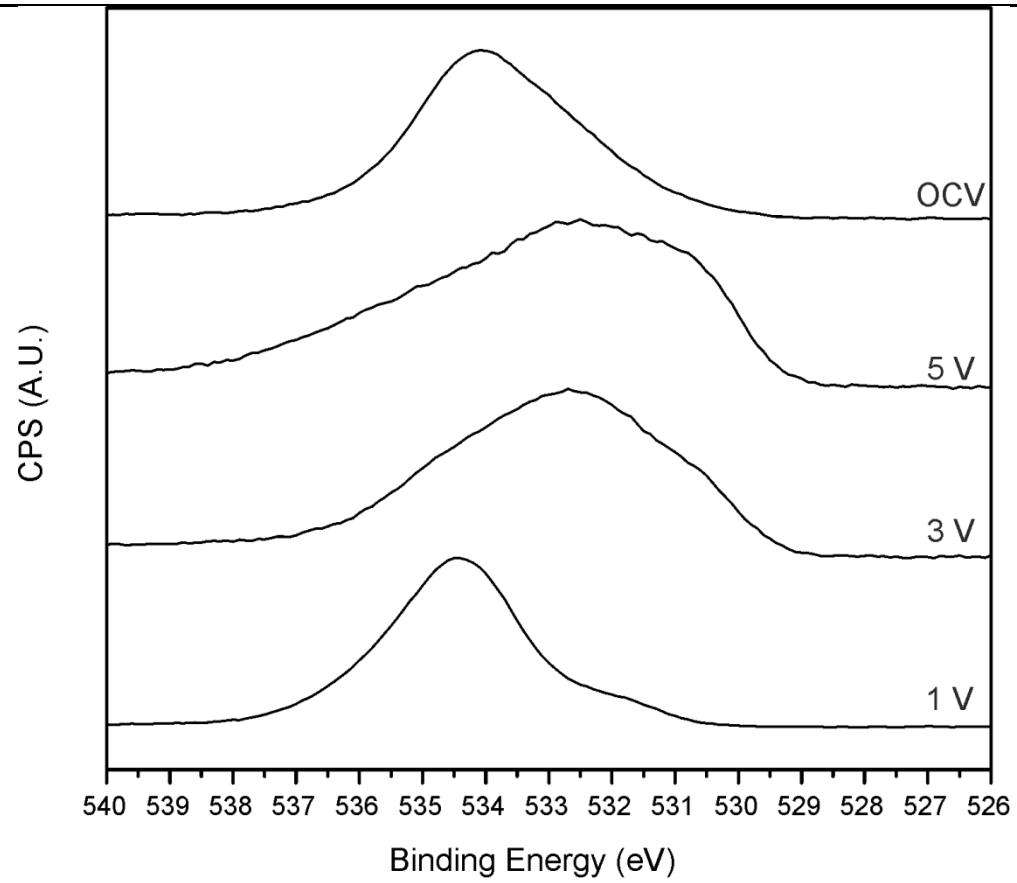

Figure 4.6.5: *Ex-situ* HAXPES O 1*s* spectra for first electrochemical cycle

The HAXPES data (obtained for the first cycle only) is consistent with the XPS data, which suggests that peroxo species responsible for the reversible anionic redox also occur in the bulk of the material in addition to at the surface, since HAXPES has a greater penetration depth of ~15 nm *cf.* XPS.

4.7 Summary of Electrochemistry

Removal of all lithium ions from $Li_{4.15}Ni_{0.85}WO_6$ would result in a charge capacity of 310 mA·h g^{-1}. From analysis of the nickel oxidation state *via* XPS and XANES, it is concluded that the nickel oxidation state does not exceed +3, which only accounts for 62 mA·h g^{-1}, whereas capacities of up to 209 mA·h g^{-1} (reversible capacity 173 mA·h g^{-}

[1]) were determined experimentally. Additionally tungsten was found to remain in the +6 oxidation state, as expected. The majority of the capacity (64-70%) is obtained from the redox action of lattice oxides, confirmed by XPS analysis which displays the appearance and disappearance of $(O\text{-}O)^{n-}$ peaks. Such peaks were also detected using hard X-ray photoelectron spectroscopy, which penetrates into the bulk of the cathode material. To achieve the discharge capacities observed, the anionic redox must therefore be highly reversible. The initial discharge capacity of 209 mA·h g^{-1} is composed of a contribution of 62 mA·h g^{-1} from $Ni^{3+} \rightarrow Ni^{2.18+}$ (re-intercalation of 0.82 Li^+) and the remaining 147 mA·h g^{-1} which corresponds to re-intercalation of ~2 Li^+ from the reduction of $(O_2)^{2-} + 2\ e^- \rightarrow 2O^{2-}$ (assuming the lattice oxides, O^{2-}, oxidise to superoxo-type species, O_2^{2-}). The additional capacity from this anionic redox can be accounted for by redox reaction of 1/3 of the initial lattice oxide content (2 moles of O^{2-} per mole of $Li_{4.15}Ni_{0.85}WO_6$). The reversible discharge capacity of 173 mA·h g^{-1} corresponds to the re-intercalation of ~1.5 Li^+ due to the reduction of $(O_2)^{2-}$ back to O^{2-} (*i.e.* 1/4 of the initial lattice oxide content predicted to be reversibly involved in the anionic redox).

No anionic redox was detected during cycling of Li_4NiTeO_6 explored by Sathiya *et al.*,[31] which possesses the same heavy cation ordering pattern as observed in $Li_{4.15}Ni_{0.85}WO_6$ (as discussed in Chapter 3), indicating that W5*d*^{0}-O2*p* orbital overlap may play a role in the stabilisation of the anionic redox. Should the peroxo/superoxo species oxidise fully on charge, rapid capacity fade would be expected since lattice oxygen would be lost as oxygen gas on every charge cycle, thus decomposing the cathode structure.[56, 57] If they preferentially and stably coordinate to W^{6+} as predicted, the release of oxygen gas is therefore suppressed. From the charge-discharge profiles of voltage *vs*. Li content (Figure 4.3.11), in conjunction with the estimated oxidation

states observed from XPS and XANES, the average composition at each voltage have been predicted (Table 4.7.1).

Table 4.7.1: Discharge capacity observed at given voltages in cycle 1 and 2 and equivalent number of moles of Li^+ extracted/reinserted in $Li_{4.15}Ni_{0.85}WO_6$; estimated oxidation states of Ni and O and average rock-salt species present at each voltage

	Voltage (V)	Capacity (mA·h g^{-1})	Moles Li^+	Average Estimated Species Present	Ox. State Ni	Ox. State O
	OCV	0.0	0.00	$Li_{4.15}Ni_{0.85}WO_6$	+2.18	-2
1	4	94.8	1.27	$Li_{2.88}Ni_{0.85}WO_{6-\delta}$	+2.6	-1.85
	4.5	222.6	2.98	$Li_{1.17}Ni_{0.85}WO_{6-\delta}$	+3	-1.6
	5	317.0	4.24	$Ni_{0.85}WO_{6-\delta}$	+3	-1.4
	3	28.8	0.38	$Li_{0.38}Ni_{0.85}WO_{6-\delta}$	+2.6	-1.4
	1	209.3	2.80	$Li_{2.80}Ni_{0.85}WO_{5.33}$	+2.18	-2
2	2.8	39.4	0.53	$Li_{2.27}Ni_{0.85}WO_{5.33-\delta}$	+2.18	-1.9
	4	87.9	1.18	$Li_{1.09}Ni_{0.85}WO_{5.33-\delta}$	+2.18	-1.7
	4.5	172.0	2.30	$Li_{0.50}Ni_{0.85}WO_{5.33-\delta}$	+2.6	-1.6
	5	217.0	2.90	$Ni_{0.85}WO_{5.33-\delta}$	+3	-1.4
	3	25.1	0.34	$Li_{0.34}Ni_{0.85}WO_{5.33-\delta}$	+2.6	-1.4
	1	197.7	2.64	$Li_{2.64}Ni_{0.85}WO_{5.25}$	+2.18	-2

From the *ex-situ* analytical data obtained in reference to the electrochemical profiles of the first two cycles, the overall charge reaction can be summarised in Equation 4.7.1 with the average oxidation states of Ni and O. Based on the observations of the loss of molecular oxygen from other Li-rich cathodes, it is possible that this is occurring in this material, though it has yet to be detected here (*e.g.* by mass spectrometry).[58] The overall discharge process is summarised in Equation 4.7.2. Given that the oxidation states of Ni and O are returned to those found in the pristine structure (determined

from XANES and XPS), a loss of ~0.67 moles of oxygen is predicted during the first charge to maintain an electroneutral structure. The re-lithiated structure present at the end of the cycle has been determined by *ex-situ* SXRD to maintain a rock-salt type structure (Figure 4.5.1); therefore the proposed identity of Phase 2, which cycles reversibly (Figure 4.5.2), is $Li_{2.8-x}Ni_{0.85}WO_{5.33}$, possessing octahedral vacancies due to loss of Li^+.

$$Li_{4.15}Ni^{2.18+}_{0.85}WO^{2-}_{6} \xrightarrow[\text{charge 5 V}]{} Ni^{3+}_{0.85}WO^{1.45-}_{6-\delta} + 4.15\ Li^{+} + 4.15\ e^{-} + \frac{\delta}{2}O_2 \quad (1)$$

Equation 4.7.1: Estimated first cycle charge process

$$2.8\ Li^{+} + 2.8\ e^{-} + Ni^{3+}_{0.85}WO^{1.45-}_{6-\delta} \xrightarrow[\text{discharge 1 V}]{} Li_{2.8}Ni^{2.18+}_{0.85}WO^{2-}_{5.33} \quad (2)$$

Equation 4.7.2: Estimated first cycle discharge process

Recently, the inclusion of nickel ions ordering within the lithium layer of Li_2MnO_3 (to give a composition of $Li_{1.75}Ni_{0.25}MnO_3$) was determined empirically and computationally to suppress oxygen loss *cf*. Li_2MnO_3 and to suppress Mn^{4+} migration.[59] It would therefore be of interest to determine whether nickel, in addition to tungsten, assists in the anionic redox of $Li_{4.15}Ni_{0.85}WO_6$.

Though the anionic redox process has been reported to be stabilised previously, in $Li_2Ru_{1-x}M_xO_3$ systems and $Li_{1.3}Nb_{0.3}Mn_{0.4}O_2$, it has only been reported to occur after cationic redox has occurred or simultaneously.[12, 21, 57] Here, we find the lattice oxide oxidation proceeds prior to Ni oxidation and the resultant peroxo-species are reduced at a lower discharge voltage than Ni. In addition, the Ni redox is only responsible for approximately a third of the overall capacity, the rest being due to the reversible $2O^{2-} \rightarrow O_2^{n-}$ process.

4.8 Conclusions and Future Work

The Li-rich rock-salt material $Li_{4.15}Ni_{0.85}WO_6$ was determined to display partial cation ordering in Chapter 3, and its electrochemical behaviour has been investigated in detail here. Reduction of the particle size following synthesis was achieved by mechanical ball-milling of the product, which was found to enhance the discharge capacity by over 64% (*cf.* before product ball-milling), exhibiting a first discharge capacity of 200-210 $mA{\cdot}h\ g^{-1}$, which is comparable to other Li-rich rock-salts.

Through a combination of *ex-situ* spectroscopic analyses of the first and second electrochemical cycles of $Li_{4.15}Ni_{0.85}WO_6$, a reversible anionic redox process has been confirmed as contributing ~2/3 of the practical capacity. Though the identity of the cycling species has not yet been conclusively determined, based on this analysis it is assumed to be peroxo-type species stabilised by the W^{6+} metal centre, likely aided by the mobility of lithium and nickel ions within the structure. It would be interesting to confirm the role of tungsten and nickel ions within this partially ordered Li-rich structure using computational methods. Loss of molecular oxygen is supressed in this material, as evidenced by the high reversibility of the capacity, however it would be interesting to detect and quantify how much may be released during cycling.

Future planned experiments for this material include *in-operando* SXRD collection to map out the structural changes during cycling, and hopefully conclusively identify the structures involved. HAXPES data collection for the second electrochemical cycle has also been considered. Based on the voltage shifts observed in the differential capacity plots after >10 cycles, it is possible that structural transformations are occurring

continuously, which could be confirmed by SXRD of a cathode after a larger number of cycles.

Overall, the performance of $Li_{4.15}Ni_{0.85}WO_6$ as a LIB cathode material is poor, due to the huge voltage hysteresis between the oxidation and reduction processes of both oxygen and nickel, resulting in a poor energy density. However the specific capacity is relatively high considering the inclusion of tungsten, which is less expensive than ruthenium. It is hoped that this research will assist in the deconvolution of anionic redox mechanisms and the factors which influence them, and that tungsten should not be overlooked in the development of Li-rich cathode materials.

4.9 References

1. S. Kim, M. Aykol, V. I. Hegde, Z. Lu, S. Kirklin, J. R. Croy, M. M. Thackeray and C. Wolverton, *Energy Environ. Sci.*, 2017, **10**, 2201-2211.
2. Y. Xie, M. Saubanere and M. L. Doublet, *Energy Environ. Sci.*, 2017, **10**, 266-274.
3. J. Chen, N. Zhao, G.-D. Li, F.-F. Guo, J. Zhao, Y. Zhao, T. Jia, F. Fu and J. Li, *Mater. Res. Bull.*, 2016, **73**, 192-196.
4. M. M. Thackeray, C. S. Johnson, J. T. Vaughey, N. Li and S. A. Hackney, *J. Mater. Chem.*, 2005, **15**, 2257-2267.
5. H. Chen and M. S. Islam, *Chem. Mater.*, 2016, **28**, 6656-6663.
6. Y. Shin, H. Ding and K. A. Persson, *Chem. Mater.*, 2016, **28**, 2081-2088.
7. B. Li, R. Shao, H. Yan, L. An, B. Zhang, H. Wei, J. Ma, D. Xia and X. Han, *Adv. Funct. Mater.*, 2016, **26**, 1330-1337.
8. A. C. W. P. James and J. B. Goodenough, *J. Solid State Chem.*, 1988, **74**, 287-294.
9. D. Mori, H. Kobayashi, T. Okumura and Y. Inaguma, *Electrochemistry*, 2015, **83**, 1071-1076.
10. M. Sathiya, K. Ramesha, G. Rousse, D. Foix, D. Gonbeau, A. S. Prakash, M. L. Doublet, K. Hemalatha and J. M. Tarascon, *Chem. Mater.*, 2013, **25**, 1121-1131.
11. E. Hu, Y. Lyu, H. L. Xin, J. Liu, L. Han, S.-M. Bak, J. Bai, X. Yu, H. Li and X.-Q. Yang, *Nano Lett.*, 2016, **16**, 5999-6007.

12. M. Sathiya, G. Rousse, K. Ramesha, C. P. Laisa, H. Vezin, M. T. Sougrati, M. L. Doublet, D. Foix, D. Gonbeau, W. Walker, A. S. Prakash, M. Ben Hassine, L. Dupont and J. M. Tarascon, *Nat. Mater.*, 2013, **12**, 827-835.

13. E. McCalla, A. M. Abakumov, M. Saubanère, D. Foix, E. J. Berg, G. Rousse, M.-L. Doublet, D. Gonbeau, P. Novák, G. Van Tendeloo, R. Dominko and J.-M. Tarascon, *Science*, 2015, **350**, 1516-1521.

14. T. Takayama, A. Kato, R. Dinnebier, J. Nuss, H. Kono, L. S. I. Veiga, G. Fabbris, D. Haskel and H. Takagi, *Phys. Rev. Lett.*, 2015, **114**, 077202.

15. P. E. Pearce, A. J. Perez, G. Rousse, M. Saubanère, D. Batuk, D. Foix, E. McCalla, A. M. Abakumov, G. Van Tendeloo, M.-L. Doublet and J.-M. Tarascon, *Nat. Mater.*, 2017, **16**, 580.

16. W. Wei, L. Chen, A. Pan and D. G. Ivey, *Nano Energy*, 2016, **30**, 580-602.

17. M. Gauthier, T. J. Carney, A. Grimaud, L. Giordano, N. Pour, H.-H. Chang, D. P. Fenning, S. F. Lux, O. Paschos, C. Bauer, F. Maglia, S. Lupart, P. Lamp and Y. Shao-Horn, *J. Phys. Chem. Lett*, 2015, **6**, 4653-4672.

18. E. McCalla, M. T. Sougrati, G. Rousse, E. J. Berg, A. Abakumov, N. Recham, K. Ramesha, M. Sathiya, R. Dominko, G. Van Tendeloo, P. Novák and J.-M. Tarascon, *J. Am. Chem. Soc.*, 2015, **137**, 4804-4814.

19. X. Rong, J. Liu, E. Hu, Y. Liu, Y. Wang, J. Wu, X. Yu, K. Page, Y.-S. Hu, W. Yang, H. Li, X.-Q. Yang, L. Chen and X. Huang, *Joule*, 2017, DOI: https://doi.org/10.1016/j.joule.2017.10.008.

20. J. Lee, A. Urban, X. Li, D. Su, G. Hautier and G. Ceder, *Science*, 2014, **343**, 519-522.

21. N. Yabuuchi, M. Takeuchi, M. Nakayama, H. Shiiba, M. Ogawa, K. Nakayama, T. Ohta, D. Endo, T. Ozaki, T. Inamasu, K. Sato and S. Komaba, *Proc. Natl. Acad. Sci. U. S. A.*, 2015, **112**, 7650-7655.

22. D.-H. Seo, J. Lee, A. Urban, R. Malik, S. Kang and G. Ceder, *Nat. Chem.*, 2016, **8**, 692-697.

23. M. H. Dickman and M. T. Pope, *Chem. Rev. (Washington, DC, U. S.)*, 1994, **94**, 569-584.

24. G. Amato, A. Arcoria, F. P. Ballistreri, G. A. Tomaselli, O. Bortolini, V. Conte, F. Di Furia, G. Modena and G. Valle, *J. Mol. Catal.*, 1986, **37**, 165-175.

25. R. Stomberg, *J. Less Common Met.*, 1988, **143**, 363-371.

26. M. Grzywa, W. Łasocha and D. Rutkowska-Żbik, *J. Solid State Chem.*, 2009, **182**, 973-982.

27. Y. J. Zhao, H. L. Feng, C. S. Zhao and Z. Q. Sun, *J. Inorg. Mater.*, 2011, **26**, 673-679.

28. C. L. Zhao, Q. D. Wang, Y. X. Lu, Y. S. Hu, B. H. Li and L. Q. Chen, *J. Phys. D-Appl. Phys.*, 2017, **50**.

29. J. Xu, R. D. Deshpande, J. Pan, Y.-T. Cheng and V. S. Battaglia, *J. Electrochem. Soc.*, 2015, **162**, A2026-A2035.

30. A. van Bommel and J. R. Dahn, *Electrochem. Solid-State Lett.*, 2010, **13**, A62-A64.

31. M. Sathiya, K. Ramesha, G. Rousse, D. Foix, D. Gonbeau, K. Guruprakash, A. S. Prakash, M. L. Doublet and J. M. Tarascon, *Chem. Commun. (Cambridge, U. K.)*, 2013, **49**, 11376-11378.

32. J. Bao, D. Wu, Q. Tang, Z. Ma and Z. Zhou, *Phys. Chem. Chem. Phys.*, 2014, **16**, 16145-16149.

33. K. Kang and G. Ceder, *Phys. Rev. B*, 2006, **74**, 0941051-0941057.

34. H. Konishi, T. Hirano, D. Takamatsu, A. Gunji, X. Feng and S. Furutsuki, *J. Power Sources*, 2015, **298**, 144-149.

35. M. N. Ates, S. Mukerjee and K. M. Abraham, *J. Electrochem. Soc.*, 2015, **162**, A1236-A1245.

36. T. Yamamoto, *X-Ray Spectrom.*, 2008, **37**, 572-584.

37. A. N. Mansour, C. A. Melendres, M. Pankuch and R. A. Brizzolara, *J. Electrochem. Soc.*, 1994, **141**, L69-L71.

38. R. J. Woolley, B. N. Illy, M. P. Ryan and S. J. Skinner, *J. Mater. Chem.*, 2011, **21**, 18592-18596.

39. M. Newville, in *Fundamentals of XAFS, Reviews of Minerology and Geochemistry*, eds. G. S. Henderson, D. R. Neuville and R. T. Downs, Mineralogical Society of America, 2014, vol. 78, pp. 33-74.

40. W. E. O'Grady, K. I. Pandya, K. E. Swider and D. A. Corrigan, *J. Electrochem. Soc.*, 1996, **143**, 1613-1617.

41. K. I. Pandya, R. W. Hoffman, J. McBreen and W. E. O'Grady, *J. Electrochem. Soc.*, 1990, **137**, 383-388.

42. A. K. Padhi, K. S. Nanjundaswamy and J. B. Goodenough, *J. Electrochem. Soc.*, 1997, **144**, 1188-1194.

43. S. R. S. Prabaharan, M. S. Michael, H. Ikuta, Y. Uchimoto and M. Wakihara, *Solid State Ionics*, 2004, **172**, 39-45.

44. J. Wolfenstine and J. Allen, *J. Power Sources*, 2005, **142**, 389-390.

45. J. R. Croy, M. Balasubramanian, D. Kim, S.-H. Kang and M. M. Thackeray, *Chem. Mater.*, 2011, **23**, 5415-5424.

46. B. Wu, Y. Ren, D. Mu, X. Liu and F. Wu, *J. Power Sources*, 2014, **272**, 183-189.

47. D. Aurbach, B. Markovsky, G. Salitra, E. Markevich, Y. Talyossef, M. Koltypin, L. Nazar, B. Ellis and D. Kovacheva, *J. Power Sources*, 2007, **165**, 491-499.

48. B. Markovsky, Y. Talyossef, G. Salitra, D. Aurbach, H.-J. Kim and S. Choi, *Electrochem. Commun.*, 2004, **6**, 821-826.

49. A. Kuzmin, J. Purans, A. Kuzmin and J. Purans, *Radiat. Meas.*, 2001, **33**, 583-586.

50. P. Kalyani and N. Kalaiselvi, *Sci. Tech. Adv. Mat.*, 2005, **6**, 689-703.

51. H. Arai, S. Okada, Y. Sakurai and J. i. Yamaki, *J. Electrochem. Soc.*, 1997, **144**, 3117-3125.

52. J. C. Knight and A. Manthiram, *J. Mater. Chem. A*, 2015, **3**, 22199-22207.

53. J. Zheng, G. Teng, C. Xin, Z. Zhuo, J. Liu, Q. Li, Z. Hu, M. Xu, S. Yan, W. Yang and F. Pan, *J. Phys. Chem. Lett*, 2017, **8**, 5537-5542.

54. J.-C. Dupin, D. Gonbeau, P. Vinatier and A. Levasseur, *Phys. Chem. Chem. Phys.*, 2000, **2**, 1319-1324.

55. K. Shimoda, T. Minato, K. Nakanishi, H. Komatsu, T. Matsunaga, H. Tanida, H. Arai, Y. Ukyo, Y. Uchimoto and Z. Ogumi, *J. Mater. Chem. A*, 2016, **4**, 5909-5916.

56. T. Matsuhara, Y. Tsuchiya, K. Yamanaka, K. Mitsuhara, T. Ohta and N. Yabuuchi, *Electrochemistry*, 2016, **84**, 797-801.

57. N. Yabuuchi, M. Nakayama, M. Takeuchi, S. Komaba, Y. Hashimoto, T. Mukai, H. Shiiba, K. Sato, Y. Kobayashi, A. Nakao, M. Yonemura, K. Yamanaka, K. Mitsuhara and T. Ohta, *Nat. Commun.*, 2016, **7**, 13814.

58. B. Strehle, K. Kleiner, R. Jung, F. Chesneau, M. Mendez, H. A. Gasteiger and M. Piana, *J. Electrochem. Soc.*, 2017, **164**, A400-A406.

59. M. Y. Yang, S. Kim, K. Kim, W. Cho, J. W. Choi and Y. S. Nam, *Adv. Funct. Mater.*, 2017, **27**.

Chapter 5: Synthesis and Characterisation of (1–*x*)$LiCoO_2$·*x*Li_4WO_5

5.1 Introduction

Lithium-rich layered metal oxides have garnered increasing research as lithium-ion battery cathodes in recent years. The most broadly studied method to date of achieving such materials is the incorporation of Li_2MnO_3 into the layered Li*M*O_2 structure, most notably where *M* = Co, Ni and Mn referred to as NMCs, such as $Li[Ni_{1/3}Mn_{1/3}Co_{1/3}]O_2$ (with a reversible specific capacity of up to 200 mA·h g^{-1}).[1] The incorporation of the lithium-rich Li_2MnO_3 greatly enhances the capacities of such materials, allowing capacities of 230-250 mA·h g^{-1} to be achieved.[2] In addition, the Li_2MnO_3 has a stabilising effect on the structure, exhibiting a thermal stability superior to that of the aluminium-stabilised NCA materials.[3] Elucidation of the origin of this additional capacity and stability has been extensively studied in recent years.

Some researchers propose that nano-domains of Li_2MnO_3 are incorporated within the Li*M*O_2 structure,[4, 5] as opposed to the formation of a true solid solution as suggested by others.[6, 7] Recently there has been evidence that the exact composition of the phases, cooling rate during synthesis and oxygen partial pressure all must be considered and controlled to obtain either a single phase lithium-rich layered compound or a nanocomposite material,[8-10] which may account for the discrepancy between researchers. The composite notation *x*Li_2MnO_3·(1-*x*)Li*M*O_2 and layered rock-salt notation $Li(Li_{1/3-2x/3}M_xMn_{2/3-x/3})O_2$ are therefore both used to describe lithium-rich layered oxides of this form, with the best electrochemical performances observed for $0.3 \leq x \leq 0.5$.[11]

Li_2MnO_3 can be considered as $Li(Li_{1/3}Mn_{2/3})O_2$ in the layered rock-salt Li*M*O_2 notation, whereby the lithium layers alternate with a Li and Mn layer along the *c*-axis, with a cation ratio of Li:Mn of 1:2. The manganese cations form a 'honeycomb' pattern around the lithium cations in the manganese-rich layer (Figure 5.1.1).[12] The oxide anions form a *ccp* array, whereby all cations are octahedrally coordinated by oxygen with tetrahedral interstitial sites remaining vacant. The stacking sequence of these layers can be also considered as an O3 structure where the oxygen layers are stacked in the -ABCABC- sequence (*i.e.* cubic-close packed), akin to the ideal Li*M*O_2 structure type.

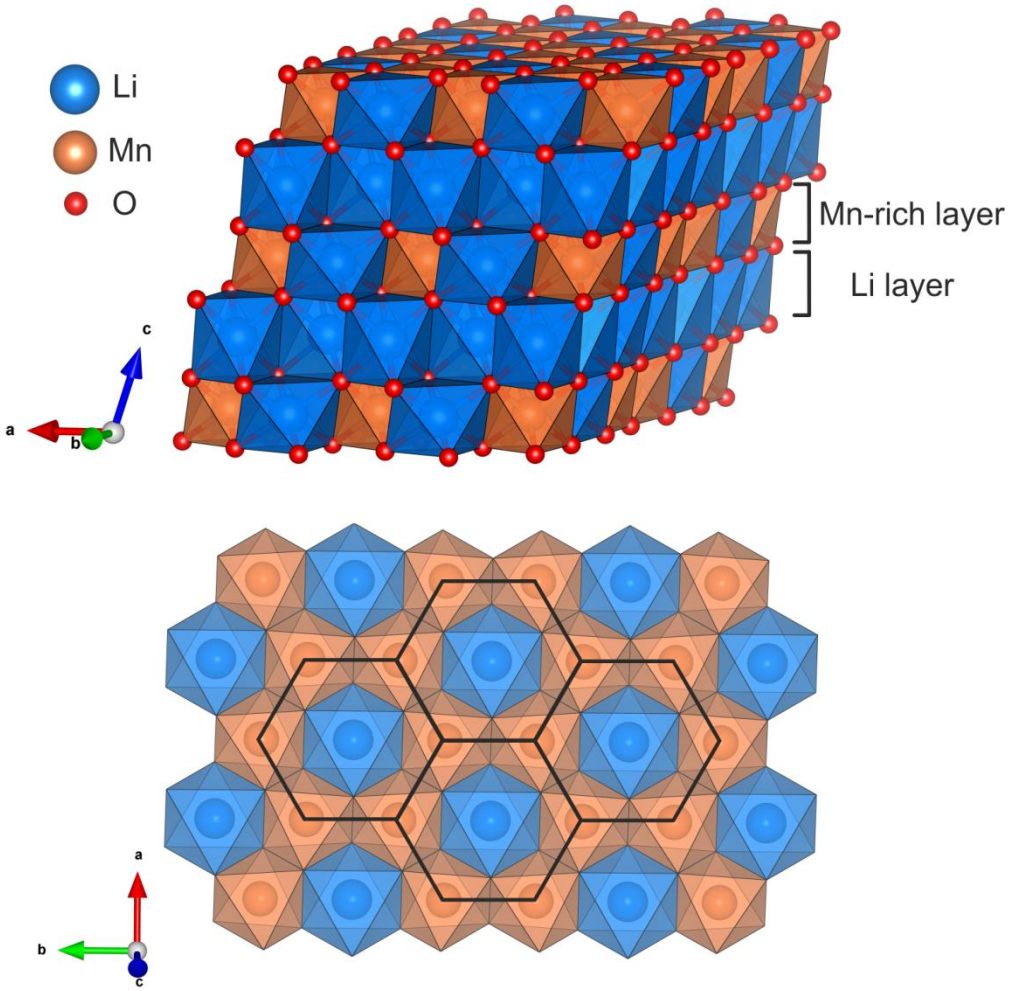

Figure 5.1.1: Representation of the Li_2MnO_3 structure showing the layered structure (*top*) and the 'honeycomb' arrangement of MnO_6 octahedra around LiO_6 octahedra in the Mn-rich layer (*bottom*)

Both Li_2MnO_3 (monoclinic unit cell, S.G. *C*2/*m*) and Li*M*O_2 (of the trigonal α-$NaFeO_2$ structure type, S.G. $R\bar{3}m$ as discussed in Chapter 1) possess fully occupied lithium layers, alternating with transition metal layers, in a close-packed rock-salt superstructure. The interlayer distance in both materials is ~4.7 Å (indicated by the position of the (001) reflection in Li_2MnO_3 and the (003) reflection in Li*M*O_2), which enables the incorporation of Li_2MnO_3 into the structure of $Li[Ni_{1/3}Mn_{1/3}Co_{1/3}]O_2$ on an atomic level.[13]

Initially Li_2MnO_3 was thought to be electrochemically inactive as a lithium ion battery cathode material, due to manganese being unable to exceed the +4 oxidation state at conventional operating voltages. However, upon charging to 4.5 V, Li_2MnO_3 phase becomes electrochemically activated towards Li^+ intercalation due to removal of oxygen from the structure during this first charge, without any oxidation of Mn^{4+}.[14] This process removes almost all of the lithium from the Li_2MnO_3 through removal of electrons from O^{2-} species, which can be represented overall as $Li_2MnO_3 \rightarrow Li_2O + MnO_2$. Only one mole of Li^+ can re-intercalate into the layers of the MnO_2 structure that remains after the loss of Li_2O,[15] attributed to oxygen vacancies in the structure. The fate of the oxygen removed from Li_2MnO_3 is thought to be deposition of Li-containing salts onto the surfaces of electrodes and some evolution of CO_2 and O_2 gas, driven by reactions with the electrolyte.[16-18] In lithium-rich layered oxide cathodes (of the form *x*Li_2MnO_3·(1-*x*)Li*M*O_2), the electrochemical activation of the Li_2MnO_3 phase results in a huge irreversible capacity loss (~200 mA·h g^{-1}) on the first cycle, however it is still higher than Li*M*O_2 alone. On subsequent electrochemical cycling, the transformation from the layered Li_2MnO_3 to a cubic spinel structure has been observed by *in-operando* XRD,[19] attributed to the migration of octahedral manganese cations to the lithium layers *via* tetrahedral sites upon delithiation.[20] The

formation of layered spinel domains results in voltage fading in these lithium-rich materials due to a lower voltage plateau *cf.* Li^+/Li^0, which would maintain the high capacity but ultimately result in a degradation of the energy density.[21] A larger domain size of Li_2MnO_3 has been found to hinder the transformation to the spinel phase, since the loss of Li_2O begins at the surface of the domains.[22, 23]

The instability of the electrochemical behaviour of lithium-rich cathodes based on the *x*Li_2MnO_3·(1-*x*)Li*M*O_2 systems was the reasoning for exploring rock-salt type Li_4WO_5 as a substitute for the Li_2MnO_3 component in such materials. The aim was to combine the lithium-rich Li_4WO_5 with Li*M*O_2-type layered lithium metal oxides in a solid solution, with a view to providing additional extractable lithium and stabilisation of the structure from the presence of W^{6+} ions. Li_4WO_5 has been reported to adopt a cubic disordered structure ($Fm\bar{3}m$, a = 4.15 Å) (Figure 5.1.2),[24] or a fully ordered $P\bar{1}$ triclinic structure (a = 5.109 Å, b = 7.716 Å, c = 5.061 Å, α = 101.8°, β = 101.78°, γ = 108.77°).[25]

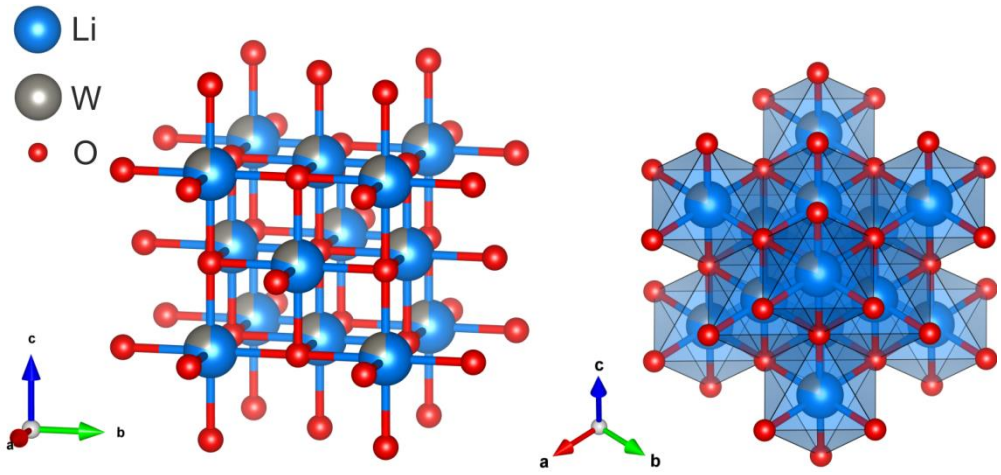

Figure 5.1.2: Representation of the cubic $Fm\bar{3}m$ Li_4WO_5 structure showing the mixed $^4/_5$Li:$^1/_5$W cation sites (*left*) and view down the (111) direction (*right*)

Interestingly the higher temperature form is the more ordered $P\bar{1}$ triclinic structure, possessing fully occupied Li layers alternating with W-rich layers, whereby the tungsten form distorted $[WO_6]^{6-}$ octahedra (Figure 5.1.3).[26] Li_4WO_5 has not to date been reported as a lithium ion battery cathode, due to the unlikely oxidation of tungsten beyond +6 at conventional LIB operating voltages. However, akin to Li_2MnO_3, it could be possible to incorporate the layered Li_4WO_5 into known Li*M*O_2 cathode materials to increase the discharge capacities by providing additional extractable lithium. In addition, this may promote anionic redox reactions without the problems of structural degradation and irreversible capacity loss due to loss of oxygen from the structure.

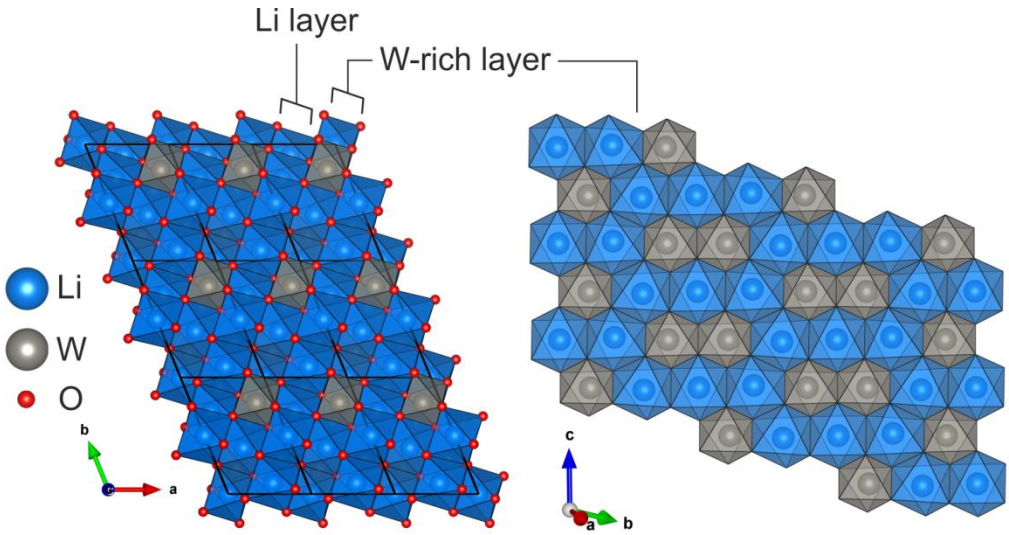

Figure 5.1.3: Representation of the triclinic $P\bar{1}$ structure of Li_4WO_5 with the unit cells outlined in black (*left*) and the tungsten ordering in the W-rich layer (*right*)

The layered lithium metal oxide chosen for doping with Li_4WO_5 was $LiCoO_2$, due to its facile synthesis of the layered structure. Additionally, the theoretical discharge capacity of $LiCoO_2$ is 273 mA·h g^{-1} but only ~137 mA·h g^{-1} (half of the available Li^+) can be safely and reversibly extracted. It has been shown that the presence of Co^{3+} in the Li*M*O_2 component of *x*Li_2MnO_3·(1-*x*)Li*M*O_2 enhances the oxygen loss from the Li_2MnO_3 component due to orbital overlap with the O^{2-} 2*p* band.[27]

For this project, a small amount of Li_4WO_5 (in comparison to Li_2MnO_3·Li*M*O_2 systems) was incorporated into the $LiCoO_2$ structure with the aim to maintain a relatively high specific discharge capacity, due to the high relative atomic mass of tungsten which, like Mn^{4+} in Li_2MnO_3, is not expected to be a redox active cation.

If we consider $LiCoO_2$ as $Li_5Co_5O_{10}$, and Li_4WO_5 as $Li_8W_2O_{10}$ so both formulae contain the same moles of oxygen, the substitution of Li_4WO_5 into $LiCoO_2$ can be considered as follows:

$$(1\text{-}x)LiCoO_2 \cdot xLi_4WO_5 \equiv (1\text{-}x)Li_5Co_5O_{10} \cdot xLi_8W_2O_{10}$$

For example, if $x = 0.1$:

$$0.9(Li_5Co_5O_{10}) + 0.1(Li_8W_2O_{10}) \equiv Li_{4.5}Co_{4.5}O_9 + Li_{0.8}W_{0.2}O_1$$

The sum of these components gives a formula of $Li_{5.3}Co_{4.5}W_{0.2}O_{10}$. Normalising to two anions in the rock-salt type formula by dividing this formula by a factor of five gives a composition of $Li_{1.06}Co_{0.90}W_{0.04}O_2$ where $x = 0.1$. The general formula can therefore be considered as $Li_{1+3x/5}Co_{1-x}W_{2x/5}O_2$, or $Li[Li_{3x/5}Co_{1-x}W_{2x/5}]O_2$, to give an electroneutral rock-salt structure (with tungsten in the +6 oxidation state and cobalt in the +3 oxidation state).

5.2 Experimental Methods

5.2.1 Synthesis

The general solid solution formula (1-*x*)$LiCoO_2$·*x*Li_4WO_5 can also be denoted as $Li[Li_{3x/5}Co_{1-x}W_{2x/5}]O_2$ in the layered rock-salt notation. Members of the series between $0.0025 \leq x \leq 0.1000$ were synthesised on a 2 g scale. For each member of the series, appropriate amounts of $LiOH·H_2O$ (99.95%, Sigma Aldrich), Co_3O_4 (99.9985%, Alfa Aesar, dried overnight at 200 °C) and WO_3 (99.9%, Sigma Aldrich, dried overnight at 200 °C) were hand ground in an agate pestle and mortar to achieve the required ratio of Li:Co:W. Pellets of the starting materials were pressed using a 13 mm diameter pellet die in a uniaxial press under a pressure of 1-2 tons. The pellets were loaded into alumina crucibles and fired at 900 °C for 20 h in air with a heating and cooling rate of 5 °C min^{-1}.

The end members of the solid solution, $LiCoO_2$, and both the cubic and triclinic polymorphs of Li_4WO_5 were also synthesised.

$LiCoO_2$ was synthesised by hand grinding stoichiometric quantities of $LiOH·H_2O$ and pre-dried Co_3O_4 in an agate pestle and mortar using the same reaction procedure as detailed for the doped materials.

Cubic Li_4WO_5 was synthesised using Li_2O_2 (99.5%, Pfaltz & Bauer) and pre-dried WO_3 with a 4:1 molar ratio of Li:W. The reagents were handled in a He-filled glove box due to the hygroscopic nature of Li_2O_2. The reagents were hand ground in a pestle and mortar and loaded into an alumina crucible, fired at 550 °C for 24 h in a tube furnace under a dynamic O_2 atmosphere. The products were stored in a desiccator due to the hygroscopic nature of Li_4WO_5.

Triclinic Li_4WO_5 was synthesised using $LiOH·H_2O$ and pre-dried WO_3 in a 4:1 molar ratio of Li:W. The same reaction conditions as detailed for the doped materials were used.

5.2.2 Powder X-Ray Diffraction

Powder diffraction data were obtained using a Co PANalytical diffractometer in Bragg-Brentano geometry. To assess the change in lattice parameters over the solid solution series, a secondary standard of highly crystalline silicon (99.999%, Alfa Aesar) was included in the sample (1:4 by wt).

5.2.3 ICP-OES

Elemental analysis by ICP-OES is detailed in Chapter 2. Samples (~10 mg) were dissolved using concentrated hydrochloric acid (10 mL, 37%, Fisher Scientific) and made up to 100 mL using deionised water.

5.2.4 Scanning Electron Microscope (SEM) Imaging

Surface imagining of the particles was achieved using a Hitachi S-4800 Field-Emission Scanning Electron Microscope operating at an accelerating voltage of 3-5 kV. The samples were sputter-coated with gold nanoparticles to aid conduction.

5.2.5 Cathode Testing

Coin cells were assembled as detailed in Chapter 2. For the rate capability measurements, initial C-rate was C/10 for the first five cycles, then the discharge rate was adjusted every ten cycles to C/2, C, 2C, 4C, 8C and C/2 between 3.0 and 4.2 V for 65 cycles in total (where 1C = 137.5 mA g^{-1}). The cathode composition was 84% active material, 8% PVDF binder and 8% Super C carbon by weight. Thanks go to Dr Nicholas Drewett (University of Liverpool) for supplying the electrochemical testing data.

5.3 Structural Analysis

5.3.1 End Members of (1-*x*)$LiCoO_2$·*x*Li_4WO_5 Series

Lithium cobalt oxide, $LiCoO_2$, crystallises into the rhombohedral $R\bar{3}m$ space group, adopting the α-$NaFeO_2$-type layered rock-salt structure (Figure 5.3.1). The intention of doping of Li_4WO_5 into the layered structure of $LiCoO_2$ is to replace a small amount of redox active Co^{3+} (L.S. ionic radius = 0.545 Å in an octahedral coordination environment) with Li^+ (0.76 Å) and W^{6+} (0.6 Å) within the cobalt layer, whilst maintaining the fully occupied lithium layers. As a result, the interlayer distance is expected to increase due to repulsion between highly charged tungsten ions, hence lengthening the *c*-axis. Additionally, expansion within the *a*-*b* plane is expected due to the larger ionic radii of the dopant cations *cf*. Co^{3+}.

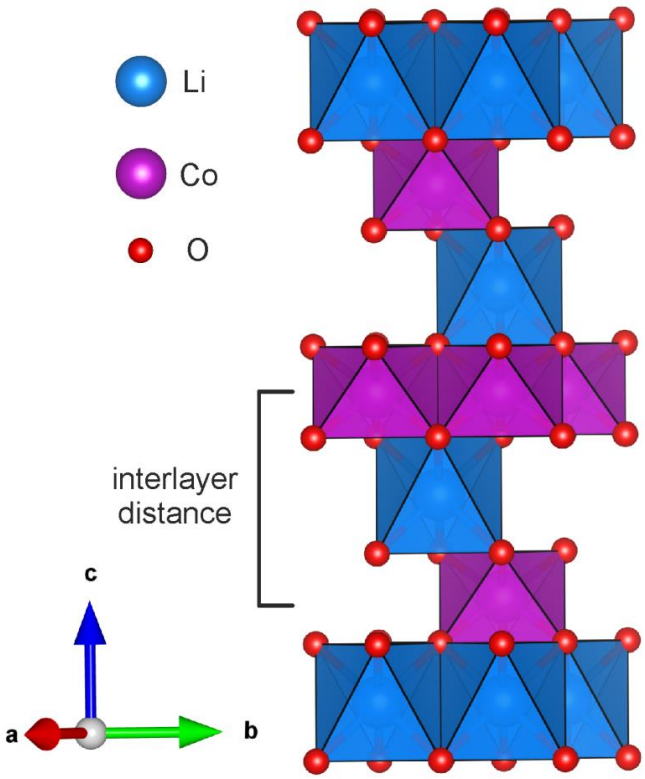

Figure 5.3.1: Representation of the layered $LiCoO_2$ structure, indicating the cobalt interlayer distance along the *c*-axis

Synthesis of Li_4WO_5 under the same reaction conditions as used for the (1-*x*)$LiCoO_2$·*x*Li_4WO_5 series resulted in the trigonal $P\bar{1}$ polymorph (Figure 5.3.2). Le Bail fitting was performed to the Li_4WO_5 $P\bar{1}$ sample, and the interlayer distance between close-packed layers was found to be 4.79 Å from the position of the $(1\bar{1}0)$ reflection. The interlayer distance for the $LiCoO_2$ was found from the (003) reflection position to be 4.69 Å, suggesting that solid solution formation should be possible due to these similar distances.

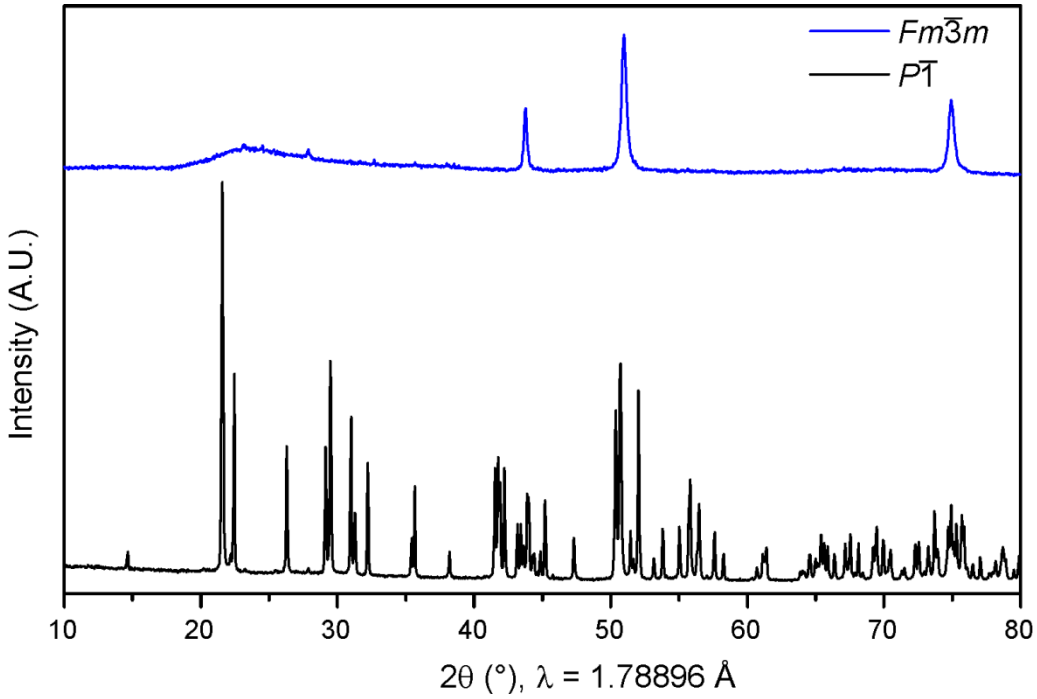

Figure 5.3.2: PXRD of $Fd\bar{3}m$ and $P\bar{1}$ polymorphs of Li_4WO_5

5.3.2 PXRD of (1-*x*)$LiCoO_2$·*x*Li_4WO_5 Series

To quantitatively assess the variation of the lattice parameters, crystalline silicon (S.G. $Fd\bar{3}m$, a = 5.43053(7) Å) was included in the samples for analysis by PXRD. The $R\bar{3}m$ symmetry of the parent $LiCoO_2$ phase was maintained, that is the Bragg reflections of (1-*x*)$LiCoO_2$·*x*Li_4WO_5 index to the $LiCoO_2$ phase (x = 0.000) but with variations in lattice parameters (Figure 5.3.3).

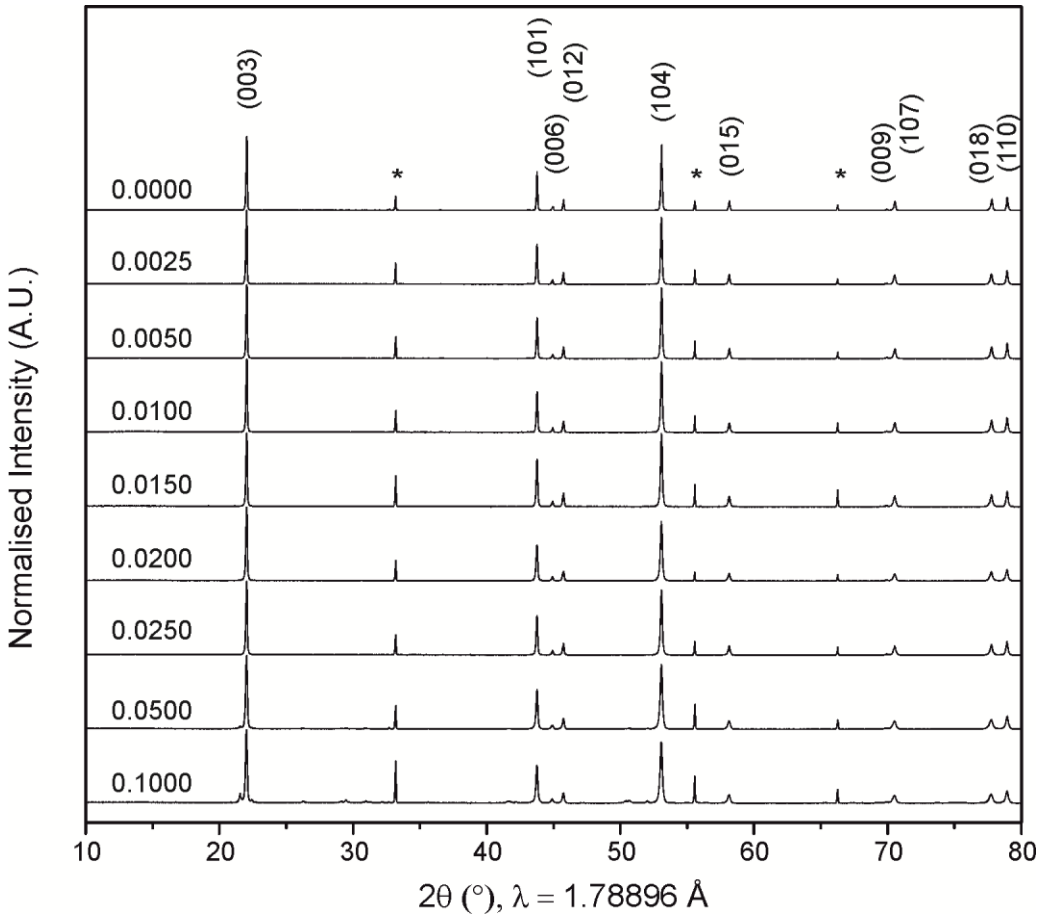

Figure 5.3.3: PXRD for varying *x* in (1-*x*)$LiCoO_2$·*x*Li_4WO_5 denoting (*hkl*) for the $R\bar{3}m$ phase;

* indicate Si internal standard peaks

A small reflection at 2θ = 21.55° appears for values of $x \geq 0.025$, which is attributed to the $P\bar{1}$ Li_4WO_5 impurity. To prove that the impurity phase is Li_4WO_5, the Le Bail fit for the sample with nominal composition $0.70LiCoO_2 \cdot 0.30Li_4WO_5$ is shown in Figure 5.3.4. The molar percentages of each phase were determined by Rietveld refinement as 89.6(8)% $LiCoO_2$ and 10.4(3)% Li_4WO_5.

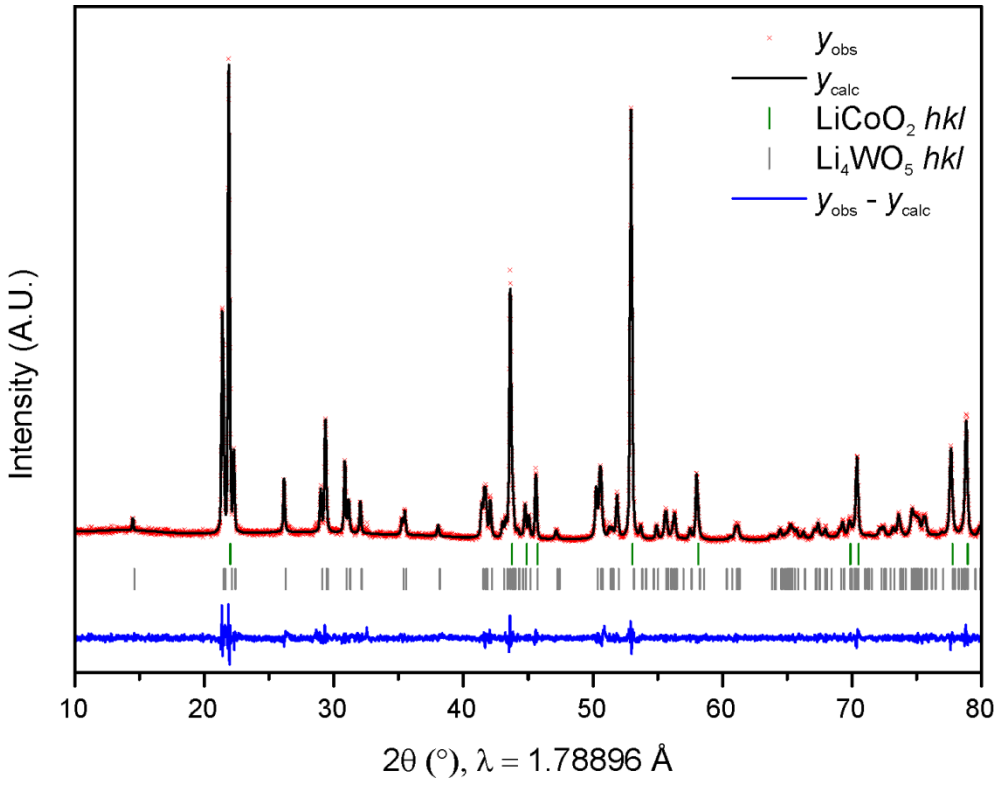

Figure 5.3.4: Le Bail fit of 0.70$LiCoO_2$·0.30Li_4WO_5 showing the presence of $LiCoO_2$ and Li_4WO_5 phases

The reflections corresponding to the $R\bar{3}m$ phase shift to lower values of 2θ with increasing values of *x* (Figure 5.3.5), providing evidence of doping of the $LiCoO_2$ phase with an increase in the lattice parameters. The peaks also visibly broaden with increasing values of *x*, which could indicate compositional heterogeneity or a decrease in the crystallinity. For the *x* = 0.100 sample, the atomic percentage of the rhombohedral $LiCoO_2$-type phase was determined to be 98.1(6)%, with the remaining 1.9(2)% being the Li_4WO_5 $P\bar{1}$ phase from Rietveld refinement. This proves that some tungsten and additional lithium must be incorporated into the parent $LiCoO_2$ structure, since 10at% of Li_4WO_5 was added. The low dopant solubility of Li^+ and W^{6+} for Co^{3+} may be due to the large difference in the ionic radii.[28]

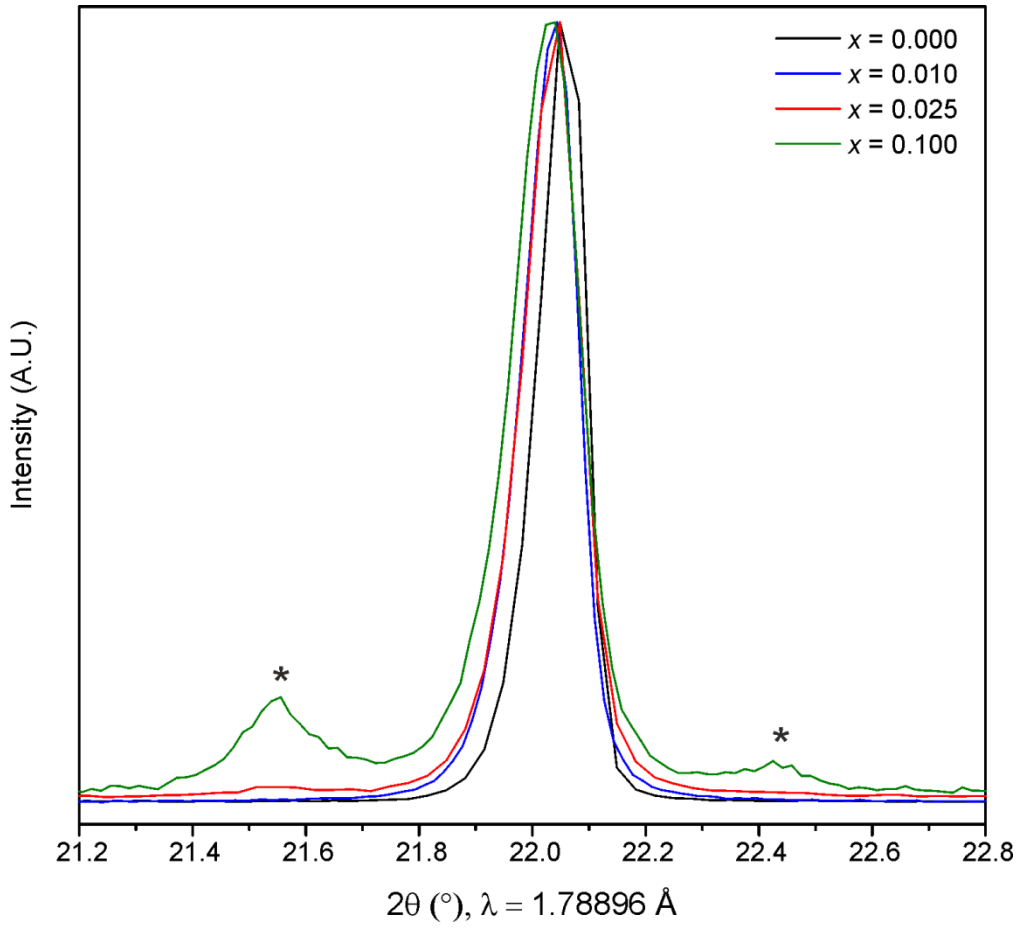

Figure 5.3.5: Normalised first Bragg reflection (003) for selected values of *x*. * indicates reflections due to Li_4WO_5 ($P\bar{1}$) phase

The lattice parameters of the (1-*x*)$LiCoO_2$·*x*Li_4WO_5 $R\bar{3}m$ phases were refined using the Le Bail method whilst fixing the lattice parameters of the silicon internal standard. The ratio of *c*/*a* unit cell parameters is a general indication of trigonal distortion in hexagonal systems,[29] with a ratio > 4.899 meaning a greater level of cation ordering. Values below this indicate distortion of the oxygen lattice.[30] Throughout this series, the ratio of *c*/*a* is > 4.992 as shown in Table 5.3.1. This ratio, along with clear splitting of the (006)/(012) and (018)/(110) doublets (indicated in for all members of the series in Figure 5.3.3) are characteristic of a layered structure without considerable cation mixing.[31]

The intensity of the peak corresponding to the (003) Miller index was greater than that of (104), which is consistent throughout all of the doped samples, as shown by the $I_{(003)}/I_{(104)}$ values in Table 5.3.1. Research into the structure of $LiCoO_2$ with varying levels of disorder has shown through Rietveld refinement that a decrease in the ratio of $I_{(003)}/I_{(104)}$ is indicative of disordering of Co^{3+} and Li^+ between layers, as the intensity of (003) decreases with increased Co^{3+} mixing with Li^+ layers.[32-34] Such disorder has been found to be detrimental to the electrochemical performance of $LiCoO_2$.[35] In the context of doped $LiCoO_2$, within the $Li_{1-x}(Mn_yCo_{1-y})_{1+x}O_2$ series for example, the $I_{(003)}/I_{(104)}$ ratio was found to decrease from 1.45 for y = 0.04, to 0.92 for y = 0.19.[33] This result indicated partial disordering of Li^+ and $(Mn_yCo_{1-y})^{3+}$ within the layered structure as an increasing amount of Mn^{3+} was substituted for Co^{3+}. The greater intensity of the (003) reflections *cf.* (104) for the (1-*x*)$LiCoO_2$·*x*Li_4WO_5 series therefore supports the conclusion that there is minimal disordering of cobalt and tungsten into the lithium layers. However, further detailed structural analysis would be required to determine if the greater intensity of the (003) reflection is due the presence of W^{6+} which has a much greater X-ray scattering factor than Co^{3+} and Li^+. Assessment of the near-spherical particle morphology of x = 0.010 and x = 0.025 by SEM imaging (Figure 5.4.4, Figure 5.4.5) suggest preferred orientation along the *c*-axis is not the reason for the greater intensity of (003) *cf.* (104) reflections.

Table 5.3.1: Values of unit cell parameters obtained by Le Bail refinement using internal standard.

Numbers in parentheses represent 3σ

x	***a*** **(Å)**	***c*** **(Å)**	***V*** **(Å^3)**	***c*/*a***	$I_{(003)}/I_{(104)}$
0.0000	2.81595(7)	14.0589(6)	96.545(6)	4.9926	1.131
0.0025	2.81610(2)	14.0634(5)	96.587(6)	4.9939	1.099
0.0050	2.81616(5)	14.0617(4)	96.579(3)	4.9932	1.038
0.0100	2.81637(6)	14.0622(5)	96.597(6)	4.9930	1.041
0.0150	2.81650(6)	14.0633(5)	96.613(6)	4.9932	1.005
0.0200	2.81687(6)	14.0647(5)	96.648(6)	4.9930	1.237
0.0250	2.81653(6)	14.0622(5)	96.608(6)	4.9927	1.130
0.0500	2.81634(6)	14.0700(6)	96.648(6)	4.9958	1.145
0.1000	2.81651(8)	14.0714(7)	96.669(6)	4.9960	1.131

5.3.3 Variation of Lattice Parameters

The trend in lattice parameters was established using the Le Bail method by fitting to the $R\bar{3}m$ cell. The *a*-axis was found to lengthen as the value of *x* increases from 0.00 to 0.020. The increase in the *a* lattice parameter is attributed to the larger ionic radii of Li^+ and W^{6+} in comparison to Co^{3+} (Figure 5.3.6). A decrease in the *a*-axis is observed from $x = 0.020$ to $x = 0.025$, further decreasing to $x = 0.050$, and gradually increases again when $x = 0.100$.

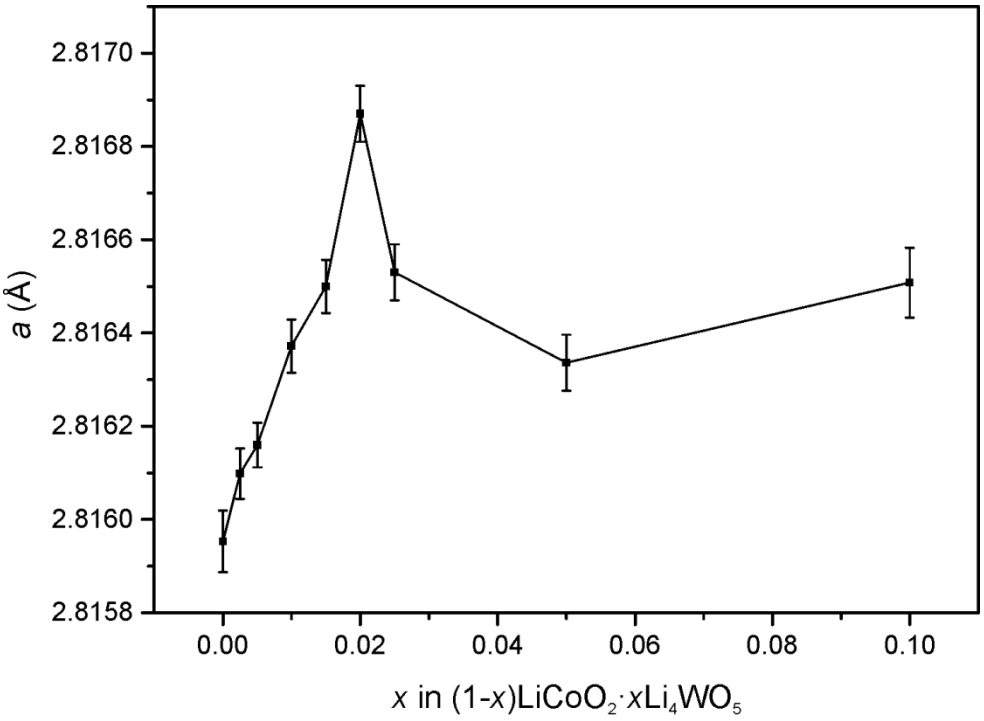

Figure 5.3.6: Variation of lattice parameter *a* with doping level. Error bars represent 3σ

The increase in the unit cell along the *c*-axis (*i.e.* the interlayer separation) can be accounted for due to the presence of tungsten ions within the CoO_6 layers, which is expected to increase the layer separation to minimise repulsion between the highly charged ions (Figure 5.3.7).

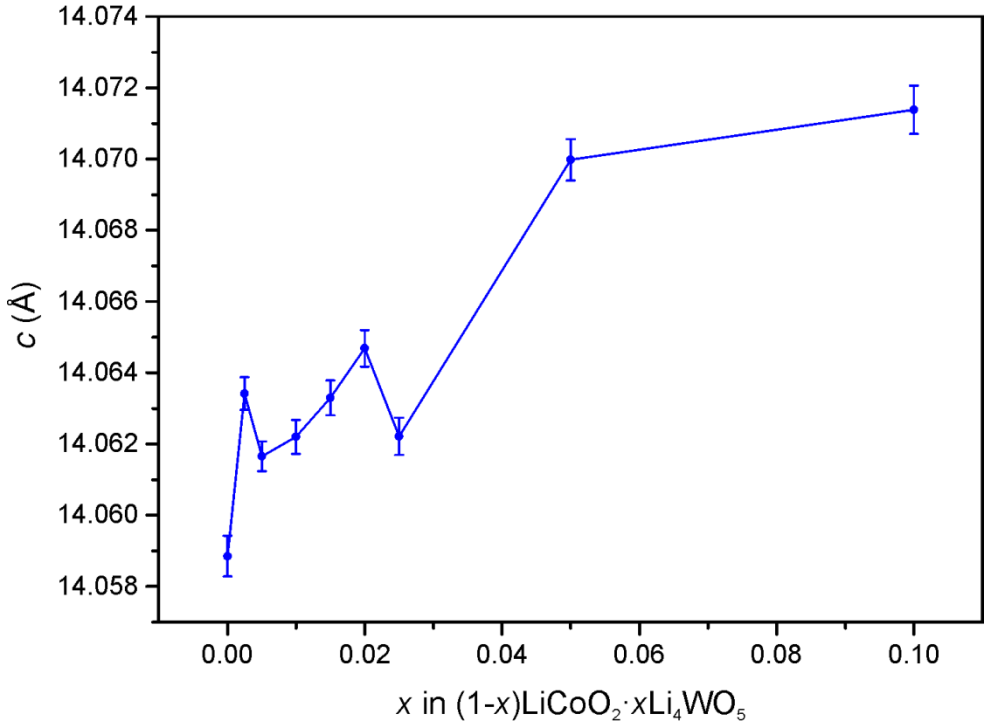

Figure 5.3.7: Variation of lattice parameter *c* with doping level. Error bars represent 3σ

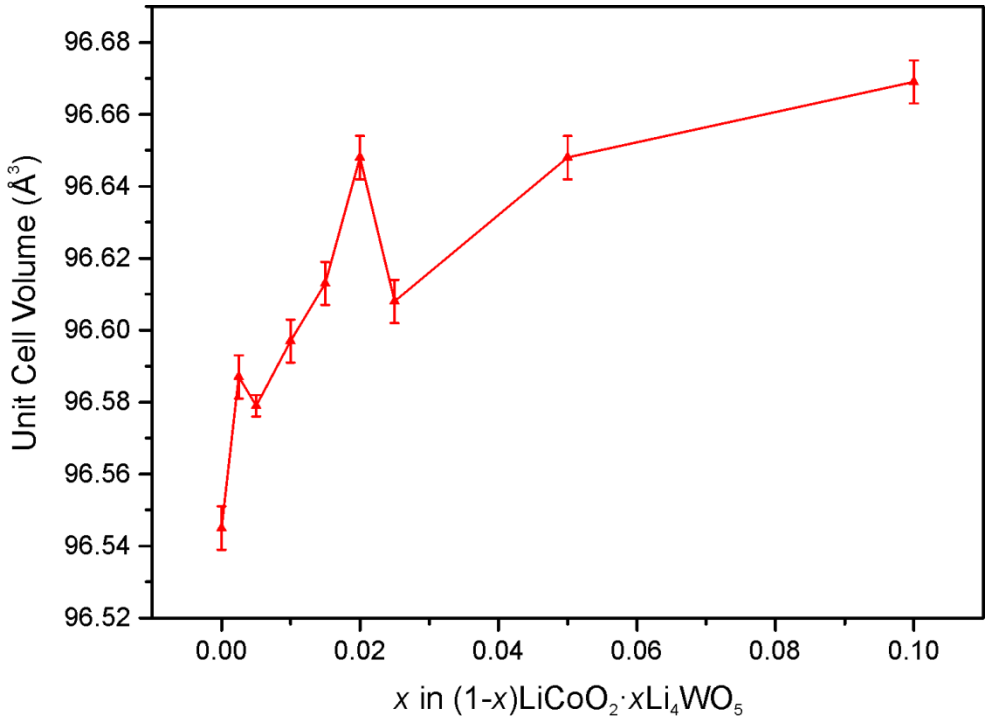

Figure 5.3.8: Variation of unit cell volume with doping level. Error bars represent 3σ

The unit cell volume generally increases with *x* (Figure 5.3.8). The decrease in lattice parameters from $x = 0.020$ to $x = 0.025$ is attributed to the separation of $P\bar{1}$ polymorph

of Li_4WO_5, meaning the doping limit to obtain a solid solution is $0.020 \leq x \leq 0.025$. Above this level of doping, biphasic samples were obtained. A similar trend was observed in the $LiCo_{1-x}Zr_xO_2$ system,[36] whereby Co^{3+} was substituted for Zr^{4+} (ionic radius 0.86 Å), the lattice parameters were also found to increase up until the doping limit of $x = 0.01$ was reached. After this limit, biphasic samples were obtained, indicated by the emergence of a Li_2ZrO_3 impurity, and the lattice parameters of the majority $R\bar{3}m$ phase were found to decrease.

The relative increase along the *c*-axis is greater than within the *a*-*b* plane (Figure 5.3.9), showing that the increase in the interlayer separation is the largest contributing factor to the increase in overall cell volume with increasing *x*. Computational and experimental studies (*e.g.* EXAFS) reported in the literature have concluded that within these $LiCoO_2$ systems, the increase in the *c*-axis (due to dopants,[36] deviation from 1:1 stoichiometry *etc.*)[37] is primarily accommodated by expansion of the lithium layer, rather than the cobalt layer.[38]

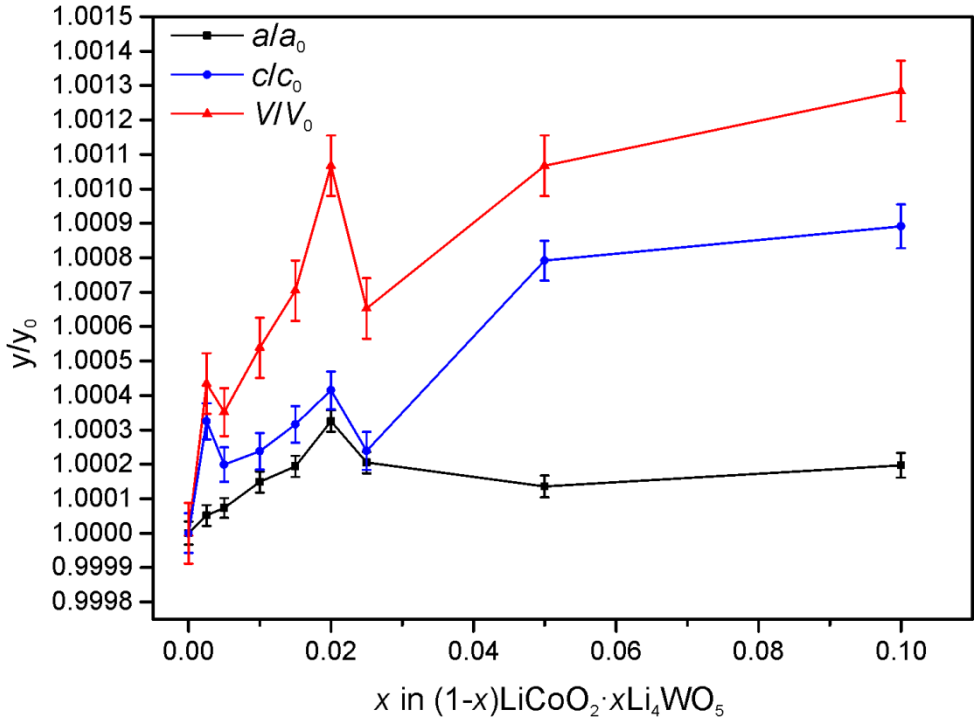

Figure 5.3.9: Trend in all lattice parameters with *x* obtained from Figure 5.3.6, Figure 5.3.7 and Figure 5.3.8), where y_0 are values for $LiCoO_2$; error bars represent 3σ

In the *x*Li_2MnO_3·(1-*x*)$LiCoO_2$ system studied by Manthiram *et al.*, an almost linear increase in unit cell parameters with *x* was observed, attributed to the greater amount of larger Li^+ ions within the lattice, since the ionic radius of Mn^{4+} is less than Co^{3+}.[27]

Elemental analysis by ICP-OES was performed on the parent $LiCoO_2$ phase, 0.99$LiCoO_2$·0.01Li_4WO_5 (*x* = 0.010) and 0.975$LiCoO_2$·0.025Li_4WO_5 (*x* = 0.025). For 0.99$LiCoO_2$·0.01Li_4WO_5 the nominal composition can be denoted as $Li_{1.006}Co_{0.99}W_{0.004}O_2$. However elemental analysis determined that the structure was slightly deficient in lithium, with a composition of $Li_{0.981(4)}Co_{1.015(3)}W_{0.00409(4)}O_2$ (normalised to two total cations per formula unit). Similarly for 0.975$LiCoO_2$·0.025Li_4WO_5, with a nominal composition of $Li_{1.015}Co_{0.975}W_{0.01}O_2$, the composition was found to be $Li_{0.982(4)}Co_{1.007(3)}W_{0.0103(3)}O_2$, however the Co and W content are within 3σ of both nominal compositions. The ionic ratio of Li:Co in the

analogously prepared parent $LiCoO_2$ was determined as 0.950(5):1.00(10); therefore it is possible that more Li than expected was lost during synthesis at 900 °C, which would give a lower ratio of Li:Co in the overall composition when normalised to two total cations per formula unit, suggesting lithium vacancies may be present.

5.4 Electrochemical Behaviour

5.4.1 Galvanostatic Cycling

Members of the solid solution where x = 0.010 and x = 0.025 were chosen for electrochemical testing. The theoretical specific capacity of x = 0.010, corresponding to a nominal rock-salt formula of $Li_{1.006}Co_{0.99}W_{0.004}O_2$ was calculated as 270.6 mA·h g^{-1}, based on the removal of 0.99 Li^+ from the structure by full oxidation of Co^{3+} to Co^{4+}. Likewise, for x = 0.025 ($Li_{1.015}Co_{0.975}W_{0.01}O_2$), the theoretical specific capacity was calculated as 265.7 mA·h g^{-1}. The end member of the solid solution, $LiCoO_2$ (x = 0.000, theoretical specific capacity of 273 mA·h g^{-1}) was also tested for comparison (Figure 5.4.1).

The voltage load curve of the doped materials is improved *cf.* the $LiCoO_2$ parent, with a smoother increase between 4-4.2 V indicating stabilisation of the charge plateau. The discharge load curve has a similar profile to $LiCoO_2$, attributed to the reduction of $Co^{3.5+}$ to Co^{3+} occurring at 3.9 V. From the load curve, the initial discharge capacity of the parent phase is 120.7 mA·h g^{-1}. Doping the parent $LiCoO_2$ with 1 at% Li_4WO_5 (0.99$LiCoO_2$·0.01Li_4WO_5) increases this capacity by 2.7% to 124.1 mA·h g^{-1}, whereas doping with 2.5 at% Li_4WO_5 (0.975$LiCoO_2$·0.025Li_4WO_5) increases the capacity by 5.8% to 128.2 mA·h g^{-1}. The greater total discharge capacity for the doped materials is attributed to the additional lithium content, but it is possible anionic redox also plays a role in providing the extra capacity akin to the lithium-rich layered oxide systems

discussed in Section 5.1, although further detailed characterisation would be required to explore this possibility.

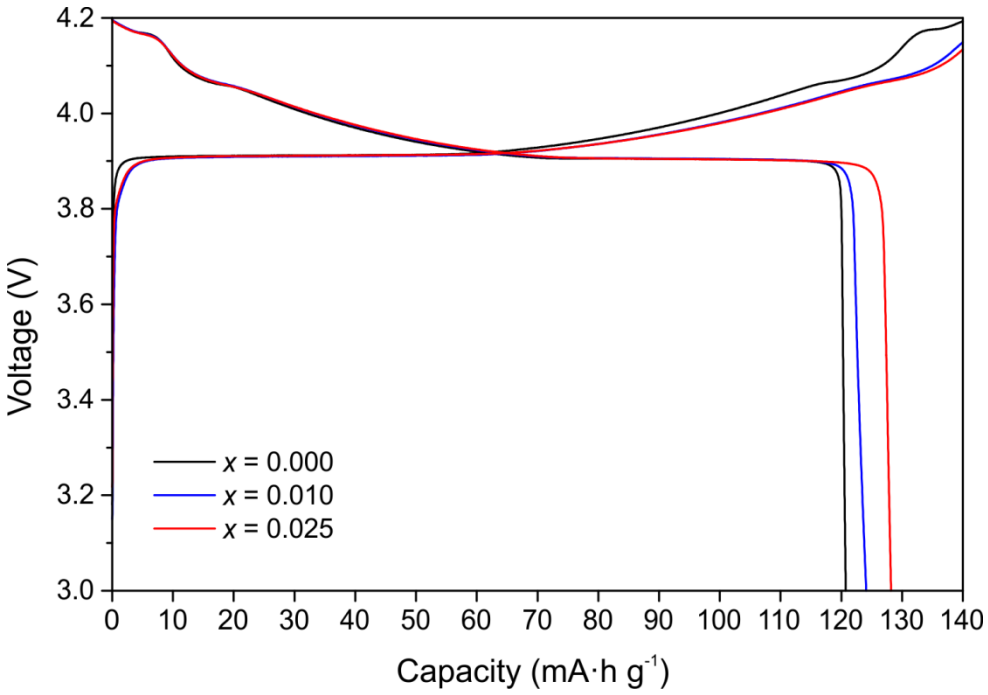

Figure 5.4.1: Voltage load curves the first electrochemical cycle of *x* = 0.000, 0.010 and 0.025 cycled between 3-4.2 V, where C = 137.5 mA g^{-1}

5.4.2 Rate Capability Measurements

As shown in Figure 5.4.2, the rate performance of the doped materials is much improved compared to the parent $LiCoO_2$, with a greater proportion of the capacity extracted at fast discharge rates and minimal loss of capacity over ten cycles as the C-rate cycles is doubled. Furthermore, although $0.975LiCoO_2·0.025Li_4WO_5$ exhibits a greater total discharge capacity, the rate capability of $0.99LiCoO_2·0.01Li_4WO_5$ is better overall: it can be seen that the reduction in capacity as the C-rate is doubled is lower than for *x* = 0.025. The capacities for the 6th and 65th cycle for each material (where the C-rate begins at and returns to C/2) and the capacity retentions between these cycles are reported in Table 5.4.1. Likewise the discharge capacities for the 46th

and 55th cycle, where the discharge rate is highest at 8C, and the capacity retention between those 10 cycles are also reported.

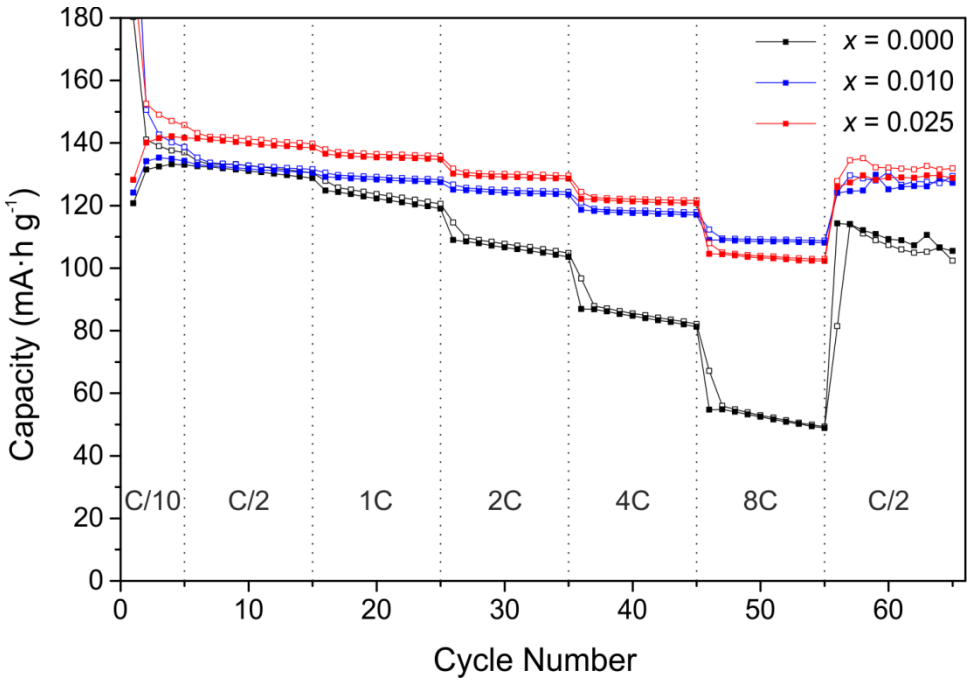

Figure 5.4.2: Rate capability measurements (waterfall plot) for *x* = 0.00, 0.010 and 0.025 cycled between 3-4.2 V, with the C-rate varied as indicated. *Filled* squares represent discharge capacity, *open* squares represent charge capacity

Table 5.4.1: Comparison of the discharge capacities and capacity retention between C/2 and 8C discharge rates of the parent $LiCoO_2$ (*x* = 0.000) and *x* = 0.010 and 0.025. Values taken from the rate capability graph

	C/2 C-rate			**8C C-rate**		
	Discharge capacity of n^{th} cycle (mA·h g^{-1})					
x	**6th**	**65th**	**Retention (%)**	**46th**	**55th**	**Retention (%)**
0.000	132.6	105.5	79.6	54.7	48.9	89.3
0.010	133.1	127.2	95.6	109.0	108.1	99.3
0.025	141.4	128.8	91.1	104.5	102.3	97.8

By comparison of the amount of capacity extracted at 8C for $x = 0.00$, 0.010 and 0.025, $x = 0.010$ exhibits the best rate capability. Increasing the discharge current rate to 8C enables 81.9% of the capacity obtained at C/2 to be extracted for $x = 0.010$. For $x = 0.025$, 73.9% can be extracted at 8C *cf.* C/2. For comparison, in the parent $LiCoO_2$, only 41.3% of the capacity obtained at C/2 is observed at 8C.

The enhanced rate capability is attributed in part to the increase in the lattice parameters, particularly along the *c*-axis within the lithium layers. Since lithium ions diffuse through the octahedral sites in the lithium layer *via* tetrahedral interstices, the expansion of this layer through doping with larger ions facilitates diffusion through the layer by lowering the activation energy barrier.[38] In addition, $1Co^{3+}$ is effectively being substituted for $^4/_5Li^+$ and $^1/_5W^{6+}$, for which the sum of these charges is +2. Therefore, the overall average oxidation state of cobalt is expected to increase slightly to maintain charge neutrality within the rock-salt structure, most likely accompanied by oxygen vacancies as occurs in the $LiCo_{1-x}Mg_xO_2$ system (whereby Co^{3+} is substituted for larger Mg^{2+} ions) as proved by ^{7}Li MAS NMR.[39, 40] The co-existence of cobalt ions in multiple oxidation states and the presence of oxygen vacancies could therefore improve the electronic conductivity within the material, contributing to the improved rate performance.[41] It is possible that the presence of additional Li^+ and W^{6+} ions stabilise the structure, as exhibited by the enhanced capacity retention *cf.* parent $LiCoO_2$. This has been known to occur in $LiCo_{1-x}Mg_{x/2}Zr_{x/2}O_2$ system for example, attributed to the dopant ions preventing vacancy ordering and stabilising the material towards lithium ion diffusion.[42-44]

5.4.3 SEM Imaging

No post-synthetic processing, such as ball milling to reduce particle size was applied to any of these materials. To explore other possible reasons for the considerable

improvement in the rate capability with low levels of dopants, the particle morphology of $LiCoO_2$, $0.99LiCoO_2·0.01Li_4WO_5$ and $0.975LiCoO_2·0.025Li_4WO_5$, were examined using SEM imaging. The parent $LiCoO_2$ (x = 0.000) exhibits large angular particles of 1-10 μm in size (Figure 5.4.3).

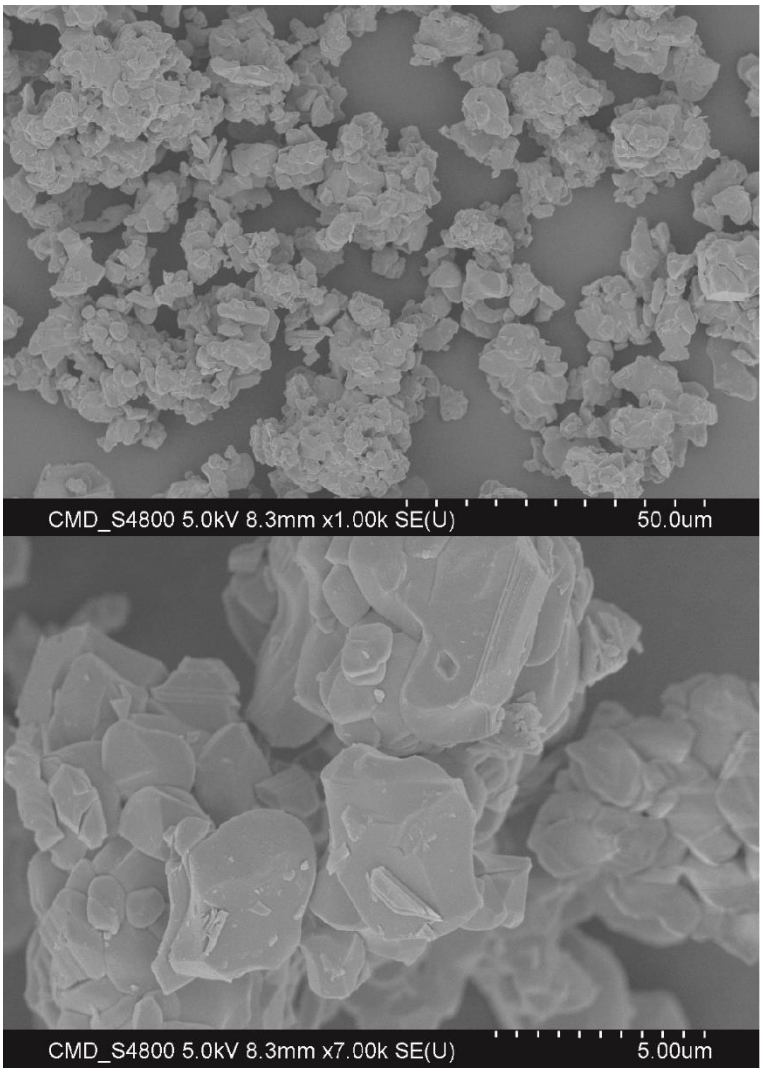

Figure 5.4.3: SEM images of parent $LiCoO_2$ phase displaying large micrometre-sized angular particles

The x = 0.010 sample exhibits larger tens of micrometre sized aggregates composed of smaller near-spherical particles of up to 1 μm (Figure 5.4.4).

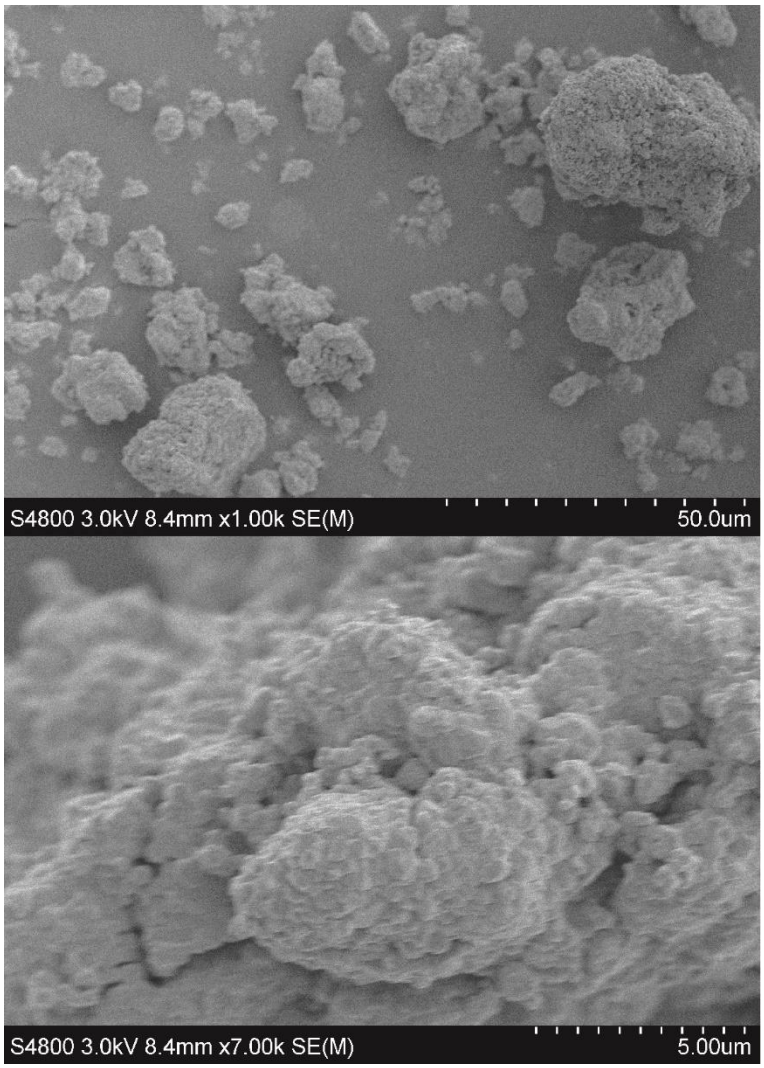

Figure 5.4.4: SEM images of 0.99$LiCoO_2$·0.01Li_4WO_5 displaying large aggregates composed of distinct smaller near-spherical particles

Similar sized large aggregates were observed for x = 0.025, but composed of smaller near-spherical particles up to ~100 nm in size (Figure 5.4.5).

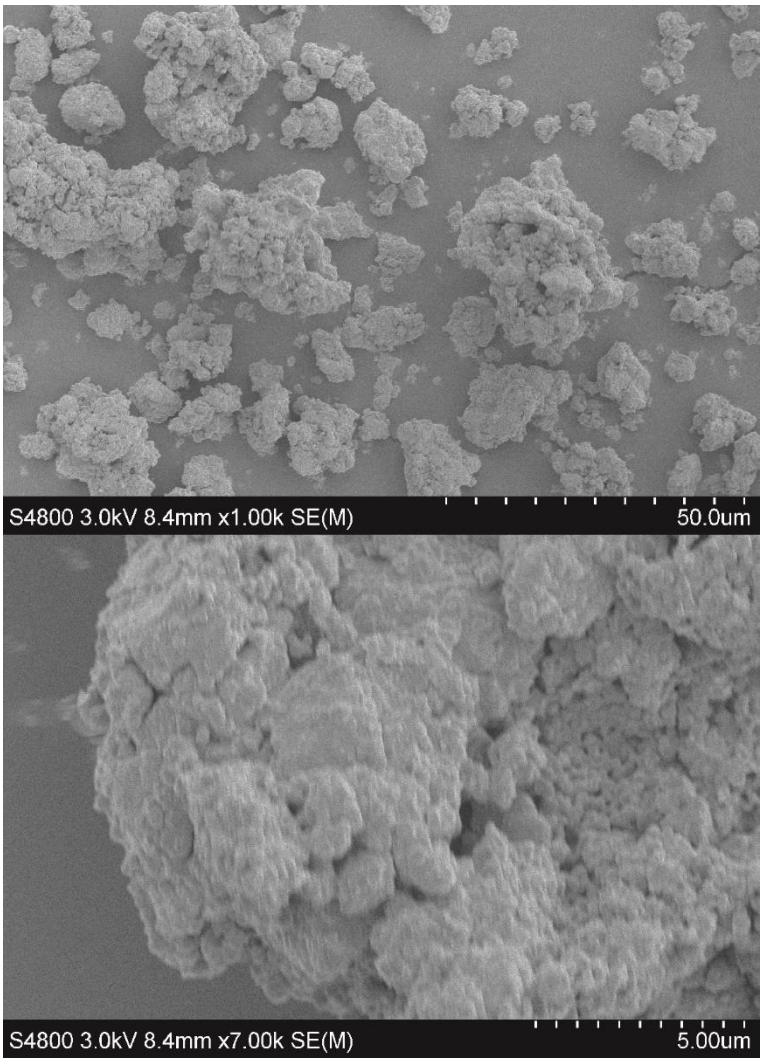

Figure 5.4.5: SEM images of 0.975$LiCoO_2$·0.025Li_4WO_5 displaying aggregates composed of distinct smaller near-spherical particles

From SEM imaging compared at the same level of magnification, it was determined that the particle size for the doped samples was much smaller (hence a larger surface area) compared to the undoped $LiCoO_2$ parent phase prepared analogously, with the smallest particle size observed for $x = 0.025$. The decreased particle size of the doped materials may account for the improved discharge capacities at high discharge rates, due to faster Li^+ diffusion at the particle surface compared to within the bulk material in $LiCoO_2$.[45, 46] A greater surface area of the cathode tends to result in rapid capacity fading due to increased reactions with the electrolyte trapping lithium within the SEI

layers (see Chapter 1 and Chapter 6), however $0.99LiCoO_2 \cdot 0.01Li_4WO_5$ and $0.975LiCoO_2 \cdot 0.025Li_4WO_5$ show much improved capacity retention *cf.* $LiCoO_2$.

This decrease in crystallite size may partly account for the peak broadening observed in the PXRD. It is possible that the inclusion of Li_4WO_5 within the phase inhibits grain growth and improves the electronic and ionic conduction through the cathode material, without degradation of the capacity over prolonged cycling. Alternatively, a number of varying compositions of (1-*x*)$LiCoO_2$·*x*Li_4WO_5 may be present, resulting in smaller agglomerates of particles of slightly different compositions. Similarly, a reduction of particle size *cf.* $LiCoO_2$ was observed in the $LiCo_{1-x}Sb_xO_2$ system, with particle size decreasing with increasing levels of antimony, attributed to variance in the exact composition of each particle.[47]

5.4.4 Summary

The presence of a small amount of Li_4WO_5 phase visible in the $x = 0.025$ PXRD does not seem to be detrimental to the capacity, although the smaller grain size may account for the lower capacity retention *cf.* $x = 0.010$. This is because a greater surface area of the cathode will be wetted by the electrolyte, promoting parasitic side reactions which lead to capacity fading (as observed in Chapter 6). The superior rate performance of the doped materials at higher discharge rates also suggests that if tungsten or cobalt cations were present in the lithium layer, either in the pristine materials or following electrochemical cycling, they are not blocking the lithium diffusion channels. This supports the conclusion that fully ordered rock-salt type structures are obtained in the as-synthesised materials, and that the ordering is maintained upon electrochemical cycling.

5.5 Conclusions and Future Work

A new series of ordered lithium-rich rock-salt type cathode materials have been synthesised, crystallising in the $R\bar{3}m$ space group and tested for their electrochemical properties. The doping limit of Li_4WO_5 into the structure of $LiCoO_2$ appeared to be $0.020 \leq x \leq 0.025$ (2-2.5at%), as determined by laboratory PXRD, for formation of a solid solution using the synthetic protocol detailed in this chapter. Above this level of doping, biphasic samples were obtained, however the electrochemical properties were still improved in comparison to the parent $LiCoO_2$. Doping was confirmed by analysis of the lattice parameters of the $R\bar{3}m$ phase using an internal standard using laboratory X-ray diffraction. Analysis of the peak intensities supports the hypothesis that the doped materials maintained the ordered, layered α-$NaFeO_2$ type structure.

By comparison to analogously prepared $LiCoO_2$, the presence of a small amount (1at% and 2.5at%) of Li_4WO_5 doped into the parent $LiCoO_2$ was found to considerably improve the discharge capacity (by 2.7% and 5.8%, respectively). In addition, the capacity retention and electrochemical performance at increased discharge rates were much improved. When increasing the rate of discharge from C/2 to 8C (*i.e.* discharging the cell 16 times quicker), only 41% of the discharge capacity obtained at C/2 could be extracted at 8C for the parent $LiCoO_2$. However, with $0.99LiCoO_2$·$0.01Li_4WO_5$, 82% of the capacity could be extracted at the highest C-rate (8C), and 74% for $0.975LiCoO_2$·$0.025Li_4WO_5$.The improved performance at high discharge rates is attributed to a combination of the increased interlayer separation, as determined from Le Bail analysis, and a decrease in particle size, both of which assists diffusion of lithium ions throughout the structure. Additionally, the dopants are thought to enhance the electronic conductivity and stability of this cathode material.

Neutron powder diffraction and high-resolution synchrotron X-ray diffraction data should be employed to allow Rietveld refinement of the materials that appeared single phase using laboratory PXRD. This would conclusively determine which atomic site the tungsten and lithium occupy.

Future work would include electrochemical testing of the higher level of dopants (*e.g.* $0.90LiCoO_2 \cdot 0.10Li_4WO_5$) to determine whether the capacity continues to increase. In addition, it would be interesting to establish whether the oxidation state of cobalt can be safely charged beyond +3.5 to allow more lithium to be extracted *via* the cationic redox process without the evolution of oxygen – it could be possible for the presence of Li_4WO_5 to suppress the formation of Co_3O_4 and $O_{2(g)}$ at elevated temperatures. Furthermore, if this were thought to be occurring, additional characterisation by XANES and HAXPES spectroscopy (as employed in Chapter 4) would help determine the oxidation states of cobalt and oxygen at various stages of electrochemical cycling.

Initial attempts at synthesis of the opposite end of the solid solution, *i.e*. doping a small amount of $LiCoO_2$ into the parent Li_4WO_5 did not result in phase pure samples and were not studied further. In addition, attempts to dope Li_4WO_5 and Li_4MoO_5 into $LiNi_{1/3}Mn_{1/3}Co_{1/3}O_2$ and $LiFeO_2$ did not result in phase pure samples. However, the synthetic options were not exhausted and perhaps mechanochemical synthesis (high energy ball milling of the starting materials to obtain the product as used in the synthesis of layered $0.5Li_2MnO_3 \cdot 0.5LiCoO_2$)[48] or sol-gel synthesis would aid the attainment of these solid solutions, or increase the values of *x* where single-phase materials could be obtained within the (1-*x*)$LiCoO_2$·*x*Li_4WO_5 system.

5.6 References

1. K. M. Shaju and P. G. Bruce, *Adv. Mater. (Weinheim, Ger.)*, 2006, **18**, 2330-2334.
2. F. Amalraj, D. Kovacheva, M. Talianker, L. Zeiri, J. Grinblat, N. Leifer, G. Goobes, B. Markovsky and D. Aurbach, *J. Electrochem. Soc.*, 2010, **157**, A1121-A1130.
3. S.-H. Kang and M. M. Thackeray, *J. Electrochem. Soc.*, 2008, **155**, A269-A275.
4. R. E. Ruther, H. Dixit, A. M. Pezeshki, R. L. Sacci, V. R. Cooper, J. Nanda and G. M. Veith, *J. Phys. Chem. C*, 2015, **119**, 18022-18029.
5. K. A. Jarvis, Z. Deng, L. F. Allard, A. Manthiram and P. J. Ferreira, *Chem. Mater.*, 2011, **23**, 3614-3621.
6. Z. Lu, Z. Chen and J. R. Dahn, *Chem. Mater.*, 2003, **15**, 3214-3220.
7. J. Bréger, M. Jiang, N. Dupré, Y. S. Meng, Y. Shao-Horn, G. Ceder and C. P. Grey, *J. Solid State Chem.*, 2005, **178**, 2575-2585.
8. E. McCalla, J. Li, A. W. Rowe and J. R. Dahn, *J. Electrochem. Soc.*, 2014, **161**, A606-A613.
9. E. McCalla, C. M. Lowartz, C. R. Brown and J. R. Dahn, *Chem. Mater.*, 2013, **25**, 912-918.
10. E. McCalla, A. W. Rowe, R. Shunmugasundaram and J. R. Dahn, *Chem. Mater.*, 2013, **25**, 989-999.
11. J. Yan, X. Liu and B. Li, *RSC Adv.*, 2014, **4**, 63268-63284.
12. M. H. Rossouw, D. C. Liles and M. M. Thackeray, *J. Solid State Chem.*, 1993, **104**, 464-466.
13. M. M. Thackeray, S.-H. Kang, C. S. Johnson, J. T. Vaughey, R. Benedek and S. A. Hackney, *J. Mater. Chem.*, 2007, **17**, 3112-3125.
14. H. Chen and M. S. Islam, *Chem. Mater.*, 2016, **28**, 6656-6663.
15. C. S. Johnson, N. Li, J. T. Vaughey, S. A. Hackney and M. M. Thackeray, *Electrochem. Commun.*, 2005, **7**, 528-536.
16. C. Jacob, J. Jian, Q. Su, S. Verkhoturov, R. Guillemette and H. Wang, *ACS Appl. Mater. Interfaces*, 2015, **7**, 2433-2438.
17. N. Yabuuchi, K. Yoshii, S.-T. Myung, I. Nakai and S. Komaba, *J. Am. Chem. Soc.*, 2011, **133**, 4404-4419.
18. B. Strehle, K. Kleiner, R. Jung, F. Chesneau, M. Mendez, H. A. Gasteiger and M. Piana, *J. Electrochem. Soc.*, 2017, **164**, A400-A406.
19. D. Mohanty, S. Kalnaus, R. A. Meisner, K. J. Rhodes, J. L. Li, E. A. Payzant, D. L. Wood and C. Daniel, *J. Power Sources*, 2013, **229**, 239-248.
20. Y. Kan, Y. Hu, C.-K. Lin, Y. Ren, Y.-K. Sun, K. Amine and Z. Chen, *Phys. Chem. Chem. Phys.*, 2014, **16**, 20697-20702.

21. M. Bettge, Y. Li, K. Gallagher, Y. Zhu, Q. Wu, W. Lu, I. Bloom and D. P. Abraham, *J. Electrochem. Soc.*, 2013, **160**, A2046-A2055.
22. S. Kaewmala, P. Chantrasuwan, N. Wiriya, S. Srilomsak, W. Limphirat, P. Limthongkul and N. Meethong, *Sci. Rep.*, 2017, **7**, 13196.
23. B. Song, H. Liu, Z. Liu, P. Xiao, M. O. Lai and L. Lu, *Sci. Rep.*, 2013, **3**, 3094.
24. G. Blasse, *Z. Anorg. Allg. Chem.*, 1964, **331**, 44-50.
25. R. Hoffmann and R. Hoppe, *Z. Anorg. Allg. Chem.*, 1989, **573**, 157-169.
26. P. Tabero and A. Frackowiak, *J. Therm. Anal. Calorim.*, 2017, **130**, 311-318.
27. X. Xiang, J. C. Knight, W. Li and A. Manthiram, *J. Phys. Chem. C*, 2014, **118**, 23553-23558.
28. Y. Koyama, H. Arai, I. Tanaka, Y. Uchimoto and Z. Ogumi, *J. Mater. Chem. A*, 2014, **2**, 11235-11245.
29. C. Julien, A. Mauger, K. Zaghib and H. Groult, *Materials*, 2016, **9**, 595.
30. K. M. Shaju, G. V. Subba Rao and B. V. R. Chowdari, *Electrochim. Acta*, 2002, **48**, 145-151.
31. Y. Gao, M. V. Yakovleva and W. B. Ebner, *Electrochem. Solid-State Lett.*, 1998, **1**, 117-119.
32. E. Zhecheva and R. Stayanova, *J. Solid State Chem.*, 1994, **109**, 47-52.
33. R. Stoyanova, E. Zhecheva and L. Zarkova, *Solid State Ionics*, 1994, **73**, 233-240.
34. R. Gupta and A. Manthiram, *J. Solid State Chem.*, 1996, **121**, 483-491.
35. J. Kim, P. Fulmer and A. Manthiram, *Mater. Res. Bull.*, 1999, **34**, 571-579.
36. S. H. Kim and C.-S. Kim, *J. Electroceram.*, 2008, **23**, 254.
37. A. Basch, L. de Campo, J. H. Albering and J. W. White, *J. Solid State Chem.*, 2014, **220**, 102-110.
38. K. Kang and G. Ceder, *Phys. Rev. B*, 2006, **74**, 094105.
39. S. Levasseur, M. Ménétrier and C. Delmas, *Chem. Mater.*, 2002, **14**, 3584-3590.
40. S. Levasseur, M. Ménétrier and C. Delmas, *J. Power Sources*, 2002, **112**, 419-427.
41. P. Ghosh, S. Mahanty and R. N. Basu, *Electrochim. Acta*, 2009, **54**, 1654-1661.
42. H. Y. Xu, S. Xie, C. P. Zhang and C. H. Chen, *J. Power Sources*, 2005, **148**, 90-94.
43. H.-S. Kim, T.-K. Ko, B.-K. Na, W. I. Cho and B. W. Chao, *J. Power Sources*, 2004, **138**, 232-239.
44. M. V. Reddy, T. W. Jie, C. J. Jafta, K. I. Ozoemena, M. K. Mathe, A. S. Nair, S. S. Peng, M. S. Idris, G. Balakrishna, F. I. Ezema and B. V. R. Chowdari, *Electrochim. Acta*, 2014, **128**, 192-197.
45. Q. Liu, M. S. Javed, C. Zhang, Y. Li, C. Hu, C. Zhang, M. Lai and Q. Yang, *Nanoscale*, 2017, **9**, 5509-5516.

46. A. Moradabadi and P. Kaghazchi, *Phys. Chem. Chem. Phys.*, 2015, **17**, 22917-22922.

47. J.-P. Yu, Z.-H. Han, X.-H. Hu, H. Zhan, Y.-H. Zhou and X.-J. Liu, *Electrochim. Acta*, 2014, **121**, 301-306.

48. S. Kim, C. Kim, Y.-I. Jhon, J.-K. Noh, S. H. Vemuri, R. Smith, K. Y. Chung, M. S. Jhon and B.-W. Cho, *J. Mater. Chem.*, 2012, **22**, 25418-25426.

Chapter 6: Synthesis by Flame Spray Pyrolysis

6.1 Introduction

6.1.1 Principles of the Technique

Flame spray pyrolysis (FSP) is a continuous synthetic technique which enables the production of typically nanosized particles from the introduction of liquid precursors into a flame. Precursors in the liquid form, such as soluble metal salts, are required for this technique as they must first be atomised before being introduced to the flame for the reaction to occur: this atomisation is achieved either by heating or using an ultrasonic nebuliser. The composition of the flame includes a fuel gas such as propane, mixed with oxygen gas, the ratios of which can be carefully adjusted to alter the temperature and size of the flame. An additional inert carrier gas such as nitrogen is often employed to aid control of the flow of atomised precursors into the flame. The generated aerosol or vapour enters the flame, either by aid of the carrier gas or externally sprayed into the flame *via* the ultrasonic nebuliser nozzle, and finally the powdered product is collected by a cooled collection plate or a bag filter, for example.[1] Vapours rapidly form from the liquid precursors in the heat of the flame, undergoing chemical reactions to form intermediate molecules. The molecules continue to undergo surface reactions and coagulate, eventually forming particles for collection as the temperature cools further from the flame by deposition onto a surface (Figure 6.1.1, Figure 6.2.1).[2]

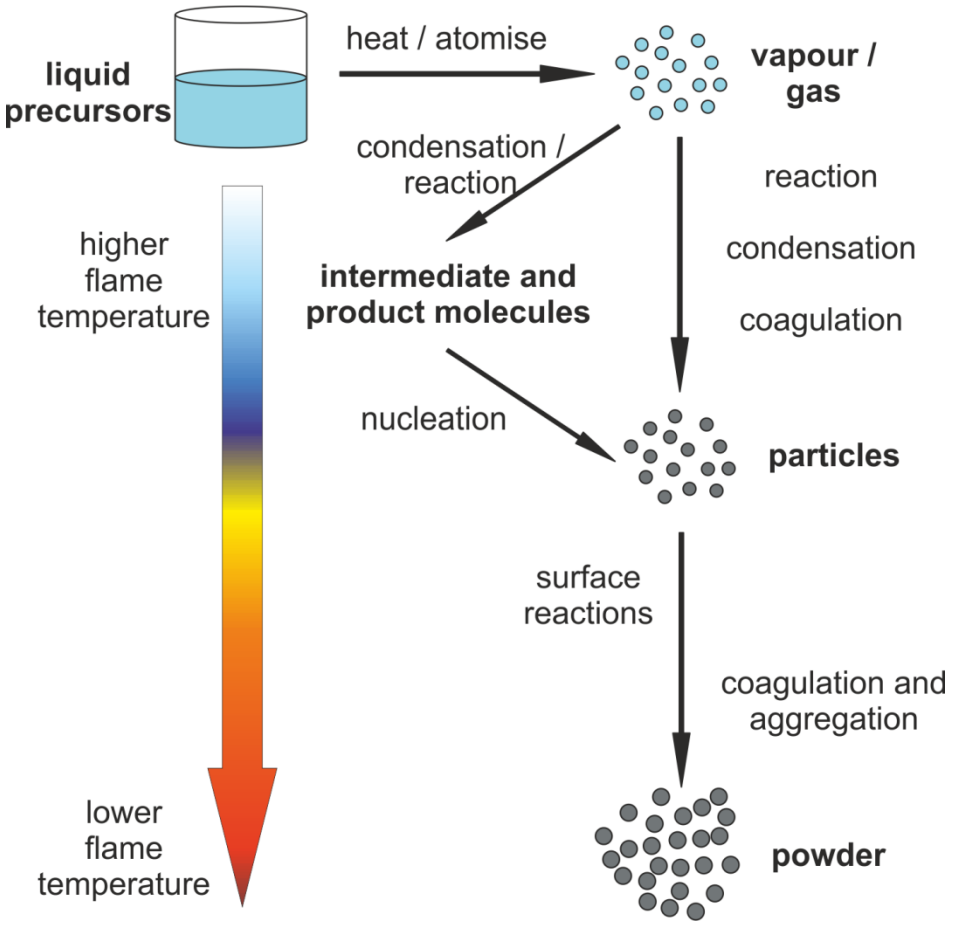

Figure 6.1.1: Schematic of particle formation from liquid precursors by flame spray pyrolysis (adapted from Pratsinis *et al.* 1998)[2]

This synthetic technique has been employed on industrial scales for the rapid production of nanocarbon and nanosized simple metal oxides such as TiO_2, SiO_2 and α-Al_2O_3.[2] FSP can also be applied to the synthesis of more complex composite materials such as lanthanide-doped phosphors and metal/metal oxide catalysts.[3-6] This technique is not limited to simple oxides, and has been utilised for the synthesis of pure metal nanoparticles, metal carbonates, metal phosphates and metal halides.[3,7-11]

The particle size and morphology of the product depends on many variable synthetic conditions: the gas flow rates (hence flame temperature), the nature and rate of injection and concentration of the precursors, presence of additives, the solvents employed *etc*.[12-17]

Flame spray pyrolysis has been shown to allow access to metastable kinetic phases, in contrast to the thermodynamic phases expected from traditional ceramic synthesis.[18] For example, synthesis of $Y_3Al_5O_{12}$ (YAG) by Nyman *et al.* was found to be unsuccessful by spray pyrolysis, instead obtaining a variety of kinetic products.[19] Synthesis by FSP employs shorter residence times coupled with fast heating rates, which leads to effective quenching. Quenching is caused by fast particle exits and is controllable by increasing the carrier gas flow which decreases residence times in the high temperature region of the flame. Overall, this affords particles of lower diameter. Conversely, increasing the flow rate of liquid precursors is thought to increase residence times in the flame by creating larger flames and prolonging the sintering and coalescence processes resulting in larger, more crystalline particles.[20] Additional heat treatment following synthesis by FSP is often required to improve crystallinity; fast reaction time periods limit the crystallisation period which can result in undesired amorphous products.[21] Unfortunately this post-synthetic heat treatment results in the agglomeration of nanoparticles, increasing the mean particle diameter.[22] Careful tuning of the annealing process is required to have mild conditions for a short period of time, in order to balance the effect of improved crystallinity *vs*. the increase in particle size, in addition to maintaining the kinetic phase, if it were obtained.

6.1.2 LIB Cathodes by FSP

It is known that the size, morphology and crystallinity of a given cathode composition in LIBs all impact on the cell performance; ergo it is crucial to control, characterise and optimise these parameters. It has been shown that a smaller particle size can improve lithium diffusion kinetics through the cathode material,[23] but this can increase the likelihood of parasitic reactions with the liquid electrolyte as more particle surface is exposed and hence cyclability can be compromised. Nanoparticles of cathodes have

been shown to increase the reactivity of $LiCoO_2$ with the dimethyl carbonate (DMC) component in the electrolyte, in comparison to commercial $LiCoO_2$, generating ethane and oxygen gas.[24] The passivating SEI film that forms on the surface of the cathode particles can increase impedance by lowering particle contact, resulting in lower capacity and cyclability and hindering lithium ion diffusion, particularly at higher C-rates.[25] It is apparent that a balance needs to be struck between minimising parasitic reactions with electrolytes but maximising lithium ion conduction and electrical conductivity. The lithium ion diffusivity and electronic conduction (hence optimum cathode particle size) is dependent on the microstructure of the electrode, the phase transitions occurring during cycling *etc*.

Particle morphology affects electrochemical performance in a number of ways. For example, $LiMnO_2$ nanorods were shown to have considerably better discharge capacities and cyclability than their nanoparticles analogues, despite having a larger particle size.[26] This may be attributed to the mechanism of Li^+ ion diffusion facilitated parallel in one dimension due to the particle shape, or perhaps the improved packing density of rods in comparison to spheres improving electronic and ionic conduction. It is also important to consider how Li^+ ion diffusion across grain boundaries may be assisted or impeded by the packing of particles with unusual morphology.[27]

Materials with higher crystallinity, indicated by X-ray diffraction experiments, have been shown to have better electrochemical performance due to strong interactions between atoms in the lattice resulting in broadening of the energy bands giving better overlap, demonstrated in the case of lithium manganese oxide spinels.[28]

Most commonly lithium metal oxide cathodes have been synthesised by FSP, leaving the realm of polyanionic cathode synthesis largely unexplored. The rationale behind

using this technique is to produce highly crystalline, pure nanoparticles of cathode materials with a rapid rate of controllable synthesis, allowing an increased surface area and improved lithium intercalation efficiency. However, a larger surface area will increase contact with the liquid electrolytes and promote the likelihood of parasitic reactions of the cathode with the electrolyte, resulting in consumption of the cathode material, capacity fading and a loss of cyclability. For this reason the coating of nanoparticles by inert metal oxides has been explored to help reduce the reactivity of the cathode with the electrolyte and potentially improve electrochemical performance whilst reducing electrolyte oxidation.[29] It is thought that some coatings can enhance the structural stability of delithiated cathodes and suppress phase transitions, the extent of which would be dependent on the combination of the cathode and the identity and thickness of the coating material.[30]

Considering that the surface structure of cathode materials is important to the electrochemical performance of lithium ion batteries, surface coating is a viable method to help overcome the disadvantages associated with the use of cathode nanoparticles and has been demonstrated by FSP methods; such as coating $LiCoO_2$ with lithium boron oxide (LBO) glass,[31] and carbon-coating $LiFePO_4$.[32] However it is important to consider Li^+ and electronic conduction (or the viability of electron tunnelling) through the coatings, the possible reduction of surface area and the loss of specific capacity caused by an increase in overall mass in comparison to the mass of the electrochemically active material.

The synthesis of common LIB metal oxide cathodes such as $LiCoO_2$, $LiMn_2O_4$, $LiNi_{0.5}Mn_{1.5}O_4$, $LiNi_{1/3}Co_{1/3}Mn_{1/3}O_2$ and LiV_3O_8 have been demonstrated by FSP.[31,33-36] Typical particle diameters varied from 40-100 nm, with heat treatment proving necessary to improve crystallinity and hence electrochemical performance, but found

in all cases to decrease the surface area.[37] Often metal oxide impurities were present (*e.g.* Co_3O_4, Mn_3O_4, β-$Li_{0.33}V_2O_5$), with the amount of impurity present decreasing following post synthetic heat treatment, affording discharge capacities comparable to those synthesised by other methods. In most literature reported syntheses, additional lithium was added to account for any lost due to its volatility in the high temperature flame. Synthesis of $LiFePO_4$ by FSP is currently the only reported polyanionic cathode successfully synthesised by this method: it is worth noting that a similar, lower temperature method, ultrasonic spray pyrolysis or simply 'spray pyrolysis' has occasionally been used for other polyanionic cathodes such as $LiMnPO_4$.[38] In the case of $LiFePO_4$, the particles were carbon coated in situ using two flames, then annealed in a reducing atmosphere. The particles were successfully coated in acetylene carbon black, which was found to hinder crystal growth and limit the particle size. These reducing conditions led to the presence of Fe_2P impurities, though this was thought to limit the grain size. The coated samples exhibited better cyclability and higher rate capability than the commercially available $LiFePO_4$, attributed to the protective surface coating and reduced particle size.[32]

The rationale behind synthesis of lithium ion battery cathode materials by flame spray pyrolysis was primarily to improve the electrochemical performance of known cathodes by reduction of particle size.

6.2 Experimental Methods

Two laboratory setups for the synthesis of lithium ion battery cathodes by FSP were used, both housed in a fume hood to minimise exposure to nanosized particulates and the removal of any gaseous side products such as NO_x.

6.2.1 Original Setup

The first setup used for experiments was a low-technology laboratory set up (Figure 6.2.1). An ultrasonic nebuliser, with the resonant crystal in the nozzle operating at a frequency of 130 kHz, generates aerosols from mixed aqueous precursors. The precursors feed into the nebuliser *via* the syringe driver, operating at an injection rate of 1 mL min^{-1}. A blowtorch utilising a mix of propane and oxygen gas as the fuel source provides the flame for the conditions of the reaction. The nozzle of the nebuliser is positioned close to the flame to inject the working solutions into the hot blue cone of the flame, whereby reaction occurs and particles are transferred to a collection plate 10 cm away from the nozzle of the blowtorch. The stainless-steel collection plate is cooled using a flow of air behind the collection plate, whereby the product can be easily recovered once cooled.

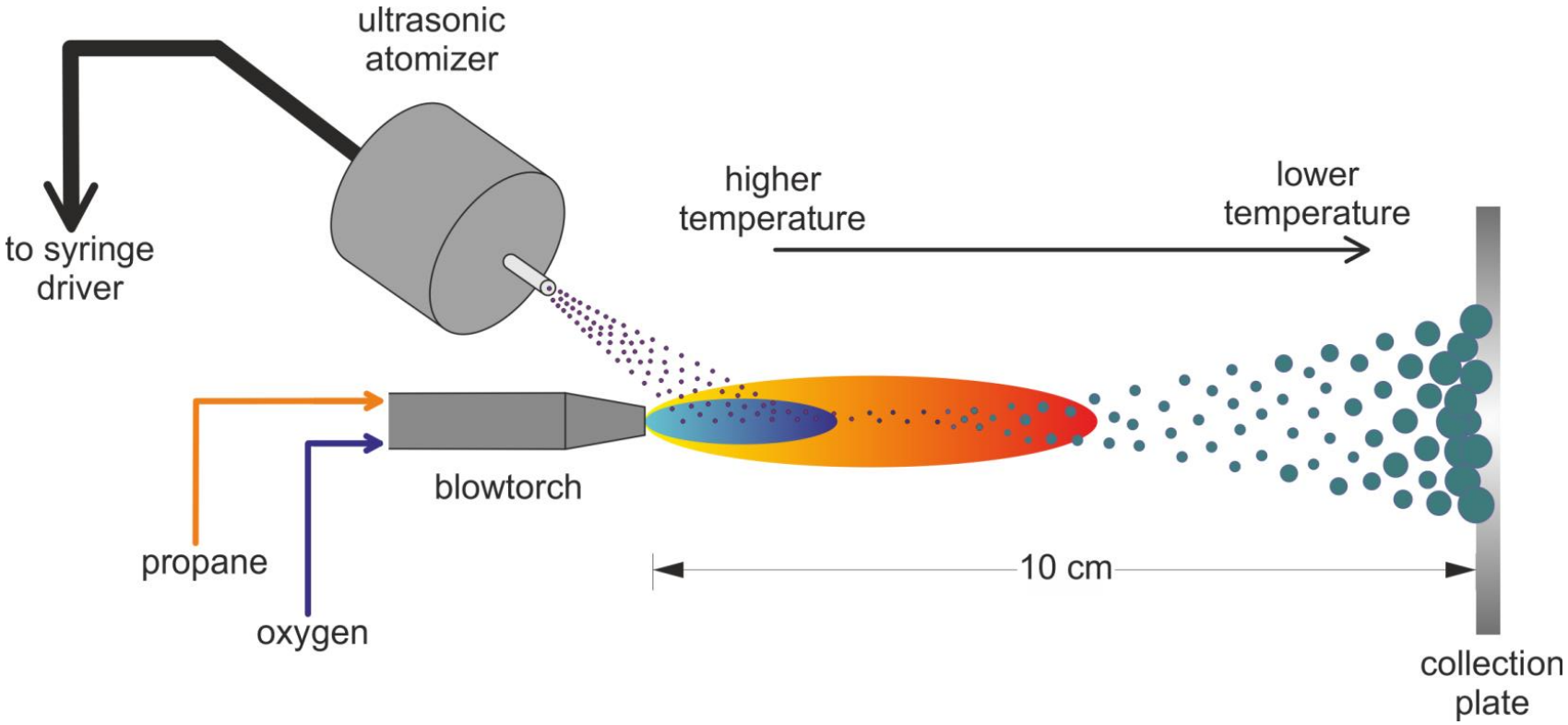

Figure 6.2.1: Schematic annotated diagram of the original FSP setup

6.2.2 Advanced Setup

A safer, more advanced FSP machine allowing greater control of the experimental variables was supplied to us by Saflame Ltd. (Skelmersdale, UK) (Figure 6.2.2). This setup includes mass flow controllers (MFC) for propane and oxygen, in addition to a nitrogen carrier gas inlet, which can be controlled using specifically designed computer software to adjust flame temperature, oxygen level and velocity. A spreadsheet is also employed to confirm safe operating conditions by calculating factors such as flame velocity and the oxygen stoichiometry parameter. Flashback arrestors are also included which can be manually reset, and a UV flame detector allows automatic cessation of gas flow if the flame extinguishes during operation.

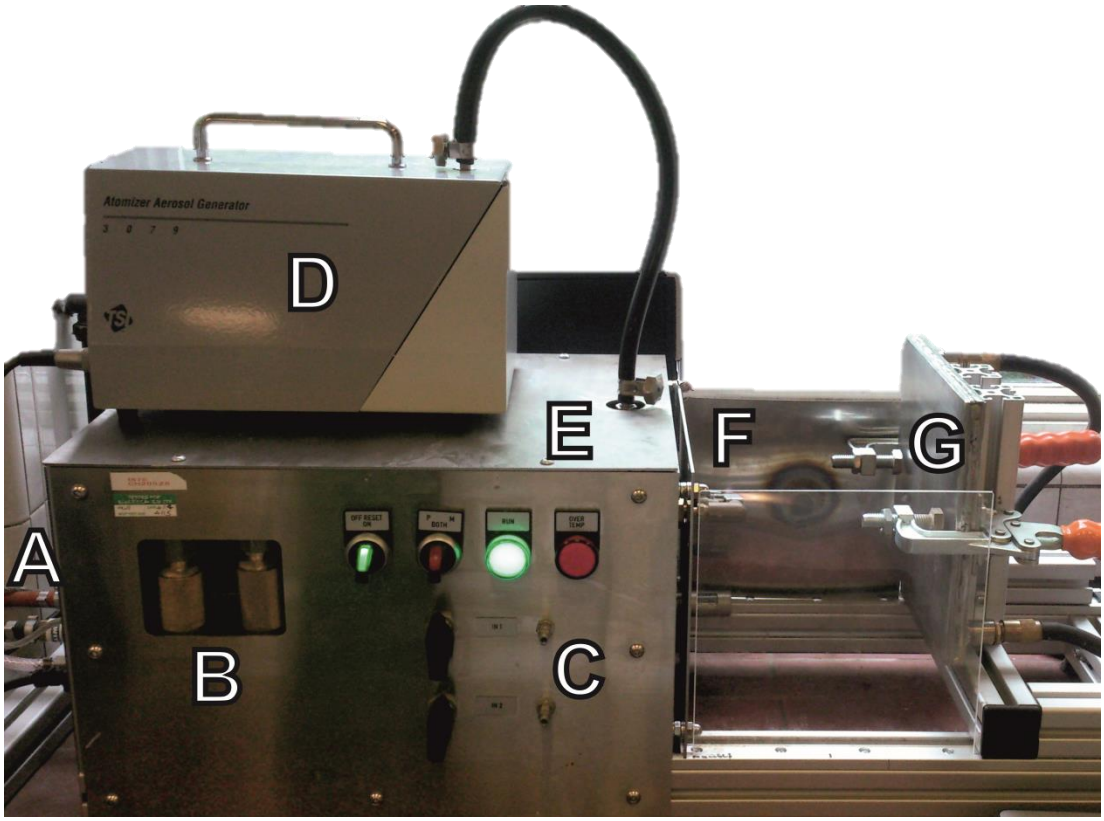

Figure 6.2.2: Annotated photograph of the advanced FSP setup. (A) gas inlets with MFCs; (B) flashback arrestors; (C) syringe inlets; (D) aerosol generator; (E) mixing chamber within the machine; (F) flame with adjacent UV detector and (G) water cooled holder with clamped glass collection plate

There are two methods of precursor introduction: *via* the two syringe inlets, whereby volatile precursors are heated and mixed in the mixing chamber, or mixed in the aerosol generator then introduced to the mixing chamber. From the mixing chamber the precursors flow into the flame to react. Quartz glass plates (100 cm^2) are clamped to a stainless steel collection plate holder and cooled by water flowing through the plate holder. The distance from the flame to the glass collection plate is easily variable as it is housed on a sliding mechanism.

6.2.3 Synthetic Methods

Specific synthetic conditions of each compound are detailed in the following sections. A number of known LIB cathodes were synthesised to validate whether our laboratory setup of the FSP equipment would result in the target compounds.

6.2.4 Powder X-Ray Diffraction

The powders were characterised using laboratory diffractometers, using a Co, Cu or Mo source (depending on the compatibility of the elements present in the sample) as detailed in Chapter 2.

6.2.5 Compositional Analysis

Elemental analysis of the samples was performed using ICP-OES analysis. Dissolution was achieved using microwave-assisted acid digestion, whereby Teflon liners were loaded with ~10 mg of the material and 10 mL of H_2SO_4 (97%, Fisher Scientific), 2 mL HNO_3 (65%, Fisher Scientific) and 2 mL H_2O_2 solution (30% vol, Sigma Aldrich) added dropwise. The Teflon liners were sealed in microwave vessels fitted with burst disks and the temperature and pressure within the vessel monitored. Temperatures of 175-200 °C were used over 55 min for complete digestion, and the acidic solutions made up to 100 mL with deionised water.

6.2.6 Scanning Electron Microscope (SEM) Imaging

Surface imagining of the particles was achieved using a Hitachi S-4800 Field-Emission Scanning Electron Microscope operating at an accelerating voltage of 5 kV. The samples were sputter-coated with gold nanoparticles to aid conduction.

6.2.7 Cathode Testing

Coin cells were assembled as detailed in Chapter 2. Cells were cycled between 3.0-4.2 V. For the cyclability measurements, C/2 C-rate (68.75 mA g^{-1}) was used over 100 cycles. For the rate capability measurements, C-rate was varied between C/10 and 8C, with the C-rate adjusted every five cycles for 35 cycles in total. Cathode composition: 84% active material, 8% PVDF binder and 8% Super C carbon by weight. Thanks go to Filipe Braga-Noguiera (University of Liverpool) for the electrochemical data.

6.3 $LiCoO_2$

6.3.1 FSP Synthesis of $LiCoO_2$

The original FSP setup was used for this synthesis. Aqueous stock solutions of $Li(CH_3COO)\cdot 2H_2O$ (100 mL, 2 mol dm^{-3}, ≥99.0%, Sigma Aldrich) and $Co(CH_3COO)_2\cdot 4H_2O$ (250 mL, 0.8 mol dm^{-3}, ≥98.0%, Sigma Aldrich) were prepared. Synthesis using molar excesses of lithium of 0, 10 and 20% were explored to account for any volatilisation of lithia that may occur within the flame. Appropriate volumes of each stock solution were combined in a beaker and withdrawn into a 20 mL syringe to provide the working solution, with the ratio of Li:Co being 1:1, 1.1:1 and 1.2:1 depending on the lithium excess used. The solutions were injected into the flame *via* the syringe driver at a rate of 1 mL min^{-1} and the powders recovered from the air cooled stainless-steel collection plate. Typical mass yields were very low, ranging from 7 to 17%. The samples were then annealed at 700 °C for 3 hr in air to improve crystallinity.

6.3.2 Solid State synthesis of $LiCoO_2$

$LiCoO_2$ was also synthesised by the solid state method to allow comparison of particle size, crystallinity, purity, surface area and electrochemical performance with those prepared by FSP. A stoichiometric amount of $LiOH{\cdot}H_2O$ (99.95%, Sigma Aldrich) and Co_3O_4 (99.9985%, Alfa Aesar) were hand ground in an agate pestle and mortar. A pellet of the mixture was pressed by applying a uniaxial pressure of 1-2 tons and transferred to an alumina crucible and fired at 900 °C for 20 h in air.

6.3.3 PXRD and Elemental Composition

Powder diffraction data for samples prepared by the solid state method and FSP were obtained using a Co PANalytical diffractometer in Bragg-Brentano geometry. Lithium cobalt oxide prepared by the solid state method (SS) appeared phase pure by PXRD (Figure 6.3.1), crystallising into the rhombohedral $R\bar{3}m$ space group $a = b = 2.8148(2)$ Å, $c = 14.0474(9)$ Å, $V = 96.39(2)$ Å^3. The ratio of Li:Co was 0.950(5):1.00(10) as determined by ICP elemental analysis (normalised so that the value of Co = 1.00).

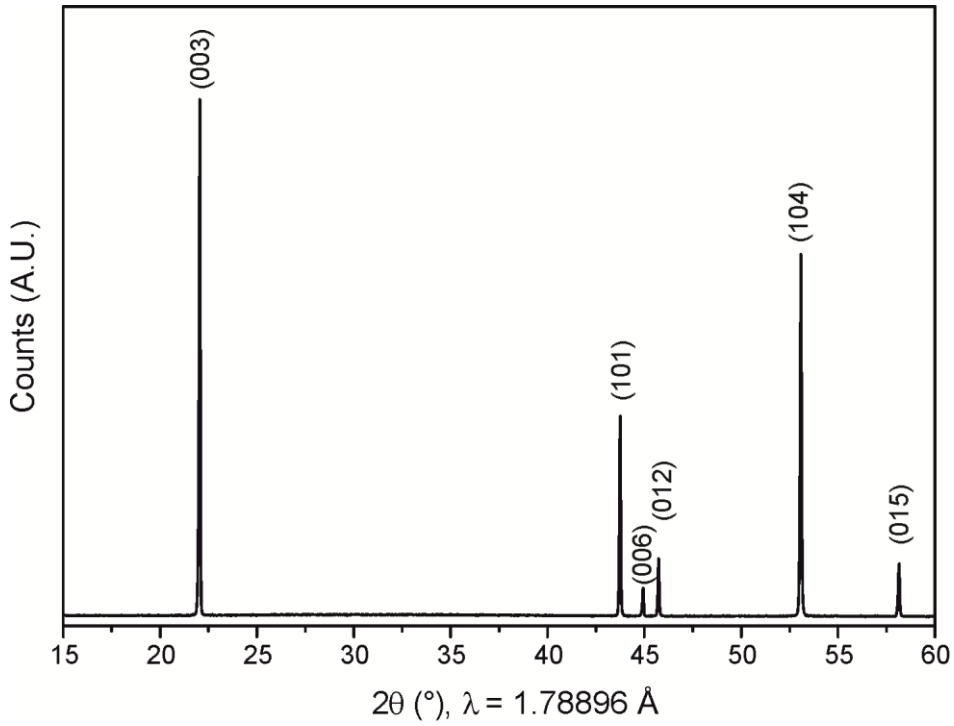

Figure 6.3.1: PXRD of $LiCoO_2$ prepared by the solid state method with $R\bar{3}m$ *hkl* reflections labelled

The effect of heat treatment on $LiCoO_2$ synthesised with 10% Li excess was examined by PXRD (Figure 6.3.2). Unfortunately, $LiCoO_2$ as-synthesised by FSP contained CoO and Li_2CO_3 impurities, which remained in the sample despite annealing. The lattice parameters of the main phase and weight percentages of the phases present were determined by Rietveld refinement (Table 6.3.1), indicating a Co-rich composition.

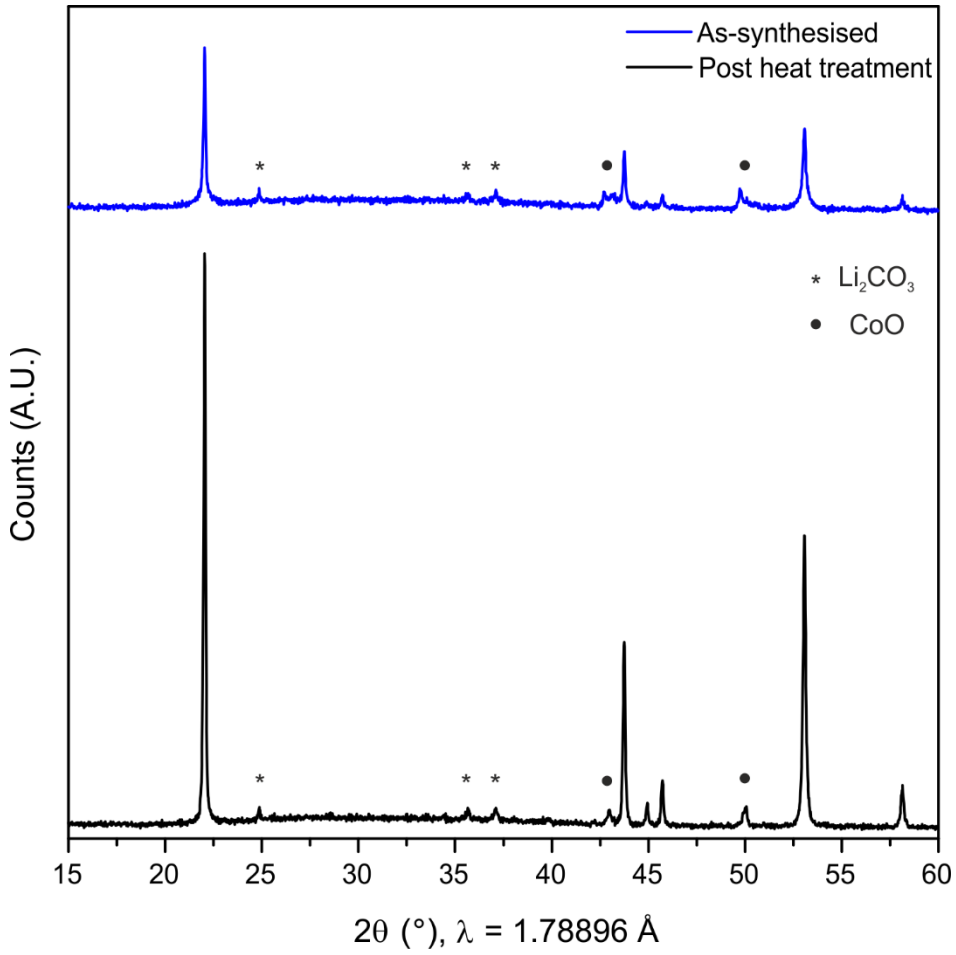

Figure 6.3.2: PXRD of $LiCoO_2$ synthesised using FSP using 10% molar lithium excess before heat treatment (*top*) and after heat treatment (*bottom*)

Table 6.3.1: Comparison of effect of annealing for FSP-synthesised $LiCoO_2$ with 10% molar Li excess. Numbers in parentheses represent 3σ as determined from Topas software

	Weight of phase (%)			**$LiCoO_2$ unit cell parameters**		
	$LiCoO_2$	**Li_2CO_3**	**CoO**	***a* (Å)**	***c* (Å)**	***V* (Å^3)**
As-synthesised	65(6)	26(2)	8(2)	2.8162(6)	14.058(3)	96.56(7)
Post heat treatment	85(2)	12(2)	3.1(5)	2.8162(2)	14.055(3)	96.54(2)

The weight percentages of the impurity phases are considerably reduced on annealing, whilst the lattice parameters of $LiCoO_2$ are maintained, suggesting lithium is not lost from the structure following the annealing process. The reflections of the $LiCoO_2$ phase in the PXRD become sharper and more intense upon annealing; therefore crystallinity is improved upon heat treatment. The Scherrer equation was applied to estimate particle size from the full width at half maximum (FWHM) of the first low-angle Bragg reflection, determining a crystallite size of 90-100 nm before annealing and < 349 nm after (hence crystallite size post annealing is too large for estimation by this method).[39]

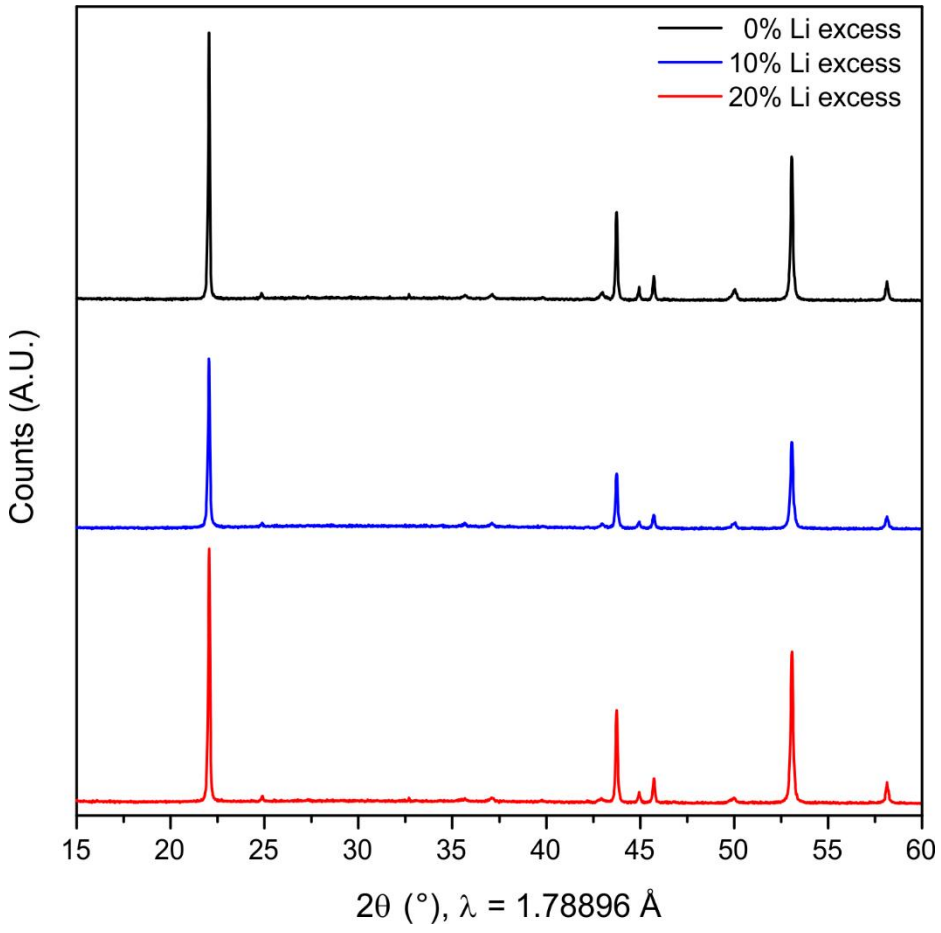

Figure 6.3.3: PXRD of $LiCoO_2$ synthesised with 0, 10 and 20% molar excess of lithium using the original FSP setup, post heat treatment

Table 6.3.2: Comparison of the effects of Li excess for FSP post heat treatment and solid state (SS) synthesised $LiCoO_2$. Numbers in parentheses represent 3σ; ǂ denotes global atomic ratios obtained from ICP analysis normalised to 1.00 Co

Molar Li excess (%)	Weight of phase (%)			$LiCoO_2$ unit cell parameters			Li:Co^{ǂ}
	$LiCoO_2$	CoO	Li_2CO_3	*a* (Å)	*c* (Å)	*V* (Å^3)	
0	90(2)	2.9(4)	7(2)	2.8164(1)	14.055(1)	96.56(1)	-
10	85(2)	3.1(5)	12(2)	2.8162(2)	14.055(3)	96.54(2)	1.28(4):1.0(2)
20	91(2)	1.5(4)	8(2)	2.8166(1)	14.054(1)	96.56(2)	-
SS	100	0	0	2.8166(2)	14.0574(9)	96.58(1)	0.95(2):1.0(2)

The lattice parameters for the target $LiCoO_2$ phase are comparable to those in the sample prepared by traditional solid state synthesis (Table 6.3.2). The ratio of Li:Co in the 10% Li excess sample is greater than expected. This is attributed to the formation of nanosized CoO, all of which may not have coated onto the sample plate for collection, even though the ratio of Li:Co in the working solution was 1.1:1. The higher percentage of impurities in this sample compared to the other molar excesses is attributed to some deposition of solid within the blowtorch nozzle which was noted during synthesis, as multiple batch processes were repeated for this sample only. This deposition possibly led to more reducing conditions, producing $Co^{(II)}O$ and Li_2CO_3. The slight lithium deficiency in the solid state sample is attributed to a small percentage of Li_2O volatilisation which occurs rapidly at temperatures ≥ 900 °C, resulting in a deviation from the expected 1:1 stoichiometry.

6.3.4 Particle Size and Morphology

The particle size and morphology of $LiCoO_2$ as-synthesised by FSP (Figure 6.3.4) and after the annealing process (Figure 6.3.5) were examined using SEM imaging. For

comparison, SEM imaging was also performed on $LiCoO_2$ prepared by solid state synthesis (Figure 6.3.6).

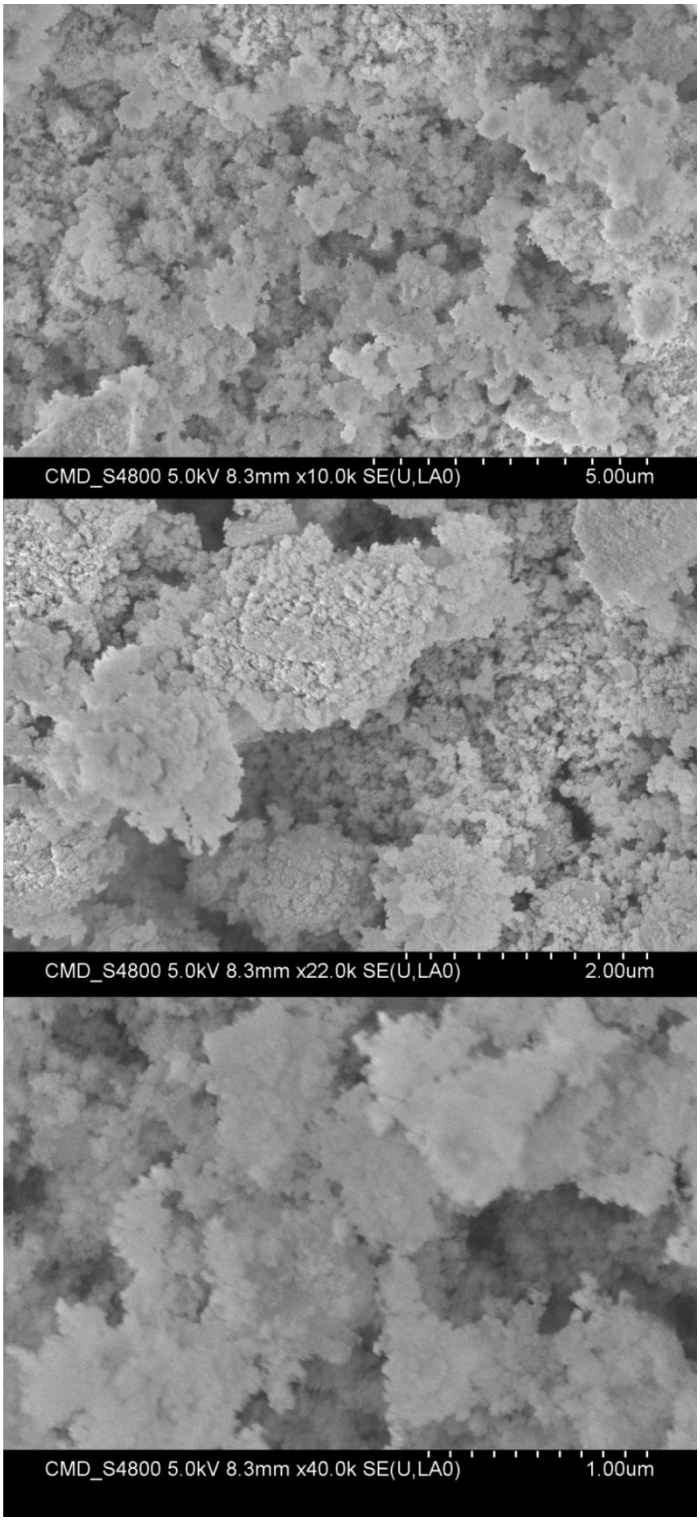

Figure 6.3.4: SEM images at various magnifications of $LiCoO_2$ as-synthesised by FSP using 10% molar Li excess exhibiting particles of <100 nm

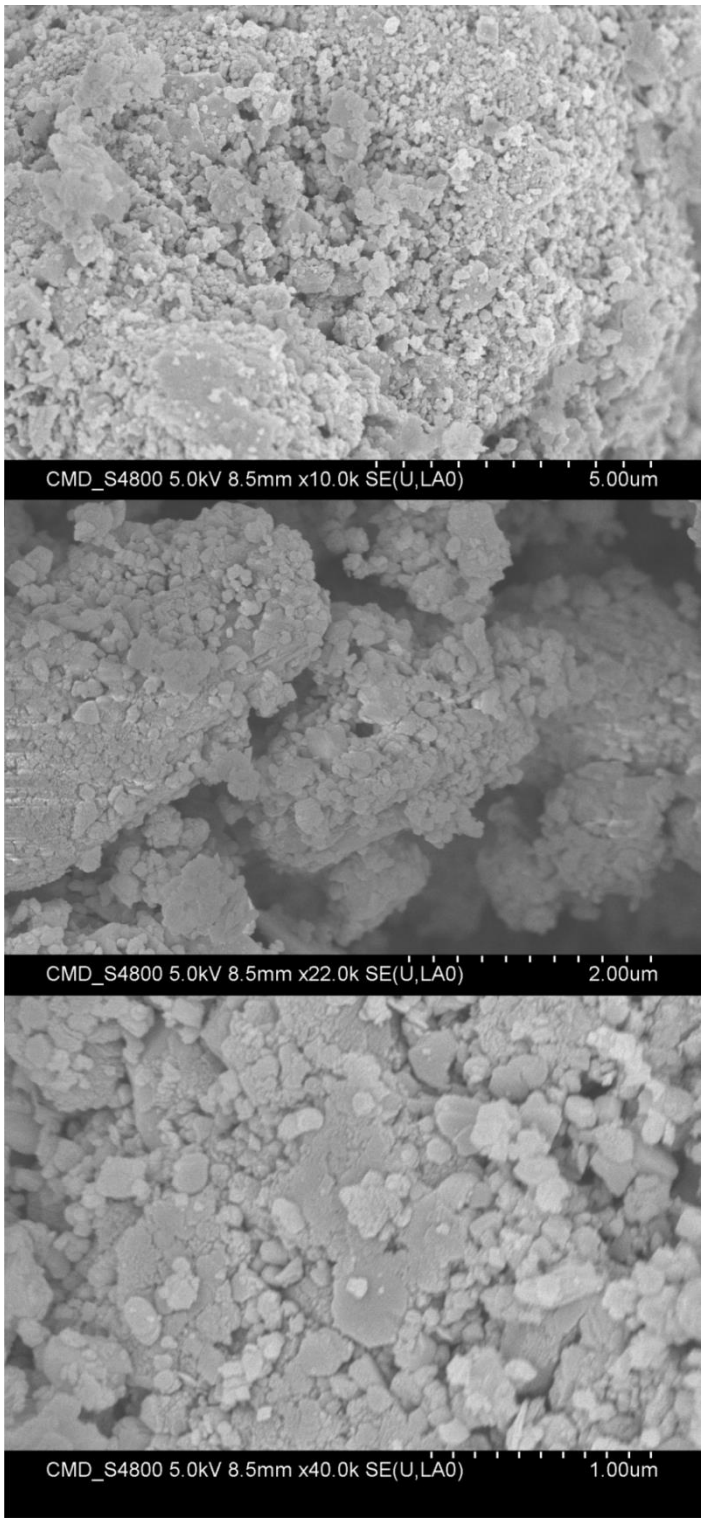

Figure 6.3.5: SEM images at various magnifications of $LiCoO_2$ synthesised by FSP using 10% molar Li excess following annealing at 700 °C for 3 h; exhibiting aggregates of smaller particles >100 nm

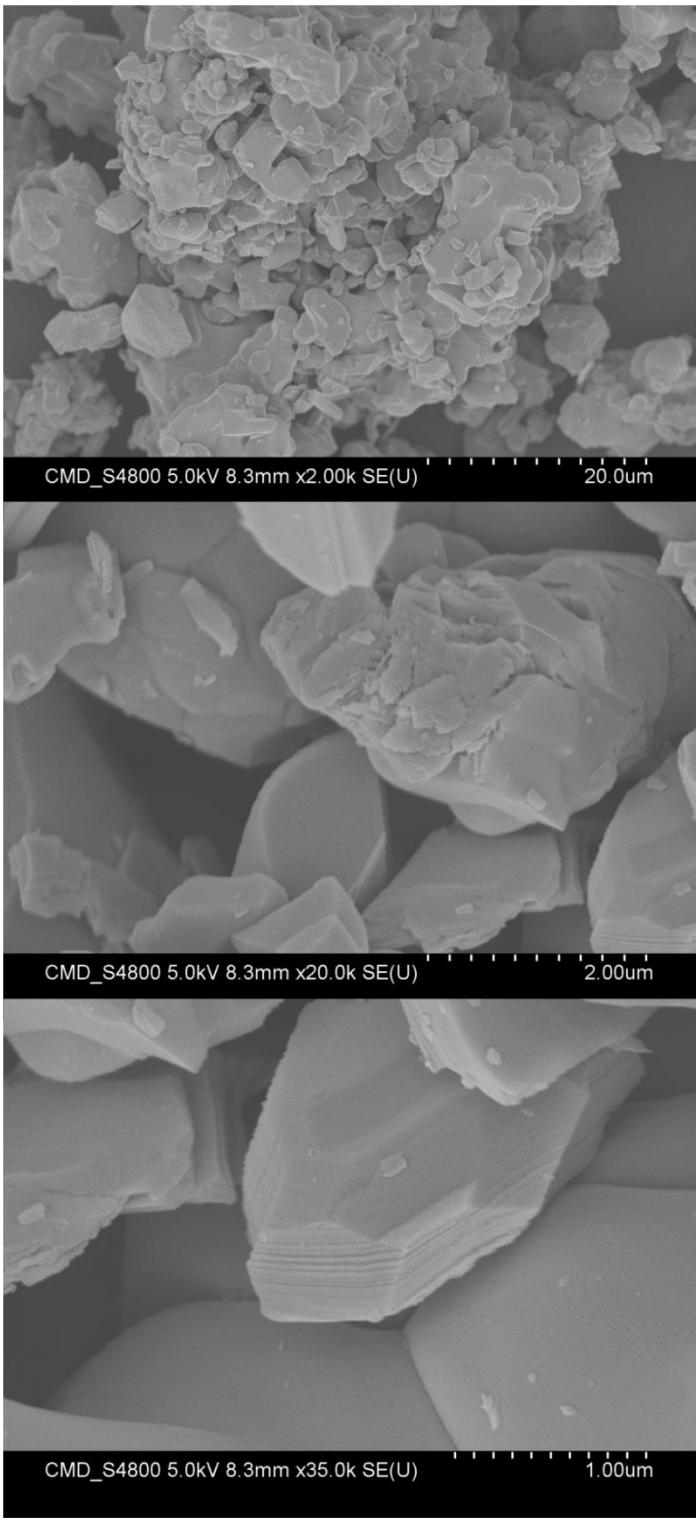

Figure 6.3.6: SEM images at various magnifications of $LiCoO_2$ synthesised by the solid state method, exhibiting angular 1-10 μm sized particles

In the as-synthesised sample (before heat treatment) it is clear that nanosized particles of the order of tens of nanometres are obtained, coagulating onto larger micrometre sized aggregates. The heat treatment at 700 °C for 3 h has the effect of sintering these small nanoparticles, increasing the grain size in the >100 nm range, which is consistent with the crystallite size estimates derived from the Scherrer equation.

6.3.5 Cathode Testing

Synthesis of $LiCoO_2$ *via* FSP using a 10% molar excess of lithium was repeated multiple times to obtain an adequate mass for cathode testing, and the same post synthetic heat treatment was applied. For comparison, coin cells using the $LiCoO_2$ synthesised *via* the solid state method and commercially available $LiCoO_2$ (Sigma Aldrich) were also tested under the same conditions.

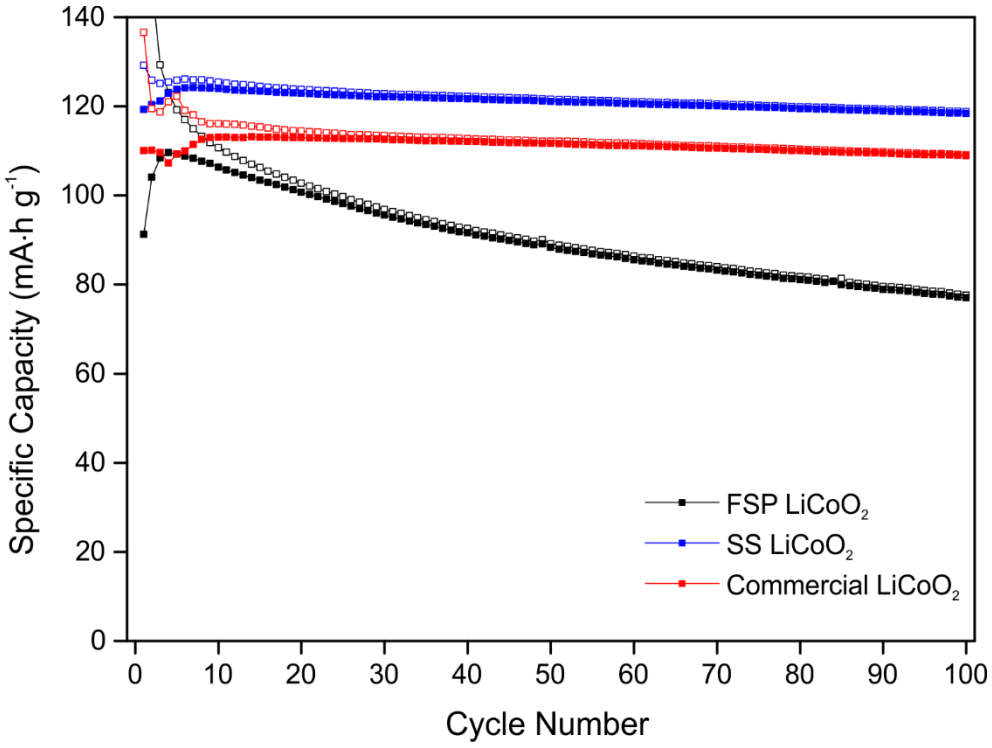

Figure 6.3.7: Cyclability testing of $LiCoO_2$ prepared by various methods (C/2, 3-4.2 V). Open squares represent charge capacity, filled squares represent discharge capacity

The solid state sample (SS $LiCoO_2$) affords an initial discharge capacity of 124 $mA{\cdot}h\ g^{-1}$ and good cyclability, with a capacity retention of 95% over 100 cycles, which is comparable to the performance of the commercially available sample and literature samples prepared *via* the solid state method.[31] The testing data for the FSP sample was normalised to only account for the active mass of the $LiCoO_2$ phase, displaying an initial discharge capacity of 110 $mA{\cdot}h\ g^{-1}$ and a 50^{th} cycle capacity retention of 81%. These values compare well to a similarly prepared sample tested under similar conditions in the literature (discharge capacity 111 $mA{\cdot}h\ g^{-1}$, 50^{th} cycle capacity retention of 86%).[40] The capacity retention for the FSP material is considerably lower than the solid state sample, which is attributed to its greater surface area, increasing side reactions with the liquid electrolyte and consumption of the cell components, leading to a more rapid decrease in overall cell capacity. In the case of $LiCoO_2$, Li^+ ion diffusion kinetics and the rate of lithium insertion/extraction is not a limiting factor on its electrochemical performance, so producing this cathode by FSP was not expected to enhance the cyclability.

The rate capability measurements show similar profiles between the SS and FSP sample (Figure 6.3.8); indicating a similar proportion of lithium ions can be extracted at higher discharge rates. The capacity extracted at higher C-rates over five cycles is superior for the FSP $LiCoO_2$, particularly evident at 8C where the capacity extracted shows minimal decrease over five cycles (2.4% loss in capacity from cycle 26 to cycle 30) compared to the SS sample (5.1% capacity loss). This is attributed to the smaller particle size of the FSP sample aiding lithium ion and electronic conduction through the material allowing consistent discharge capacities when a high discharge current is employed.

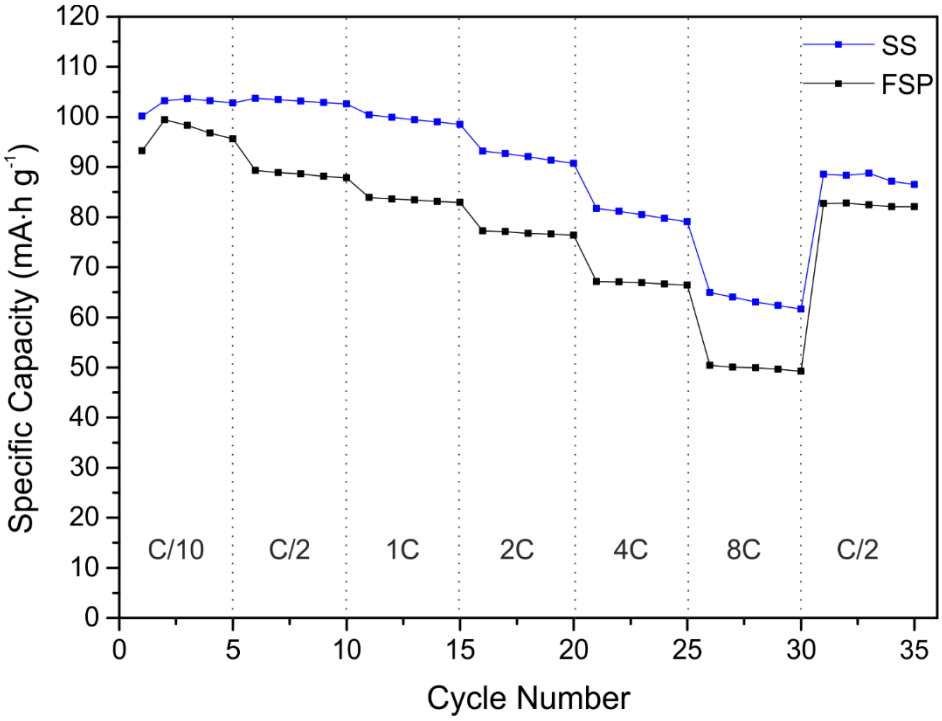

Figure 6.3.8: Rate capability cathode testing of $LiCoO_2$ prepared by FSP and solid state. Graph shows the discharge capacity as the C-rate was varied every five cycles as indicated

6.4 $LiMn_2O_4$

6.4.1 FSP Synthesis of $LiMn_2O_4$

The original FSP setup was used for this synthesis. Aqueous stock solutions of $LiNO_3$ (100 mL, 2 mol dm^{-3}, ≥98.0%, Sigma Aldrich) and $Mn(NO_3)_2 \cdot 4H_2O$ (100 mL, 2 mol dm^{-3}, ≥98.0%, Sigma Aldrich) were prepared. Appropriate volumes of each stock solution were combined in a beaker and withdrawn into a 20 mL syringe to provide the working solution, with the ratio of Li:Mn being 1:2, 1.1:2 and 1.2:2 depending on the lithium excess used. Typical total mass yield was 3-5%. The samples were annealed at 700 °C for 3 h in air to improve crystallinity. A brown-black powder was obtained.

6.4.2 Solid State synthesis of $LiMn_2O_4$

A stoichiometric amount of $LiOH{\cdot}H_2O$ (99.95%, Sigma Aldrich) and MnO_2 (99.9%, Alfa Aesar) were hand ground in an agate pestle and mortar. A pellet of the mixture was pressed, transferred to an alumina crucible and fired at 650 °C and 900 °C in air for 12 h and 24 h respectively, with hand grinding and pelletising in between firings. A blue-black powder was obtained.

6.4.3 PXRD and Elemental Composition

Powder X-ray diffraction patterns were collected using a Bruker D8 diffractometer employing a molybdenum metal anode in Debye-Scherrer geometry. Samples were loaded into borosilicate capillaries of 0.5 mm internal diameter for these measurements. A molybdenum source was utilised in preference to cobalt or copper because the fluorescence of manganese is minimal at Mo(Kα) λ = 0.70930 Å. Due to considerable geometric aberration of the first Bragg reflection as a result of axial divergence, a full axial model was used in the Le Bail and Rietveld refinements to obtain a better fit to the experimental data.

The powder diffraction pattern for the solid state sample shows a phase pure material with the cubic spinel structure (S.G. $Fd\bar{3}m$, a = 8.24468(10) Å, V = 560.4(2) $Å^3$) (Figure 6.4.1). The ratio of Li:Mn was determined by ICP analysis as 0.93(5):2.00(6), which within 3σ is the target stoichiometry.

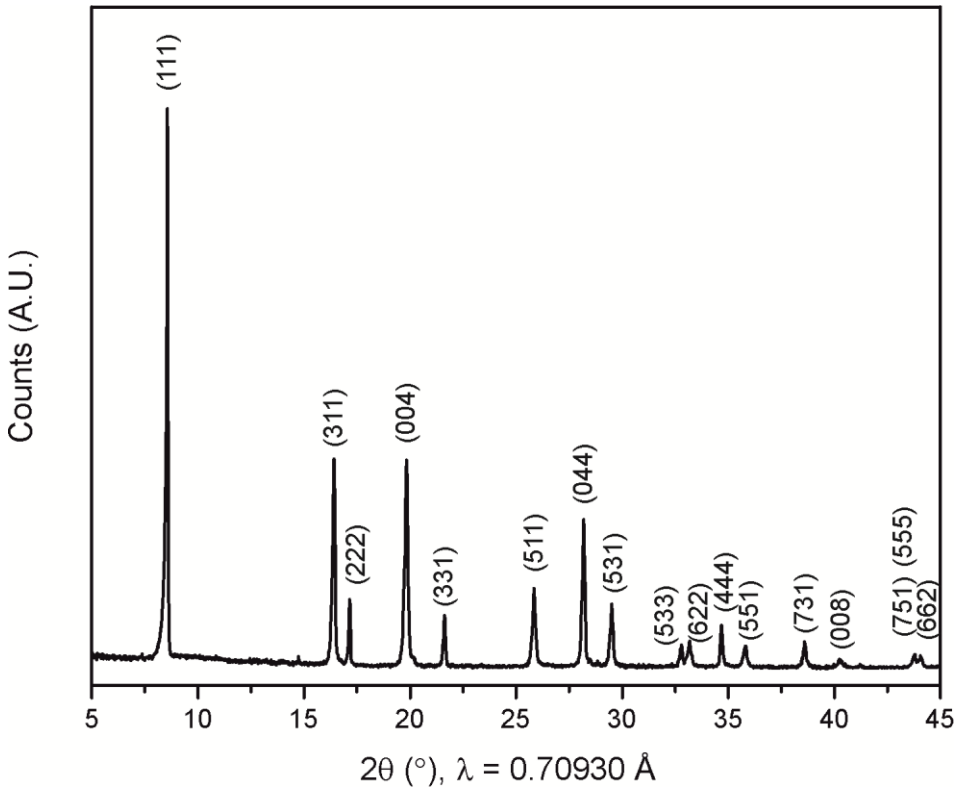

Figure 6.4.1: PXRD of $LiMn_2O_4$ prepared by the solid state method with *Fd*$\bar{3}$*m hkl* reflections labelled

For the as-synthesised FSP sample, Mn_3O_4 (18(2)% wt) and MnO (1.2(7)% wt) impurities were identified in the sample prior to heat treatment by Rietveld refinement of the PXRD and determined to be phase pure after heat treatment (Figure 6.4.2). The unit cell parameters are considerably reduced in comparison to the phase pure solid state sample (a = 8.201(1) Å, V = 551.6(2) $Å^3$). This can be explained by the formation of a lithium-deficient spinel structure ($Li_{1-x}Mn_2O_4$), whereby the oxidation state of manganese will increase from +3.5 in the stoichiometric (x = 0) structure to maintain charge neutrality and as a result decreasing the average ionic radius of manganese, in addition to the presence of lithium ion vacancies.[41]

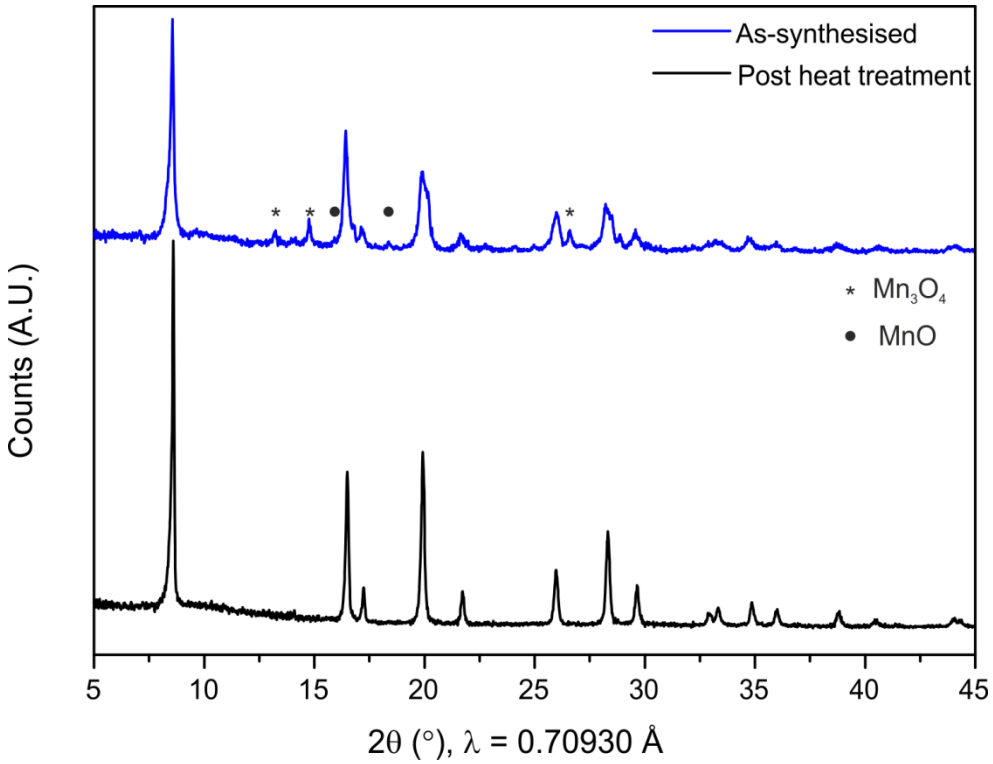

Figure 6.4.2: PXRD of $Li_{1-x}Mn_2O_4$ synthesised by FSP with 10% molar Li excess before heat treatment (*top*) and after heat treatment (*bottom*)

The Scherrer equation was applied to estimate the particle size from the FWHM of the first low-angle Bragg reflection from the PXRD using the Topas software, giving estimates of 12 nm crystallites before heat treatment and >100 nm after heat treatment. Due to the lithium deficiency and inadequate product mass obtained, no further characterisation was undertaken on this material.

6.5 $LiNi_{0.5}Mn_{1.5}O_4$

Substitution of a quarter of the manganese cations for nickel in the parent $LiMn_2O_4$ spinel results in $LiNi_{0.5}Mn_{1.5}O_4$, which can retain the face-centred cubic spinel structure ($Fd\bar{3}m$), whereby the nickel and manganese ions are disordered over the 16*d* octahedral sites. Alternatively manganese and nickel can order on the 4*a* and 12*d* sites respectively, resulting in an ordered lower symmetry spinel structure crystallising in

the primitive cubic space group $P4_332$.[42] This ordering is common in spinel structures with two distinct *B*-site cations are present in a 3:1 ratio,[43] with the structure obtained dependent on the synthetic conditions employed. Both structures have been reported to display similar discharge capacities,[44] but the ordered structure has been found to display a two-step phase transition upon lithiation (*cf.* one-step for the disordered structure), which reduces the reversibility at high discharge rates.[45]

6.5.1 FSP Synthesis of $LiNi_{0.5}Mn_{1.5}O_4$

The original FSP setup was used for this synthesis. Aqueous stock solutions of $LiNO_3$ (100 mL, 2 mol dm^{-3}), $Ni(NO_3)_2 \cdot 6H_2O$ (100 mL, 2 mol dm^{-3}, 99.999%, Sigma Aldrich) and $Mn(NO_3)_2 \cdot 4H_2O$ (100 mL, 2 mol dm^{-3}) and were prepared. Appropriate volumes of each stock solution were combined in a beaker and withdrawn into a 20 mL syringe to provide the working solution, with the ratio of Li:Ni:Mn being 1:0.5:1.5, 1.1:0.5:1.5 and 1.2:0.5:1.5 depending on the lithium excess used. Typical total mass yield was 4-8%. The samples were annealed at 700 °C for 3 h in air to improve crystallinity, appearing as a dark brown powder.

6.5.2 Solid State Synthesis of $LiNi_{0.5}Mn_{1.5}O_4$

The cubic spinel phase of $LiNi_{0.5}Mn_{1.5}O_4$ was prepared using $Li(CH_3COO) \cdot 2H_2O$, $Ni(CH_3COO)_2 \cdot 4H_2O$ (≥99%, Sigma Aldrich) and $Mn(CH_3COO)_2 \cdot 4H_2O$ (≥99%, Sigma Aldrich) in a 1:0.5:1.5 molar ratio. The reagents were hand ground together in an agate pestle and mortar and calcined as a loose powder at 500 °C for 5 h to remove the organic ligands. The calcined powder was hand ground and a pellet of the mixture was pressed, transferred to an alumina crucible and fired at 900 °C and 700 °C in air for 10 h at each temperature, with hand grinding in between firings. Attempts to obtain both the ordered and disordered spinel by varying the reaction conditions were unsuccessful and both resulted in the disordered cubic phase.

6.5.3 PXRD and Elemental Composition

Powder X-ray diffraction patterns were collected as detailed for $LiMn_2O_4$. The solid state sample was determined to be phase pure cubic disordered spinel (a = 8.1740(4) Å, V = 546.14(8) Å^3) (Figure 6.5.1), which is in good agreement with the literature.

As expected due to the high temperature of the flame, and following the heat treatment, the disordered spinel phase was obtained for the sample synthesised with 20% excess Li (a = 8.1619(8) Å, V = 543.7(2) Å^3). Additionally, a $Li_{1-x}Ni_2O_4$ impurity was also present following heat treatment (7(1)% wt), presenting as shoulders on the main phase peaks (Figure 6.5.1, *bottom*). The presence of this impurity phase indicates the main spinel phase obtained is actually deficient in Li and Ni, which explains the reduction in the unit cell volume compared to the solid state sample.

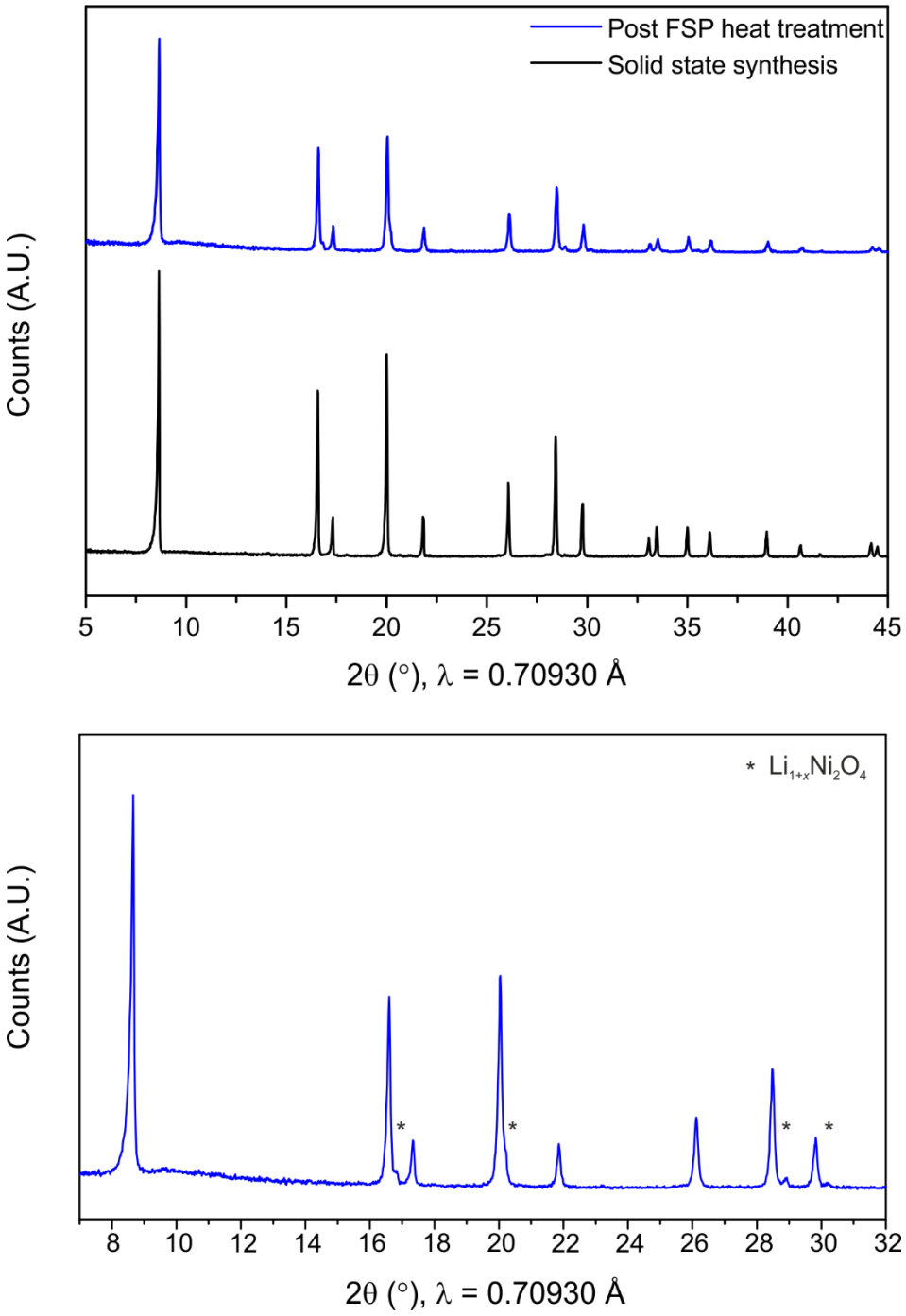

Figure 6.5.1: PXRD of $LiNi_{0.5}Mn_{1.5}O_4$ synthesised by FSP with 20% molar Li excess and annealed (*top*, *blue*) compared to that prepared by solid state (*top*, *black*). Bottom figure is a magnification of the low angle impurity region showing the presence of $Li_{1+x}Ni_2O_4$ impurity in the annealed FSP sample

Table 6.5.1: Comparison of the elemental composition of Li excesses used for FSP post heat treatment and solid state (SS) synthesised $LiNi_{0.5}Mn_{1.5}O_4$. Global atomic ratios obtained from ICP analysis were normalised to 1.50 Mn, numbers in parentheses represent 1σ

Molar Li excess (%)	Li	Ni	Mn
0	0.91(8)	0.44(5)	1.50(4)
10	1.06(5)	0.41(7)	1.50(6)
20	1.16(7)	0.41(4)	1.50(8)
SS	0.90(7)	0.49(5)	1.50(4)

Elemental analysis of these materials by ICP suggests all FSP-synthesised $LiNi_{0.5}Mn_{1.5}O_4$ may be deficient in nickel, as this analysis also accounts for the presence of the $Li_{1+x}Ni_2O_4$ impurity.

6.6 Li_2MnO_3

As discussed in previous chapters, Li_2MnO_3 itself is not an appropriate lithium ion battery cathode material. However this material was explored to investigate whether high-lithium content materials can be synthesised using this high-temperature method.

6.6.1 FSP Synthesis of Li_2MnO_3

Synthesis was analogous to that employed for FSP-$LiMn_2O_4$, but with molar ratios of Li:Mn of 2:1, 2.2:1 or 2.4:1 depending on whether a molar excess of 0, 10 or 20% Li was used, with the same post synthetic heat treatment conditions. Typical total mass yield was 15-17%, appearing as a brown-orange powder.

6.6.2 Solid State Synthesis of Li_2MnO_3

Synthetic conditions were analogous to that employed for SS-$LiMn_2O_4$, but with a 2:1 Li:Mn molar ratio. A bright orange powder was obtained.

6.6.3 PXRD and Elemental Composition

Powder X-ray diffraction patterns were collected as detailed for $LiMn_2O_4$. The solid state sample was determined to be phase pure, with Li_2MnO_3 crystallising in the *C*2/*m* space group (a = 4.929(2) Å, b = 8.530(2) Å, c = 5.024(1) Å, β = 109.28(2)°, V = 199.4(1) Å^3) which are slightly smaller than those determined in the literature.[46] This suggests a slight Li-deficiency in the solid state sample, which was confirmed by ICP analysis which gave a ratio of Li:Mn as 1.81(7):1.00(4). The broad peaks between 9.5-10.5° 2θ is attributed to stacking fault defects present within the material (Figure 6.6.1) and was excluded from the Le Bail analyses of both materials to obtain more accurate unit cell parameters.

The sample synthesised by FSP with 10% Li excess and after heat treatment contains Li_2CO_3 (25(4)% wt) and $LiMnO_2$ (6(2)% wt), which indicates the flame conditions may not have been sufficiently oxidising. The unit cell parameters for the FSP-Li_2MnO_3 were determined from Le Bail analysis as a = 4.931(3) Å, b = 8.540(2) Å, c = 5.022(2) Å, β = 109.33(5)°, V = 199.6(2) Å^3 which, within error (3σ) match well to the SS-Li_2MnO_3 sample. Again this suggests that the target phase is actually deficient in lithium, attributed in part to volatilisation of Li_2O in the flame and the formation of a considerable mass of Li_2CO_3 impurities.

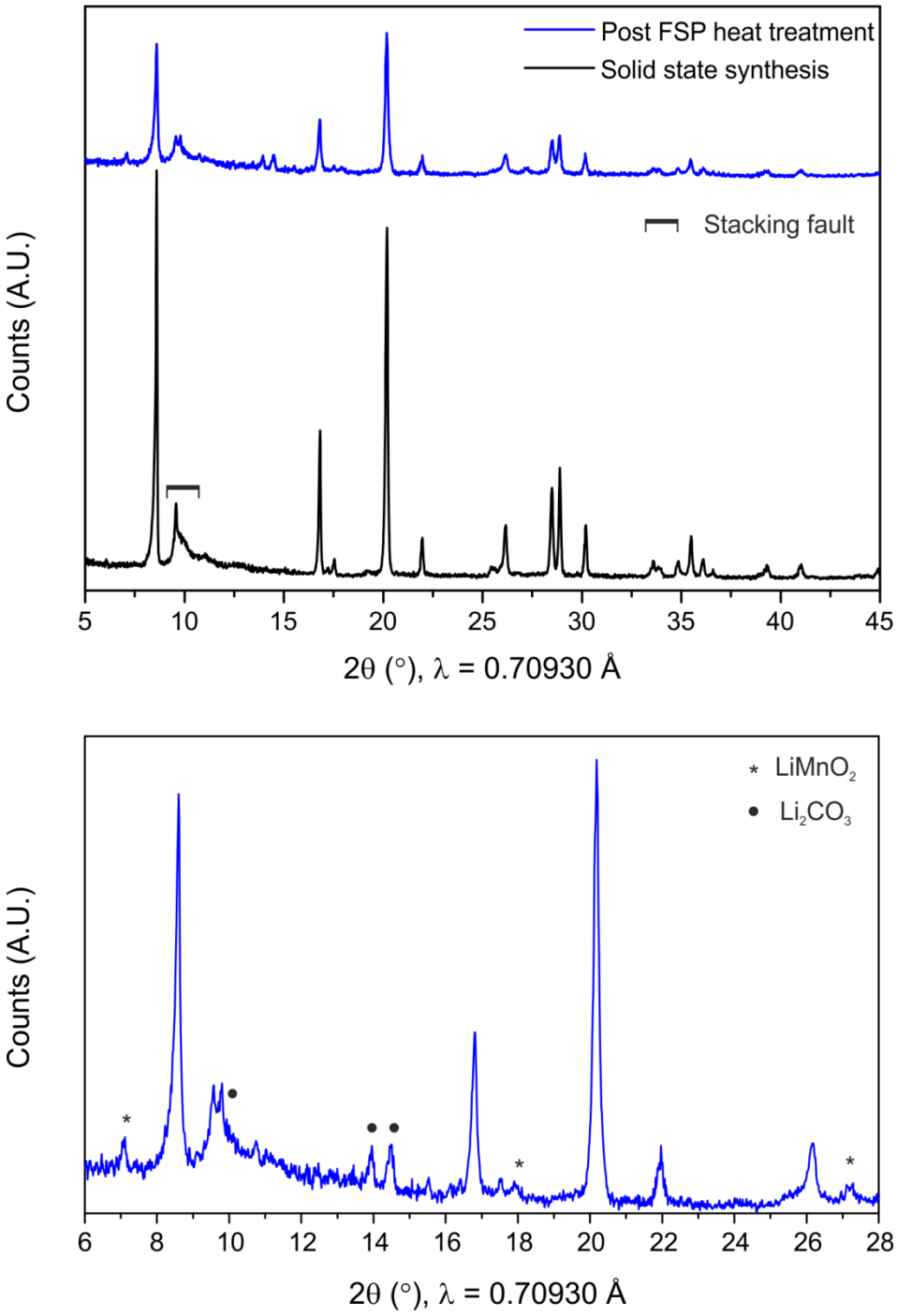

Figure 6.6.1: PXRD of Li_2MnO_3 synthesised by FSP with 10% molar Li excess and annealed (*top*, *blue*) compared to that prepared by solid state (*top*, *black*). Bottom figure is a magnification of the low angle impurity region in the annealed FSP sample

6.7 Polyanionic LIB Cathodes

The benefits and limitations of the use of polyanionic lithium-ion battery cathodes have been discussed in Chapter 1, with particular focus on the olivine type materials such as $LiFePO_4$. It is known that slow lithium ion diffusion kinetics and poor electronic conduction are the primary limiting factors for the use of polyanionic cathodes over lithium to metal oxides. Pyrophosphates are a more stable anion compared to phosphates, with a greater inductive effect in comparison to phosphates, allowing for an increased redox potential of the transition metal couple, making them a potential target for high voltage, high stability cathodes. For example, the $M^{2+/3+}$ redox potential occurs at 3.5 V in $Li_2FeP_2O_7$ (*cf.* 3.45 V for $LiFePO_4$), 4.45 V for $Li_2MnP_2O_7$ and 4.8 V for the Co analogue.[47,48] However, the theoretical specific capacities are still limited (typically ~ 110 mA·h g^{-1} for one-electron reactions), due to the excess anion weight decreasing the gravimetric energy density but providing structural stability. Due to the potential for removal of up to two lithium ions per transition metal, the theoretical capacity will double should the $M^{2+/3+/4+}$ redox couples be realised in practice.[49]

Materials adopting the NASICON-type structure have been studied extensively as ionic conductors, investigated for electrolyte and electrode applications. The term 'NASICON' refers to the $Na_{1+x}Zr_2Si_xP_{3-x}O_{12}$ Sodium Super-Ionic Conductor; some examples of LIB cathodes include $Li_3Fe_2(PO_4)_3$ and $Li_3V_2(PO_4)_3$ composed of MO_6 octahedra and PO_4 tetrahedra with three-dimensional Li^+ diffusion channels.[50] These structures adopt a rhombohedral (NASICON) or less symmetric monoclinic (anti-NASICON) system,[51] the former of which displays better ionic conduction due to a more open framework, aiding lithium insertion/extraction.[52] Both structures possess MO_6 octahedra sharing oxygen vertices with PO_4 tetrahedra (Figure 6.7.1).

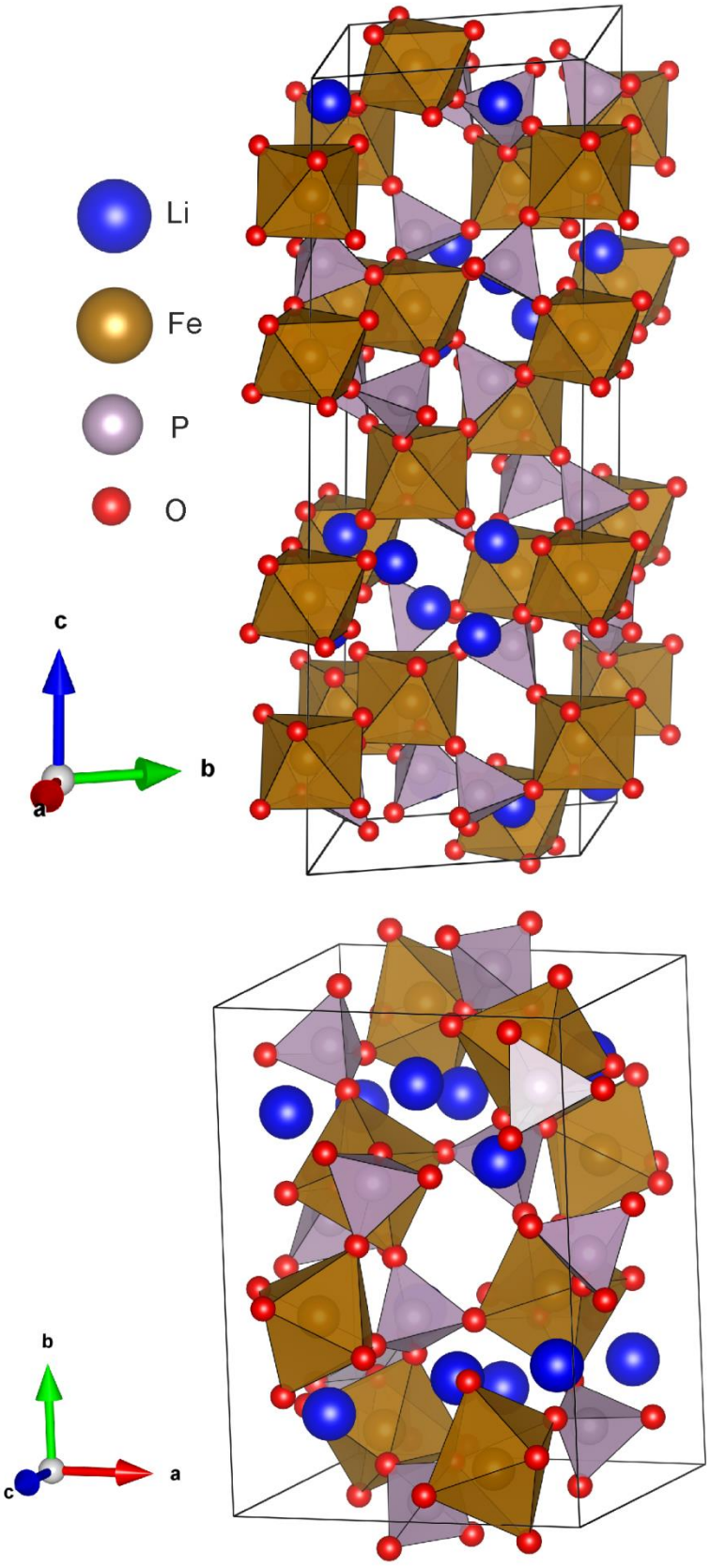

Figure 6.7.1: Representation of the rhombohedral NASICON-type (*top*) and monoclinic anti-NASICON-type (*bottom*) structures of $Li_3Fe_2(PO_4)_3$

Unfortunately, the materials are poor electronic conductors due to isolation of the MO_6 units by the PO_4 tetrahedra, which can be overcome by carbon coating or nanostructuring, for example.

6.7.1 Synthesis of Lithium Metal Phosphates by FSP

The advanced FSP setup was primarily used for the synthesis of polyanionic lithium ion battery cathodes in this section.

The olivine-type $LiFePO_4$ phase was targeted for synthesis by FSP in order to determine if it were possible to produce Li-phosphates using the laboratory setup, with iron in the +2 oxidation state. Aqueous stock solutions of $LiNO_3$ (4 mol dm^{-3}, 100 mL), $Fe(NO_3)_3 \cdot 9H_2O$ (100 mL, 4 mol dm^{-3}, ≥98%, Sigma Aldrich) and $NH_4H_2PO_4$ (100 mL, 2 mol dm^{-3}, 99.995%, Sigma Aldrich) were prepared. A small amount of aqueous phosphoric acid was added to the ammonium hydrogen phosphate solution to prevent the formation of a precipitate (under the assumption that any small excess of phosphate anions would likely volatilise during synthesis). The solutions were combined into a 20 mL syringe with a ratio of 1.1:1:1 Li:Fe:P and fed into the FSP machine *via* a syringe driver. Products were annealed for a total of 15 h under dynamic N_2 atmosphere at 700 °C.

$LiMnPO_4$ was targeted for synthesis by FSP since its cathode properties have not previously been optimised by this method. Aqueous stock solutions of $LiNO_3$ (4 mol dm^{-3}, 100 mL), $Mn(NO_3)_2 \cdot 4H_2O$ (4 mol dm^{-3}, 100 mL) and acidified $NH_4H_2PO_4$ (2 mol dm^{-3}, 100 mL, 99.995%, Sigma Aldrich) were prepared. The solutions were combined into a 20 mL syringe with a ratio of 1.1:1:1 Li:Mn:P and fed into the FSP machine *via* a syringe driver. The ionic ratios were also adjusted to 3.3:2:3

to target the unreported NASICON-type $Li_3Mn_2(PO_4)_3$ phase. Products were not annealed in this instance.

6.7.2 PXRD and SEM

The lithium iron phosphates were analysed using a Co PANalaytical diffractometer in Bragg-Brentano geometry. The lithium manganese phosphates were analysed using a Mo Bruker D8 diffractometer in Debye-Scherrer geometry. Targeted synthesis of $LiFePO_4$ was found to result in $Li_{3-x}Fe_2(PO_4)_3$ (95.0(9)% wt) and Fe_2O_3 (5.0(9)% wt) as an impurity phase (Figure 6.7.2). The monoclinic anti-NASICON phase of $Li_{3-x}Fe_2(PO_4)_3$ was obtained (Figure 6.7.1), crystallising in the monoclinic $P2_1/n$ space group with unit cell parameters of a = 8.5658(8) Å, b = 12.0175(10) Å, c = 8.6176(7) Å, γ = 90.488(7)° and V = 887.1(1) Å^3, which are in good agreement with the structure reported in the literature.[53]

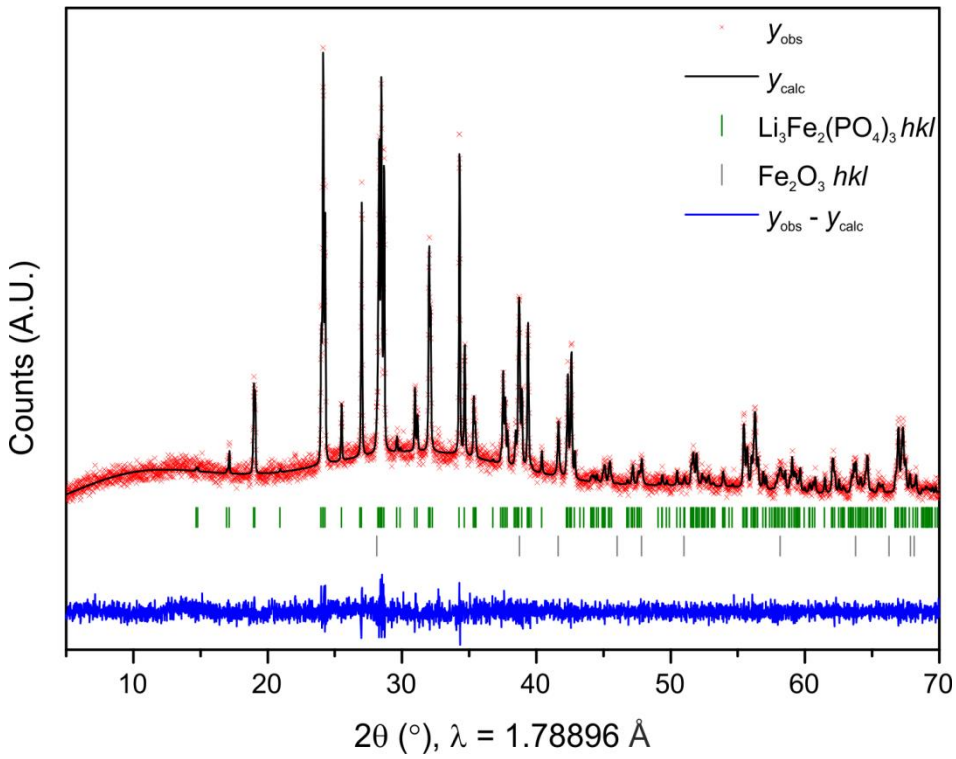

Figure 6.7.2: Le Bail fit of targeted $LiFePO_4$ synthesised by FSP after heat treatment, showing the positions of the *hkl* reflections of the $Li_3Fe_2(PO_4)_3$ phase and Fe_2O_3 impurity. χ^2 = 1.14

The monoclinic polymorph of $Li_3Fe_2(PO_4)_3$ is reported to be the low-temperature phase.[54] The oxidation state of iron in $LiFePO_4$ is +2, but +3 in $Li_3Fe_2(PO_4)_3$, which suggests the conditions of the flame were not reducing enough to obtain this phase as iron (III) nitrate was used in the working solution for synthesis, hence the anti-NASICON phase was synthesised preferentially over $LiFePO_4$, with excess iron in the working solution forming an iron(III) oxide impurity. The global elemental composition of the product was analysed by ICP, giving a ratio of 2.51(5):2.45(3):3.00(8) Li:Fe:P (normalised so that P = 3.00), indicating the structure is deficient in lithium.

The synthesis of $Li_3Fe_2(PO_4)_3$ has previously been reported by ultrasonic spray pyrolysis (USP), but not FSP, whereby particles of 0.4-2 μm were obtained.[55] Assessment of the particle size of $Li_3Fe_2(PO_4)_3$ synthesised in this work by SEM showed large aggregates composed of smaller sub-micron sized particles (Figure 6.7.3). The aggregation of particles is attributed to the 15 hr annealing time required to get adequately crystalline samples for PXRD analysis.

Despite $Li_3Fe_2(PO_4)_3$ being synthesised here with a lithium-ion deficit, this potential lithium iron phosphate cathode is synthesised in the literature in its delithiated (fully charged) state, since iron is in the +3 oxidation state. During discharge, the structure is lithiated from Li^+ present in the electrochemical cell, forming $Li_5Fe_2(PO_4)_3$ with iron in the +2 oxidation state, with a theoretical discharge capacity of 128 $mA{\cdot}h\ g^{-1}$, hence the lithium deficiency is not overly problematic for this LIB cathode material.[56]

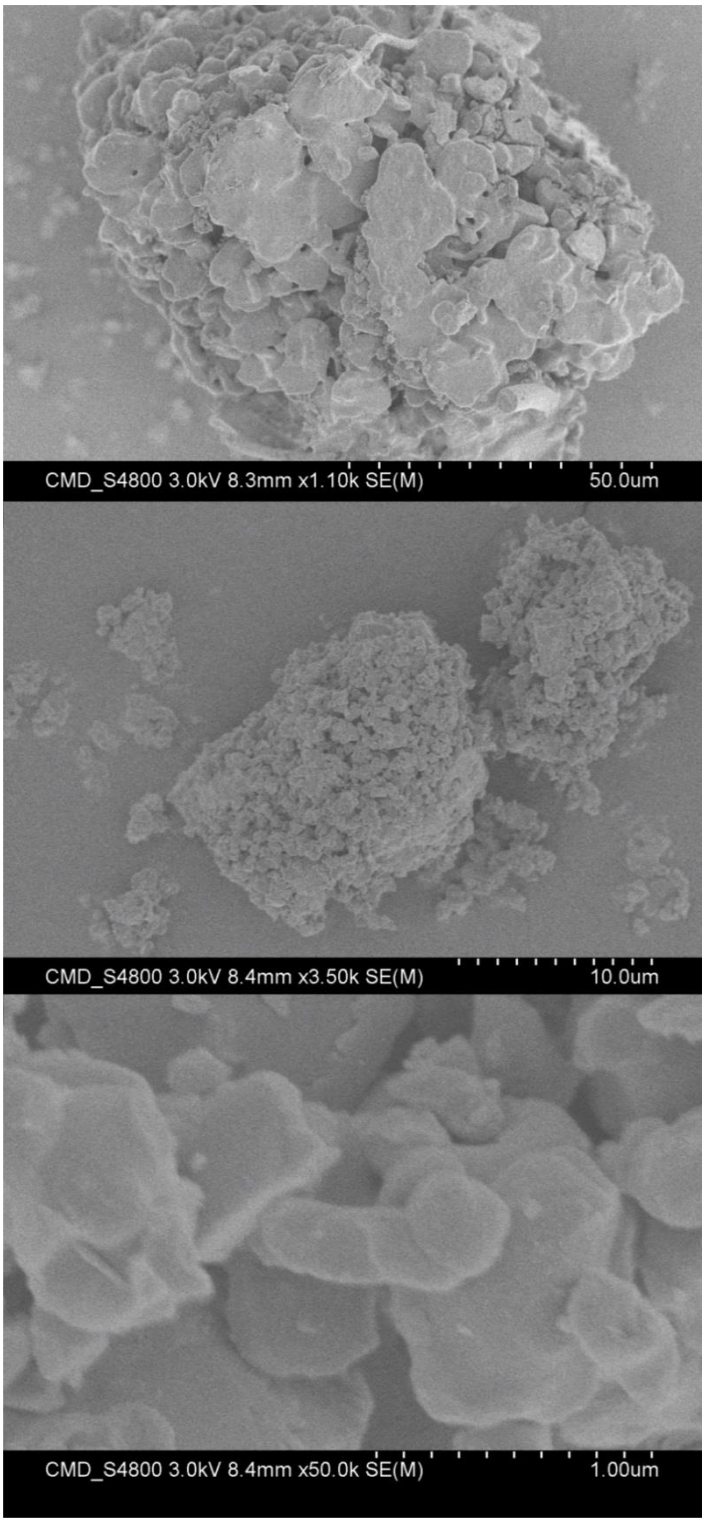

Figure 6.7.3: SEM images at various magnifications of $Li_3Fe_2(PO_4)_3$ synthesised by FSP using 10% molar Li excess following heat treatment, displaying particles up to 1 μm in size

The lithium manganese phosphates synthesised by FSP were analysed by PXRD. Firstly, the $LiMnPO_4$ olivine type was targeted for synthesis, which is as of yet

unreported by FSP. Olivine-type $LiMnPO_4$ (S.G. *Pmnb*) was determined to be obtained by PXRD analysis, with unit cell parameters of a = 10.442(3) Å, b = 6.096(2) Å, c = 4.742(4) Å, V = 301.9(1) $Å^3$ (Figure 6.7.4), in close agreement with the structure reported in literature.[57] Cubic $Mn^{(II)}O$ impurity was identified (6(1)% wt) with a further impurity unable to be conclusively identified, but is most likely to be a lithium or manganese pyrophosphate phase. The sample appeared poorly crystalline by PXRD as this sample was not heat treated after synthesis.

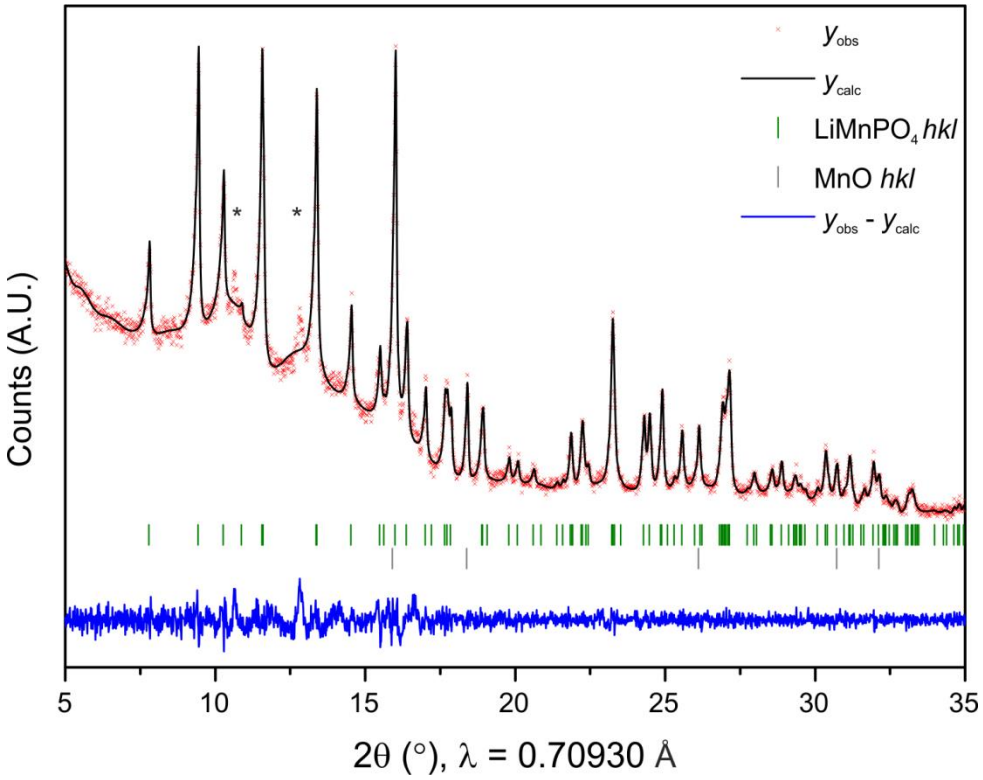

Figure 6.7.4: Le Bail fit of $LiMnPO_4$ synthesised by FSP without heat treatment, showing the *hkl* reflections of the $LiMnPO_4$ phase and 6(1)% MnO impurity. * indicate unidentified impurity peaks. χ^2 = 1.46

Attempts to synthesise the unreported $Li_3Mn_2(PO_4)_3$ structure, which is expected to also adopt a NASICON-type structure akin to the Fe analogue, were unsuccessful by FSP and by exploratory solid state and sol-gel synthesis. Adjusting the ratio of precursors to 3.3:2:3 (Li:Mn:P) for FSP synthesis resulted in primarily $LiMnPO_4$ and

possible pyrophosphate impurities such as $Li_2MnP_2O_7$, but due to the low crystallinity of the as-synthesised product and overlap of reflections with the main $LiMnPO_4$ phase, this could not be conclusively identified.

6.8 Conclusions and Future Work

First and foremost, very low mass yields (typically 5-10%) were obtained using both FSP setups, requiring multiple batch processes to obtain enough material for characterisation and electrochemical studies, which can increase product variance between batches. The sample was recovered from the collection plate after each batch run of ~20 mL total working solution to avoid further sintering of particles on the collection plate due to the heat of the flame and hence broadening the size distribution of particles and increasing average size beyond the desired nanometre range. Traces of chromium, vanadium and iron above background levels were detected by ICP-OES analysis when the stainless-steel collection plate was used, and was determined not to have originated from the metal nitrate precursors. For this reason, quartz plates were used in the advanced setup; however they were often scorched by the high temperature of the flame suggesting possible contamination of the product.

The requirement for liquid or aqueous precursors, such as soluble metal salts, provides limitations for the range of materials that can be viably produced for this method. Additionally, although often soluble, fluoride and chloride metal salts were not employed for synthesis to prevent the formation of harmful and acidic hydrogen halide gases. Numerous problems were encountered with solids precipitating when mixed in the syringe *via* the single injection method, and deposited within the instruments before reaching the flame. This was particularly apparent when metal acetate and phosphate precursors were used, which meant the equipment had to be dismantled and

cleaned which proved difficult. Due to this, there was unfortunately considerable down-time required while fixing and cleaning this equipment which limited the exploration of synthesis of new materials and the attainment of a sufficient mass of sample for full analysis.

This project has proved we can synthesise known lithium-ion battery cathode materials using a non-traditional industrial technique in a laboratory setting using relatively low-technology equipment. In addition, $LiMnPO_4$ has not been reported to be synthesised by this method but was achieved here, where nanosized particles are necessary to improve the rate capability. For all samples synthesised, post-synthetic annealing was determined necessary by assessment of the PXRD to improve the purity and crystallinity of the LIB cathodes (and hence the electrochemical performance); the additional sintering of which produces particles of greater size than the tens of nanometres range which was the primary target of the synthesis of LIB cathodes by FSP, and may promote the formation of metal oxide impurities. Potential methods for overcoming the low mass yield include using a bag filter for particle collection as often used in industry, or using a specially designed quartz funnel to collect more solid particles produced from the flame that divert away from the collection plate.

Although the laboratory setups of the FSP equipment were not appropriate for the sufficient production and analysis of phase pure lithium ion battery cathodes, it presents a useful method for the production of simple metal oxides or carbonaceous materials which have applications for LIB anode materials, whereby rate capability is often a limiting factor to performance; therefore nanostructuring is a widely used method for improving the electronic and ionic conductivity.

6.9 References

1. A. Purwanto, W. N. Wang and K. Okuyama, in *Handbook of Atomization and Sprays*, ed. N. Ashgriz, Springer US, New York City (NY), 1st edn., 2011, ch. 39, pp. 869-879.
2. S. E. Pratsinis, *Progr. Energy Combust. Sci.*, 1998, **24**, 197-219.
3. A. Stepuk, K. W. Krämer and W. J. Stark, *KONA Powder. Part. J.*, 2013, **30**, 267-275.
4. G. A. Sotiriou, M. Schneider and S. E. Pratsinis, *J. Phys. Chem. C*, 2010, **115**, 1084-1089.
5. B. Pongthawornsakun, S.-i. Fujita, M. Arai, O. Mekasuwandumrong and J. Panpranot, *Appl. Catal., A*, 2013, **467**, 132-141.
6. M. Piacentini, R. Strobel, M. Maciejewski, S. E. Pratsinis and A. Baiker, *J. Catal.*, 2006, **243**, 43-56.
7. J. M. Mäkelä, H. Keskinen, T. Forsblom and J. Keskinen, *J. Mater. Sci.*, 2004, **39**, 2783-2788.
8. R. Strobel, M. Maciejewski, S. E. Pratsinis and A. Baiker, *Thermochim. Acta*, 2006, **445**, 23-26.
9. T. Rudin and S. E. Pratsinis, *Ind. Eng. Chem. Res.*, 2012, **51**, 7891-7900.
10. S. Loher, W. J. Stark, M. Maciejewski, A. Baiker, S. E. Pratsinis, D. Reichardt, F. Maspero, F. Krumeich and D. Günther, *Chem. Mater.*, 2004, **17**, 36-42.
11. R. N. Grass and W. J. Stark, *Chem. Commun. (Cambridge, U. K.)*, 2005, 1767-1769.
12. L. Mädler, H. K. Kammler, R. Mueller and S. E. Pratsinis, *J. Aerosol Sci.*, 2002, **33**, 369-389.
13. Y. Iwako, Y. Akimoto, M. Omiya, T. Ueda and T. Yokomori, *J. Lumin.*, 2010, **130**, 1470-1474.
14. S. E. Pratsinis, W. Zhu and S. Vemury, *Powder Technol.*, 1996, **86**, 87-93.
15. J. Seok Lee, S. J. Kim, T. K. Kim, R. K. Singh and M. B. Ranade, *J. Mater. Res.*, 2009, **24**, 2584-2588.
16. G. A. Sotiriou, A. Teleki, A. Camenzind, F. Krumeich, A. Meyer, S. Panke and S. E. Pratsinis, *Chem. Eng. J. (Lausanne)*, 2011, **170**, 547-554.
17. L. Mädler and S. E. Pratsinis, *J. Am. Ceram. Soc.*, 2002, **85**, 1713-1718.
18. J. Azurdia, J. Marchal and R. M. Laine, *J. Am. Ceram. Soc.*, 2006, **89**, 2749-2756.
19. M. Nyman, J. Caruso, M. J. Hampden-Smith and T. T. Kodas, *J. Am. Ceram. Soc.*, 1997, **80**, 1231-1238.
20. A. J. Gröhn, S. E. Pratsinis, A. Sánchez-Ferrer, R. Mezzenga and K. Wegner, *Ind. Eng. Chem. Res.*, 2014, **53**, 10734-10742.
21. T. Tani, L. Mädler and S. E. Pratsinis, *Part. Part. Syst. Char.*, 2002, **19**, 354-358.

22. A. I. Y. Tok, F. Y. C. Boey and X. L. Zhao, *J. Mater. Process. Tech.*, 2006, **178**, 270-273.
23. K. Kai, Y. Kobayashi, H. Miyashiro, G. Oyama, S.-i. Nishimura, M. Okubo and A. Yamada, *ChemPhysChem*, 2014, **15**, 2156-2161.
24. N. Liu, H. Li, Z. Wang, X. Huang and L. Chen, *Electrochem. Solid-State Lett.*, 2006, **9**, A328-A331.
25. M. Jo, Y.-S. Hong, J. Choo and J. Cho, *J. Electrochem. Soc.*, 2009, **156**, A430-A434.
26. X. Xiao, L. Wang, D. Wang, X. He, Q. Peng and Y. Li, *Nano Res.*, 2009, **2**, 923-930.
27. D. Liu, J. Han and J. B. Goodenough, *J. Power Sources*, 2010, **195**, 2918-2923.
28. Y. Shin and A. Manthiram, *Electrochim. Acta*, 2003, **48**, 3583-3592.
29. M. Xu, S. Dalavi and B. L. Lucht, in *Lithium Batteries*, eds. B. Scrosati, K. M. Abraham, W. A. van Schalkwijk and J. Hassoun, John Wiley & Sons, Inc., Hoboken (NJ), 1st edn., 2013, ch. 4, pp. 71-87.
30. G. G. Amatucci, A. Blyr, C. Sigala, P. Alfonse and J. M. Tarascon, *Solid State Ionics*, 1997, **104**, 13-25.
31. S. H. Choi, J. H. Kim, Y. N. Ko, K. M. Yang and Y. C. Kang, *J. Power Sources*, 2013, **244**, 129-135.
32. O. Waser, R. Büchel, A. Hintennach, P. Novák and S. E. Pratsinis, *J. Aerosol Sci.*, 2011, **42**, 657-667.
33. X. Zhang, H. Zheng, V. Battaglia and R. L. Axelbaum, *J. Power Sources*, 2011, **196**, 3640-3645.
34. J. H. Yi, J. H. Kim, H. Y. Koo, Y. N. Ko, Y. C. Kang and J.-H. Lee, *J. Power Sources*, 2011, **196**, 2858-2862.
35. J. H. Kim, Y. J. Hong, B. K. Park and Y. C. Kang, *J. Ind. Eng. Chem.*, 2013, **19**, 1204-1208.
36. J. H. Kim, J. H. Yi, Y. N. Ko and Y. C. Kang, *Mater. Chem. Phys.*, 2012, **134**, 254-259.
37. H. Chang, H. D. Jang, S. M. Shin, S. W. Cho and D. S. Kil, *Mater. Lett.*, 2011, **65**, 757-759.
38. T. N. L. Doan and I. Taniguchi, *J. Power Sources*, 2011, **196**, 1399-1408.
39. A. L. Patterson, *Physical Review*, 1939, **56**, 978-982.
40. L. Li, R. Chen, X. Zhang, F. Wu, J. Ge and M. Xie, *Chin. Sci. Bull.*, 2012, **57**, 4188-4194.
41. M. Y. Saïdi, J. Barker and R. Koksbang, *Electrochim. Acta*, 1996, **41**, 199-204.
42. M. Kunduraci and G. G. Amatucci, *J. Electrochem. Soc.*, 2006, **153**, A1345-A1352.
43. V. M. Talanov, M. V. Talanov and V. B. Shirokov, *Crystallogr. Rep.*, 2016, **61**, 159-169.
44. R. Amin and I. Belharouk, *J. Power Sources*, 2017, **348**, 311-317.

45. J. H. Kim, S. T. Myung, C. S. Yoon, S. G. Kang and Y. K. Sun, *Chem. Mater.*, 2004, **16**, 906-914.

46. P. Strobel and B. Lambert-Andron, *J. Solid State Chem.*, 1988, **75**, 90-98.

47. P. Barpanda, S.-i. Nishimura and A. Yamada, *Adv. Energy Mater.*, 2012, **2**, 841-859.

48. M. Tamaru, P. Barpanda, Y. Yamada, S.-i. Nishimura and A. Yamada, *J. Mater. Chem.*, 2012, **22**, 24526-24529.

49. S.-i. Nishimura, M. Nakamura, R. Natsui and A. Yamada, *J. Am. Chem. Soc.*, 2010, **132**, 13596-13597.

50. B. E. Francisco, C. R. Stoldt and J.-C. M'Peko, *Chem. Mater.*, 2014, **26**, 4741-4749.

51. C. Masquelier and L. Croguennec, *Chem. Rev. (Washington, DC, U. S.)*, 2013, **113**, 6552-6591.

52. N. Plylahan, C. Vidal-Abarca, P. Lavela and J. L. Tirado, *Electrochim. Acta*, 2012, **62**, 124-131.

53. A. B. Bykov, A. P. Chirkin, L. N. Demyanets, S. N. Doronin, E. A. Genkina, A. K. Ivanov-shits, I. P. Kondratyuk, B. A. Maksimov, O. K. Mel'nikov, L. N. Muradyan, V. I. Simonov and V. A. Timofeeva, *Solid State Ionics*, 1990, **38**, 31-52.

54. G. Butt, N. Sammes, G. Tompsett, A. Smirnova and O. Yamamoto, *J. Power Sources*, 2004, **134**, 72-79.

55. A. K. Ivanov-Schitz, A. V. Nistuk and N. G. Chaban, *Solid State Ionics*, 2001, **139**, 153-157.

56. H. Karami and F. Taala, *J. Power Sources*, 2011, **196**, 6400-6411.

57. O. García-Moreno, M. Alvarez-Vega, J. García-Jaca, J. M. Gallardo-Amores, M. L. Sanjuán and U. Amador, *Chem. Mater.*, 2001, **13**, 1570-1576.

Chapter 7: Conclusions

The most promising class of lithium-ion battery cathodes were determined to be lithium-rich rock-salt superstructures, offering greater discharge capacity by comparison to stoichiometric cathodes (such as $LiCoO_2$) due to the additional lithium content. The mechanisms of lithium ion extraction and insertion into cathode materials are discussed in relation to their structures. In addition to the classical cation redox, observed in layered rock-salt type $LiCoO_2$ for example, particular attention is focused on the factors involved in enabling the anionic redox process in lithium-rich materials. The discovery of the anionic redox originates from the extensive research into lithium-rich layered composite rock-salts of the general form $xLi_2MnO_3{\cdot}(1\text{-}x)LiMO_2$ (M = Co, Ni, Mn, etc.), whereby lattice oxide (O^{2-}) has been determined to oxidise to O_2 gas on charging enabling extraction of lithium from the Li_2MnO_3 component. Suppression of the oxidation of oxide to form intermediate peroxo-type species (O_2^{n-}), as opposed to full oxidation to O_2 gas, is a key requirement to utilising the lattice oxygen reversibly to extract additional capacity without compromising the safety and longevity of the battery materials. Through evaluation of the structural conditions determined for reversible anionic redox processes, new compounds of the form $Li_{4+x}Ni_{1-x}WO_6$ were synthesised.

Within this thesis, the synthesis and structural refinement of new Li-rich rock-salt materials exhibiting partial cation order are reported, using combined Rietveld refinement of SXRD and NPD data. Li_4NiWO_6 was found to crystallise in the monoclinic $C2/c$ space group (a = 5.84579(10) Å, b = 17.58769(35) Å, c = 5.109138(9) Å, β = 124.768(1)°, V = 431.506(2) Å^3), determined to be a

monoclinic distortion of the $Li_3Ni_2TaO_6$ (orthorhombic space group *Fddd*) rock-salt archetype, possessing mixed cation sites. The structural model for the *C*2/*c* Li_4NiWO_6 was obtained from transformation of the $Li_3Ni_2TaO_6$ structure, since *C*2/*c* space group is an isomorphic subgroup of *Fddd*. The deviation from orthorhombic symmetry is attributed to distortion of WO_6 octahedra, with possible regions of disorder observed in the high-resolution SXRD data (due to broadening observed between monoclinic Bragg reflections). The broadening was modelled by inclusion of a more disordered model, obatined by transformation of the Li_4NiWO_6 *C*2/*c* structure back to the *Fddd* space group setting. The ratio of cations were confirmed using ICP-OES and TEM-EDX analysis. Li_4NiWO_6 was tested as a lithium-ion battery cathode material, exhibiting a modest discharge capacity of 82 mA·h g^{-1}, which decreased to ~50 mA·h g^{-1} after 20 electrochemical cycles when cycled between 1-5 V. The poor electrochemical performance is attributed to the absence of fully occupied lithium layers, which still enables some capacity to be extracted due to an alternate Li^+ ion percolation network. The rapid capacity fade may be due to increasing the amount of cation disorder between lithium and nickel, in addition to the presence of W^{6+} in every *ccp* oxide layer hindering Li^+ diffusion throughout the material.

Adding 12 mol% lithium excess during the synthesis of Li_4NiWO_6 targeted a compositionally related phase with a different crystal structure, which through combined Rietveld refinement (in addition to ICP and TEM-EDX) was determined to be $Li_{4.1}Ni_{0.9}WO_6$, with a small amount of a $Li_{0.3}Ni_{0.7}O$ impurity phase. $Li_{4.1}Ni_{0.9}WO_6$ was found to adopt the *Cm* structure (a = 5.113747(23) Å, b = 8.791326(40) Å, c = 5.093213(23) Å, β = 110.1564(12)°, V = 214.950(2) $Å^3$); a non-centrosymmetric variant of the layered Li_5ReO_6 archetype (*C*2/*m*). The structure possesses two different types of alternating layers with mixed cation sites. The greatest proportion of Ni is

located in the W layer, which alternates with a Li-rich layer. The presence of the $Li_{0.3}Ni_{0.7}O$ lead to the conclusion that altering the Li:Ni ratios would likely result in a phase pure compound, resulting in the synthesis of $Li_{4.15}Ni_{0.85}WO_6$. $Li_{4.15}Ni_{0.85}WO_6$ was also determined to adopt the *Cm* structure and was determined to be phase pure by SXRD.

$Li_{4.15}Ni_{0.85}WO_6$ was tested as a LIB cathode material. Ball-milling the material after synthesis to decrease particle size and increase surface area was found to enhance the initial discharge capacity by over 64%, giving an initial discharge capacity of 200-210 mA·h g^{-1} and a reversible discharge capacity of ~173 mA·h g^{-1} which is comparable to other Li-rich rock-salt cathodes. Unfortunately ball-milling also had the effect of accelerating the capacity fading over numerous cycles, attributed to structural transformations (as determined from shifts in the voltages of the redox processes and *ex-situ* SXRD of the material at various stages of (de)lithiation throughout the first and second cycles) and increased side-reactions with the electrolyte (due to cycling at voltages beyond the stability window of the carbonate-based electrolytes used for testing). The practical capacity of this material was determined to exceed the theoretical capacity, which was calculated solely on the reversible cationic redox of nickel, therefore additional *ex-situ* characterisation of the electrochemical behaviour was undertaken. XPS and XANES spectroscopy were used to observe the changes in the nickel oxidation state at various stages of the first two electrochemical cycles, which was determined to reach the +3 oxidation state at full charging to 5 V, and the reduction of nickel on discharge was found to occur in two stages. Tungsten was determined to remain in the +6 oxidation state throughout cycling. The source of additional capacity was confirmed to be the result of anionic redox processes, with peroxo-type species detected using XPS and HAXPES of the O1*s* energy level, with

an average oxidation state of $O^{1.45(5)-}$ detected at full charge. The use of HAXPES (XPS using hard X-rays with a high flux to penetrate into the bulk of the material) suggests that the peroxo-species are formed in the bulk of the material (*i.e.* likely to be solid state peroxo-species) and not just occurring at the surface. $Li_{4.15}Ni_{0.85}WO_6$ was determined to exhibit unusual electrochemical behaviour, with the anionic redox occurring at lower voltages than the cationic redox, and the anionic redox accounting for ~2/3 of the observed practical capacity. Unfortunately a wide voltage window (1-5 V) is required to extract the maximum amount of capacity possible, which will enhance the degradation of the electrolyte (which is only stable up to ~4.7 V). In addition, despite the relatively high capacity, the energy density of the material is poor due to the huge voltage hysteresis determined for both the anionic and nickel redox processes. The reversibility of the capacity however indicates that oxygen evolution is suppressed in this material, which (by comparison to the poor performance of the structurally related Li_4NiTeO_6 system) is attributed to the influence of W^{6+} ($5d^0$) acting to stabilise the peroxo species and suppressing full oxidation of lattcie oxide to O_2 gas. At the time of writing, a journal publication is in preparation regarding the electrochemical behaviour of $Li_{4.15}Ni_{0.85}WO_6$.

Since research into Li-rich composite cathodes to date largely centres around $Li_2MO_3{\cdot}LiTMO_2$ systems (*M* = Mn, Mo *etc.*; *TM* = Co, Ni, Mn *etc.*), the synthesis and characterisaiton of unreported $(1\text{-}x)LiCoO_2{\cdot}xLi_4WO_5$ were explored in this thesis. Both $LiCoO_2$ ($R\bar{3}m$) and Li_4WO_5 ($P\bar{1}$) possess fully occupied lithium layers with rock-salt type superstructures, hence are deemed compatible for formation of a lithium-rich solid solution/composite Li-rich cathode. Effectively, $1Co^{3+}$ ion is replaced with $^4/_5Li^+$ and $^1/_5W^{6+}$, with a view to increasing the total Li content and adding structural stabilisation with W^{6+}. The doping limit using the solid state synthetic method reported

here was determined to be between 2-2.5% by PXRD analysis, with a variation in lattice parameters observed throughout the doping series which retain the $R\bar{3}m$ unit cell structure. Members of the series where $x = 0.010$ and $x = 0.025$ were tested for their electrochemical properties in comparison to the parent $LiCoO_2$, and the doped materials were found to exhibit superior discharge capacities, rate capabilities and capacity retention. The greater discharge capacities of the doped materials are attributed to the additional lithium content (as determined by compositional analysis by ICP-OES), with the superior rate capabilities attributed to the presence of W^{6+} ions broadening the lithium-ion diffusion channels and promoting facile ionic and electronic conduction. In addition, the particle size of the doped materials was found to be smaller *cf.* $LiCoO_2$ through SEM imaging, which likely acts to enhance Li^+ diffusion throughout the cathode.

The use of flame spray pyrolysis (FSP) in a simple laboratory setup was used to assess the properties of synthesising known cathodes using this technique, which is often used in industrial settings for nanoparticle production. A cobalt-rich $LiCoO_2$-type material was synthesised by FSP and subject to electrochemical testing, which exhibited rapid capacity degradation by comparison to $LiCoO_2$ synthesised by the solid state method. The synthesis of more Li-metal oxide cathodes was also reported. The feasibility of synthesising polyanionic cathodes by this method was explored, for which slow Li^+ diffusion kinetics and electronic conduction are limiting factors in their electrochemical performance. Unfortunately, the FSP setups described in this thesis afforded very low product yields (typically 5-10%), with impurities detected in all samples by PXRD. However this rapid high-temperature synthetic method did result in nanoparticle-sized products (as determined by SEM imaging), but the requirement for additional annealing to improve crystallinity and purity negates the purpose of

synthesis by this method. The more advanced FSP setup was deemed unsuitable for the production of polyanionic cathodes, since the requirement for liquid precursors resulted in precipitation prior to reaching the flame.

In summary, it is hoped that the work presented in this thesis will contribute towards the understanding of the anionic redox mechanisms occurring in lithium-rich rock-salt type oxides; and that the chemistry of heavier 5*d*-metals such as tungsten should not be overlooked in the development of new, high energy density rechargeable battery materials.